Towards control of the optoelectronic properties of organic-inorganic perovskites

Gelvez Rueda, Maria

DOI
10.4233/uuid:5ecb27b4-746c-49db-8b4d-491f2c6f8155

Publication date
2020

Document Version
Final published version

Citation (APA)
Gelvez Rueda, M. (2020). *Towards control of the optoelectronic properties of organic-inorganic perovskites*. [Dissertation (TU Delft), Delft University of Technology]. https://doi.org/10.4233/uuid:5ecb27b4-746c-49db-8b4d-491f2c6f8155

Important note
To cite this publication, please use the final published version (if applicable).
Please check the document version above.

Towards control of the optoelectronic properties of organic-inorganic perovskites

Towards control of the optoelectronic properties of organic-inorganic perovskites

Dissertation

for the purpose of obtaining the degree of doctor
at Delft University of Technology,
by the authority of the Rector Magnificus prof. dr. ir. T. H. J. J. van der Hagen,
chair of the Board of Doctorates,

to be defended publicly on
Thursday 23 January 2020 at 10:00 a.m.

by
María Camila GÉLVEZ RUEDA

Master of Science in Sustainable Energy Technologies,
Delft University of Technology, Netherlands
born in Bucaramanga, Colombia

This dissertation has been approved by the promotors:

Dr. F.C. Grozema
Dr. ir. T.J. Savenije

Composition of the doctoral committee:

Rector Magnificus	chairperson
Dr. F.C. Grozema	Delft University of Technology, promotor
Dr. ir. T.J. Savenije	Delft University of Technology, promotor

Independent members:

Prof. dr. D. Vanderzande	Hasselt University, Belgium
Prof. dr. G. Rumbles	University of Colorado, USA
Dr. E.L. von Hauff	Vrije Universiteit Amsterdam
Prof. dr. B. Dam	Delft University of Technology
Prof. dr. ir. H.S.J. van der Zant	Delft University of Technology

The work described in this thesis was funded by the European Research Council.

ISBN:

Cover design by Camila Serrano Rueda
Printed by
An electronic version of this thesis is freely available at
http://repository.tudelft.nl

about (science), photography and life

i constantly think about the forces that bind us together
the (electrical and magnetic) fields that drag us apart
the (polarized) differences that enhance or decrease, ignite or extinguish our connections
how we are, but not are, at a certain moment, in a certain place

but, ironically, how we (collapse) in a certain state
without moving
trapped in our own (forbidden) energy levels, our own (defect) layers
without (delocalizing) to (generate) our flow back
or at least hop(e) from external warmth
failing to understand that we all are (superposed) on each and every one
that is what life and death are

i pursue what makes us not realize
trying to find that moment in space that we let go away
that is beautiful because is ephemeral
that is nowhere and everywhere in a different way
that (recombines) to bind us again
and (light) what was always there and we miss to appreciate

Table of contents

Chapter 1
Introduction: Organic-Inorganic Metal-Halide Perovskites

The term "perovskite" refers to a broad class of materials with a ABX_3 chemical structure (Figure 1.1a) that have the same crystal structure as $CaTiO_3$, the first member of this class of materials discovered in 1839. In this general structure, A and B are cations and X is an anion that coordinates with B. The B-site cation is six-coordinated with the X-site anion to form a BX_6 octahedra. These octahedra from a three-dimensional (3D) framework by corner-sharing the X-site anions while the A-site cations are located in the cavities of the framework balancing the charge of the structure. Currently, close to two thousand materials are known that exhibit the $CaTiO_3$ perovskite structure and many more have been theoretically predicted to be stable. These perovskite materials exhibit an extreme range of interesting properties for materials science, including superconductivity, magnetoresistance, ionic conductivity, ferroelectricity, ferroelasticity and a multitude of dielectric properties.[1] In recent years, a specific class of perovskite materials: hybrid organic-inorganic metal halide perovskites (HOIPs) have attracted a lot of research attention due to their outstanding semiconductor properties for photovoltaic applications.[2] In these HOIPs, A consists of an organic cation such as methylammonium (MA) or formamidinium (FA), B is a divalent metal ion such as lead (Pb) or tin (Sn), and X is a halide ion such as iodide (I), bromide (Br), chloride (Cl). Solar cells utilizing 3D HOIPs as the main absorber have reached solar to power efficiencies of 25.2%,[3] approaching established materials for solar cell application such as silicon. The high efficiencies achieved, combined with low cost related to their wet chemical processing, make them an alternative that is able to dictate the progress of third generation photovoltaic solar cells.[4] The outstanding opto-electronic properties of 3D HOIPs include high absorption coefficient, high static dielectric constant, low effective mass of charge carriers, ambipolar charge-carrier mobilities, high tolerance to defects and long lifetime and diffusion length.[1,2,4]

A particularly aspect of HOIPs is that they exhibit a high chemical versatility.[1] It is possible to synthesize 3D HOIPs in the pure ABX_3 form or with mixtures of each component (like $FA_{1-x}MA_xPbI_3$ or $MAPbI_{3-x}Br_x$, among others). In addition, there are HOIPs with crystal structures that are not in the ABX_3 form but are still considered to be related to perovskites due to the preservation of the divalent-metal halogen [BX_6] octahedra. For example, replacing the divalent metal for a combination of a monovalent and a trivalent metal results in so called halide double perovskite structures ($A_2M^+M^{3+}X_6$) (Figure 1.1b). Replacements of the A cation is also possible but to maintain a 3D structure only small variations are possible and the stable 3D HOIP structures reported are largely dominated by MA, FA or a Cs ions. Interestingly, introduction of larger organic cations that do not fit in the 3D octahedra framework can result in lower-dimensional structures such as two-dimensional (2D) layered perovskites (A_2MX_4) (Figure 1.1c). The optoelectronic properties of these 2D layered and double HOIPs significantly differ from ABX_3 perovskites and extend the applicability of HOIPs to other optoelectronic devices such as light-emitting diodes, nano-lasers, photocatalysts. In general,

the optoelectronic properties of HOIPs are intrinsically linked to the nature of its components (size, polarity) and interaction within the crystal structure.

The major theme of this thesis is to study how the optoelectronic properties of HOIPs can be tuned and optimized by varying the individual components. This results in changes in the structure from 'traditional' 3D perovskite to double perovskites and lower-dimensional 2D perovskites and 1D 'perovskitoids' structures (Figures 1.1 and 1.2). The central goal is not only to understand how the optoelectronic properties are affected by the components but to be able to achieve control over these properties. The main focus will be on variations in the organic cation as synthetic organic chemistry allows the introduction of a wide range of functionalities. Ultimately, it is shown that it is possible to reach a synergetic effect where the combination of the inorganic framework with well-designed organic chromophores leads to new built-in functionality.

In the sections below, an overview is given of the HOIPs structures studied in this thesis with a more detailed description of the structural and optoelectronic properties.

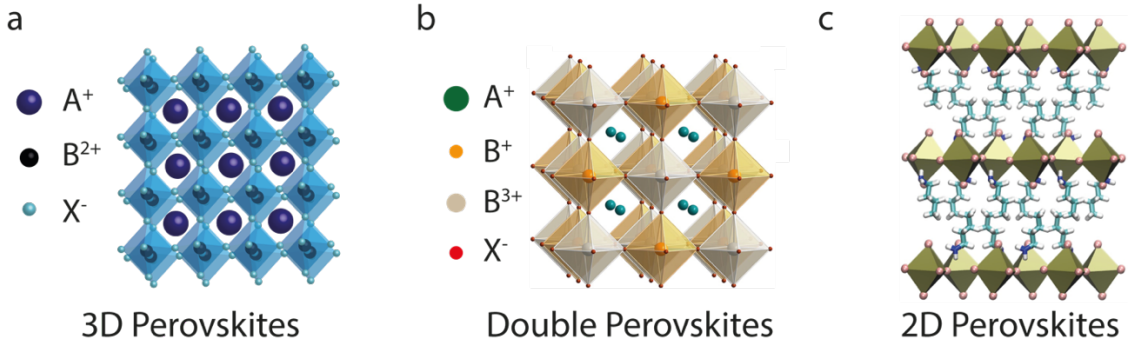

Figure 1.1. Crystal structures of hybrid organic-inorganic metal halide perovskites (HOIPs). a) three dimensional (3D). **b)** double perovskites (alternating metal halide octahedral). **c)** two-dimensional.

1.1. Three-dimensional organic-inorganic metal halide perovskites

Three-dimensional (3D) hybrid organic-inorganic metal halide perovskites (HOIPs) (Figure 1.1a) have been extensively studied in the last 10 years due to their high solar to power efficiency (25.2%)[3] when used as the main absorber in solar cells. The properties that make these materials so efficient for solar cell application, and potentially also to light-emitting devices, are their high absorption coefficient, a high static dielectric constant, low effective mass of charge carriers, high ambipolar charge-carrier mobilities, a high tolerance to defects and a long lifetime and diffusion length of the charge carriers.[1,2,4,5] In addition, the exciton binding energies in 3D HOIPs are rather low, even though the debate on the exact values is

not fully settled as values ranging from 5 meV to 30 meV have been reported.[6–9] Even for the higher values in this range virtually all excitations result in free electrons in the CB and holes in the VB at room temperature (thermal energy ~26 meV) while the excitation density is below 10^{16} photons/cm^3.[10] The combination of all these properties is rather unusual, which makes these materials and their properties quite unique. For instance, a large carrier mobility is generally accompanied by fast recombination of charges, which does not turn out to be the case in 3D HOIPs. Explanations such as 3D HOIPs being indirect[11] semiconductors or the presence of photon reabsorption[12] are still under discussion and their exact unravelling is complicated by the presence of structural variations and trap states, that depend on the synthesis and deposition method.

Finding the origin of all these properties requires a careful analysis of the structure of these materials. Regardless of the large impact of these materials in the field of photovoltaics, their composition is limited to only a few components: I, Br, Cl in the X-site and Pb or Sn in the B-site. The resulting BX_3- octahedral framework can only accommodate small organic cations, such as methylammonium (MA) and formamidinium (FA). In general, the electronic band structure of these semiconductors is dominated by the orbitals of the inorganic octahedra. The valence band maximum (VB) is mainly composed of *s*-orbitals on the divalent metal and *p*-orbitals on the halide, while the conduction band minimum mainly consists of *p*-orbitals on the divalent metal. The halogen atom has a direct influence on the band gap of 3D HOIPs.[13,14] On changing the halide ion from Cl to Br to I, the valence band contribution changes from 3p to 4p to 5p. This causes a decrease of the exciton binding energy (lower ionization potential) and a decreasing of the band gap from 2.96 eV to 2.22 eV to ~1.53 eV as observed in experiments.[15] Even though the orbitals on the organic cation do not contribute directly to the band structure, the presence of these cations can indirectly influence the electronic properties by distortions of the inorganic octahedral framework. In fact, the displacements of the A- and B-sites, and the off-center tilting of the BX_6 octahedral framework are the main factors that cause distortions of the structure and symmetry variations in HOIPs.[16,17] The orientation and position of the organic cations in the inorganic framework are relatively disordered, leading to variations in the hydrogen bonding and dispersion forces. This, in turn, leads to complicated phase transitions in the materials that can have a significant effect on the dielectric properties.[18,19] In addition, when the organic cation has a large dipole moment (for example, MA) specific alignments of these dipoles can arise, for instance resulting in bulk electric ordering.[20] Currently, no clear picture is available that directly relates the structural properties (crystal structure) to the transport properties of charge carriers and their decay by recombination and trapping in HOIPs. Transport mechanisms such as carrier-phonon scattering or interaction of the charge carriers with the lattice (polaron formation) have been proposed but it is not entirely clear how the distortions of inorganic octahedral lattice or the

dynamic disorder of the organic cation affect the charge dynamics.[21,22] In this thesis, **Chapter 3** and **Chapter 4**, focus on determining by time-resolve microwave conductivity the charge carrier dynamics of HOIPs as a function of distortions in the crystal structure caused by thermal energy (temperature) and the dynamic disorder of the organic cation (function of its polarity and interaction with the inorganic framework).

1.2. Double halide perovskites

The presence of lead (Pb) in the chemical structure of 3D perovskites raises toxicity concerns for large scale commercial application.[23,24] An alternative, which has the added advantage of a high stability, is to replace the lead ions by a combination of a monovalent and a trivalent metal cation such as silver (Ag^+) and bismuth (Bi^{3+}). This results in a modified halide double perovskite (HDP) structure ($Cs_2AgBiBr_6$) with ordered monovalent and trivalent metal-sites alternating in the lattice (Figure 1.1b). $Cs_2AgBiBr_6$ has a very high stability but also an indirect band gap that is much larger than for lead-iodide based HOIPs (2.07 eV), making it unsuitable for application in single-junction solar cells.[25] Nonetheless, this HDP material exhibits a photoluminescent (PL) lifetime comparable to 3D perovskites but with a low PL intensity consistent with its indirect band gap nature.[25] Although these materials have some promising electronic properties further research is necessary to clarify their charge carrier dynamics and improve their optical absorption properties. In addition, similar as in oxide perovskites, these materials could exhibit exotic magnetic ground state properties arising from spin frustration[26] or unusual electronic states such as metallic ferromagnetism[27] or large magneto-resistance.[28] In **Chapter 5** we have investigated the opto-electronic properties of double perovskites by TRMC techniques.

1.3. Two-dimensional organic-inorganic metal halide perovskites

2D organic-inorganic metal halide perovskites are layered materials that are formed by partially or fully replacing the small methylammonium (MA) cation with a larger cation. This reduces the 3D perovskite framework to 2D layered structures due to steric hindrance (Figure 1.1c).[29] 2D perovskites with a large organic cation were extensively studied in the 90s for their unique quantum-well structure that enhances exciton confinement beyond predictions for 2D systems.[30–35] The additional confinement is caused by the large difference between the dielectric constants of the organic compound "barrier" and the inorganic "well".[36–39] Recently, layered 2D perovskites have gained significant attention because of their improved moisture stability compared to 3D perovskites, promising device efficiency, and intriguing optical properties.[40–49] Generation of long-lived (Wannier-Mott) excitons with exciton binding

energies of several hundreds of meV,[36,38] renders these materials good candidates for photo-luminescent applications such as lasers and light emitting diodes (LDs and LEDs),[50,51] nonlinear optical[52] and polaritonic devices.[40,53–56] However, in many cases they exhibit inefficient luminescence at room temperature possibly due to thermal quenching of the excitons or strong exciton-phonon interactions.[31,35,49,57–60] A detailed understanding of these materials, especially the photo-generation and transport of charges, is currently lacking.[2]

An interesting feature of 2D hybrid perovskites is the high tunability of their chemical and physical properties. The layered structure lifts the size requirements for the organic cation that can fit in between the inorganic octahedra layers. In principle, there are endless possibilities of compounds that could be introduced in this organic layer to tune and "design" the properties of 2D perovskites. For example, it is possible to combine the large organic cations with small organic cations such as MA. This leads to quasi-2D materials where multiple layers of inorganic octahedra, containing for instance MA, are separated by the larger organic cations. In this way the thickness of $[(MA)_{n-1}Pb_nI_{3n+1}]^{2-}$ slabs can be controlled through the value of n (Figure 1.2a).[32,36,42,61] These structures can form Ruddlesden-Popper (RP) or Dion-Jacobson (DJ) phases.[41,62,63] These phases vary by the relative stacking of the inorganic octahedral layers. RP phases are characterized by two offset layers per unit cell while DJ feature divalent interlayer spacer molecules so that they stack in a perfect (0,0 displacement) or imperfect (0, ½ or ½, ½ displacement).[62–64] Highly efficient solar cells (PCE of 12.5%)[45] and LEDs (EQE of 8.8%)[49] based on these materials have been reported recently. These devices were based on RP 2D perovskites with butylammonium (BA) and phenylethylammonium (PEA) as the bulky organic cations. **Chapter 6** focuses specifically on how the exciton binding energy (i.e. probability of dissociation of excitons and the recombination of charges) of Ruddlesden-Popper phases is affected by the number of inorganic layers n. This systematic study of phases in between 2D and 3D aims to clarify the nature of the photo-excited excitons, as well as the exciton binding energy values for 2D and 3D perovskites**.** In **Chapter 7** the emphasis is on the relation between the nature of the large organic cation and the properties and lifetime of the excited states in 2D perovskites with n=1.

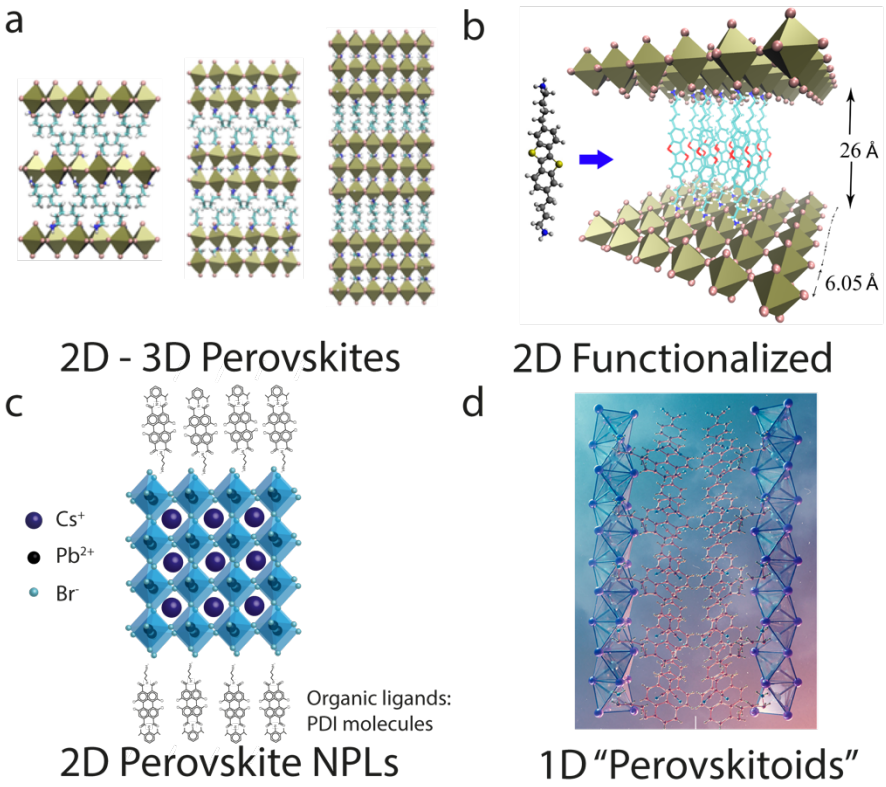

Figure 1.2. Structural tunability of 2D hybrid perovskites. a) Ruddlesden-Popper 2D – 3D Perovskites (n=1, 2, 3). **b)** 2D perovskites with functional organic cations, in this case a benzothiophene BTBT donor molecule. **c)** 2D perovskite colloidal $CsPbBr_3$ nanoplatelets (NPLs) with perylene diimide molecules as organic ligands. **d)** 1D "perovskitoids".

The presence of large organic moieties in between the inorganic layers in 2D perovskites offer the interesting possibility to introduce functionality in the organic cation. An example is the inclusion of strongly electron withdrawing or donating molecules (Figure 1.2b). Until now, in the majority of studies, the large organic cation used has been an alkylammonium (mostly butyl) or phenyl-alkylammonium. These compounds lack specific functionality and do not directly contribute to the opto-electronic properties other than by affecting the structure of the inorganic octahedral layers. However, it has been shown theoretically that functional donor or acceptor molecules could directly contribute to the band structure.[65] This could result in enhanced charge separation, compared to current 2D perovskites where the organic cation merely acts as a non-functional dielectric spacer-layer (resulting in high exciton binding energy ranging from ~190-400 meV for pure 2D[36–38,46]). It should be noted that it is hard to predict a priori whether stable 2D materials will be formed, and other dimensionalities are sometimes obtained because of the interactions between the organic chromophores and/or changes in the connectivity of the inorganic octahedrals from corner-shared to face or edge-shared.[66–69]

In **Chapter 8** an attractive approach is explored to study the effect of organic molecules on the photo physics of 2D perovskites by attaching them to colloidal 2D perovskite

nanoplatelets (NPLs) in solution (Figure 1.2c).[70–72] This reduces the packing requirements of the organic molecules as only a small fraction of the ligands can be replaced with the conjugated molecules. In **Chapter 9** the photophysical properties are studied of 2D perovskites where donor, acceptors, and complete organic charge-transfer complexes have been introduced in between the inorganic layers. Finally, in **Chapter 10** the synthesis and optoelectronic properties of non-perovskites 1D structures formed when bulky organic chromophores are introduced (Figure 1.2d). Although these structures are not formally perovskites they been referred to as "perovskitoids" in literature[73–75] as they preserve the inorganic octahedral layer with face or edge-shared connectivity. In the remainder of this thesis they will be called 1D perovskites.

1.4. Outline of this thesis

In this thesis we have aimed to tune and control the optoelectronic properties of organic-inorganic metal halide perovskites by systematically changing components in the structure and studying the dynamics of charge carriers in the resulting materials. In **Chapter 3** and **Chapter 4** time-resolved microwave conductivity experiments are presented on common 3D perovskites, methylammonium-leadhalide and formamidinium leadhalide perovskite. Particular attention is paid to the relation between the rotational dynamics of the organic cations and the charge dynamics in these materials. It is shown, that for dipolar cations, marked effects can be observed, especially at low temperatures where the rotational dynamics is frozen.

A common concern for commercial application of organic-inorganic perovskites is the high toxicity from lead. In **Chapter 5**, the charge carrier dynamics is discussed of alternative materials with lower-toxicity such as lead replacement with tin (Sn) and monovalent and trivalent metals such as silver (Ag) and bismuth (Bi) forming the so-called double perovskites. TRMC experiments discussed in this chapter reveal the charge carriers dynamics in these materials and give some clues on how to improve the properties for device applications.

In **Chapter 6** and **Chapter 7** the attention is turned to 2D perovskites that are formed when organic cations are introduced with a size that is too large to form a 3D structure. It is shown that the charge carrier dynamics in these materials differs markedly from their 3D counterparts. In **Chapter 6**, we studied the effect of varying the number of inorganic layers in between the large organic cations. As the number of inorganic layers increases, the opto-electronic properties behave more as in 3D hybrid perovskites. It is shown that the exciton binding energy is much higher than in 3D perovskites but that it can be tuned to a large extent by varying the thickness of the inorganic layers. In **Chapter 7 the** effect of the structure of the large organic cation on the optoelectronic properties is considered. In all compounds studied

in this chapter, there is no direct contribution of the organic cation to the electronic structure but the optoelectronic properties are affected because changes in the organic component leads to distortions in the inorganic octahedral layers.

In the 2D structures studied in chapter 6 and 7 the large organic cations act as a barrier without contributing to the charge transport. However, it is also possible to introduce specific functionality in the organic cations, for instance strong electron donors or acceptors to enhance the dissociation of excitons in 2D hybrid perovskites. This idea is explored in **Chapter 8**, **Chapter 9** and **Chapter 10**. The focus in these chapters is on the incorporation of functional organic cations in 2D hybrid perovskites to overcome that large exciton binding energies in these systems and achieve efficient charge separation. In **Chapter 8**, a solution phase model system consisting of colloidal 2D perovskite nanoplatelets in solution is used to explore whether it is possible to achieve more efficient charge separation by incorporating strong electron donors molecules in the organic part of the material. In **Chapter 9**, the attention is turned to the solid state and different organic donors, acceptors and complete charge-transfer complexes are introduced in the structure. Finally, **Chapter 10** describes the properties of perovskite-like one-dimensional compounds that are obtained when bulky functional organic cations are introduced in the synthesis.

1.5. References

1. Li, W. *et al.* Chemically diverse and multifunctional hybrid organic-inorganic perovskites. *Nat. Rev. Mater.* **2**, (2017).
2. Brenner, T. M., Egger, D. A., Kronik, L., Hodes, G. & Cahen, D. Hybrid organic - Inorganic perovskites: Low-cost semiconductors with intriguing charge-transport properties. *Nat. Rev. Mater.* **1**, 1–16 (2016).
3. NREL. Best Research-Cell Efficiencies. *Best Research-Cell Efficiencies* (2019). Available at: https://www.nrel.gov/pv/assets/pdfs/best-research-cell-efficiencies-190416.pdf.
4. Jena, A. K., Kulkarni, A. & Miyasaka, T. Halide Perovskite Photovoltaics: Background, Status, and Future Prospects. *Chem. Rev.* **119**, 3036–3103 (2019).
5. Stranks, S. D. *et al.* Electron-hole diffusion lengths exceeding 1 micrometer in an organometal trihalide perovskite absorber. *Science (80-.).* **342**, 341–344 (2013).
6. March, S. A. *et al.* Simultaneous observation of free and defect-bound excitons in CH3NH3PbI3 using four-wave mixing spectroscopy. *Sci. Rep.* **6**, 1–7 (2016).
7. Bokdam, M. *et al.* Role of Polar Phonons in the Photo Excited State of Metal Halide Perovskites. *Sci. Rep.* **6**, 1–8 (2016).
8. Miyata, A. *et al.* Direct measurement of the exciton binding energy and effective masses for charge carriers in organic-inorganic tri-halide perovskites. *Nat. Phys.* **11**, 582–587 (2015).
9. D'Innocenzo, V. *et al.* Excitons versus free charges in organo-lead tri-halide perovskites. *Nat. Commun.* **5**, 1–6 (2014).
10. Hutter, E. M. Revealing the Fate of Photo-Generated Charges in Metal Halide Perovskites. (Delft University of Technology, 2018). doi:https://doi.org/10.4233/uuid:f8e21539-bd26-4694-b170-6d0641e4c31a
11. Hutter, E. M. *et al.* Direct-indirect character of the bandgap in methylammonium lead iodide perovskite. *Nat. Mater.* **16**, 115–120 (2017).
12. Crothers, T. W. *et al.* Photon Reabsorption Masks Intrinsic Bimolecular Charge-Carrier Recombination in CH3NH3PbI3 Perovskite. *Nano Lett.* **17**, 5782–5789 (2017).
13. Frost, J. M. *et al.* Atomistic origins of high-performanc1. Frost, J. M. et al. Atomistic origins of high-

performance in hybrid halide perovskite solar cells. Nano Lett. 14, 2584–90 (2014).e in hybrid halide perovskite solar cells. *Nano Lett.* **14**, 2584–90 (2014).
14. Chen, Q. *et al.* Under the spotlight: The organic-inorganic hybrid halide perovskite for optoelectronic applications. *Nano Today* **10**, 355–396 (2015).
15. Stoumpos, C. C., Malliakas, C. D. & Kanatzidis, M. G. Semiconducting tin and lead iodide perovskites with organic cations: Phase transitions, high mobilities, and near-infrared photoluminescent properties. *Inorg. Chem.* **52**, 9019–9038 (2013).
16. Howard, C. J. & Stokes, H. T. Group-Theoretical Analysis of Octahedral Tilting in Perovskites. Erratum. *Acta Crystallogr. Sect. B Struct. Sci.* **54**, 782–789 (1998).
17. Stokes, H. T., Kisi, E. H., Hatch, D. M. & Howard, C. J. Group-theoretical analysis of octahedral tilting in ferroelectric perovskites. *Acta Crystallogr. Sect. B Struct. Sci.* **58**, 934–938 (2002).
18. Noriko Onoda-Yamamuro, Matruo, T. & Suga, H. Calorimetric and IR Spectroscopic Studies of Phase Transitions in MAPbX3. **51**, 1383–1395 (1990).
19. Onoda-Yamamuro, N., Matsuo, T. & Suga, H. Dielectric study of CH3NH3PbX3 (X = Cl, Br, I). *J. Phys. Chem. Solids* **53**, 935–939 (1992).
20. Ptak, M. *et al.* Experimental and theoretical studies of structural phase transition in a novel polar perovskite-like [C2H5NH3][Na0.5Fe0.5(HCOO)3] formate. *Dalt. Trans.* **45**, 2574–2583 (2016).
21. Brenner, T. M. *et al.* Are Mobilities in Hybrid Organic-Inorganic Halide Perovskites Actually 'high'? *J. Phys. Chem. Lett.* **6**, 4754–4757 (2015).
22. Zhu, X. Y. & Podzorov, V. Charge Carriers in Hybrid Organic-Inorganic Lead Halide Perovskites Might Be Protected as Large Polarons. *J. Phys. Chem. Lett.* **6**, 4758–4761 (2015).
23. Hao, F., Stoumpos, C. C., Cao, D. H., Chang, R. P. H. & Kanatzidis, M. G. Lead-free solid-state organic-inorganic halide perovskite solar cells. *Nat. Photonics* **8**, 489–494 (2014).
24. Noel, N. K. *et al.* Lead-free organic-inorganic tin halide perovskites for photovoltaic applications. *Energy Environ. Sci.* **7**, 3061–3068 (2014).
25. Slavney, A. H., Hu, T., Lindenberg, A. M. & Karunadasa, H. I. A Bismuth-Halide Double Perovskite with Long Carrier Recombination Lifetime for Photovoltaic Applications. *J. Am. Chem. Soc.* **138**, 2138–2141 (2016).
26. Karunadasa, H., Huang, Q., Ueland, B. G., Schiffer, P. & Cava, R. J. (Ba2LnSbO6 and Sr2LnSbO6 (Ln = Dy, Ho, Gd) double perovskites: Lanthanides in the geometrically frustrating fcc lattice. *PNAS* **100**, 8097–8102 (2003).
27. Erten, O. *et al.* Theory of half-metallic ferrimagnetism in double perovskites. *Phys. Rev. Lett.* **107**, 1–4 (2011).
28. Kobayashi, K.-I., Kimura, T., Sawada, H., Terakura, K. & Tokura, Y. Room-temperature magnetoresistance in an oxide materialwith an ordered double-perovskite structure. *Nature* **395**, 677–680 (1998).
29. Mitzi, D. B., Chondroudis, K. & Kagan, C. R. Design, Structure, and Optical Properties of Organic–Inorganic Perovskites Containing an Oligothiophene Chromophore. *Inorg. Chem.* **38**, 6246–6256 (1999).
30. Ishihara, T. Optical properties of PbI-based perovskite structures. *J. Lumin.* **60–61**, 269–274 (1994).
31. Ishihara, T., Hong, X. & Ding, J. Dielectric confinement effect for exciton and biexciton states in Pbla-based two-dimensional semiconductor structures. 1–4 (1992).
32. Mitzi, D. B., Wang, S., Feild, C. A., Chess, C. A. & Guloy, A. M. Conducting Layered Organic-inorganic Halides Containing -Oriented Perovskite Sheets. *Science* **267**, 1473–6 (1995).
33. Mitzi, D. B., Medeiros, D. R. & Malenfant, P. R. L. Intercalated organic-inorganic perovskites stabilized by fluoroaryl-aryl interactions. *Inorg. Chem.* **41**, 2134–2145 (2002).
34. Mitzi, D. B. A Layered Solution Crystal Growth Technique and the Crystal Structure of $(C_6H_5C_2H_4NH_3)_2PbCl_4$. *J. Solid State Chem.* **704**, 694–704 (1999).
35. Chondroudis, K. & Mitzi, D. B. Electroluminescence from an Organic - Inorganic Perovskite Incorporating a Quaterthiophene Dye within Lead Halide Perovskite Layers. 3028–3030 (1999).
36. Tanaka, K. & Kondo, T. Bandgap and exciton binding energies in lead-iodide-based natural quantum-well crystals. *Sci. Technol. Adv. Mater.* **4**, 599–604 (2003).
37. Tanaka, K., Takahashi, T., Kondo, T. & Ema, K. Image charge effect on two-dimensional excitons in an inorganic-organic quantum-well crystal. 1–6 (2005). doi:10.1103/PhysRevB.71.045312
38. Muljarov, E. A., Tikhodeev, S. G., Gippius, N. A. & Ishihara, T. Excitons in self-organized semiconductor/insulator superlattices: PbI-based perovskite compounds. *Phys. Rev. B* **51**, 14370–14378 (1995).
39. Ishihara, T. & Takahashi, J. Optical properties due to electronic transitions in two-dimensional semiconductors (CnH2n+1NH3)2PbI4. *Phys. Rev. B* **42**, 99–107 (1990).

40. Lanty, G. *et al.* UV polaritonic emission from a perovskite-based microcavity UV polaritonic emission from a perovskite-based microcavity. **081101**, 2006–2009 (2016).
41. Stoumpos, C. C. *et al.* Ruddlesden-Popper Hybrid Lead Iodide Perovskite 2D Homologous Semiconductors. *Chem. Mater.* **28**, 2852–2867 (2016).
42. Cao, D. H., Stoumpos, C. C., Farha, O. K., Hupp, J. T. & Kanatzidis, G. Two-dimensional homologous perovskites as light absorbing materials for solar cell applications. **2**, 1–9
43. Wu, X., Trinh, M. T. & Zhu, X. Excitonic Many-Body Interactions in Two-Dimensional Lead Iodide Perovskite Quantum Wells. (2015). doi:10.1021/acs.jpcc.5b00148
44. Yaffe, O. *et al.* Excitons in ultrathin organic-inorganic perovskite crystals. **045414**, 1–7 (2015).
45. Tsai, H. *et al.* High-efficiency two-dimensional ruddlesden-popper perovskite solar cells. *Nature* **536**, 312–317 (2016).
46. Blancon, J. C. *et al.* Scaling law for excitons in 2D perovskite quantum wells. *Nat. Commun.* **9**, 1–10 (2018).
47. Milot, R. L. *et al.* Charge-Carrier Dynamics in 2D Hybrid Metal − Halide Perovskites. (2016). doi:10.1021/acs.nanolett.6b03114
48. Lanty, G. *et al.* Room-Temperature optical tunability and inhomogeneous broadening in 2D-layered organic-inorganic perovskite pseudobinary alloys. *J. Phys. Chem. Lett.* **5**, 3958–3963 (2014).
49. Yuan, M. *et al.* Perovskite energy funnels for efficient light-emitting diodes. *Nat. Nanotechnol.* **11**, 872–877 (2016).
50. Hattori, T., Taira, T., Era, M., Tsutsui, T. & Saito, S. Highly efficient electroluminescence from a heterostructure device combined with emissive layered-perovskite and an electron-transporting organic compound. *Chem. Phys. Lett.* **254**, 103–108 (1996).
51. Gebauer, T. & Schmid, G. Inorganic-organic Hybrid Structured LED ' s Anorganisch-organische Hybrid-LEDs. **5**, 4–8 (1999).
52. Kondo, T. *et al.* Resonant third-order optical nonlinearity in the layered perovskite-type material (C6H13NH3)2PbI4. **105**, 503–506 (1998).
53. Fujita, T., Sato, Y., Kuitani, T. & Ishihara, T. Tunable polariton absorption of distributed feedback microcavities at room temperature. **57**, 428–434 (1998).
54. Yablonskii, A. L., Muljarov, E. A., Gippius, N. A. & Tikhodeev, S. G. Polariton Effect in Distributed Feedback Microcavities. **70**, 1137–1144 (2001).
55. Brehier, A. *et al.* Strong exciton-photon coupling in a microcavity containing layered perovskite semiconductors Strong exciton-photon coupling in a microcavity containing layered perovskite semiconductors. **171110**, 2004–2007 (2016).
56. Wenus, J. *et al.* Hybrid organic-inorganic exciton-polaritons in a strongly coupled microcavity. 1–6 (2006). doi:10.1103/PhysRevB.74.235212
57. Dou, L. *et al.* Atomically thin two-dimensional organic-inorganic hybrid perovskites. **349**, (2015).
58. Zhang, S. *et al.* Efficient Red Perovskite Light-Emitting Diodes Based on Solution-Processed Multiple Quantum Wells. **1606600**, 1–6 (2017).
59. Li, R. *et al.* Room-temperature electroluminescence from two-dimensional lead halide perovskites Room-temperature electroluminescence from two-dimensional lead halide perovskites. **151101**, (2016).
60. Gauthron, K. *et al.* Optical spectroscopy of two-dimensional layered (C 6 H 5 C 2 H 4 -NH 3) 2 -PbI 4 perovskite. **18**, 5912–5919 (2010).
61. Wu, X. *et al.* Trap States in Lead Iodide Perovskites. (2015). doi:10.1021/ja512833n
62. Mao, L. *et al.* Hybrid Dion-Jacobson 2D Lead Iodide Perovskites. *J. Am. Chem. Soc.* **140**, 3775–3783 (2018).
63. Mao, L., Stoumpos, C. C. & Kanatzidis, M. G. Two-Dimensional Hybrid Halide Perovskites: Principles and Promises. *J. Am. Chem. Soc.* **141**, 1171–1190 (2019).
64. Li, Y. *et al.* Bifunctional Organic Spacers for Formamidinium-Based Hybrid Dion-Jacobson Two-Dimensional Perovskite Solar Cells. *Nano Lett.* **19**, 150–157 (2019).
65. Maheshwari, S., Savenije, T. J., Renaud, N. & Grozema, F. C. Computational Design of Two-Dimensional Perovskites with Functional Organic Cations. *J. Phys. Chem. C* **122**, 17118–17122 (2018).
66. Kamminga, M. E. *et al.* Confinement Effects in Low-Dimensional Lead Iodide Perovskite Hybrids. *Chem. Mater.* **28**, 4554–4562 (2016).
67. Kamminga, M. E., De Wijs, G. A., Havenith, R. W. A., Blake, G. R. & Palstra, T. T. M. The Role of Connectivity on Electronic Properties of Lead Iodide Perovskite-Derived Compounds. *Inorg. Chem.* **56**, 8408–8414 (2017).
68. Evans, H. A. *et al.* Mono- and Mixed-Valence Tetrathiafulvalene Semiconductors (TTF)BiI4 and (TTF)4BiI6

with 1D and 0D Bismuth-Iodide Networks. *Inorg. Chem.* **56**, 395–401 (2017).
69. Kamminga, M. E. *et al.* Electronic mobility and crystal structures of 2,5-dimethylanilinium triiodide and tin-based organic-inorganic hybrid compounds. *J. Solid State Chem.* **270**, 593–600 (2019).
70. Bohn, B. J. *et al.* Boosting Tunable Blue Luminescence of Halide Perovskite Nanoplatelets through Postsynthetic Surface Trap Repair. *Nano Lett.* **18**, 5231–5238 (2018).
71. Weidman, M. C., Seitz, M., Stranks, S. D. & Tisdale, W. A. Highly Tunable Colloidal Perovskite Nanoplatelets through Variable Cation, Metal, and Halide Composition. *ACS Nano* **10**, 7830–7839 (2016).
72. Bekenstein, Y., Koscher, B. A., Eaton, S. W., Yang, P. & Alivisatos, A. P. Highly Luminescent Colloidal Nanoplates of Perovskite Cesium Lead Halide and Their Oriented Assemblies. *J. Am. Chem. Soc.* **137**, 16008–16011 (2015).
73. Stoumpos, C. C., Mao, L., Malliakas, C. D. & Kanatzidis, M. G. Structure-Band Gap Relationships in Hexagonal Polytypes and Low-Dimensional Structures of Hybrid Tin Iodide Perovskites. *Inorg. Chem.* **56**, 56–73 (2017).
74. Mercier, N. Hybrid Halide Perovskites: Discussions on Terminology and Materials. *Angew. Chemie Int. Ed.* **10**, 1002 (2019).
75. Mitchell, R. H., Welch, M. D. & Chakhmouradian, A. R. Nomenclature of the perovskite supergroup: A hierarchical system of classification based on crystal structure and composition. *Mineral. Mag.* **81**, 411–461 (2017).

Chapter 2

Experimental Techniques

Apart from relatively common techniques such as steady state optical absorption and emission spectroscopy and time-resolved optical absorption and emission spectroscopy, the work in this thesis relies to a large extent on less common techniques to characterize charge transport. The technique we use to characterize charge transport is time-resolved microwave conductivity (TRMC), which measures changes in conduction without having to apply electrodes. TRMC detection can be combined with laser excitation to measure the photoconductivity of thin films, or with excitation with a short electron pulse which gives direct insight in the mobility of charges. The essential aspects of the TRMC technique are briefly described in this chapter.

Parts of this chapter have been published in:

María C. Gélvez-Rueda, Duyen H. Cao, Sameer Patwardhan, Nicolas Renaud, Constantinos C. Stoumpos, Geroge C. Schatz, Joseph T. Hupp, Omar K. Farha, Tom J. Savenije, Mercouri G. Kanatzidis, Ferdinand C. Grozema. Effect of Cation Rotation on Charge Dynamics in Hybrid Lead Halide Perovskites. J. Phys. Chem. C 2016, 120, 16577-16585.

María C. Gélvez-Rueda, Eline M. Hutter, Duyen H. Cao, Nicolas Renaud, Constantinos C. Stoumpos, Joseph T. Hupp, Tom J. Savenije, Mercouri G. Kanatzidis, Ferdinand C. Grozema. Interconversion Between Free Charges and Bound Excitons in 2D Hybrid Lead Halide Perovskites. J. Phys. Chem. C 2017, 121 (47), 26566-26574.

2.1. Time-resolved microwave conductivity techniques (TRMC)

In this thesis the methods of choice to determine the charge carrier dynamics of organic-inorganic perovskites are time-resolved microwave conductivity (TRMC) techniques. We use two different TRMC techniques that fundamentally differ in the way charge carriers are generated. We generate charges either by irradiation with a short pulse of high-energy electrons (PR-TRMC) or by laser excitation (photoconductivity TRMC). A schematic representation of TRMC set-ups is shown in Figure 2.1.

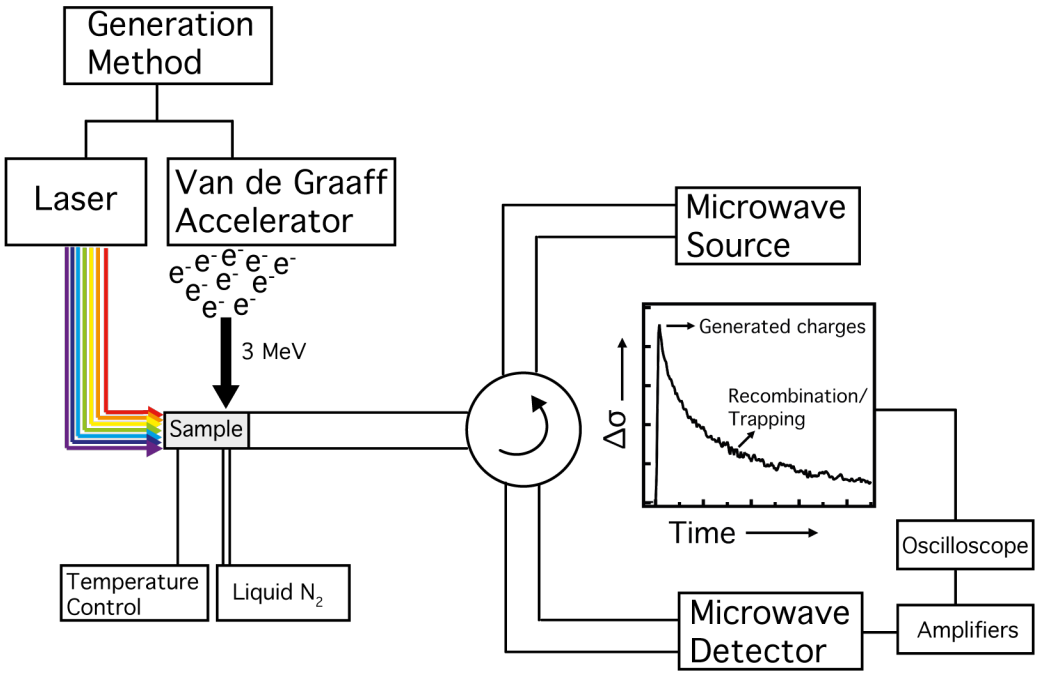

Figure 2. 1. Schematic representation of TRMC techniques. The inset shows the typical signal obtained from the measurements: change in conductivity (Δσ) of the material (in this case, $MAPbI_3$) upon irradiation with a laser or electron pulse as a function of time.

In TRMC techniques, changes in conductivity of a sample are probed as a function of time using continuous-wave high frequency microwaves with an oscillation frequency in the range of tens of GHz. A change in conductivity in the sample can be induced by generation of charges using pulsed excitation, either by a laser pulse or by irradiation with pulse of high-energy electrons. In our experiments, the sample consisting of either a thin film on a quartz substrate or a 'bulk' solid (pulse radiolysis) is placed inside a cell constructed from gold-plated X-band (8.2-12.4 GHz) or a Ka-band (28-38 GHz) microwaveguide. The changes in conductivity on irradiation with a laser or an electron pulse are probed continuously with microwaves (GHz) before and after generation of charge carriers.

If the excitation pulse leads to the generation of mobile charge carriers this leads to an increase in the conductivity in the materials. The mobile charge carriers will interact with the oscillating electric field of the microwaves and in this way absorb part of the microwave power. The fractional change in microwave reflected by the microwave cell ($\Delta P/P$) is directly proportional to the change in conductivity (Δσ) upon generation of charges through the sensitivity factor, *A*.

$$\frac{\Delta P}{P} = -A\,\Delta\sigma \qquad \text{(Eq. 2.1)}$$

By definition, the (macroscopic) change in conductivity of the material is related to the concentration of charge carriers in the material, (electrons and holes and their respective charge carrier mobilities. Since it is not possible to selectively generate positive or negative charges, the change in conductivity determined by the TRMC techniques is the sum of the electron and hole concentrations (n_0) and mobilities (∑μ).

$$\Delta\sigma = e\left(n_n\mu_n + n_p\mu_p\right) = e\sum n_0\,\mu \qquad \text{(Eq. 2.2)}$$

If the initial concentration of mobile charge carriers generated by a laser of electron pulse (n_0) is known, it is possible to derive the mobilities (∑μ) of the charges immediately after the excitation. After the end of the generation pulse, the conductivity starts to decay due to recombination and trapping of charges (see inset in Figure 2.1). Hence the decay of the conductivity contains valuable information on the decay mechanisms and more information can be obtained by varying the initial concentration of charged species to distinguish for instance first order trapping processes from second order charge recombination processes. It is important to point out that the decay detected by TRMC is not directly comparable to the decay from time-resolved photoluminescent (PL) measurements. In PL measurements, only radiative recombination processes are detected, while TRMC is sensitive to all mobile charge carriers, including the ones that do not recombine radiatively. In comparison to DC experiments the use of ultra-high frequency oscillating microwaves has several advantages. The first is the absence of electrodes. In a DC-experiment, electrodes are required to inject charges and probe their transport properties, which may introduce problems related to charge injection and extraction. Since there are no electrodes and charges are generated by an excitation pulse TRMC circumvents these problems. A second advantage is that measuring the conductivity with high frequency microwaves leads to a local probe of transport that is not affected by grain boundaries. In a DC measurement, transport is measured over macroscopic distances and grain boundaries can strongly influence the transport. Therefore, TRMC gives a measure of the intrinsic charge transport properties in well-ordered domains. The overall intrinsic time response of the PR-TRMC set up is limited by the rise time of the detector diode that is used, approximately 1 ns. In the photoconductivity TRMC experiment,

we often use a microwave cavity, which increases the sensitivity by one or two orders of magnitude. This does lead to a limitation of the time resolution as the rise time of the cavity is approximately 18 ns.

As mentioned above, we use two fundamentally different methods to generate charge carriers in the semiconductor material; by irradiation with a short pulse of high-energy electrons (PR-TRMC) or by laser excitation (Photoconductivity TRMC). When a sample is irradiated with a short laser pulse, the distribution of excitations through is determined by the optical density and the penetration depth is usually very limited, ~100 nm. This means that only thin films on a quartz substrate can be studied. An additional issue with laser excitation is that is not necessarily the case that each absorbed photon leads to the formation of a free electron-hole pair, but depending on the exciton binding energy stable bound exciton can be formed. As a result, the quantity obtained from such measurements is the product of the dissociation yield (the fraction of absorbed photons that leads to free charges) and the mobility of the charges.

In the pulse radiolysis experiments the samples are irradiated with a short pulse of electrons with and energy of 3 MeV electrons. The penetration depth in this case does not depend on the optical density but depends on the electron density in the materials and is typically several millimeters. This means that we can perform experiments on 'bulk' solid powers or crystals without first depositing them in thin films. An additional difference, as compared to the laser excitation, is the energy transferred per ionization of scattering event. The average energy transferred per event in the pulse radiolysis experiment is ~ 20 eV. This means that electron hole pairs are generated with a large initial separation distance, immediately forming free charge carriers, regardless of the exciton binding energy.

From the above it is clear that the information obtained from the two experiments is different: photoconductivity TRMC gives a product of dissociation yield and charge mobility, while PR-TRMC give a direct measure of the charge carrier mobility. Using these two complementary techniques is especially powerful since combining allows to estimate the dissociation yield on photoexcitation and can give direct information on the exciton binding energy as shown in **Chapter 6** for 2D perovskites. The details of the two TRMC methods are described in more detail below.

2.2. Pulse-radiolysis microwave conductivity (PR-TRMC)

In Pulse-Radiolysis Time-Resolved Microwave Conductivity (PR-TRMC)[1,2] measurements charges are generated by irradiation with a short pulse of high-energy electrons, while the changes in conductivity due to mobile charge carriers are monitored using high frequency

microwaves (28-38 GHz). The high-energy electron pulse is produced by a Van de Graaff accelerator with kinetic energies of approximately 3 MeV. A Van de Graaff accelerator works by charging a metal hemispherical capacitor to 3 MV, with electrons transported to it by an insulating rubber belt. The electrons are emitted by a heated cathode and accelerated to 3 MV in a drift-tube with a uniform electric field. The electrons gain a kinetic energy of 3 MeV and come out with a velocity close to the speed of light through an aluminum window. The electron pulses are generated by temporarily removing the negative bias on a grid close the surface of the cathode. The pulse duration can be varied from 200 ps to 250 ns and are charaxcterized by measuring the amount of charge (Q in nanoCoulumb, nC) per pulse with an electrometer. The fluctuation in the amount of charge at each pulse duration is typically less than 2%.

The high-energy electron pulse ionizes the charges in the material via Coulomb interactions. These interactions are caused by the rapidly changing electric field of the electrons in the pulse. This mechanism is similar to the oscillating electric field of a photon. However, it has a much larger penetration depth and a higher average energy transferred per ionization event (~20 eV). This results in the generation of a uniform concentration of pairs of charge carriers at an average distance of ~200 nm from each other. The thermal relaxations of the charges that are produced in this way occurs well within a nanosecond and hence it does not influence recombination of the charge carriers (in hybrid perovskites well within 100 ps[3]). The advantages of this technique include its high penetration power and non-specificity of high-energy radiation that ensure that the energy deposition is uniform and insensitive of the color or morphology of the sample.

2.2.1. Determination of the Sensitivity factor (A)

The change in conductivity ($\Delta\sigma$) due to generated mobile charge carriers is determined from the fractional change in the microwave power, $\Delta P/P$, reflected from the microwave cell and the sensitivity factor, A (Eq. 2.1). The sensitivity factor depends on the geometry of the cell, dielectric medium and the frequency of the microwaves (28-38 GHz). The overlap of the electric field strength of the microwaves in the dielectric medium changes with frequency and with interference effects of the incoming and reflected waves in the cell as shown in Figure 2.2.

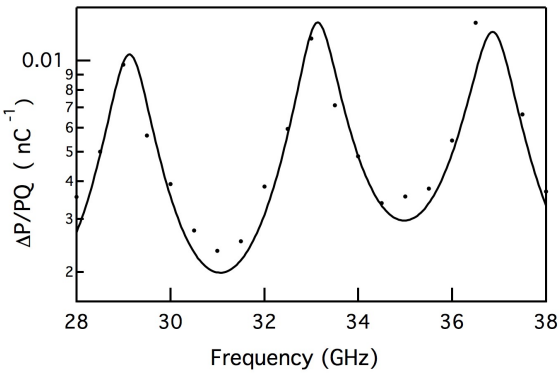

Figure 2.2. Maximum fractional microwave power absorbed (ΔP/P) per unit beam charge (Q) as a function of the frequency of the microwaves. $MAPbI_3$ at room temperature and 200 ps electron pulse.

For the frequency of maximum sensitivity, an analytical expression to relate ΔP/P to Δσ can be derived in a microwave reflection cell with an uniform dielectric material of length *d*:[4]

$$\left(\frac{\Delta P}{P}\right)^{max} = -\frac{2\,\lambda_a\, f_{max}\, d}{\varepsilon_o c^2}\,\Delta\sigma \qquad \text{(Eq. 2.3)}$$

where λ_a is the wavelength of the microwaves in air (inside the waveguide), *d* is the total length of the dielectric medium, ε_0 is the permittivity of free space and *c* is the velocity of light in vacuum. The frequency where the sensitivity is maximum is determined by the dielectric constant of the medium. It can be shown that these maxima occur when the medium is exactly an odd number of quarter wavelengths long: [4]

$$d\ = (2\,n+1)\,\frac{\lambda_l}{4} \qquad \text{(Eq. 2.4)}$$

In this equation, λ_l is the wavelength inside the sample. The frequencies at which maxima in absorption occur for a given sample-length d are:

$$f_{max} = \frac{c}{2\sqrt{\varepsilon_r}}\left[\left(\frac{2\,n+1}{2d}\right)^2 + \left(\frac{1}{a}\right)^2\right]^{\frac{1}{2}} \qquad \text{(Eq. 2.5)}$$

with ε_r the relative dielectric constant of the medium and a the broad dimension of the waveguide. The value of λ_a that corresponds to f_{max} is given by:

$$\lambda_a = \frac{2\,\pi}{\left[\left(\frac{2\,\pi\, f_{max}}{c}\right)^2 - \left(\frac{\pi}{a}\right)^2\right]^{\frac{1}{2}}} \qquad \text{(Eq. 2.6)}$$

The values of f_{max} and λ_a can be replaced in equation 2.3 to obtain the sensitivity factor A.

2.2.2. Determination of initial concentration of charge carriers (n_0)

The mobility of the charge carriers can be derived from the maximum change in conductivity (Δσ) if the charge carrier concentration at the end of the electron pulse (n_0) is known (Eq. 2.4). In PR-TRMC technique, the initial concentration of charge carriers (n_0) is a function of the mass of material (m), volume of the sample holder (V_{sh}), irradiation energy deposited in the sample (D) and of the radiation-ionization energy required for the generation of an electron-hole pair (E_p).

$$n_0 = \frac{D}{E_p * 1.6 * 10^{-19} \frac{J}{eV}} \frac{m}{V_{sh}} \qquad \text{(Eq. 2.7)}$$

The energy deposited in the sample per unit beam charge from the high-energy electrons (D) has been determined by dosimetry experiments using thin-film radiochromic dosimeters (Nylon foil impregnated with a radiation sensitive dye, Far West Technology Nr.92). The dose is proportional to the electron density of the material and for perovskites has been determined to be ~1 J/Kg/nC. The radiation-ionization energy required for the generation of an electron-hole pair (E_p) has been determined according to Klein's theoretical model and Alig's equation for semiconductor materials (Equation 6), which relates it to the band gap of the material, phonon losses and the residual kinetic energy.[5–7]

$$\mathrm{E}_p = 2.73\, E_g + 0.55\, [eV] \qquad \text{(Eq. 2.8)}$$

In the PR-TRMC set up, the microwave cell is contained in a cryostat in which the temperature can be varied between -150°C and 200°C. The temperature is maintained for ~15 minutes before performing the actual measurement in order to assure the equilibrium of the system. The irradiation intensity was varied between pulse lengths of 200 ps and 10 ns (irradiation charge in between ~0.4 nC and 30 nC). We emphasize that the radiation doses used in our experiment are not sufficient to cause significant radiation damage. Klein-Kedem et al.[8] found that perovskites solar cells are unstable under absorbed radiation power ~10^9 W cm^{-3}. The radiation power that is typically absorbed in our experiments is 3 orders of magnitude lower (~10^6 W cm^{-3}).

2.3. Photoconductivity TRMC

Photoconductivity TRMC[9] measurements involve the generation of charge carriers by laser-excitation and the monitoring of the change in photoconductance (ΔG) due to mobile charge carriers using high frequency microwaves (8.2 to 12.4 GHz). Photoexcitation is done by laser pulses with a duration of 3 ns to 5 ns full-width at half maximum (FWHM) with a tunable wavelength at a repetition frequency of 10 Hz. The maximum light intensity is on the order of

10^{16} photons/cm^2 per pulse. Metallic, neutral density filters with different optical densities are placed in between the laser and the sample to vary the photon fluence (and hence the density of absorbed photons in the sample). The fraction of microwave power absorbed is related to the photoconductance (ΔG) by the proportionality factor (*K*). By definition, a change in photoconductance (ΔG) is related to the change in conductivity (Δσ) through the inner dimensions of the cell (β) and the thickness of the material film (L) according to:

$$\frac{\Delta P}{P} = -K\,\Delta G = -K\,\Delta\sigma\,\beta\,L \qquad \text{(Eq. 2.9)}$$

2.3.1. Determination of the Sensitivity factor (K)

The magnitude of the sensitivity factor (K) depends on the dimensions of the microwave cell, the dielectric properties of all the media in the cell and the microwave frequency. The sample is placed at ¾ of the cell length Λ so that its position corresponds to the maximum electric field strength for microwaves with wavelength Λ. For each sample, the maximum ΔP/P is determined as a function of frequency obtaining a trend as the one shown in Figure 2.3. The maximum value for *K* is typically found at a frequency around 8.5 GHz (maximum overlap of the sample with the electric field). At 11 GHz the opposite is true: the electric field strength of the microwaves has a node here (minimum overlap between field strength and sample).

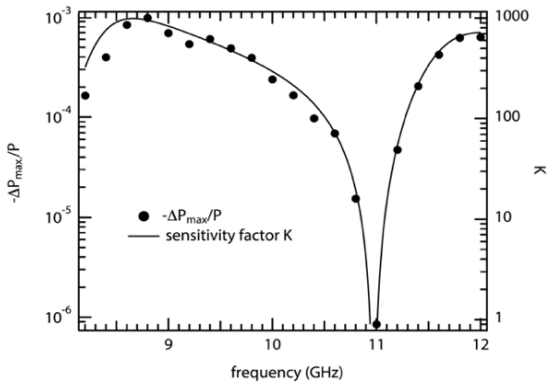

Figure 2.3. Fractional microwave power absorbed (ΔP/P) as a function of the frequency of the microwaves. Cell filled with nitrogen and $MAPbI_3$ thin-film (250 nm) on a 1 mm quartz substrate (room temperature). Figure taken from Hutter (2018).[10]

2.3.2. Determination of the charge carrier mobility (∑μ) and charge carrier yield of free charges (ϕ)

After determining the sensitivity factor K, is possible to determine the change in photoconductance (ΔG) and change in conductivity (Δσ) (according to Eq. 2.9). However, the change in conductivity will depend on the thickness of the material film (L), complicating the comparison between different samples. As discussed in section 2.1., effectively, the

photoconductivity signal measured on excitation by a laser pulse is a product of the yield of free charge carriers (ϕ) and their mobility (∑μ). The yield of free charge carriers (ϕ) can be defined as the concentration of photogenerated electron-hole pairs (n_0) per absorbed photons ($F_A I_0/L$) according to equation 2.10. Then, the product of the yield (ϕ) and mobility (∑μ) (Eq. 2.11) can be obtained from the maximum photoconductance (ΔG_{max}) combining equations 2.2, 2.9 and 2.10.

$$\varphi = \frac{L\, n_0}{F_A I_0} \qquad \text{(Eq. 2.10)}$$

$$\varphi \sum \mu = \frac{L\, n_0}{F_A I_0} \frac{\Delta\sigma}{e\, n_0} = \frac{L}{F_A I_0} \frac{\Delta G_{max}}{e\, \beta\, L} = \frac{\Delta G_{max}}{\beta\, e\, I_0 F_A} \qquad \text{(Eq. 2.11)}$$

As the thickness of the layers cancels out, through equation 2.11 is possible to directly compare the product of ϕ∑μ from TRMC experiments for different material samples. However, the yield of free charges strongly depends on the exciton binding energy of the material. The equilibrium between photogenerated free charge carriers (x) and excitons (1-x) has been described by the Saha equation (Eq. 2.12).

$$\frac{x^2}{1-x} = \frac{1}{n} \left(\frac{2\pi\mu k_B T}{h^2}\right)^{3/2} e^{\frac{-E_B}{k_B T}} \qquad \text{(Eq. 2.12)}$$

This equation relates the yield of free charges (x) to the excitation density (photons/cm^3), the density of states, the exciton binding energy (E_B) and the thermal energy ($k_B T$). In Chapter 6 this equation will be used to determine the exciton binding energy of 2D and quasi 2D-3D perovskites.

2.4. Modelling of Kinetic Data

As discussed above the decay of the conductivity signals contains valuable information on the recombination and trapping of charge carriers. By varying the excitation density, it is possible to gain additional insight on the decays processes and whether they decay occurs by a first or second order process. However, in practice, there are multiple decay processes operative at the same time and it is hard to disentangle them directly from the experimental data. Therefore, in this thesis we use a kinetic model to extract quantitative data from the charge carrier dynamics determined by TRMC measurements on organic-inorganic perovskites.[11,12] This model accounts for the time-dependent concentration of charge carriers (electrons in the conduction band (CB), holes in the valence band (VB)). Initially, the concentrations of generated CB electrons (Δn_e) and VB holes ($-\Delta n_h$) are equal, but they start differing from each other in time, depending on the recombination and trapping pathways. Based on previous

analogous models and the experimental data, the model designed accounts for the rates (k) at which the following processes occur:

- Generation of charge carriers **(G_p (t), k_G)**,
- Second order bimolecular recombination (radiative recombination function of the amount of charges created) **(k_{rad})**,
- Second order charge trapping with a limited amount of traps (trap filling is a function of the amount of traps available) **(k_t),** and
- Second order recombination with trapped charges **(k_{dt})**.

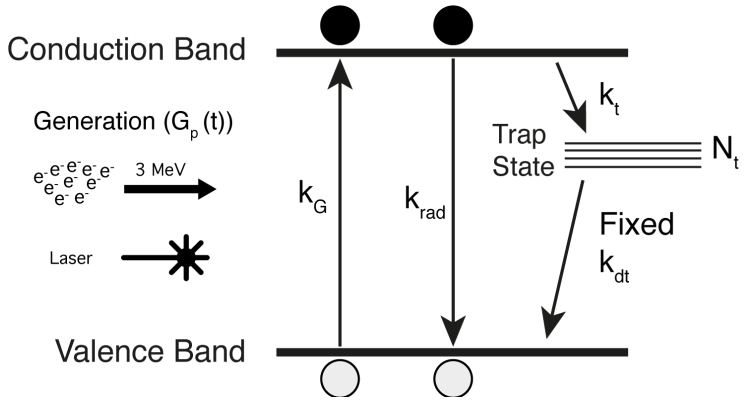

Figure 2. 4. Schematic representation of the charge carrier dynamic model. N_t is for the (limited) concentration of trap states.

The time-dependent generation of charge carriers, denoted by $G_p(t)$, takes into account the temporal generation profile depending on the generation method. The generation profile (G_p) in the PR-TRMC is determined by the electron pulse length and shape (rectangular) while in the photoconductivity experiment the generation profile follows the shape of the laser pulse. G_p is non-zero only for the duration of the excitation pulse.

The differential equations that describe this sequence of processes are listed below. They describe the variation in time of the electron concentration in the valence band (n_h), in the conduction band (n_e) and in trap states (n_T). A finite concentration of trap states (N_t) is defined in the system. In addition, it is assumed that the initial concentration of excitations is fully homogeneous. This means that every charge carrier experiences the same rate dynamics. In photoconductivity TRMC this is achieved when the semiconductor material is excited with an energy close to the band-gap energy and no large variations in the concentration are present.

$$\frac{dn_h(t)}{dt} = -G_p(t)\,k_G + k_{rad}\,[n_h(t)]\,[n_e(t)] + k_{dt}\,[n_T(t)]\,[n_h(t)] \qquad \text{(Eq. 2.13)}$$

$$\frac{dn_e(t)}{dt} = G_p(t)\,k_G - k_{rad}\,[n_h(t)]\,[n_e(t)] - k_t\,[n_e(t)]\,(N_t - [n_T(t)]) \qquad \text{(Eq. 2.14)}$$

$$\frac{dn_T(t)}{dt} = k_t\,[n_e(t)]\,(N_t - [n_T(t)]) - k_{dt}\,[n_T(t)]\,[n_h(t)] \qquad \text{(Eq. 2.15)}$$

From this kinetic model temporal evolution of the concentrations of electrons and holes is obtained. The variation in conductivity as a function of time can then be calculated defining the mobility of electrons and holes separately (Eq. 2.16). This differs from the total mobility (∑μ) that is experimentally determined from the TRMC experiment. This feature was included in the model in order to obtain more information regarding the charge carrier dynamics. The kinetic scheme implemented is defined by a set of coupled differential equations (Eqs. 2.13, 2.14 and 2.15), where only the electrons in the conduction band and holes in the valence band contribute to the pulse-induced change in conductivity. We find that for each sample a unique set of kinetic parameters is able to reproduce all TRMC transients with different initial concentration of charge carriers.

$$\Delta\sigma\,(t) = e\,(n_e(t)\,\mu_e + \,n_h(t)\,\mu_h) \qquad \text{(Eq. 2.16)}$$

2.5. References

1. Warman, J. M., Gelinck, G. H. & De Haas, M. P. The mobility and relaxation kinetics of charge carriers in molecular materials studied by means of pulse-radiolysis time-resolved microwave conductivity: Dialkoxy-substituted phenylene-vinylene polymers. *J. Phys. Condens. Matter* **14**, 9935–9954 (2002).
2. Warman, J., Haas, M. De, Dicker, G. & Grozema, F. Charge Mobilities in Organic Semiconducting Materials Determined by Pulse-Radiolysis Time-Resolved Microwave Conductivity:-Bond-Conjugated Polymers. *Chem. Mater* 4600–4609 (2004).
3. Madjet, M. E. A. *et al.* Enhancing the carrier thermalization time in organometallic perovskites by halide mixing. *Phys. Chem. Chem. Phys.* **18**, 5219–5231 (2016).
4. Infelta, P. P., Haas, M. P. D. E. & Warman, J. M. The study of the transient conductivity of pulse irradiated dielectric liquids on a nanosecond timescale using microwaves. *Radiat. Phys. Chem.* **10**, 353–365 (1977).
5. Alig, R. C. & Bloom, S. Electron-hole-pair creation energies in semiconductors. *Phys. Rev. Lett.* **35**, 1522–1525 (1975).
6. Alig, R. C., Bloom, S. & Struck, C. W. Scattering by ionization and phonon emission in semiconductors. *Phys. Rev. B* **22**, 5565–5582 (1980).
7. Klein, C. A. Bandgap dependence and related features of radiation ionization energies in semiconductors. *J. Appl. Phys.* **39**, 2029–2038 (1968).
8. Klein-Kedem, N., Cahen, D. & Hodes, G. Effects of Light and Electron Beam Irradiation on Halide Perovskites and Their Solar Cells. *Acc. Chem. Res.* **49**, 347–354 (2016).
9. Savenije, T. J., Ferguson, A. J., Kopidakis, N. & Rumbles, G. Revealing the dynamics of charge carriers in polymer:fullerene blends using photoinduced time-resolved microwave conductivity. *J. Phys. Chem. C* **117**, 24085–24103 (2013).
10. Hutter, E. M. Revealing the Fate of Photo-Generated Charges in Metal Halide Perovskites. (Delft University of Technology, 2018). doi:https://doi.org/10.4233/uuid:f8e21539-bd26-4694-b170-6d0641e4c31a
11. Hutter, E. M., Eperon, G. E., Stranks, S. D. & Savenije, T. J. Charge Carriers in Planar and Meso-Structured Organic-Inorganic Perovskites: Mobilities, Lifetimes, and Concentrations of Trap States. *J. Phys. Chem. Lett.* **6**, 3082–3090 (2015).
12. Stranks, S. D. *et al.* Recombination Kinetics in Organic-Inorganic Perovskites: Excitons, Free Charge, and Subgap States. *Phys. Rev. Appl.* **2**, 1–8 (2014).

Chapter 3

Effect of Cation Rotation on Charge Dynamics in Three-Dimensional (3D) Methyl Ammonium Lead Halide Perovskites

This chapter links fundamental semiconductor properties such as mobility, lifetime, and recombination kinetics of charge carriers of three-dimensional (3D) organic-inorganic perovskites to their characteristic phase transitions and correlated intrinsic dynamic disorder of the organic cation. There is a consensus that the organic cation does not influence the charge carrier properties of 3D perovskites as it does not contribute to the formation of the electronic bands. We determined by pulse-radiolysis time-resolved microwave conductivity (PR-TRMC) that the mobility and lifetime of charge carriers in methyl ammonium lead halide perovskites ($MAPbX_3$, X= I, Br) abruptly increase (2 to 6 times, respectively) and deviate from the band-like transport characteristic of inorganic semiconductors upon going through the tetragonal (β) to orthorhombic (γ) phase transition. This phase transition is linked to the reduction of the dynamic disorder of the organic cation. We propose that these observations are due to the dynamics of the organic cation. In the low temperature orthorhombic (γ) phase the organic cation freezes with a certain orientation of dipoles, leading to local charged states that separate the electrons and the holes and increasing their mobility and lifetime. These results highlight the importance of the organic cation in the charge carrier dynamics of 3D perovskites.

This chapter is based on:

María C. Gélvez-Rueda, Duyen H. Cao, Sameer Patwardhan, Nicolas Renaud, Constantinos C. Stoumpos, Geroge C. Schatz, Joseph T. Hupp, Omar K. Farha, Tom J. Savenije, Mercouri G. Kanatzidis, Ferdinand C. Grozema. Effect of Cation Rotation on Charge Dynamics in Hybrid Lead Halide Perovskites. J. Phys. Chem. C 2016, 120, 16577-16585.

3.1. Introduction

As mentioned in **Chapter 1**, three dimensional (3D) organic-inorganic halide perovskites are a promising class of materials for photovoltaic application with reported power efficiencies over ~24%.[1] This high efficiency is a result of outstanding opto-electronic properties commonly linked to the inorganic octahedral $(MX_6)^{4-}$ sublattice, as the electronic bands are formed only by orbitals of the divalent metal (M) and halogen atoms (X).[2] Nevertheless, the opto-electronic properties and charge carrier dynamics in 3D perovskites can also be influenced by the interaction of the organic cation with the crystal structure.[3–6]

It has been shown that the size of the organic cation alters the bandgap of 3D perovskites due to the deformation caused to the crystal structure.[3,7,8] Moreover, the low symmetry and permanent dipole moment of the organic cation results in orientational disorder and rotational dynamics inside the PbX_6 octahedron. This rotational freedom has been confirmed by a large variety of techniques (infrared (IR)[9,10], dielectric[11,12] spectroscopy, nuclear magnetic resonance (NMR)[10], quasielectric[13] and high-resolution[14] neutron scattering, and 2D infrared vibrational spectroscopy[15]) and is the most likely source of the high dielectric constant of these materials at low frequencies.[12,16] In addition, the inherent thermal (dynamic) disorder of the organic cation is intricately linked to the characteristic phase transitions that 3D perovskites exhibit at different temperatures. On cooling, the thermal motion decreases, leading to changes in the geometry of the unit cell and the formation of ordered domains.[10] These transitions have been observed by abrupt changes in differential scanning calorimetry (DSC)[9,10], dielectric measurements[11,12], IR[9,10] and NMR[10] spectroscopy. The dynamics of the organic cations have been linked to the dielectric response[12], ferroelectric behavior[17], hysteresis in the I-V curves[18] and different electronic properties for polar or nonpolar isotropic configurations of the organic cations.[19] Additionally, Monte Carlo simulations suggest the formation of ferroelectric domains below the β/γ phase transition temperature.[4,5,13] So far, the organic cation dynamics and characteristic phase transitions have not been correlated to fundamental semiconductor properties, such as mobility, lifetime, and recombination kinetics of charge carriers.

In this chapter, we report on the relationship between the organic cation dynamics, phase transitions and charge carrier properties in bulk 3D methylammonium lead halide perovskites, abbreviated as $MAPbX_3$ (X = I, Br, Cl). We use the pulse-radiolysis time-resolved microwave conductivity (PR-TRMC) technique to determine the mobility and lifetime of charge carriers at a variety of temperatures. We observe abrupt changes in mobility and lifetime on going through the β/γ phase transition in contrast to a recent THz conductivity study.[20] These effects are attributed to changes in the dynamics of the organic cations.

Reduction of the rotational motion of the organic cations in the orthorhombic (γ) low temperature phase creates a static energy landscape in which the organic cations freeze with a certain orientation of dipoles. This leads to local charged states that separate the charge carriers (electrons and holes), thereby increasing the mobility and lifetime. Moreover, we find that the bimolecular recombination rate decreases as the temperature decreases in contradiction to Langevin's theory used in inorganic semiconductors.[21] We propose that different mechanisms, related to the dynamic disorder of the organic cations, influence the charge dynamics of 3D organic-inorganic lead halide perovskites.

3.2. Results and Discussion

3.2.1. Pulse-Radiolysis Time-Resolved Microwave Conductivity (PR-TRMC) measurements

The charge carrier dynamics of polycrystalline bulk three-dimensional (3D) methyl ammonium lead halide perovskites ($MAPbX_3$; X=I, Br) were studied by measuring the change of conductivity (Δσ) in time after high energy electron irradiation with PR-TRMC technique (described in **Chapter 2**). The 3D perovskites used in this study were prepared by reacting MAX and PbX_2 salts via grinding and post-annealing as described in the section 3.4. (see characterization in Appendix Figures A3.1 and A3.2). Typical PR-TRMC conductivity transients at different temperatures are shown in Figure 3.1. The conductivity initially increases during the pulse as mobile charge carriers are generated and gradually decays after the pulse as the charges recombine or get trapped.

In Figure 3.1. it is shown that the change in conductivity and lifetime of $MAPbI_3$ and $MAPbBr_3$ are similar and both increase when the temperature decreases. Noticeably, when the $MAPbI_3$ compound goes through the phase transition from tetragonal (β) to orthorhombic (γ) at -115˚C, not only does the conductivity increase but also the carrier lifetime becomes much longer. The change in lifetime for $MAPbBr_3$ is smaller.

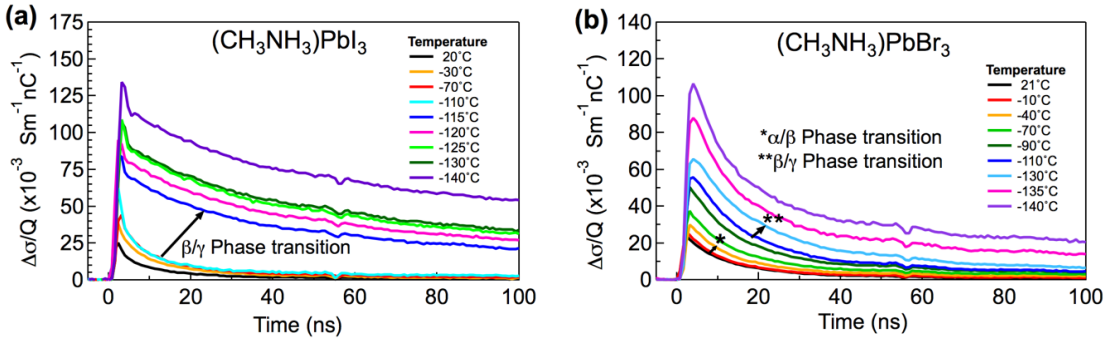

Figure 3. 1. Change of Conductivity as a function of time and temperature. a) $MAPbI_3$. b) $MAPbBr_3$. Phase transitions are highlighted in the figures.

In Figure 3.2. the calculated charge carrier mobility (see section 2.2 for details) and half-lifetime are shown as a function of temperature for $MAPbI_3$ and $MAPbBr_3$. At room temperature, the charge carrier mobilities for both materials are ~1-2 $cm^2V^{-1}s^{-1}$. Likewise, the mobility of charges in mixed halide $MAPbI_2Br$ and $MAPbIBr_2$ were found to be similar (see Appendix Figure A3.3.). From this we conclude that the charge carrier mobility in 3D perovskites is not significantly affected by varying the halogen between Iodine and Bromide. This contrasts with the large effect the halogen atom has on the unit cell size and optical band gap (Appendix Figure A3.2).[3] It is worth to notice that the charge carrier mobility values obtained by PR-TRMC are lower than previously reported values determined by transient tera-Hertz spectroscopy and microwave photoconductivity on spin coated $MAPbI_3$ thin films (~6-35 $cm^2V^{-1}s^{-1}$).[20,22,23] These lower values could stem from an overestimation of the charge carriers generated by electron irradiation. The radiation-ionization energy required for the generation of an electron-hole pair (E_p) in 3D perovskites may be higher than in typical inorganic semiconductors.[24,25] Moreover, the bulk polycrystalline materials (see SEM in Appendix Figure A3.1) used in this study exhibit small domain sizes (nm to µm scale), which increases the probability of recombination of the charge carriers and decreases their mobility. When the temperature is decreased, the charge carrier mobility of both $MAPbI_3$ (Figure 3.2.a) and $MAPbBr_3$ (Figure 3.2.b) increases reaching values of up to ~6 $cm^2V^{-1}s^{-1}$ at -130°C. In contrast to a previous study[20], an abrupt change is observed in the mobility trend upon going through the tetragonal to orthorhombic (β/γ) phase transition.

The trends with temperature of the charge carrier mobility and half-lifetime of $MAPbI_3$, shown in Figure 3.2.a, do not exhibit abrupt changes around the cubic to tetragonal (α/β) phase transition at 57°C. In the temperature range between 90°C down to -110°C, the charge carrier mobility follows band–like transport behavior characteristic of classic inorganic semiconductors such as silicon ($\mu=T^{-1.5}$).[26] In addition, the half-lifetime slightly decreases. Both trends are consistent with reduction of phonon scattering or lattice vibrations of the inorganic $(PbX_6)^{4-}$ framework at lower temperatures. Acoustic phonon-electron scattering behavior in $MAPbI_3$ has also been recently reported.[20,27] As mentioned, there are sudden changes in charge carrier mobility and lifetime at temperatures below the tetragonal to orthorhombic (β/γ) phase transition (-110°C). The charge carrier mobility increases following a strong deviation from the acoustic phonon scattering behavior ($\mu=T^{-1.5}$) and the half-lifetime shows a sudden rise that continues increasing as the temperature decreases further.

The behavior of $MAPbBr_3$ shown in Figure 3.2.b is similar than to $MAPbI_3$. Significant changes in charge carrier mobility and lifetime are not observed when crossing the (α/β) phase transition (-36°C). Around these phases, the mobility gradually increases following band–like transport behavior. After the (β/γ) phase transition (-124°C) the mobility suddenly rises and the half-lifetime slightly increases. The half-lifetime increment is obscured at low

temperature due to fast trapping of charges during the first 10 ns. This behavior will be further discussed in section 3.2.2. where the recombination and trapping dynamics of the charges are analyzed.

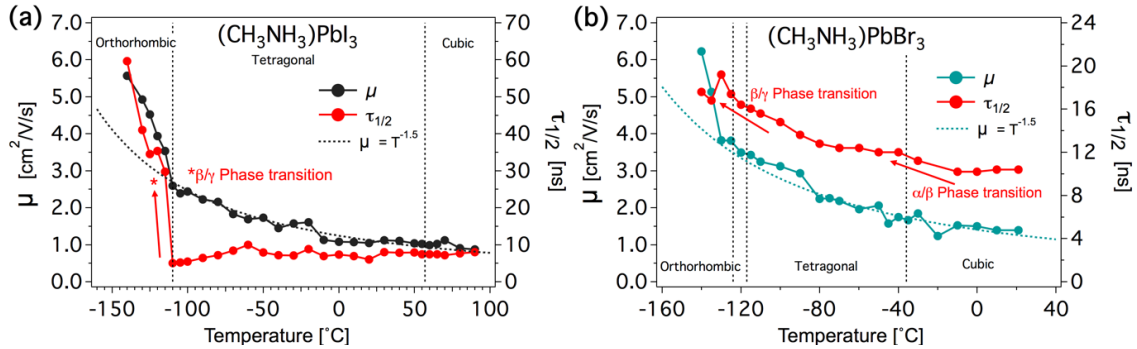

Figure 3.2. Charge carrier mobility and half-life time as a function of temperature. a) $MAPbI_3$. b) $MAPbBr_3$.

In order to confirm the change in the charge carrier dynamics at temperatures below the tetragonal to orthorhombic (β/γ) phase transition, we synthesized $MAPbI_3$ and $MAPbBr_3$ crystals in solution by different methods.[3,28] The samples obtained vary in size from similar polycrystalline crystals to millimeter single crystals. The mobility of charges as a function of temperature for these samples is shown in Appendix Figure A3.4. It is clear that the behavior is similar to the described above and an abrupt change of the dynamics is observed below the tetragonal to orthorhombic (β/γ) phase transition. This sudden variation cannot be attributed entirely to the reduction of the phonon scattering. We argue that different charge carrier dynamics related to the dynamic disorder of the organic cation are present in 3D perovskites.

The rotational freedom of the MA^+ cation in the 3D perovskite crystal lattice has been confirmed by several techniques.[9–11,13–15] At room temperature, the organic cation constantly reorients.[15] At low temperatures, the thermal motion of the organic cation reduces[14] leading to phase transitions in the crystal structure. Transitioning from the cubic to tetragonal (α/β) phase, the organic cation preserves its dynamic disorder. But below the tetragonal to orthorhombic (β/γ) phase transition temperature its orientation becomes fixed. This restriction has been observed by dielectric spectroscopy[11,12], NMR measurements[10], high-resolution neutron scattering[14] and a variety of computational studies.[4,5,13,15] The rotational motion of the organic cation influences the dielectric constant and internal electric field of the material.[12] As a consequence, it can directly influence the charge carrier dynamics[15,29] as observed in our temperature dependent PR-TRMC measurements.

When the perovskite lattice is in the cubic phase (room temperature and higher), the time for the rotation of the organic cation is of the order of ~0.3 ps for a wobbling-in-a-cone motion and ~3 ps for 90° jumps.[15] Such fast rotation creates a relatively homogeneous disordered (non-ferroelectric) energy landscape where electrons and holes easily recombine, decreasing

the lifetime of charge carriers. As the temperature decreases, the movement of the organic cation reduces, inducing the transition to the tetragonal (β) phase. However, in the β phase the organic cation preserves its rotational freedom. This explains why the charge carrier mobility continues to follow a band-like behavior on going through the α/β phase transition.

Below the (β/γ) phase transition temperature the organic cation motion is restricted, specifically the 90° jumps.[15] As these jumps occur on a similar time scale (3 ps) as charge transport, the dynamically disordered energy landscape at room temperature is replaced by a static one. The organic cation freezes with a certain fixed orientations of dipoles. This leads to local charged states that can enhance the separation of the charge carriers (electrons and holes), thereby increasing the charge carrier mobility and lifetime as observed in our PR-TRMC measurements. This local charged state mechanism in 3D perovskites has been widely proposed in theoretical studies with specific orientation of the organic dipoles, predicting this internal dissociation of electron and hole and reduced recombination rates. [5,6,30,31]

The efficiency of this mechanism most likely depends on the dipole moment of the organic cation and interaction with the inorganic crystal lattice. As methylammonium (MA^+) has a high dipole moment, this mechanism has a significant effect on the charge carrier dynamics. In order to further test the influence of the organic cation on the charge dynamics, we performed similar PR-TRMC measurements on 3D perovskites with organic cations with small (formamidinium, FA^+) or zero (Cesium, Cs) dipole moment. The influence of the organic cation dipole moment and interaction with the crystal lattice is discussed in **Chapter 4.**

3.2.2. Charge recombination and trapping

In order to further study the effect of the organic cation on $MAPbX_3$ (X=I, Br) perovskites, we measured the recombination dynamics as a function of the initial concentration of charge carriers. For this, the pulse length was varied from 0.2 ns to 1 ns, resulting in initial concentration densities between ~$4x10^{14}$ cm^{-3} to ~$4x10^{15}$ cm^{-3}. These concentrations are lower than those generated under 1.5 AM standard illumination conditions (10^{16}-10^{17} cm^{-3}).[32] Nevertheless, these low intensities allow us to observe the charge dynamics of hybrid perovskites at conditions that are not feasible in transient tera-Hertz spectroscopy and microwave photoconductivity experiments (up to ~10^{18} cm^{-3}).[20,23] The experimental results are shown at different temperatures in Figures 3.3a,b for $MAPbI_3$. The results for $MAPbBr_3$ are similar and are shown in Appendix Figure A3.5 and Table A3.1. In Figures 3.3a,b is observed that the conductivity decays faster for higher initial concentration of charges, which is consistent with second-order charge recombination. Nevertheless, the end-of-pulse conductivity also increases for longer pulses. This behavior points to the presence of a limited concentration of trap states in the material for either electrons or holes. Based on this, we

modeled the experimental data using the kinetic model described in section 2.4. [23]This model assumes second-order bimolecular recombination, second-order trapping with a limited concentration of traps and second-order recombination of electrons with trapped charges according to Figure 2.4. The results obtained using this model accurately describe the main features of the conductivity decay and are shown in Figures 3.3c, d and Table 3.1.

The total mobilities obtained are in good agreement with the experimental values shown in Figure 3.2. Higher mobility values can be expected from the model as the experimental signals are limited by recombination during the pulse. In our kinetic model the trap states have an electronic nature.[23,33,34] As the most mobile charge gets trapped first, the mobility of the electrons is higher than for the holes. It should be noted that the nature of the trap states (either electrons or holes) is not known. In our experiment we cannot discriminate between the positive and negative charges and the reverse situation is also mathematically valid. In fact, by DFT band structure calculations it was determined that the effective mass of holes is lower, which results in a slightly higher mobility of holes (~1.3-2 times) compared to electrons (Appendix Figure A3.6). Although the nature of the traps is not known, we deducted that the concentration of trap states (N_t) is ~$1x10^{15}$ cm^{-3} for $MAPbI_3$ and ~$5x10^{14}$ cm^{-3} for $MAPbBr_3$. These trap concentrations are high considering that the concentrations of charges generated by our experiments are of the same order of magnitude. This landscape makes the second order trap-filling rate (k_3) dominant over the recombination (k_2) and trap emptying (k_4) rates.

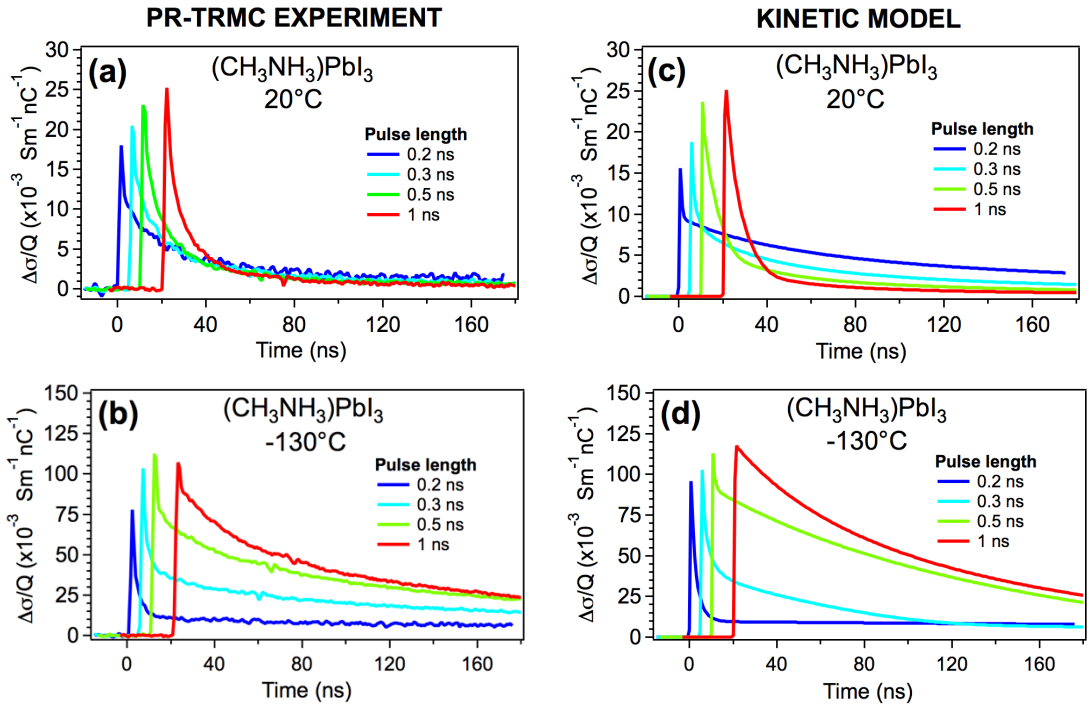

Figure 3.3. Charge Carrier decay dynamics of $MAPbI_3$ at 21°C and -130°C as a function of initial concentration of charge carriers (pulse length). a, b) Experimental data. c, d) kinetic model fit.

Table 1. Kinetic fitting parameters for MA_3PbI_3 at 20°C and -130°C

Perovskite	$CH_3NH_3PbI_3$	
Description/Temperature	**20°C**	**-130°C**
Mobility: e- / h+ [$cm^2/V/s$]	1.12 / 0.4	5.5 / 0.4
Generation yield (k_1) [$1/cm^3/nC$]	1.51E+15	1.51E+15
Second order recombination rate (k_2) [cm^3/s]	3.00E-08	2.00E-09
Second order trap filling rate (k_3) [cm^3/s]	1.90E-06	7.00E-07
Second order trap emptying rate (k_4)	2.50E-08	2.50E-09
Trap state concentration N_t [$1/cm^3$]	1.40E+15	9.80E+14

In order to compare our results to previously reported monomolecular recombination rates determined by PL decay measurements in thin films[20] we multiplied the second-order trap-filling rate (k_3) with the concentration of trap states (N_t) determined by our model. For $MAPbI_3$, our calculated monomolecular recombination rate is 2.66×10^9 s^{-1} at 20°C and 6.86×10^8 s^{-1} at -130°C. These values are two orders of magnitude faster than the previously reported ones.[20] The difference is presumably related to the morphology of the samples as the concentration of trap states is higher in polycrystalline bulk samples than in thin films. Still, the temperature trend is the same. As the temperature increases the monomolecular recombination rate increases. This behavior may be related to charge recombination with ionized impurities (originated from vacancies, substitutions or interstitials).[20] The second-order recombination rate (k_2) decreases as the temperature decreases from 3×10^{-8} cm^3 s^{-1} at 20°C to 2×10^{-9} cm^3 s^{-1} at -130°C. This trend is in agreement with previous microwave photoconductivity measurements,[35] but in contradiction to Langevin's trend of bimolecular recombination rate determined using optical-pump-Tera-Hertz (THz) probe spectroscopy.[20]

Direct comparison between PR-TRMC and THz spectroscopy, however, is hampered by differences in the time scale measured (1.5 ns in THz spectroscopy to 200 ns in PR-TRMC) and the electric field strength (~150 kV/cm[36] in THz spectroscopy to <100 V/cm[37] in PR-TRMC). Processes that occur on a sub-nanosecond timescale are not explicitly observed in the PR-TRMC experiments. The higher electric fields can also have an influence on the mobility of the charge carriers.

The observed deviation from the theory of Langevin can be explained by the disorder introduced by the dynamic rotation of the organic cation. Langevin's theory states that the probability of electron-hole recombination should increase at low temperature, as the velocity (mobility) at which an electron approaches to the Coulombic capture radius of the hole is higher and the thermal energy available to escape is lower.[21] We propose that the charge carrier dynamics in 3D methyl ammonium halide perovskites are influenced by different mechanisms that are not considered in Langevin's theory. As discussed above, the freezing of the organic cation after the (β/γ) transition at low temperature creates local charged domains. These domains lead to efficient dissociation of opposite carriers, allowing

the charges to move away from the Coulombic capture radius. This process increases the lifetime of charge carriers and reduces the second order recombination.

3.3. Conclusions

To conclude, PR-TRMC measurements were used to determine the charge carrier dynamics in bulk $MAPbX_3$ (X= I, Br) perovskites at different temperatures. We observed that the charge carrier dynamics in hybrid perovskites are not exclusively determined by phonon-electron scattering or reduction of lattice vibrations commonly present in inorganic semiconductors but that other effects have to be operative. We propose that these effects are related to the rotational freedom of the organic cation at high temperature and subsequent freezing below the tetragonal (β) to orthorhombic (γ) phase transition temperature.

At temperatures above the β/γ phase transition, the charge dynamics are dominated by the vibrations of the lattice, local inorganic $(PbX_6)^{4-}$ framework and extended $[PbX_3]^{1-}$ framework, following band-like transport behavior. The organic cations do not influence the dynamics, as their fast reorientation creates a homogeneous energy landscape. Upon going through the β/γ phase transition, the charge carrier dynamics abruptly change, deviating from band-like transport behavior characteristic of common inorganic semiconductors. The abrupt increase in charge carrier mobility and lifetime observed is consistent with the freezing of the organic counter-ions in the structure; such fixed cation position creates a static energy landscape in which local polarized domains enhance charge separation. In addition, the influence of the organic cation dynamic disorder is also seen in the decay kinetics. The decrease of the bimolecular recombination at low temperature, in contradiction to Langevin's theory, is associated with the fixed position of the organic cation in the orthorhombic phase.

Finally, the technique used in this work gives a powerful insight into the charge dynamics of materials. Using PR-TRMC we can generate electrons and holes far away from each other and determine their mobility and its trend with temperature independent of the exciton binding energy of the material. In our opinion, determining the charge carrier mobility based only on the analysis of photoconductivity measurements is not sufficient, particularly in temperature dependent measurements. At very low temperature the thermal energy available decreases and may be insufficient for the charges generated by laser excitation to dissociate (in materials with high exciton binding energy). This is a consequence of the small separation distance at which the charge carriers are generated in this type of measurements.

3.4. Experimental methods

Materials. All chemicals were purchased from Sigma-Aldrich and used as received unless otherwise stated. CH_3NH_3I (MAI) and CH_3NH_3Br (MABr) were prepared by reacting 43.3 ml of CH_3NH_2 (40wt. % in H2O) with 66.0 ml of HI (57wt. % in water) or 56.6 ml of HBr (48wt. % in water), respectively. The reactions were carried out in a round bottom flask placed in an ice bath for 3 hours with stirring. The precipitates were collected by rotary evaporation at 60oC for 1 h. Finally, the products were washed with diethyl ether, and dried at 60oC in vacuum oven overnight. PbI_2 was recrystallized with ultrapure H2O and dried in vacuum at 90°C overnight before use.

Synthesis. $MAPbX_3$ (X= I, Br, Cl) perovskites were prepared by reacting equivalent molar amount (2 mmol) of MAX and PbX_2 (X = I, Br, Cl). The starting materials were placed in an agate mortar and ground until a visually homogeneous color powder was obtained. The ground product was then loaded in a 13 mm quartz tube, evacuated and sealed at 10^{-4} mbar. The sealed quartz tube was placed in a 200^{o}C sand bath. The sand bath annealing process was carried out for 8 h.

PR-TRMC measurements. A small amount of material (~45 mg) is placed in a polyimide holder and filled by pouring droplets of poly methyl methacrylate (PMMA) dissolved in chlorobenzene at a concentration of 10mg/ml every 10 min until the perovskite material is fully covered by PMMA. Then, the sample holder is left overnight to ensure the complete evaporation of the solvent. The PMMA filling is done in order to protect the samples from moisture and air and diminish the background conductivity of the material (which affects the PR-TRMC measurements). The polyimide block with the perovskite sample is placed inside a rectangular waveguide copper cell. The cell is contained in a cryostat in which the temperature can be varied between 200°C and -150°C. Each temperature measured was maintained for ~15 min in order to assure the equilibrium of the system. The irradiation intensity was varied between pulse lengths of 200 ps and 2 ns for each temperature at a frequency of 32 GHz. The frequency scan fits were measured at a pulse length of 200 ps.

XRD measurements. XRD diffraction patterns were collected with a Bruker D8 Advance diffractometer (Bragg-Brentano geometry) equipped with a Co Kα X-ray tube (λ=1.78897) operated at 40kV and 40mA using a step size of 0.0092° and a time per step of 0.2 s. Samples were mounted in a top-loaded trough, which was rotated during data collection. Under these conditions the intensity of the strongest reflection was approximately 10000 counts.

DFT calculations. All DFT calculations were performed with VASP 5.3.3 using the experimentally determined structures of the different materials in their cubic symmetries.

The electronic structure calculations were performed using a PBE exchange and correlation functional and the corresponding projected-augmented-wave pseudopotentials. Relativistic effects and d-orbitals were not included in the calculation. A full SCF calculation on a 10x10x10 gamma-centered grid was first performed and the resulting charge density was used to compute the band structure. The effective masses were then calculated from the curvature of the band at the desired k-point via the Effective Mass Calculator (EMC) program with 10^{-2} $Bohr^{-1}$ step size.

3.5. References

1. NREL. Best Research-Cell Efficiencies. *Best Research-Cell Efficiencies* (2019). Available at: https://www.nrel.gov/pv/assets/pdfs/best-research-cell-efficiencies-190416.pdf.
2. Chen, Q. *et al.* Under the spotlight: The organic-inorganic hybrid halide perovskite for optoelectronic applications. *Nano Today* **10**, 355–396 (2015).
3. Stoumpos, C. C., Malliakas, C. D. & Kanatzidis, M. G. Semiconducting tin and lead iodide perovskites with organic cations: Phase transitions, high mobilities, and near-infrared photoluminescent properties. *Inorg. Chem.* **52**, 9019–9038 (2013).
4. Frost, J. M., Butler, K. T. & Walsh, A. Molecular ferroelectric contributions to anomalous hysteresis in hybrid perovskite solar cells. *APL Mater.* **2**, (2014).
5. Frost, J. M. *et al.* Atomistic origins of high-performanc1. Frost, J. M. et al. Atomistic origins of high-performance in hybrid halide perovskite solar cells. Nano Lett. 14, 2584–90 (2014).e in hybrid halide perovskite solar cells. *Nano Lett.* **14**, 2584–90 (2014).
6. Sherkar, T. S. & Jan Anton Koster, L. Can ferroelectric polarization explain the high performance of hybrid halide perovskite solar cells? *Phys. Chem. Chem. Phys.* **18**, 331–338 (2016).
7. Quarti, C. *et al.* Cation-Induced Band-Gap Tuning in Organohalide Perovskites: Interplay of Spin–Orbit Coupling and Octahedra Tilting. *Nano Lett.* **14**, 3608–3616 (2014).
8. Eperon, G. E. *et al.* Formamidinium lead trihalide: A broadly tunable perovskite for efficient planar heterojunction solar cells. *Energy Environ. Sci.* **7**, 982–988 (2014).
9. Noriko Onoda-Yamamuro, Matruo, T. & Suga, H. Calorimetric and IR Spectroscopic Studies of Phase Transitions in MAPbX3. **51**, 1383–1395 (1990).
10. Knop, O., Wasylishen, R. E., White, M. A., Cameron, T. S. & Oort, M. J. M. Van. Alkylammonium lead halides. Part 2. CH 3 NH 3 PbX 3 (X = Cl, Br, I) perovskites: cuboctahedral halide cages with isotropic cation reorientation. *Can. J. Chem.* **68**, 412–422 (1990).
11. Poglitsch, A. & Weber, D. Dynamic disorder in methylammoniumtrihalogenoplumbates (II) observed by millimeter-wave spectroscopy. *J. Chem. Phys.* **87**, 6373–6378 (1987).
12. Onoda-Yamamuro, N., Matsuo, T. & Suga, H. Dielectric study of CH3NH3PbX3 (X = Cl, Br, I). *J. Phys. Chem. Solids* **53**, 935–939 (1992).
13. Leguy, A. M. A. *et al.* The dynamics of methylammonium ions in hybrid organic-inorganic perovskite solar cells. *Nat. Commun.* **6**, (2015).
14. Swainson, I. P. *et al.* From soft harmonic phonons to fast relaxational dynamics in CH3NH3PbBr3. *Phys. Rev. B - Condens. Matter Mater. Phys.* **92**, 2–6 (2015).
15. Bakulin, A. A. *et al.* Real-Time Observation of Organic Cation Reorientation in Methylammonium Lead Iodide Perovskites. *J. Phys. Chem. Lett.* **6**, 3663–3669 (2015).
16. Juarez-Perez, E. J. *et al.* Photoinduced giant dielectric constant in lead halide perovskite solar cells. *J. Phys. Chem. Lett.* **5**, 2390–2394 (2014).
17. Kutes, Y. *et al.* Direct observation of ferroelectric domains in solution-processed CH3NH3PbI3 perovskite thin films. *J. Phys. Chem. Lett.* **5**, 3335–3339 (2014).
18. Snaith, H. J. *et al.* Anomalous Hysteresis in Perovskite Solar Cells. *J. Phys. Chem. Lett.* **5**, 1511–1515 (2014).
19. Quarti, C., Mosconi, E. & De Angelis, F. Interplay of orientational order and electronic structure in methylammonium lead iodide: Implications for solar cell operation. *Chem. Mater.* **26**, 6557–6569 (2014).
20. Milot, R. L., Eperon, G. E., Snaith, H. J., Johnston, M. B. & Herz, L. M. Temperature-Dependent Charge-

Carrier Dynamics in CH3NH3PbI3 Perovskite Thin Films. *Adv. Funct. Mater.* **25**, 6218–6227 (2015).
21. Langevin, P. The Recombination and Mobilities of Ions in Gases. *Ann Chim Phys* **28**, 433–530 (1903).
22. Wehrenfennig, C., Eperon, G. E., Johnston, M. B., Snaith, H. J. & Herz, L. M. High charge carrier mobilities and lifetimes in organolead trihalide perovskites. *Adv. Mater.* **26**, 1584–1589 (2014).
23. Hutter, E. M., Eperon, G. E., Stranks, S. D. & Savenije, T. J. Charge Carriers in Planar and Meso-Structured Organic-Inorganic Perovskites: Mobilities, Lifetimes, and Concentrations of Trap States. *J. Phys. Chem. Lett.* **6**, 3082–3090 (2015).
24. CA, K. Bandgap dependence and related features of radiation ionization energies in semiconductors. *J. Appl. Phys.* **39**, 2029–2038 (1968).
25. Alig, R. C. & Bloom, S. Electron-Hole-Pair Creation Energies in Semiconductors. *Phys. Rev. Lett.* **35**, 1522–1525 (1975).
26. Neamen, D. A. *Semiconductor Physics and Devices: Basic Principles*. (McGraw-Hill, 2012).
27. Karakus, M. *et al.* Phonon-Electron Scattering Limits Free Charge Mobility in Methylammonium Lead Iodide Perovskites. *J. Phys. Chem. Lett.* **6**, 4991–4996 (2015).
28. Saidaminov, M. I. *et al.* High-quality bulk hybrid perovskite single crystals within minutes by inverse temperature crystallization. *Nat. Commun.* **6**, 1–6 (2015).
29. Ma, J. & Wang, L. W. Nanoscale charge localization induced by random orientations of organic molecules in hybrid perovskite CH3NH3PbI3. *Nano Lett.* **15**, 248–253 (2015).
30. Berdiyorov, G. R., El-Mellouhi, F., Madjet, M. E., Alharbi, F. H. & Rashkeev, S. N. Electronic transport in organometallic perovskite CH3NH3PbI3: The role of organic cation orientations. *Appl. Phys. Lett.* **108**, 3–7 (2016).
31. Rashkeev, S. N., El-Mellouhi, F., Kais, S. & Alharbi, F. H. Domain walls conductivity in hybrid organometallic perovskites and their essential role in CH<inf>3</inf>NH<inf>3</inf>PbI<inf>3</inf> solar cell high performance. *Sci. Rep.* **5**, 1–8 (2015).
32. Jiang, C. S. *et al.* Carrier separation and transport in perovskite solar cells studied by nanometre-scale profiling of electrical potential. *Nat. Commun.* **6**, 1–10 (2015).
33. Stranks, S. D. *et al.* Recombination Kinetics in Organic-Inorganic Perovskites: Excitons, Free Charge, and Subgap States. *Phys. Rev. Appl.* **2**, 1–8 (2014).
34. Trapping, C. *et al.* Electronic Properties of Meso-Superstructured and Planar Organometal Halide Perovskite Films : *ACS Nano* 7147–7155 (2014).
35. Savenije, T. J. *et al.* Thermally activated exciton dissociation and recombination control the carrier dynamics in organometal halide perovskite. *J. Phys. Chem. Lett.* **5**, 2189–2194 (2014).
36. Ulbricht, R., Hendry, E., Shan, J., Heinz, T. F. & Bonn, M. Carrier dynamics in semiconductors studied with time-resolved terahertz spectroscopy. *Rev. Mod. Phys.* **83**, 543–586 (2011).
37. Warman, J., Haas, M. De, Dicker, G. & Grozema, F. Charge Mobilities in Organic Semiconducting Materials Determined by Pulse-Radiolysis Time-Resolved Microwave Conductivity:-Bond-Conjugated Polymers. *Chem. Mater* 4600–4609 (2004).

Chapter 4

Effect of Dipole Moment of the Organic Cation on the Charge Dynamics of Three-Dimensional (3D) Lead Halide Perovskites

In this chapter the influence of the organic cation on the charge carrier dynamics of three-dimensional (3D) organic-inorganic perovskites is further explored by introducing cations with different intrinsic properties. The effect of the dipole moment and interaction with the inorganic lattice was tested by using cations with low (formamidinium, FA) or zero dipole moment (cesium, Cs). Apart from their dipole moment, these cations also differ in nature (organic – inorganic) and size. Using pulse-radiolysis time-resolved microwave conductivity (PR-TRMC) measurements we have determined that the mobility and lifetime of charge carriers in formamidinium and cesium lead halide perovskites does not deviate from the band-like transport as in methyl ammonium (MA) lead halide perovskites. We attribute this behavior to the low dipole moment (or lack of it) resulting in the absence of a significant temperature dependence of the orientational disorder. This chapter confirms that the charge carrier dynamics in hybrid perovskites are affected by the intrinsic properties of the organic cation and its interaction within the inorganic framework.

This chapter is based on:

María C. Gélvez-Rueda, Duyen H. Cao, Sameer Patwardhan, Nicolas Renaud, Constantinos C. Stoumpos, Geroge C. Schatz, Joseph T. Hupp, Omar K. Farha, Tom J. Savenije, Mercouri G. Kanatzidis, Ferdinand C. Grozema. Effect of Cation Rotation on Charge Dynamics in Hybrid Lead Halide Perovskites. J. Phys. Chem. C 2016, 120, 16577-16585.

María C. Gélvez-Rueda, Nicolas Renaud, Ferdinand C. Grozema. Temperature Dependent Charge Carrier Dynamics in Formamidinium Lead Iodide Perovskite. J. Phys. Chem. C 2017, 121, 23392-23397.

4.1. Introduction

The opto-electronic properties of organic-inorganic metal halide perovskites strongly depend on their composition and the degrees of freedom within the structure.[1,2] Interactions related to the motion of the organic cation, soft rotation of the inorganic octahedra and the stereochemistry of Pb^{2+} have been shown to affect properties such as the mobility of charges,[3–5]charge carrier lifetime,[3–5] band gap,[6–9] geometry of the unit cell[10] and dimensionality of the crystal structure.[6,10,11] The latter effect is critical in formamidinium lead iodide ($FAPbI_3$) as it can lead to the formation of a non-perovskite yellow phase that hinders its photovoltaic performance.[10,12] Replacing methylammonium (MA) by formamidinium (FA) is a desired alternative as it leads to a decrease in the bandgap of $FAPbI_3$ to 1.47 eV and therefore an improvement in the absorption in the infrared region.[12–16] However, the formation of the non-perovskite yellow phase decreases the stability, solar cell efficiency and complicates the understanding of its intrinsic opto-electronic properties.[17,18] There are limited studies of the opto-electronic properties of $FAPbX_3$ (X= I, Br). Photo-luminescent measurements at room temperature have shown that the diffusion length of the charge carriers is considerably longer in $FAPbX_3$ than in $MAPbX_3$ (X= I, Br) perovskites.[15,16,19–21] Furthermore, based on a line-width analysis of photoluminescence measurements, it has been argued that charge transport is dominated by scattering from optical phonons (Fröhlich interactions) instead of acoustic phonons as has been assumed for $MAPbX_3$.[22] Currently, there are no studies that focus on properties such as charge mobility and recombination mechanisms as a function of temperature. Moreover, there are no studies that relate changes in these properties to the presence of the organic cation within the perovskite structure.

The reorganization of the organic cation in the perovskite lattice of $MAPbI_3$ has a large influence on the crystal phase geometry,[10] the charge carrier dynamics (mobility and recombination mechanisms) [3–5] and the optical-electronic transitions (direct-indirect band gap,[8,9] Rashba splitting[9]). Replacing MA by FA, should affect the reorientation of the organic cation due to the larger size and smaller dipole moment of FA. It has been calculated that the time constant for the rotation of FA is one order of magnitude longer than for MA.[23,24] This is consistent with the larger size of FA, which reduces its rotational freedom in the structure. In addition, temperature dependent dielectric measurements show that, compared to $MAPbI_3$, the static dielectric permittivity (ε_r') of $FAPbI_3$ is lower and has a negligible temperature dependence.[25–27] This is consistent with the smaller dipole moment of FA.[27] Moreover, at temperatures below the tetragonal (β) to orthorhombic (γ) phase transition, the ε_r' of $FAPbI_3$ continues increasing while in $MAPbI_3$ abruptly decreases.[25–27] This means that the rotational freedom of FA is maintained and is less affected by temperature than the rotational freedom of MA, which is drastically reduced at low temperatures.[27] We have shown that in the low-

temperature orthorhombic phase of $MAPbI_3$, where the MA orientation is static, the charge carrier mobility and lifetime abruptly increase.[5] This behavior is attributed to the formation of polar charged domains that increase charge separation and reduce recombination.[3–5]

In this chapter we have studied the temperature dependence of the mobility and lifetime of charge carriers in $FAPbI_3$ using time-resolved microwave conductivity measurements, coupled with generation of charges by irradiation with high-energy electrons (PR-TRMC). We show that the charge carrier mobility of $FAPbI_3$ increases at low temperature following phonon scattering behavior ($\mu=T^{-1.5}$). Interestingly, in contrast to the results shown in **Chapter 3** for $MAPbI_3$,[5] we do not observe sudden changes in the mobility and lifetime of charge carriers at temperatures below the β/γ phase transition. We attribute this to the persisting rotational freedom of FA in the orthorhombic phase. As FA does not become fixed in the structure, it does not form charged domains that suddenly increase the mobility and lifetime at the phase transition. This smaller temperature dependence of the orientational freedom of FA on temperature is primarily related to its smaller dipole moment, compared to MA. In order to further test this claim, we studied the charge carrier dynamics of 3D perovskites introducing a cation without a dipole moment, cesium (Cs). As for FA based 3D perovskites, the charge carrier mobility increases at low temperature with phonon scattering behavior ($\mu=T^{-1.5}$), without abrupt changes at the phase transitions. This confirms that when the dipole moment and orientational freedom are low (absent) there is no significant effect on the charge carrier dynamics. The results shown here and in **Chapter 3** indicate that the charge carrier dynamics in 3D hybrid perovskites are affected by the intrinsic properties of the organic cation and its interaction within the structure.

4.2. Results and Discussion

4.2.1. Charge carrier Mobility and Lifetime of FAPbI3 determined by Pulse-Radiolysis Time-Resolved Microwave Conductivity (PR-TRMC)

The charge carrier dynamics of polycrystalline bulk three-dimensional (3D) formamidinium lead iodide ($FAPbI_3$) were studied by measuring the change of conductivity ($\Delta\sigma$) in time after high energy electron irradiation with PR-TRMC technique (described in **Chapter 2**). $FAPbI_3$ was prepared by dissolving FAI and PbI_2 in anhydrous DMF and evaporating under reduced pressure as described in section 4.4. The synthesis conditions were optimized in order to isolate black α-$FAPbI_3$ (see XRD in Appendix Figure A4.1.). The black α-$FAPbI_3$ phase was obtained and stabilized at higher temperature (160°C for at least 1h) in comparison to the yellow phase (140°C). This procedure is in agreement with literature, where the black phase is stabilized at 185°C for 1 h under ambient pressure conditions.[19,21]

Typical conductivity transients for black $FAPbI_3$ as a function of temperature are shown in Figure 4.1.a, where it is observed that the change in conductivity at the end of the pulse increases as the temperature decreases. We estimate the mobility knowing the initial concentration of charge carriers as described in section 2.2. The charge carrier mobility of black $FAPbI_3$ is ~2.5 cm^2/Vs at room temperature (Figure 4.1.b). This value is lower than the determined for thin-films by tera-Hertz spectroscopy (~27 cm^2/Vs) but comparable to values obtained by photoluminescent quenching method (PLQ) (μ_h = 3.5 cm^2/Vs and μ_e = 0.2 cm^2/Vs).[28] On $FAPbI_3$ single crystals, space-charge-limited-current (SCLC) experiments have also resulted in a higher charge mobility (μ_h = 35 cm2/Vs).[28] The lower value obtained here may be related to the polycrystalline nature the crystals studied (see SEM in Appendix Figure A4.1). As comparison, we show that the charge carrier mobility of black $FAPbI_3$ is two orders of magnitude higher than for the yellow $FAPbI_3$ (0.009 cm^2/Vs at 20°C). This is fully consistent with DFT calculations that show that the effective mass of electrons and holes in the yellow phase are up to one order of magnitude higher than in the black phase (Appendix Table A4.1). In addition, in Figure 4.1.b is shown that the charge carrier mobility of black $FAPbI_3$ increases as the temperature decreases, up to ~9.5 cm^2/Vs at -150°C, following acoustic phonon-electron scattering (lattice vibration) trend ($\mu=T^{-1.5}$).[29] In contrast to the results shown in **Chapter 3** for $MAPbI_3$[5], we do not observe a deviation from this phonon-scattering trend at temperatures below the tetragonal (β) to trigonal (γ) phase transition (-133°C[26,27]).

The charge carrier lifetime of $FAPbI_3$ shown in Figure 4.1.a., is long and does not decay in the first 200 ns. The conductivity decay is shown on a logarithmic timescale in Figure 4.1.c., where it can be seen that the carrier lifetime increases from ~600 ns at room temperature to ~2 µs at -150°C. The lifetime obtained at room temperature is comparable with photoluminescence measurements, ~100 to 600 ns.[19–21] Using the charge mobility and lifetime determined by PR-TRMC, we estimate a carrier diffusion length of ~1 µm by Einstein-relation.[30,31] This value is comparable to $FAPbI_3$ polycrystalline thin films (3.1 µm)[15,20] and single crystals (6.6 µm).[19,21] The diffusion length of $MAPbI_3$ prepared with similar conditions is ~0.6 µm (See Appendix Figure A4.2). This is consistent with previous photo-luminescence studies, in which the carrier lifetime of $FAPbI_3$ is longer than in $MAPbI_3$.[15,16,19–21] We believe that the longer carrier lifetime of $FAPbI_3$ is caused by the reduced rotational freedom of FA as compared with MA. It has been shown, both experimentally and theoretically, that the time for the rotation of MA is ~0.3 ps for a wobbling-in-a-cone motion and ~3 ps for 90° jumps.[23] In the case of FA the theoretical rotation is ~2 ps for the rollover process.[24] This slower rotation leads to polar rotations and distorted domains that also distort the inorganic cages, ultimately facilitating charge separation and reducing recombination.[21] In addition, we do not observe an abrupt increase of the carrier lifetime of $FAPbI_3$ at temperatures below the β/γ-phase transition. In fact, fitting the conductivity decay of $FAPbI_3$ to a double exponential time constant (τ_1 and τ_2)

shows that at low temperature the values of τ_1 and τ_2 do not significantly change (see Appendix Figure A4.3). These results confirm that at temperatures below the γ-phase transition neither the charge carrier mobility nor lifetime of $FAPbI_3$ abruptly increase as it occurs for $MAPbI_3$.

For hybrid perovskites ($MAPbI_3$ and $FAPbI_3$), the dependence of the charge carrier dynamics on temperature have been mainly related to phonon scattering mechanisms dominated by interactions between charge carriers and optical phonons (Fröhlich interactions).[22] However, the influence of only Fröhlich interactions do not explain the low charge carrier mobility of hybrid perovskites (compared to inorganic semiconductors with similar Fröhlich coupling strengths),[22,32] neither the abrupt increase of the charge carrier mobility and lifetime of $MAPbI_3$ at temperatures below the tetragonal (β) to orthorhombic (γ) phase transition.[5,32] This latter effect has been related to the fixed orientation of MA in the γ-phase,[25,33,34] which leads to strong polar domains that increase charge separation and reduce recombination. [3–5] In the case of $FAPbI_3$, the mobility and lifetime of $FAPbI_3$ do not abruptly increase in the γ-phase. This is consistent with the persistent reorientation of FA in the γ-phase observed by dielectric experiments.[27] The static dielectric permittivity (ε_r'), which indirectly probes the motion of the organic cation, does not decrease on going through the β/γ phase transition and continues increasing in the γ-phase.[27] The reorientation of FA is mildly inhibited at these temperatures.[27] The low ε_r' and its minimal dependence on the temperature are consistent with the small dipole moment of FA.[27] This behavior is completely opposite to $MAPbI_3$, in which the ε_r' abruptly decreases due to the reduced rotational freedom of MA on going through the β/γ phase transition.[25] Comparing the present experiments on $FAPbI_3$, with the results shown in **Chapter 3** on $MAPbI_3$, it is clear that the charge carrier dynamics strongly depend on the nature of the organic cation. We believe that the vibrational mechanisms are affected by the organic cation rotation (dipole scattering) within the structure.[5,32] This interaction strongly depends on the intrinsic properties of the organic cation, such as size and strength of dipole moment.

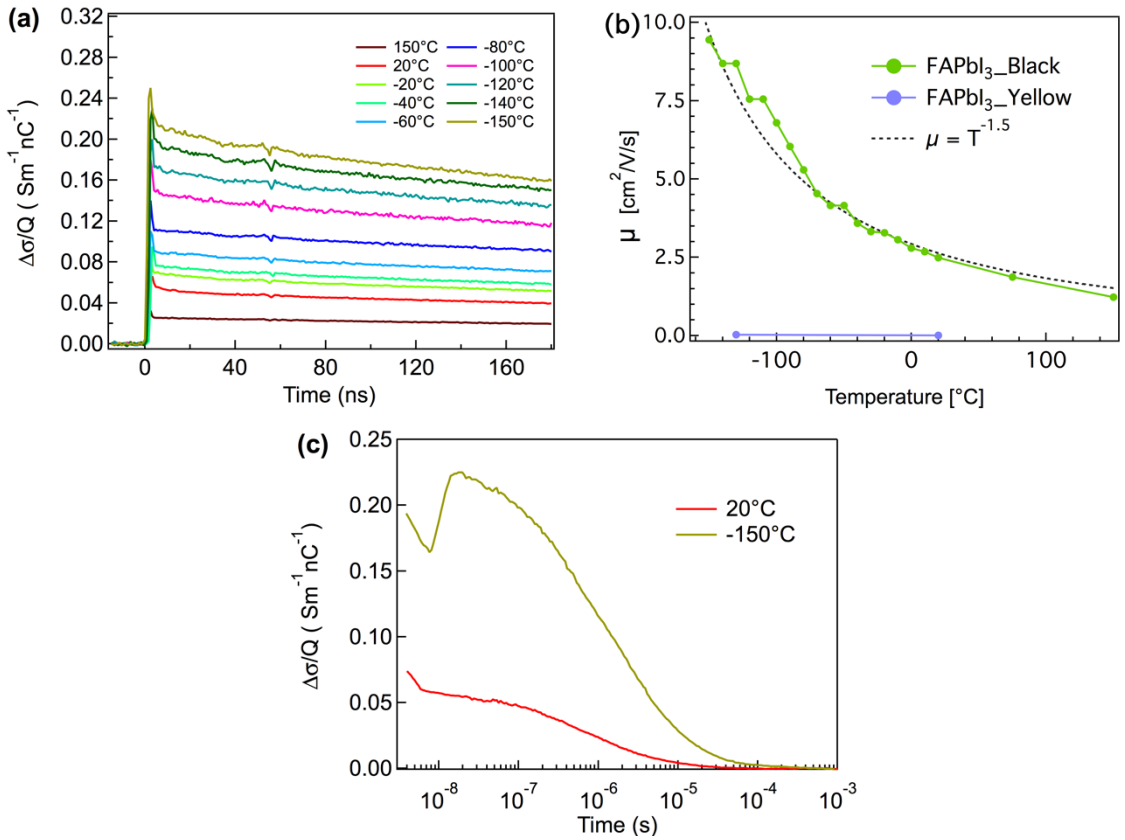

Figure 4.1. PR-TRMC experiments on $FAPbI_3$. a) Temperature dependence of the radiation induced conductivity for black $FAPbI_3$ as a function of time using a 0.2 ns electron pulse. **b)** Charge carrier mobility as a function of temperature). **c)** Long-time decay of the carrier life time of $FAPbI_3$ at 20°C and -150°C.

In order to further test the influence of the organic cation on the charge dynamics, we have performed similar PR-TRMC measurements on an inorganic based perovskite: $CsPbBr_3$. $CsPbI_3$ was not tested as the temperatures at which its black cubic perovskite phase is stable (T>310°C)[10,35] are out of our experimental possibilities. The absence of a dipole moment in the inorganic cation, Cesium (Cs), allows us to assess the effect of the phase transitions and the freezing of the organic cation on the $MAPbBr_3$ charge carrier dynamics. We determined the mobility and half-lifetime of $CsPbBr_3$ in a temperature range between -140°C and 180°C. The phase transition from cubic to tetragonal (α/β) phase in $CsPbBr_3$ occurs at 130°C, while the tetragonal to orthorhombic (β/γ) transition occurs at 88°C.[36] As a consequence, $CsPbBr_3$ is in the orthorhombic phase at room temperature and remains in this phase at temperatures down to -260°C.[36] The mobility and half-lifetime of $CsPbBr_3$ are shown as a function of temperature in Figure 4.2. In this figure it can be seen that the charge carrier mobility does not exhibit abrupt changes on going through the α/β and β/γ phase transitions. In fact, the mobility behavior with temperature for $CsPbBr_3$ does not exhibit strong deviations from the acoustic phonon-electron scattering behavior of normal semiconductors ($\mu=T^{-1.5}$) in the temperature range tested. In addition, also the conductivity half-lifetime does not exhibit abrupt changes on going through the phase transitions. Nevertheless, it varies along the

temperature range, especially around room temperature. These results seem to indicate that the charge carrier dynamics in $CsPbBr_3$ are only influenced by the vibrations of the lattice, local inorganic $(PbX_6)^{4-}$ framework and extended $[PbX_3]^{1-}$ framework, as the temperature is varied. This is in agreement with the results shown above and in **Chapter 3**, from which we conclude that abrupt changes in the charge carrier dynamics are observed only when the organic cation rotation has a large dipole moment (as in MA).

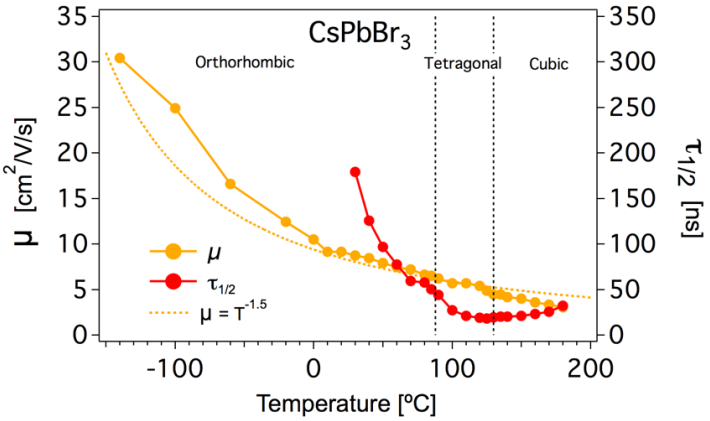

Figure 4.2. Charge carrier mobility and half-lifetime of $CsPbBr_3$ as a function of temperature.

4.2.2. Charge carrier recombination and trapping of $FAPbI_3$

Similar to the experiments described in section 3.2.2., we varied the initial concentration of charges (varying the length of the electron pulse) to obtain information about trapping, recombination processes, and carrier lifetimes from the temporal decay of the conductivity. In Figure 4.3. (a, b) we show the experimental conductivity as a function of time at 20°C and -130°C, varying the pulse length between 0.2 ns to 0.5 ns. This results in initial concentrations between $6x10^{14}$ cm^{-3} and $3x10^{15}$ cm^{-3}. This generation rate is lower than with a 1.5 AM solar simulator (10^{16} cm-3).[37] Nevertheless, it allows to study the dynamics at conditions that are not feasible with a laser-TRMC or THz experiments (10^{16}-10^{18} cm^{-3}). In Figure 4.3. (a, b) we observe that the conductivity at the end of the pulse increases with the initial concentration of carriers while the lifetime becomes shorter. This behavior is similar to that previously reported for $MAPbX_3$ (X= I, Br) in **Chapter 3**.[5] We then modeled the charge carrier dynamics of $FAPbI_3$ with the model described in section 2.4 assuming second order recombination with the presence of a limited concentration of trap states (for either the electron of the hole). This model allows to determine the trap concentration, the recombination rates of all processes and the mobilities of the charged species (see Table 4.1.).

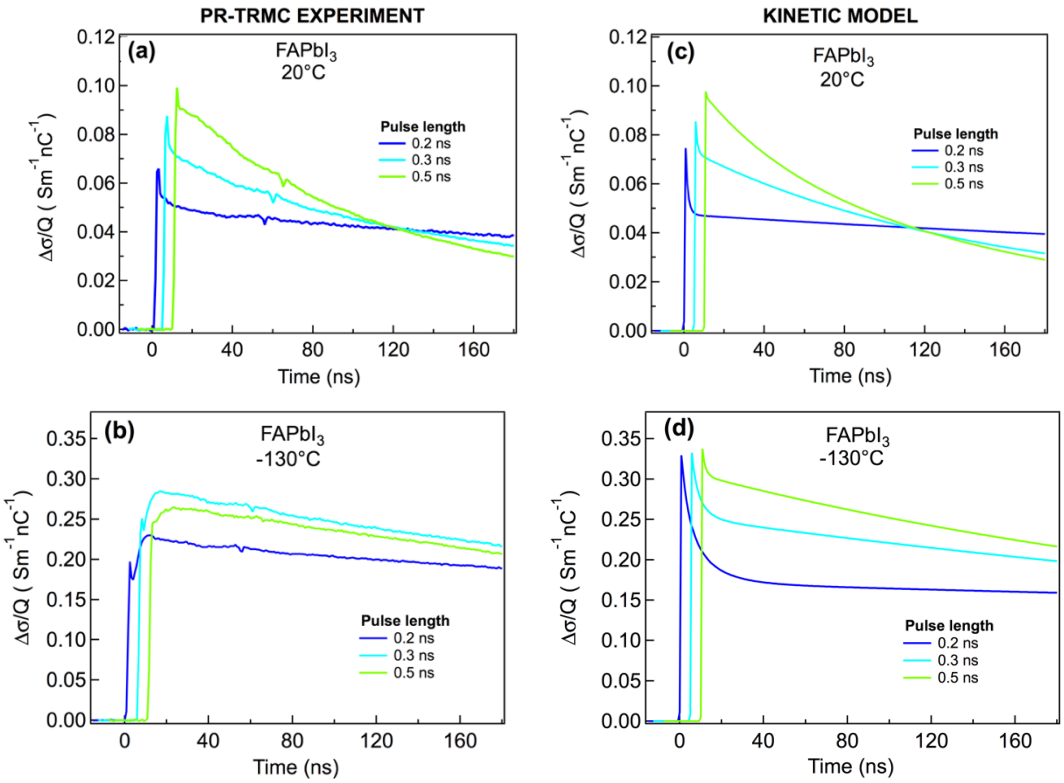

Figure 4.3. Charge Carrier decay dynamics of $FAPbI_3$ at 20°C and -130°C as a function of initial concentration of charge carriers (pulse length). a, b) Experimental data. **c, d)** kinetic model fit.

Table 4.1. Kinetic fitting parameters for $FAPbI_3$ at 20°C and -130°C.

$FAPbI_3$		
Description/Temperature	**20°C**	**-130°C**
Mobility: e- / h+ [$cm^2/V/s$]	2.7 / 1.8	7.0 / 6.5
Generation yield (k_1) [$1/cm^3/nC$]	1.65E+15	1.65E+15
Second order recombination rate (k_2) [cm^3/s]	3.50E-09	6.50E-10
Second order trap filling rate (k_3) [cm^3/s]	2.00E-06	3.00E-07
Second order trap emptying rate (k_4)	2.00E-09	8.00E-10
Trap state concentration N_t [$1/cm^3$]	9.00E+14	7.80E+14

In Figure 4.3. (c, d) it is shown that the kinetic model reproduces the main features of the conductivity as a function of temperature. In general, the results of the fits are similar as for $MAPbI_3$.[5] The mobility of the individual charges (electrons/holes) determined by our fits are similar with the electron mobility being slightly higher. This is in agreement with our DFT band structure calculations (Appendix Table A4.1.). In this analysis we assumed that the electrons become trapped,[12,38] however, the nature of the traps is not known. The concentration of traps determined, ~8 x 10^{14} cm^{-3}, is in agreement to previous work under similar conditions,[5] but is substantially larger than for single crystals (1.13 x 10^{10} cm^{-3}) as determined by SCLC.[21] This high concentration of traps shows that the second order trap-filling (k_3) process is dominant here. Taking the product of the trap concentration and the second order rate constants above results in quasi-first order trapping rates of 1.8 x 10^9 s^{-1} at 20°C and 2.3 x 108 s^{-1} -130°C. This rate increases with temperature pointing to charge

recombination with ionized impurities.[39] The rate for second-order recombination of free electrons and holes (k_2) decreases as the temperature decreases from 3.5 x 10^{-9} cm^3 s^{-1} at 20°C to 6.5 x 10^{-10} cm^3 s^{-1} at -130°C. If this process would be limited by (homogeneous) charge transport, an opposite trend would be expected here: faster recombination at higher charge mobility. This shows that recombination in these materials exhibits a complicated temperature dependence in which the local dielectric environment of the charges plays an important role. Because of the disorder in the mutual orientations of the slightly dipolar formamidinium cations a disordered energy landscape is present.[40] This disorder may result from both the electric field due to the orientation and position of the FA cation and from local distortions of the Pb-I lattice caused by the organic cation. At lower temperature, the thermal motion the orientation of the organic cation is reduced, resulting in a different, more static disorder, which may lead to the formation of separate domains for the positive and negative charges, leading to slower recombination. We have previously reported such behavior also for methylammonium-based lead perovskites,[5] however, in this case the effect was much stronger and a very abrupt change in both the charge mobility and the carrier lifetime was observed at the phase transition between tetragonal and orthorhombic phases. In the present case, due to the very small dipole moment of FA, the effect is smaller and much more gradual, however, the results do show that also in this case the orientational disorder of the organic cation plays a role in the recombination kinetics of the charges.

4.3. Conclusions

In this chapter we have shown that the interaction of the organic cation with the structure has a large influence on the charge carrier dynamics of perovskite materials. Depending on the rotational freedom and dipole moment of the organic cation, properties such as the mobility, lifetime and recombination rates will be affected. In $FAPbI_3$, the reduced rotational freedom of FA makes its lifetime longer than the lifetime of $MAPbI_3$. At the same time, these reduced rotational freedom and smaller dipole moment (dielectrical behavior) have a low temperature dependence compared to $MAPbI_3$. This result in charge dynamics in which the mobility follows band like-transport without presenting abrupt changes after the β/γ phase transition as in $MAPbI_3$. We confirm this behavior by introducing a cation without a dipole moment, Cs, in which a similar band-like transport behavior is observed **Chapter 3** and **Chapter 4** demonstrate that the charge carrier dynamics in 3D hybrid perovskites are affected by the intrinsic properties of the organic cation and its interaction within the structure.

4.4. Experimental Methods

Starting materials. All chemicals were purchased from Sigma-Aldrich and used as received. Formamidinium iodide (FAI) was synthesized by neutralizing equimolar amounts of 57wt% aqueous hydriodic acid (HI) and 99wt% formamidine acetate salt ($HN=CHNH_2 \cdot CH_3COOH$) at 0°C for 1 hour. The white precipitate was collected by evaporation of the solvent using rotary evaporation at 50 °C under reduced pressure. The precipitate was washed three times with diethyl ether by pump air filtration, recrystallized in ethanol and dried under vacuum for 24 hours before use.

Synthesis of $FAPbI_3$. The precursors $HC(NH_2)_2I$ and PbI_2 (99.999%) were mixed at a molar ratio of 1.5:1 and dissolved in Anhydrous DMF at varying dilution rates (40wt.%, 20wt.%, 10wt.%, 0.88M). This molar ratio was used in order to obtain pure perovskites phases. The solutions were ultrasonically stirred for 15-30 min to assure complete dissolution. The resulting precursor solution was placed in a vacuum oven at 10^{-2} mbar and heated in steps of 10°C every 20 min up to 130-140°C. After the maximum temperature was reached, the samples were left 30 minutes in the vacuum oven in order to assure the complete evaporation of the solvent and annealing of the perovskite crystals. Higher temperatures are undesirable as this induces thermal degradation. The 0.88M dilution assured the synthesis of the $FAPbI_3$ black phase. This polycrystalline phase it is stable in dry air but interconverts to the yellow phase in a couple of weeks. The black phase can be recovered heating the crystals to 140°C for 30 min.

Synthesis of $CsPbBr_3$. $CsPbBr_3$ is prepared by reacting equimolar amounts of PbBr2 and CsBr in concentrated aqueous hydrobromic acid [48% HBr(aq)]. Crystal growth of mm size ingots was achieved by the vertical Bridgman method using a three-zone furnace.[36]

Preparation of PR-TRMC sample holders. A small amount of $FAPbI_3$ (~40 mg) is placed in a Polyether ether ketone (PEEK) holder and covered by poly methyl methacrylate (PMMA) dissolved in chlorobenzene (10mg/ml). The PMMA layer protects the samples from the environment and diminish the background conductivity (which affects the PR-TRMC measurements).

PR-TRMC measurements. In the PR-TRMC set up, the sample holder is placed in a microwave cell. Subsequently, the microwave cell is placed in a cryostat where the temperature can be varied between -150°C and 200°C. The temperature is maintained for ~15min before every measurement to assure the equilibrium of the system. The irradiation intensity was varied between pulse lengths of 200 ps and 1 ns for each temperature at a frequency of 32 GHz. The frequency scan (28-38 GHz) fits were measured at a pulse length of 200 ps.

DFT calculations. All DFT calculations were performed with the BAND program included in the Amsterdam Density Functional suite. During the calculation the experimental geometry was used. The electronic structure calculations were performed using a triple-zeta basis set (TZP) and without using frozen cores. The PBEsol functional was used to account for exchange and correlation. Relativistic effects were included via a scalar correction of the ZORA. The effective masses were calculated using the internal capabilities of BAND.

4.5. References

1. Brenner, T. M., Egger, D. A., Kronik, L., Hodes, G. & Cahen, D. Hybrid organic - Inorganic perovskites: Low-cost semiconductors with intriguing charge-transport properties. *Nat. Rev. Mater.* **1**, 1–16 (2016).
2. Pedesseau, L. *et al.* Advances and Promises of Layered Halide Hybrid Perovskite Semiconductors. *ACS Nano* **10**, 9776–9786 (2016).
3. Frost, J. M., Butler, K. T. & Walsh, A. Molecular ferroelectric contributions to anomalous hysteresis in hybrid perovskite solar cells. *APL Mater.* **2**, (2014).
4. Frost, J. M. *et al.* Atomistic origins of high-performanc1. Frost, J. M. et al. Atomistic origins of high-performance in hybrid halide perovskite solar cells. Nano Lett. 14, 2584–90 (2014).e in hybrid halide perovskite solar cells. *Nano Lett.* **14**, 2584–90 (2014).
5. Gélvez-Rueda, M. C. *et al.* Effect of cation rotation on charge dynamics in hybrid lead halide perovskites. *J. Phys. Chem. C* **120**, 16577–16585 (2016).
6. Kamminga, M. E. *et al.* Confinement Effects in Low-Dimensional Lead Iodide Perovskite Hybrids. *Chem. Mater.* **28**, 4554–4562 (2016).
7. Motta, C. *et al.* Revealing the role of organic cations in hybrid halide perovskite CH<inf>3</inf> NH<inf>3</inf>PbI<inf>3</inf>. *Nat. Commun.* **6**, 1–7 (2015).
8. Hutter, E. M. *et al.* Direct-indirect character of the bandgap in methylammonium lead iodide perovskite. *Nat. Mater.* **16**, 115–120 (2017).
9. Zheng, F., Tan, L. Z., Liu, S. & Rappe, A. M. Rashba spin-orbit coupling enhanced carrier lifetime in CH 3 NH 3 PbI 3. *Nano Lett.* **15**, 7794–7800 (2015).
10. Stoumpos, C. C., Malliakas, C. D. & Kanatzidis, M. G. Semiconducting tin and lead iodide perovskites with organic cations: Phase transitions, high mobilities, and near-infrared photoluminescent properties. *Inorg. Chem.* **52**, 9019–9038 (2013).
11. Stoumpos, C. C. *et al.* Ruddlesden-Popper Hybrid Lead Iodide Perovskite 2D Homologous Semiconductors. *Chem. Mater.* **28**, 2852–2867 (2016).
12. Eperon, G. E. *et al.* Formamidinium lead trihalide: A broadly tunable perovskite for efficient planar heterojunction solar cells. *Energy Environ. Sci.* **7**, 982–988 (2014).
13. Koh, T. M. *et al.* Formamidinium-containing metal-halide: An alternative material for near-IR absorption perovskite solar cells. *J. Phys. Chem. C* **118**, 16458–16462 (2014).
14. Lee, J. W., Seol, D. J., Cho, A. N. & Park, N. G. High-efficiency perovskite solar cells based on the black polymorph of HC(NH2)2PbI3. *Adv. Mater.* **26**, 4991–4998 (2014).
15. Pellet, N. *et al.* Mixed-organic-cation perovskite photovoltaics for enhanced solar-light harvesting. *Angew. Chemie - Int. Ed.* **53**, 3151–3157 (2014).
16. Hanusch, F. C. *et al.* Efficient planar heterojunction perovskite solar cells based on formamidinium lead bromide. *J. Phys. Chem. Lett.* **5**, 2791–2795 (2014).
17. Pang, S. *et al.* NH 2 CH═NH 2 PbI 3 : An Alternative Organolead Iodide Perovskite Sensitizer for Mesoscopic Solar Cells - supporting information. *Chem. Mater.* **26**, 1485–1491 (2014).
18. Binek, A., Hanusch, F. C., Docampo, P. & Bein, T. Stabilization of the trigonal high-temperature phase of formamidinium lead iodide. *J. Phys. Chem. Lett.* **6**, 1249–1253 (2015).
19. Han, Q. *et al.* Single Crystal Formamidinium Lead Iodide (FAPbI3): Insight into the Structural, Optical, and Electrical Properties. *Adv. Mater.* **28**, 2253–2258 (2016).
20. Fang, H. H. *et al.* Photoexcitation dynamics in solution-processed formamidinium lead iodide perovskite thin films for solar cell applications. *Light Sci. Appl.* **5**, e16056-7 (2016).
21. Zhumekenov, A. A. *et al.* Formamidinium Lead Halide Perovskite Crystals with Unprecedented Long

Carrier Dynamics and Diffusion Length. *ACS Energy Lett.* **1**, 32–37 (2016).
22. Wright, A. D. *et al.* Electron-phonon coupling in hybrid lead halide perovskites. *Nat. Commun.* **7**, (2016).
23. Bakulin, A. A. *et al.* Real-Time Observation of Organic Cation Reorientation in Methylammonium Lead Iodide Perovskites. *J. Phys. Chem. Lett.* **6**, 3663–3669 (2015).
24. Weller, M. T., Weber, O. J., Frost, J. M. & Walsh, A. Cubic Perovskite Structure of Black Formamidinium Lead Iodide, α-[HC(NH<inf>2</inf>)<inf>2</inf>]PbI<inf>3</inf>, at 298 K. *J. Phys. Chem. Lett.* **6**, 3209–3212 (2015).
25. Onoda-Yamamuro, N., Matsuo, T. & Suga, H. Dielectric study of CH3NH3PbX3 (X = Cl, Br, I). *J. Phys. Chem. Solids* **53**, 935–939 (1992).
26. Fabini, D. H. *et al.* Dielectric and Thermodynamic Signatures of Low-Temperature Glassy Dynamics in the Hybrid Perovskites CH3NH3PbI3 and HC(NH2)2PbI3. *J. Phys. Chem. Lett.* **7**, 376–381 (2016).
27. Fabini, D. H. *et al.* Reentrant Structural and Optical Properties and Large Positive Thermal Expansion in Perovskite Formamidinium Lead Iodide. *Angew. Chemie - Int. Ed.* **55**, 15392–15396 (2016).
28. Herz, L. M. Charge-Carrier Mobilities in Metal Halide Perovskites: Fundamental Mechanisms and Limits. *ACS Energy Lett.* **2**, 1539–1548 (2017).
29. Neamen, D. A. *Semiconductor Physics and Devices: Basic Principles*. (McGraw-Hill, 2012).
30. Einstein, A. Über die von der molekularkinetischen Theorie der Wärme geforderte Bewegung von in ruhenden Flüssigkeiten suspendierten Teilchen. *Ann. Phys.* **322**, 549–560 (1905).
31. von Smoluchowski, M. Zur kinetischen Theorie der Brownschen Molekularbewegung und der Suspensionen. *Ann. Phys.* **326**, 756–780 (1906).
32. Li, B. *et al.* Polar rotor scattering as atomic-level origin of low mobility and thermal conductivity of perovskite CH 3 NH 3 PbI 3. *Nat. Commun.* **8**, 1–9 (2017).
33. Swainson, I. P. *et al.* From soft harmonic phonons to fast relaxational dynamics in CH3NH3PbBr3. *Phys. Rev. B - Condens. Matter Mater. Phys.* **92**, 2–6 (2015).
34. Knop, O., Wasylishen, R. E., White, M. A., Cameron, T. S. & Oort, M. J. M. Van. Alkylammonium lead halides. Part 2. CH 3 NH 3 PbX 3 (X = Cl, Br, I) perovskites: cuboctahedral halide cages with isotropic cation reorientation. *Can. J. Chem.* **68**, 412–422 (1990).
35. Eperon, G. E. *et al.* Inorganic caesium lead iodide perovskite solar cells. *J. Mater. Chem. A* **3**, 19688–19695 (2015).
36. Stoumpos, C. C. *et al.* Crystal growth of the perovskite semiconductor CsPbBr3: A new material for high-energy radiation detection. *Cryst. Growth Des.* **13**, 2722–2727 (2013).
37. Jiang, C. S. *et al.* Carrier separation and transport in perovskite solar cells studied by nanometre-scale profiling of electrical potential. *Nat. Commun.* **6**, 1–10 (2015).
38. Hutter, E. M., Eperon, G. E., Stranks, S. D. & Savenije, T. J. Charge Carriers in Planar and Meso-Structured Organic-Inorganic Perovskites: Mobilities, Lifetimes, and Concentrations of Trap States. *J. Phys. Chem. Lett.* **6**, 3082–3090 (2015).
39. Milot, R. L., Eperon, G. E., Snaith, H. J., Johnston, M. B. & Herz, L. M. Temperature-Dependent Charge-Carrier Dynamics in CH3NH3PbI3 Perovskite Thin Films. *Adv. Funct. Mater.* **25**, 6218–6227 (2015).
40. Hilczer, M. & Tachiya, M. Unified theory of geminate and bulk electron-hole recombination in organic solar cells. *J. Phys. Chem. C* **114**, 6808–6813 (2010).

Chapter 5
Replacement of the Divalent Lead ion: Tin-Based and Double Perovskites

In this chapter the opto-electronic properties of organic-inorganic perovskites with non-toxic divalent metals (replacement of lead by tin (Sn) or two cations M^+M^{3+}) are discussed. This modification is of high interest for commercial applications of perovskite materials. Replacement of lead by tin leads to three-dimensional (3D) perovskites with a low stability because Sn^{2+} is extremely prone to oxidation to Sn^{4+}. We found that introduction of SnF_2 reduces the amount of oxidation improving the electronic properties of 3D Sn(II)-based perovskites. Another option is to replace lead by two cations (Ag^+Bi^{3+}), changing the structure into a so-called double perovskite. These materials are very stable and exhibit slow trap-assisted recombination but also have large band gaps unsuitable for application in a single-junction solar cell. We found that through doping with antimony (Sb^{3+}), the band gap can be tuned to optimum values for solar cells while maintaining the favorable electronic properties of undoped 3D lead-based perovskites (band-like transport).

This chapter is based on:

Davide Bartesaghi, Adam H. Slavney, María C. Gélvez-Rueda, Bridget A. Connor, Ferdinand C. Grozema, Hemamala I. Karunadasa and Tom J. Savenije. Charge Carrier Dynamics in $Cs_2AgBiBr_6$ Double Perovskite. J. Phys. Chem. C 2018, 122, 4809−4816.

Eline M. Hutter, María C. Gélvez-Rueda, Davide Bartesaghi, Ferdinand C. Grozema and Tom J. Savenije. Band-Like Charge Transport in $Cs_2AgBi_{1-x}Sb_xBr_6$ Halide Double Perovskites. ACS Omega 2018, 3, 11655−11662.

Yousra El Ajjouri, Federico Locardi, María C. Gélvez-Rueda, Mirko Prato, Michele Sessolo, Maurizio Ferretti, Ferdinand C. Grozema, Francisco Palazon and Henk J. Bolink. Mechanochemical Synthesis of Sn(II) and Sn(IV) Iodide Perovskites and Study of Their Structural, Chemical, Thermal, Optical, and Electrical Properties. Energy Technol. 2019, 1900788.

5.1. Introduction

Three-dimensional (3D) organic-inorganic lead halide perovskites are rapidly developing alternative materials for solar cell applications due to the high power conversion efficiency that has been reached(>25%).[1] However, the presence of lead (Pb) in the chemical structure raises toxicity concerns for large scale commercial application.[2,3] The most straightforward alternative is to replace lead with less-toxic divalent tin (Sn^{2+}) as they share a similar electronic configuration (group 14) and ionic radiuses.[2,3] Although Sn-based 3D perovskites have been shown to have a higher charge carrier mobility than Pb-based materials,[4,5] their lower ambient stability and Sn oxidation from Sn^{2+} to Sn^{4+} lead to relatively low solar-to-power efficiency of ~6-8%.[2,3] Another alternative is to replace lead by a combination of a monovalent and a trivalent metal cation such as silver (Ag^{+}) and bismuth (Bi^{3+}). This results in a modified halide double perovskite (HDP) structure ($Cs_2AgBiBr_6$) with very high stability but an indirect large band gap (2.07 ev) that is unsuitable for application in single-junction solar cells.[6] Nonetheless, this HDP exhibits a photoluminescent (PL) lifetime comparable to 3D perovskites but a low PL intensity consistent with its indirect band gap nature.[6] Although these materials have some promising electronic properties further research is necessary to clarify their charge carrier dynamics.

In this chapter we studied the charge carrier dynamics by time-resolved microwave conductivity (TRMC) techniques of Sn-based perovskites and AgBi-based double perovskites. These materials were synthesized in dry conditions by mechanochemical thermal synthesis in order to maintain precise stoichiometry and solvent-free conditions.[6–8] In the case of Sn-based perovskites, we synthesized pure Sn and mixed Sn-Pb iodide perovskites in 3D Sn(II) form ($ASnI_3$ and $ASn_xPb_{1-x}I_3$) and pure 0D Sn (IV) vacancy ordered perovskites (A_2SnI_6) with varied cations (A = Cesium (Cs) and Formamidinium (FA)) and accounting for the influence of SnF_2 as additive to reduce Sn-oxidation.[9–11] Apart from determining the elemental, chemical, and structural characteristics of the as-prepared compounds, we investigated the charge carrier mobility and lifetime of 3D Sn(II)-based perovskite and 0D Sn(IV)-based structure revealing that the effective mobility is two orders of magnitude larger for 3D Sn(II)-based perovskites as compared with 0D Sn(IV)-based structures. In addition, these measurements show that the electronic properties of fully inorganic Sn(II)-based perovskites are improved during synthesis by Pb-mixing and addition of SnF_2 by reducing the oxidation to Sn^{4+}.

For the case of halide double perovskites, we investigated the charge carrier dynamics of $Cs_2AgBiBr_6$, showing that while large concentrations of (10^{16} cm^{-3}) trap states are present they are energetically shallow. As a result, trap-assisted recombination in the bulk is slow. However, in thin films, surface states recombination is fast. This shows that surface

passivation is required in these materials to increase their potential for application in solar cell devices. Finally, we also explored the doping of these $Cs_2AgBiBr_6$ parent HDP structure with antimony (Sb) in order to reduce their bandgap to values more suitable for single-junction solar cells. We synthesized $Cs_2AgBi_{1-x}Sb_xBr_6$, which show a red shift in the absorption spectrum with increasing x, reaching ~1.6 eV upon replacing 40% of the Bi^{3+} with Sb^{3+} (i.e. x = 0.4). Interestingly, we find that the charge carrier mobility decreases only marginally on increasing x and, independent of the antimony content, the charge mobility follows band-like transport of charge carriers. This charge-transport mechanism is very similar to 3D lead-based perovskites discussed in **Chapter 3** and **Chapter 4**,[12,13] highlighting the potential of HDP as non-toxic alternatives.

5.2. Results and Discussion

5.2.1. Electronic properties of Sn-based perovskites

3D Sn(II)-based ($CsSnI_3$, $Cs(SnPb)I_3$, $FASnI_3$, $FA(SnPb)I_3$) and Sn(IV)-based compounds (Cs_2SnI_6, FA_2SnI_6) were synthesized by dry ball-milling of stoichiometric mixtures of the different precursors (see section 5.4 for details). The high phase purity and match with reference XRD patterns highlight the potential of mechanochemical synthesis to obtain high-quality materials (XRD in Appendix Figure A5.1). It was revealed by thermal analysis that addition of SnF_2 is crucial in the synthesis of $CsSnI_3$ and $Cs(SnPb)I_3$ (but not in the synthesis of $FASnI_3$ and $FA(SnPb)I_3$) to avoid the formation of SnI_4 (Appendix Figure A5.2). The purity and stoichiometry of the samples was further confirmed by XPS measurements (Appendix Figure A5.3). In addition, the optical characterization and ultra-violet photoelectron spectroscopy (UPS) results are shown in Appendix Figure A5.4. It is worth highlighting that all compounds have an absorption onset in the near-infrared (NIR) region, suitable for single-junction solar cells as well as for use as the rear-absorber in perovskite–perovskite tandem devices. Regarding the UPS measurements, we observe an apparent p-type doping in $FASnI_3$ which may be ascribed to a partial oxidation of Sn(II) to Sn(IV).[14] In contrast, mixed $FA(SnPb)I_3$ seems to be rather n-type. The origin of this effect is not fully elucidated. However, we noted in the XPS data (Appendix Figure A5.3) that tin appeared to be slightly reduced, which might explain the n-type character observed here. These effects do not seem to be significant for inorganic Cs-based $CsSnI_3$ and $Cs(SnPb)I_3$, as both appear rather intrinsic semiconductors. It must be noted though that these perovskites were formed with addition of SnF_2. We therefore infer that SnF_2 helps maintaining the intrinsic nature of the semiconductor by preventing oxidation of tin. In the case of Sn(IV) compounds, Cs_2SnI_6 and FA_2SnI_6 seem to be heavily n-doped, which agrees with literature reports.[15]

We have performed pulse-radiolysis TRMC (PR-TRMC) on all Sn-based compounds discussed above to study the mobility and lifetime of charge carriers. In most of the compounds, it was not possible to obtain meaningful results because of high or even complete absorption of the microwaves without irradiation. This is indicative of a considerable dark conductivity that hinders the detection of changes in conductivity upon irradiation. This behavior matches with the UPS results discussed above (Appendix Figure A5.4), where we observe that most samples are doped either with a p-type character, most likely caused by oxidation of Sn^{2+} to Sn^{4+}, or a n-type character. It has been shown in the literature that the presence of low concentrations of dark charge carriers has a detrimental effect on the electronic properties.[9,16–18] In fact, we are able to observe change of reflection (not quantifiable) that is very short-lived (<5 ns), which indicates that the generated charge carriers recombine or are trapped within the time resolution of the PR-TRMC experiment (Appendix Figure A5.5a). Nevertheless, we were able to obtain meaningful results on two compounds: 3D Sn(II)-based $CsSnPbI_3$ and 0D Sn(IV)-based FA_2SnI_6, which, here after, are simply referred to as 3D and 0D samples (Figure 5.1a). The fact that we can measure these samples matches with the intrinsic semiconductor character of $CsSnPbI_3$ seen in UPS measurements. As mentioned, this intrinsic character is most likely achieved during synthesis. Decreasing tin content with lead and adding SnF_2 suppresses Sn^{2+} oxidation to Sn^{4+} and as a result decreases the concentration of dark charge carriers. This is also in line with reported improved stabilities of tin-based perovskites when lead cations are present.[19]

As can be seen in Figure 5.1a, the mobility of charges in the 3D sample is two orders of magnitude higher than in the 0D sample (0.2 and 0.004 $cm^2\ V^{-1}s^{-1}$, respectively). This is not surprising if we consider that the higher dimensionality of the 3D sample leads to a higher overlap of molecular orbitals. In both cases, the mobility was not found to significantly change when cooling from room temperature to 173 K. This indicates that the charge carrier mobility is not dominated by lattice scattering, but may be controlled by defects. The mobility of the 3D sample is of the same order of magnitude as for 3D lead-based perovskite samples prepared without the use of solvents,[12] whereas it is one to two orders of magnitude lower than 3D lead-based perovskites prepared by precipitation or single crystals, respectively.[12,13] This points out that dry mechanochemical synthesis as performed here might lead to a higher density of defects as opposed to solution-processing. Nonetheless, we believe that the synthesis may be optimized, for example by reducing the grinding time, which in this case was 5 h. Such a long time is probably unnecessary to yield phase-pure perovskites, and reducing it will likely limit detrimental effects of prolonged grinding (i.e., tin oxidation).

The time-resolved conductivity (Figure 5.1b) of the 3D sample shows a fast-initial decay followed by a long-tail that does not decay to zero, even at very long times. Also, the maximum change in conductivity increases with the initial concentration of charge carriers

(increase pulse length; Appendix Figure A5.5b). This behavior is similar to the observed for 3D $MAPbX_3$ samples[12] in **Chapter 3** and is attributed to second-order recombination with a limited concentration of trap states.[12] The fast-initial decay is caused by trapping of one of the charges, and the long tail signal comes from the remaining free charges.[12,13] As for the mobility, the carrier lifetime seems almost unaffected by temperature (Appendix Figure A5.6), indicating that the decay is still dominated by the recombination with a similar concentrations of trap states as at room temperature. In the case of the 0D sample, the conductivity signal is very low and decays in less than 50 ns (Figure 5.1b). A slight conductivity increase is observed at low temperatures, which may be related to reduced thermal vibration of the lattice (Appendix Figure A5.6). Still, we demonstrated that the dark carrier conductivity in inorganic 3D Sn(II)-based compounds can be improved by the addition of Pb and/or SnF_2 during synthesis.

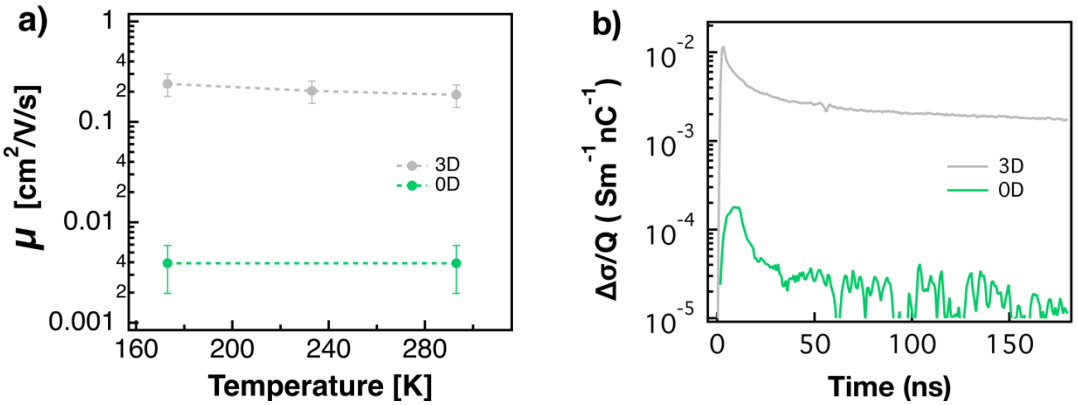

Figure 5.1. PR-TRMC experiments on Sn(II) 3D perovskite (grey) and a Sn(IV) 0D vacancy-ordered perovskite (green). a) Mobility of charge carriers as a function of temperature. **b)** change of conductivity as a function of time.

5.2.2. Electronic properties of halide double perovskites: $Cs_2AgBiBr_6$ and $Cs_2AgBi_{1-x}Sb_xBr_6$

In the experiments described in the first part of this section, crystals of $Cs_2AgBiBr_6$ were precipitated from a concentrated HBr solution containing stoichiometric CsBr, AgBr, and $BiBr_3$.[6] Transmittance experiments show that the absorption properties are independent of temperature, suggesting the absence of an excitonic contribution at low temperature (Appendix Figure A5.7).[6,20,21] Photoconductivity TRMC measurements on the single crystals for photoexcitation at 500 nm (above band gap) and 580 nm (close to band gap) are shown in Appendix Figure A5.8. The photoconductivity TRMC signals reveal a rapid initial decay when the penetration depth is low (500 nm). A slowly decaying long-lived tail is observed when the penetration depth is large enough so that charges are mainly generated further from the surface in the bulk of the material (580 nm). This suggests that fast surface recombination has a significant effect on the charge carrier dynamics. The photoinduced conductivity on

photoexcitation at 500 nm is almost independent of temperature, whereas photoexcitation at 580 nm results in decreasing photoconductivity on decreasing the temperature. In addition, the long-lived tail in the conductivity transients is suppressed (Appendix Figure A5.8). To explain the suppression of the long-lived tail, we have studied the rapid recombination or immobilization of charges at low temperatures by varying the photon fluence in the TRMC experiments (Figure 5.2a,b,c). Additionally, we have also determined the temperature dependence of the charge mobility by pulse radiolysis (PR) TRMC (Figure 5.2d,e). As discussed in **chapter 2,** these measurements differ by the fact that photoconductivity TRMC gives the product of charge mobility ($\Sigma\mu$) and yield of charge dissociation (ϕ) while from PR-TRMC measurements we directly obtain the mobility of free charge carriers.

As discussed above, no excitonic features have been observed in $Cs_2AgBiBr_6$ (Appendix Figure A5.7). This leads to the conclusion that the yield (ϕ) of charge separation is independent of temperature. Therefore, we primarily focus here on the temperature dependence of the mobility of charge carriers. The radiation induced conductivity traces for $Cs_2AgBiBr_6$ obtained from PR-TRMC are shown in Figure 5.2d for temperatures ranging from 198 to 348 K. The decays are very similar to those measured upon laser excitation at 580 nm. The maximum change in radiation-induced conductivity is plotted versus temperature in Figure 5.2e. A clear increase in the maximum conductivity, and hence in $\Sigma\mu$, is observed with decreasing temperatures. Analogous to lead-based perovskites,[12,13,22] this dependence can be attributed to a reduction in phonon scattering at low temperatures, which is typical for the band-like transport. As the charge mobility ($\Sigma\mu$) increases upon cooling, the suppression of the lifetime tail cannot be explained by a decrease of the charge mobilities. Therefore, we attribute the disappearance of the long-lived component in the conductivity to additional fast nanosecond recombination or trapping of charges at lower temperatures. The similarity of the PR-TRMC and TRMC at various temperatures is in line with this explanation.

To clarify this fast recombination we show the excitation intensity-normalized TRMC traces for $Cs_2AgBiBr_6$ at 198, 298 and 348 K upon optical excitation at 580 nm in Figure 5.2a,b,c. At 348 K, increasing intensity (I_0) results in a faster decay of the TRMC signals. At 198 K, the intensity dependence is opposite: a long-lived tail is observable only at high I_0. The transition between these two regimes is gradual; at intermediate temperatures, the TRMC signals show almost no dependence on I_0 (Figure 5.2b). Based on these results, we propose the kinetic model shown in Figure 5.2e for carrier recombination in $Cs_2AgBiBr_6$. The intensity dependence at high temperature (signal size decreasing with higher laser fluences) is typical of higher-order recombination processes, for example, bimolecular or Auger recombination.[23] In contrast, the opposite intensity dependence observed at low temperature is a signature of charge trapping: at low fluence, all the photogenerated charges are captured by trap states, while saturation of traps at higher fluence leaves some mobile charge carriers in the

conduction and valence bands (charge density of ca. 10^{16} cm^{-3}). Thus, the suppression of the long-lived tail upon cooling is assigned to the immobilization of charges in shallow trap states with a upper limit for the density in the order of 10^{16} cm^{-3}, which is 3 orders of magnitude higher than the value proposed for lead-based perovskite single crystals.[24] It is important to realize that both the positive and negative charge carriers are trapped due to the complete suppression of the tail and the similar effective masses reported for electrons and holes in $CsAgBiBr_6$.[20,25] The temperature-assisted release of trapped charges back to the band does not require high activation energies; already at 348 K ($k_BT \approx 30$ meV) the intensity-dependent TRMC traces show second-order kinetics. This is an indication of shallow trapping, with trap states lying only a few tens of milli-electron volts away from the band edges. The nature of such trap states remains unknown; calculations have suggested that point defects such as silver vacancies and silver-on-bismuth anti-sites have low formation enthalpies and may act as electron or hole traps because of their energy levels in the bandgap.[15] Although these traps are present in large amounts, they are energetically shallow. Trap-assisted recombination of charges in the bulk appears to be slow as evidenced by the observation of mobile charges several microseconds after excitation (Appendix Figure A5.9). These results are promising for application in photovoltaics.

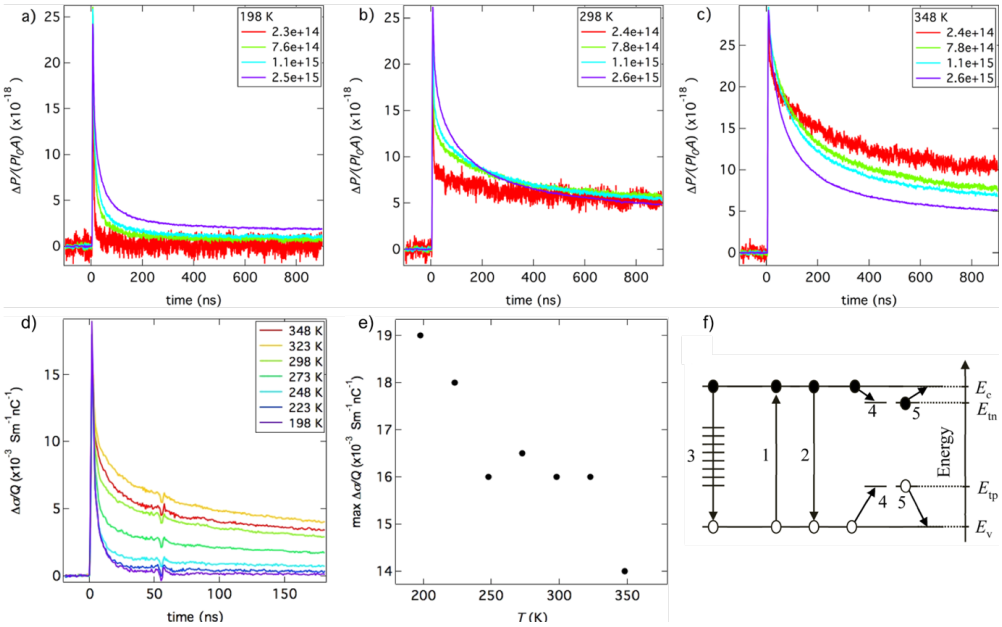

Figure 5.2. TRMC experiments on $Cs_2AgBiBr_6$ single crystals. a, b, c) TRMC traces recorded at different photon fluences for upon pulsed laser excitation (λ = 580 nm) at (a) 198 K, (b) 298 K, and (c) 348 K. The values of the photon fluence in the legends are expressed in photons/cm^2. **d)** PR-TRMC traces at different temperatures for $Cs_2AgBiBr_6$ crystals. The duration of the electron pulse was 1 ns. **e)** maxima in the PR-TRMC traces plotted against the temperature. **f)** Schematic representation of the band structure of $Cs_2AgBiBr_6$. Upon absorption of laser pulse, free electrons and holes are generated (1) in the conduction (Ec) and valence band (Ev), respectively. Subsequently, charges can recombine via band-to-band recombination (2) or via surface states (3). In the bulk of the material, shallow electron traps (at the energy level E_{tn}) and hole traps (at the energy level E_{tp}) are present. Free charges can be captured by these trap states (4), whereas trapped charges can be thermally released to the band edges (5).

In the previous section we demonstrated that HDPs exhibit some favorable properties for application in solar cells such as slow trap-assisted recombination and band-like transport. However, a major drawback of HDPs is their poor visible light absorption (indirect band gap ~2 eV).[6,20] It has been shown that a possible route to overcome this is the introduction of antimony defects.[26] Doping of $Cs_2AgBiBr_6$ with antimony (Sb) can decrease its band gap to values more suitable for single-junction photovoltaic application (down to ~1.86 eV).[26] In this section we synthesized mixed antimony-bismuth $Cs_2AgBi_{1-x}Sb_xBr_6$ HDPs, where the expected fraction of Bi that is replaced by Sb, x, ranges from ~0 to 0.4. These compounds were prepared by ground-mixing and heating of the stoichiometric precursors: CsBr, AgBr, $BiBr_3$, and $SbBr_3$.[26] The content of Sb in each sample was estimated using X-ray photoelectron spectroscopy (XPS), in which despite some slight variation from the x expected, the Sb content increases with $SbBr_3$ addition(Appendix Table A5.1). The absorption spectra, measured using an integrating sphere, of $Cs_2AgBi_{1-x}Sb_xBr_6$ powders with x = 0, 0.05, 0.1, and 0.4, attached to quartz substrates using optically clear adhesive is shown in Appendix Figure A5.10a. Consistent with the previous reports,[26,27] these spectra show that increasing the Sb content gradually reduces the band gap, resulting in absorption onset values close to 1.6 eV for x = 0.4. Furthermore, all of the samples show X-ray reflections characteristic of the double perovskite structure (Appendix Figure A5.10b,c,d), which monotonically shifts to larger angles on increasing x, supporting the replacement of Bi^{3+} with the smaller Sb^{3+}.

To investigate the suitability of $Cs_2AgBiBr_6$ and mixed antimony−bismuth HDPs for photovoltaic applications, we studied the transport of free charges in powders of these materials using PR-TRMC (Appendix Figure A5.11). As mentioned in **Chapter 2**, the total density of free charges (n_0) created by the electron pulse can be varied by changing the electron pulse length. Similar to the photoconductivity TRMC,[28] the end-of-pulse charge density (*n)* can still be affected by fast trapping or recombination of mobile charges within the instrumental response time of 1 ns. Therefore, we choose a pulse length at which losses are minimized so that n/n_0 is closest to unity. In Figure 5.3a is shown the sum of electron and hole mobility (Σμ) for $Cs_2AgBi_{1-x}Sb_xBr_6$ with x = 0, 0.05, 0.1, and 0.4 at temperatures ranging from 140 K to 420 K. From here, we find that at room temperature, Σμ is at least 0.3 $cm^2/(V\ s)$ for $Cs_2AgBiBr_6$ (x =0) powders. This value is only four times lower than the mobility of $CsPbBr_3$ crystals shown in **Chapter 4** using the same technique.[12]

The lower mobility of $Cs_2AgBiBr_6$ is consistent with its larger effective masses of electrons and holes (compared to lead-based $CsPbBr_3$).[25,29] In addition, the scattering times may be shorter because of enhanced scattering with phonons or defects. On partially replacing the Bi^{3+} with Sb^{3+}, slightly reduced mobilities are observed, although at each temperature, the absolute values stay within the same order of magnitude. Furthermore, independent of x, the mobility increases with decreasing temperatures in between 420 K and 140 K. On further analysis of

the data, we find that Σμ scales with $T^{-1.15}$ for x = 0, $T^{-1.62}$ (x = 0.05), $T^{-1.19}$ (x = 0.1), and $T^{-1.34}$ (x = 0.4). These negative powers indicate that phonon scattering (i.e., $\mu \propto T^{-1.5}$) is the dominant scattering mechanism determining the charge carrier mobility in these HDPs. In fact, these mobility dependences with temperature are within the same range as the state-of-the-art lead-based perovskites, for which Σμ scales with ($T^{-1.2 \text{ to } -1.6}$).[12,13,22,30] Additionally, these negative powers are very similar independently of the Sb^{3+} content in the $Cs_2AgBiBr_6$ lattice, this means that there is band-like transport of charges with no indication of substantial defect scattering.

As mentioned above, charge carrier losses within the instrumental response time lead to a reduction of n/n_0. Therefore, to get insight into sub-nanosecond recombination processes, we can plot $(n/n_0)\Sigma\mu$ as a function of n_0 (cm^{-3}). This is shown in Figure 5.3b for $Cs_2AgBiBr_6$ (upper panel) and $Cs_2AgBi_{0.9}Sb_{0.1}Br_6$ (lower panel) for temperatures ranging from 140 K to 420 K. At each temperature, $(n/n_0)\Sigma\mu$ initially rises on increasing the charge carrier densities. This behavior was observed in lead-based perovskites and described in section 3.2.2., where we attributed this to sub-nanosecond charge carrier trapping, leading to low yields if the trap density is higher than the charge carrier density.[12,31] Gradual saturation of these traps then results in increased n values for higher n_0, and thus an enhancement of n/n_0. On further increasing n_0, n/n_0 decreases again, which is typically observed if higher order recombination starts to dominate.[12,23] Therefore, the charge carrier concentration at which $(n/n_0)\Sigma\mu$ reaches maximum values represents the regime in which band-to-band recombination is in competition with trap-assisted recombination and can thus be used as an indication of the trap saturation density (cm^{-3}).

Figure 5.3c displays the densities at which the traps are saturated as a function of temperature for $Cs_2AgBi_{1-x}Sb_xBr_6$ antimony doped samples (x > 0) and for $Cs_2AgBiBr_6$ (x = 0). For $Cs_2AgBiBr_6$, there is a clear increase of density of traps from 3×10^{15} cm^{-3} at 140 K to more than 3×10^{16} cm^{-3} at T > 340 K. The room-temperature value of 1.2×10^{16} cm^{-3} is close to the previously suggested upper limit of 10^{16} cm^{-3} for a $Cs_2AgBiBr_6$ single crystal.[32] Interestingly, the temperature dependence of $(n/n_0)_{max}$ suggests that the trap density is enhanced with increasing temperatures, which could be because the origin of the traps is related to vacancies or interstitials, resulting from thermal displacement of ions. Alternatively, it might be that trap states originate from thermal ionization of defects, which also results in an increased number of available traps at higher temperatures. For the Sb containing HDPs, the trap saturation densities at 140 K are 2×10^{15} cm^{-3} to 4×10^{15} cm^{-3} and thus close to the antimony-free $Cs_2AgBiBr_6$. Also here, an enhancement is observed as the temperature rises, with (n/n_0) reaching a maximum just below 10^{16} cm^{-3} at 380 K for $Cs_2AgBi_{0.9}Sb_{0.1}Br_6$ (see bottom panel in Figure 5.3b) and the other mixed antimony−bismuth HDP powders (Appendix Figure A5.12). Most importantly, at and above room temperature, the trap-saturation

densities for x > 0 are about a factor three lower than that for x = 0, see Figure 5.3c. If indeed the trap states in $Cs_2AgBiBr_6$ are related to thermal ionic motion or defect ionization, these results suggest that this can be partially suppressed by Sb^{3+} substitution.

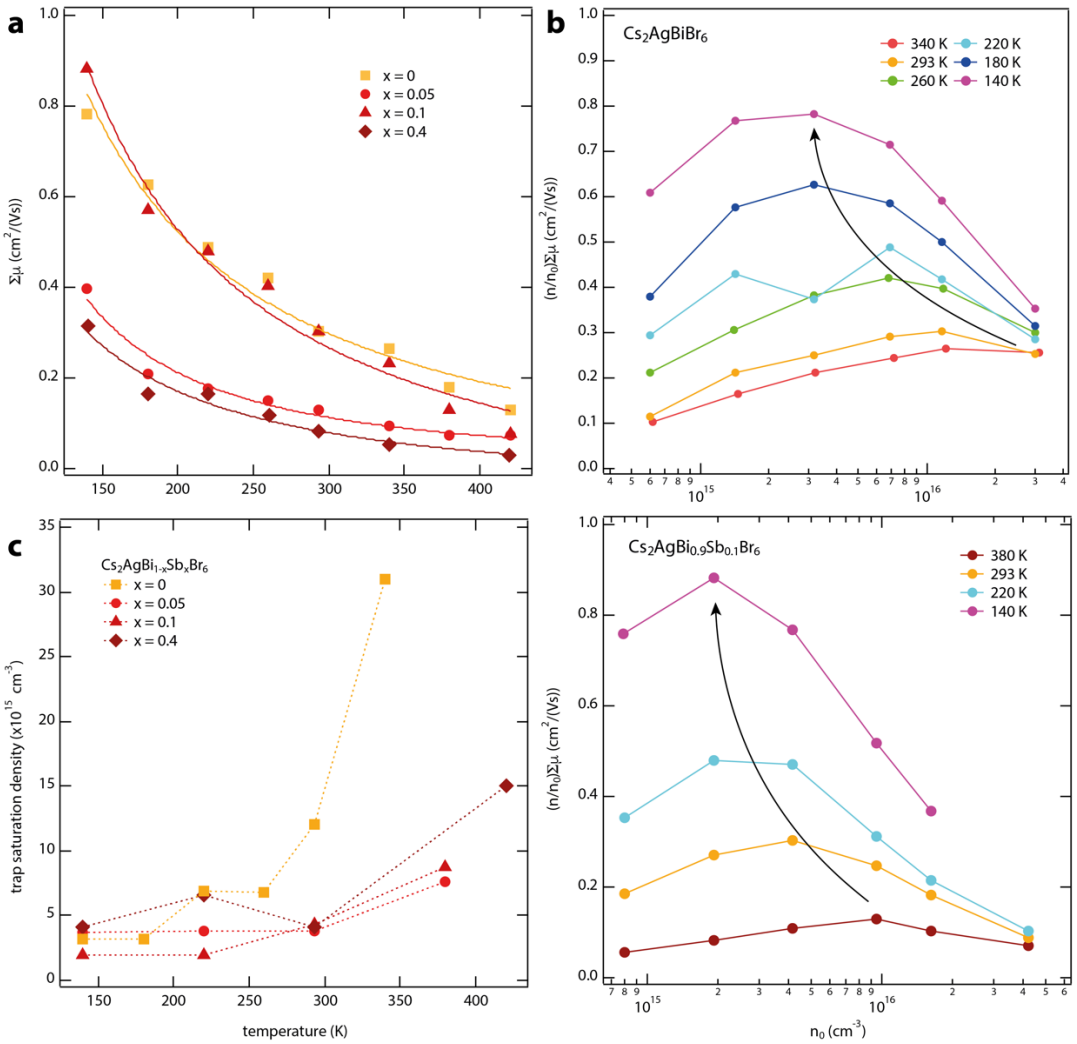

Figure 5.3. PR-TRMC experiments on $Cs_2AgBi_{1-x}Sb_xBr_6$ powders. a) Dots: mobility of charge carriers (Σμ) as function of temperature for x = 0 (squares), x = 0.05 (spheres), x = 0.1 (triangles), and x = 0.4 (diamonds). On fitting these mobilities to $\mu(T) \propto T^{-p}$, added as solid lines, we obtained p-values of 1.15 (x = 0), 1.62 (x = 0.05), 1.19 (x = 0.1), and 1.34 (x = 0.4). **b)** $(n/n_0)\Sigma\mu$ as function of n_0 and temperature for x = 0 (top) and x = 0.1 (bottom). **c)** Trap saturation density as a function of temperature for x = 0 (squares), x = 0.05 (spheres), x = 0.1 (triangles), and x = 0.4 (diamonds), obtained from the maximum n/n_0.

5.3. Conclusions

To summarize, we have investigated the optoelectronic properties of possible divalent metal substitutions that are less toxic than lead: Sn-based 3D perovskites and halide double perovskites (HDP). In general, it is clear that these substitutions come with additional stability or opto-electronic limitations that need to be studied in order to optimize the properties for photovoltaic applications. We show that we can improve the properties of Sn based

perovskites during synthesis by Pb-mixing and addition of SnF_2. In the case of $Cs_2AgBiBr_6$ and mixed antimony-bismuth $Cs_2AgBi_{1-x}Sb_xBr_6$ HDPs, we show that the charge trapping is slow and the band gap can be tuned from 2.0 to 1.6 eV by increasing the antimony content. In addition, for both $Cs_2AgBiBr_6$ and mixed trivalent metal $Cs_2AgBi_{1-x}Sb_xBr_6$, the charge-transport mechanism is similar to the state-of-the-art lead-based perovskites (phonon scattering, $\mu \propto T^{-1.5}$). The combination of band-like transport and band gap tunability highlights the potential of these materials as nontoxic alternatives to lead based perovskites. Nevertheless, these modifications are limited to a few specific elements. In the following chapters we modify the organic cation in organic-inorganic perovskites. This changes the crystal structure to either layered two-dimensional lattices (Chapter 6, 7, 9) or one-dimensional ribbons (Chapter 10), depending on the nature of the organic molecules. In the coming chapters we focus on studying the opto-electronic properties of these compounds which also extend their application to other devices such as light-emitting diodes, nano-lasers, photocatalists.

5.4. Experimental Methods

Mechanochemical Synthesis. AI:SnI_2 (1:1), AI:$(Sn_{0.5}Pb_{0.5})I_2$ (1:1) and AI:SnI_4 (2:1) powders (A = Cs or FA) were mixed inside a nitrogen-filled glovebox. Then, approximately 3 grams of the mixed precursors powder was introduced inside 10 mL zirconia ball-mill jars with 2 zirconia beads of 10 mm in diameter. The jars were closed under nitrogen, preventing the powders to be exposed to air. Eventually ball milling was performed with a MM-400 straight ball-mill from Retsch, at a frequency of 30 Hz for 5 hours.

DTA/TG. Differential thermal analysis (DTA)/thermogravimetry (TG) were performed using a LabsysEvo 1600 DTA/TGA (Setaram). The samples (~ 15 mg) were put in an alumina crucible and heated from 30 to 1000 °C, at 45 °C min^{-1} under an He atmosphere (30 ml min^{-1}). The DTA and TGA curves were elaborated using the dedicated software Calisto (Setaram).

Synthesis of $Cs_2AgBi_{1-x}Sb_xBr_6$ Powders. 1 mmol CsBr, 0.5 mmol AgBr, (1 − x)0.5 mmol $BiBr_3$, and 0.5x mmol $SbBr_3$ were ground until fine powders were obtained. The mixtures were sealed in glass tubes under vacuum and heated in a box furnace to 320 °C (heating rate of 3 °C/min) and kept at this temperature for 3 h.10 After cooling down to room temperature (cooling rate of 3 °C/min), the closed tubes containing the products were transferred to a nitrogen-filled glovebox. For this work, x was varied between 0 and 0.4; attempts to prepare higher concentrations of x failed.

$Cs_2AgBi_{1-x}Sb_xBr_6$ Thin Films. $Cs_2AgBi_{1-x}Sb_xBr_6$ (0.5 mmol) was dissolved in 1 mL of DMSO at 75 °C under magnetic stirring in a nitrogen-filled glovebox.[33] Quartz substrates were cleaned with isopropanol and treated with an ozone plasma for 30 min. The $Cs_2AgBi_{1-x}Sb_xBr_6$/DMSO

solutions were filtered and kept at 75 °C. Then, 100 µL of the filtered solution was spin-coated on a quartz substrate using a two-step procedure starting at 500 rpm for 30 s (ramping speed of 100 rpm/s), followed by 60 s at 5000 rpm (ramping speed of 5000 rpm/s). The $Cs_2AgBiBr_6$ (x = 0) films were annealed at 200 °C for 3 min, and the Sb-containing films were annealed at 90 °C for 3 min.

X-ray Diffraction. XRD patterns were obtained with a Bruker D8 diffractometer in a Bragg−Brentano configuration, using Cu Kα (λ = 1.54 Å) radiation.

X-ray Photoelectron Spectroscopy. XPS measurements were performed with a Thermo Scientific K-alpha instrument, equipped with an Al Kα X-ray source and a flood gun to avoid charging of the sample. For the high-resolution scans of C 1s, O 1s, Ag 3d, Bi 4f, Br 3d, Sb 3d, and Cs 3d signals, the following parameters were used: spot size of 400 µm, pass energy of 50 eV, energy step size of 0.1 eV, dwell time of 50 ms, and 10 scans. XPS spectra were corrected using the atmospheric carbon C peak position (284.8 eV). Elemental quantification was performed using the Avantage software. High-resolution scans of each element were fit with a mixture of Gaussian and Lorentzian functions; the area under each peak was used to determine the concentration of each element.

Optical Characterization. Absorption and transmission spectra were recorded with a PerkinElmer Lambda 1050 spectrophotometer equipped with an integrated sphere. The thin $Cs_2AgBi_{1-x}Sb_xBr_6$ films were placed in front of the sphere to measure the fraction of the transmitted light (F_T) and under an angle of 10° inside the sphere to detect the total fraction of reflected and transmitted photons (F_{R+T}). The $Cs_2AgBi_{1-x}Sb_xBr_6$ powders were attached to quartz substrates using optically clear adhesive tape (Thorlabs).

PR-TRMC Measurements. About 30 mg of each $Cs_2AgBi_{1-x}Sb_xBr_6$ powder was put in a sample holder and covered with polymethyl methacrylate (PMMA), drop-casted from a 10 mg/mL PMMA/chlorobenzene solution, to protect from moisture and air. Subsequently, were placed in an airtight copper microwave cell. The temperature was maintained for ∼15 min before every measurement to assure the equilibrium of the system.

Laser-Induced TRMC Measurements. The thin films on quartz substrates were placed in an airtight microwave cell inside a N_2-filled glovebox. The TRMC technique was used to measure the change in microwave (8.5 GHz) power after pulsed excitation (repetition rate 10 Hz) of the samples at various excitation wavelengths. Neutral density filters were used to vary the intensity of the incident light. The illuminated sample area is ∼2.5 cm^2. Before and during the photoconductance measurements, the samples were not exposed to moisture and air to prevent degradation.

5.5. Acknowledgements

The materials studied in this chapter were prepared and characterized by Y.E.A, F.P. and H.J.B from the University of Valencia (Sn-based) and by A.H.S, E.M.H and T.J.S from Stanford University and Delft University of Technology (Halide Double perovskites).

5.6. References

1. NREL. Best Research-Cell Efficiencies. *Best Research-Cell Efficiencies* (2019). Available at: https://www.nrel.gov/pv/assets/pdfs/best-research-cell-efficiencies-190416.pdf.
2. Hao, F., Stoumpos, C. C., Cao, D. H., Chang, R. P. H. & Kanatzidis, M. G. Lead-free solid-state organic-inorganic halide perovskite solar cells. *Nat. Photonics* **8**, 489–494 (2014).
3. Noel, N. K. *et al.* Lead-free organic-inorganic tin halide perovskites for photovoltaic applications. *Energy Environ. Sci.* **7**, 3061–3068 (2014).
4. Stoumpos, C. C., Malliakas, C. D. & Kanatzidis, M. G. Semiconducting tin and lead iodide perovskites with organic cations: Phase transitions, high mobilities, and near-infrared photoluminescent properties. *Inorg. Chem.* **52**, 9019–9038 (2013).
5. Herz, L. M. Charge-Carrier Mobilities in Metal Halide Perovskites: Fundamental Mechanisms and Limits. *ACS Energy Lett.* **2**, 1539–1548 (2017).
6. Slavney, A. H., Hu, T., Lindenberg, A. M. & Karunadasa, H. I. A Bismuth-Halide Double Perovskite with Long Carrier Recombination Lifetime for Photovoltaic Applications. *J. Am. Chem. Soc.* **138**, 2138–2141 (2016).
7. El Ajjouri, Y., Palazon, F., Sessolo, M. & Bolink, H. J. Single-Source Vacuum Deposition of Mechanosynthesized Inorganic Halide Perovskites. *Chem. Mater.* **30**, 7423–7427 (2018).
8. El Ajjouri, Y. *et al.* Low-dimensional non-toxic A3Bi2X9 compounds synthesized by a dry mechanochemical route with tunable visible photoluminescence at room temperature. *J. Mater. Chem. C* **7**, 6236–6240 (2019).
9. Kumar, M. H. *et al.* Lead-free halide perovskite solar cells with high photocurrents realized through vacancy modulation. *Adv. Mater.* **26**, 7122–7127 (2014).
10. Koh, T. M. *et al.* Formamidinium tin-based perovskite with low Eg for photovoltaic applications. *J. Mater. Chem. A* **3**, 14996–15000 (2015).
11. Sabba, D. *et al.* Impact of anionic Br - substitution on open circuit voltage in lead free perovskite (CsSnI 3-x Br x) solar cells. *J. Phys. Chem. C* **119**, 1763–1767 (2015).
12. Gélvez-Rueda, M. C. *et al.* Effect of cation rotation on charge dynamics in hybrid lead halide perovskites. *J. Phys. Chem. C* **120**, 16577–16585 (2016).
13. Gélvez-Rueda, M. C., Renaud, N. & Grozema, F. C. Temperature Dependent Charge Carrier Dynamics in Formamidinium Lead Iodide Perovskite. *J. Phys. Chem. C* **121**, 23392–23397 (2017).
14. Lee, S. J. *et al.* Reducing Carrier Density in Formamidinium Tin Perovskites and Its Beneficial Effects on Stability and Efficiency of Perovskite Solar Cells. *ACS Energy Lett.* **3**, 46–53 (2018).
15. Xiao, Z., Meng, W., Wang, J. & Yan, Y. Thermodynamic Stability and Defect Chemistry of Bismuth-Based Lead-Free Double Perovskites. *ChemSusChem* **9**, 2628–2633 (2016).
16. Gupta, S., Bendikov, T., Hodes, G. & Cahen, D. CsSnBr3, A Lead-Free Halide Perovskite for Long-Term Solar Cell Application: Insights on SnF2 Addition. *ACS Energy Lett.* **1**, 1028–1033 (2016).
17. Kontos, A. G. *et al.* Structural Stability, Vibrational Properties, and Photoluminescence in CsSnI3 Perovskite upon the Addition of SnF2. *Inorg. Chem.* **56**, 84–91 (2017).
18. Lee, S. J. *et al.* Fabrication of Efficient Formamidinium Tin Iodide Perovskite Solar Cells through SnF 2 - Pyrazine Complex. *J. Am. Chem. Soc.* **138**, 3974–3977 (2016).
19. Leijtens, T. *et al.* Tin-lead halide perovskites with improved thermal and air stability for efficient all-perovskite tandem solar cells. *Sustain. Energy Fuels* **2**, 2450–2459 (2018).
20. McClure, E. T., Ball, M. R., Windl, W. & Woodward, P. M. Cs2AgBiX6 (X = Br, Cl): New Visible Light Absorbing, Lead-Free Halide Perovskite Semiconductors. *Chem. Mater.* **28**, 1348–1354 (2016).
21. Filip, M. R., Hillman, S., Haghighirad, A. A., Snaith, H. J. & Giustino, F. Band Gaps of the Lead-Free Halide Double Perovskites Cs2BiAgCl6 and Cs2BiAgBr6 from Theory and Experiment. *J. Phys. Chem. Lett.* **7**,

2579–2585 (2016).
22. Milot, R. L., Eperon, G. E., Snaith, H. J., Johnston, M. B. & Herz, L. M. Temperature-Dependent Charge-Carrier Dynamics in CH3NH3PbI3 Perovskite Thin Films. *Adv. Funct. Mater.* **25**, 6218–6227 (2015).
23. Hutter, E. M., Eperon, G. E., Stranks, S. D. & Savenije, T. J. Charge Carriers in Planar and Meso-Structured Organic-Inorganic Perovskites: Mobilities, Lifetimes, and Concentrations of Trap States. *J. Phys. Chem. Lett.* **6**, 3082–3090 (2015).
24. Bi, Y. *et al.* Charge Carrier Lifetimes Exceeding 15 µs in Methylammonium Lead Iodide Single Crystals. *J. Phys. Chem. Lett.* **7**, 923–928 (2016).
25. Volonakis, G. *et al.* Lead-Free Halide Double Perovskites via Heterovalent Substitution of Noble Metals. *J. Phys. Chem. Lett.* **7**, 1254–1259 (2016).
26. Du, K. Z., Meng, W., Wang, X., Yan, Y. & Mitzi, D. B. Bandgap Engineering of Lead-Free Double Perovskite Cs2AgBiBr6 through Trivalent Metal Alloying. *Angew. Chemie - Int. Ed.* **56**, 8158–8162 (2017).
27. Tran, T. T., Panella, J. R., Chamorro, J. R., Morey, J. R. & McQueen, T. M. Designing indirect-direct bandgap transitions in double perovskites. *Mater. Horizons* **4**, 688–693 (2017).
28. Savenije, T. J., Ferguson, A. J., Kopidakis, N. & Rumbles, G. Revealing the dynamics of charge carriers in polymer:fullerene blends using photoinduced time-resolved microwave conductivity. *J. Phys. Chem. C* **117**, 24085–24103 (2013).
29. Yin, J. *et al.* Molecular behavior of zero-dimensional perovskites. *Sci. Adv.* **3**, 2–10 (2017).
30. Karakus, M. *et al.* Phonon-Electron Scattering Limits Free Charge Mobility in Methylammonium Lead Iodide Perovskites. *J. Phys. Chem. Lett.* **6**, 4991–4996 (2015).
31. Hutter, E. M. *et al.* Vapour-Deposited Cesium Lead Iodide Perovskites: Microsecond Charge Carrier Lifetimes and Enhanced Photovoltaic Performance. *ACS Energy Lett.* **2**, 1901–1908 (2017).
32. Bartesaghi, D. *et al.* Charge Carrier Dynamics in Cs2AgBiBr6 Double Perovskite. *J. Phys. Chem. C* **122**, 4809–4816 (2018).
33. Greul, E., Petrus, M. L., Binek, A., Docampo, P. & Bein, T. Highly stable, phase pure Cs2AgBiBr6 double perovskite thin films for optoelectronic applications. *J. Mater. Chem. A* **5**, 19972–19981 (2017).

Chapter 6

Charge and Excited State Dynamics in 2D HOIPs: Exciton Binding Energy of 2D Ruddlesden-Popper $BA_2MA_{n-1}Pb_nI_{3n+1}$

This chapter describes how the opto-electronic properties of hybrid perovskites can be tailored in two-dimensional (2D) perovskites by varying the dimensionality of the inorganic framework. Specifically, mixing the common short organic cation (methyl ammonium (MA)) with a larger one (e.g. butyl ammonium (BA)) results in layered 2D perovskites with one or more inorganic layers separated by the large organic cation. A detailed understanding of the dissociation and recombination of electron-hole pairs in such materials is of prime importance for applications such as photodetectors and solar cells. In this chapter we give a clear experimental demonstration of the interconversion between excitons and free charges as a function of temperature by combining microwave conductivity techniques with photoluminescence measurements. We demonstrate that the exciton binding energy varies strongly (between 80 meV and 370 meV) with the thickness of the inorganic layers. Additionally, we show that the mobility of charges increases with the layer thickness, in agreement with calculated effective masses from electronic structure calculations.

This chapter is based on:

María C. Gélvez-Rueda, Eline M. Hutter, Duyen H. Cao, Nicolas Renaud, Constantinos C. Stoumpos, Joseph T. Hupp, Tom J. Savenije, Mercouri G. Kanatzidis, Ferdinand C. Grozema. Interconversion Between Free Charges and Bound Excitons in 2D Hybrid Lead Halide Perovskites. J. Phys. Chem. C 2017, 121 (47), 26566-26574.

6.1. Introduction

Organic-inorganic halide perovskites are intensively studied materials for opto-electronic applications such as photovoltaic solar cells, light emitting diodes and lasers.[1-2] Their attractiveness is a result of their ease of preparation and tunable opto-electronic properties.[3] Solar cells based on three-dimensional (3D) perovskites, AMX_3 (with A = Cs, $CH_3NH_3^+$, $HC(NH_2)_2^+$, M = Pb_2^+, Sn_2^+, Ge_2^+; X = I^-, Br^-, Cl^-), have surpassed an overall power conversion efficiency of 25%.[4-5] Recently, the family of layered 2D Ruddlesden–Popper perovskite materials has gained significant attention because of their improved moisture stability, promising device efficiency, and intriguing optical properties.[6-13] 2D perovskites are layered materials that are formed by partially or fully replacing the small methylammonium (MA) cation with a larger cation, reducing the 3D perovskite framework to 2D layered structures due to steric hindrance.[3] A detailed understanding of these materials, especially the photo-generation and transport of charges, is currently lacking.[2] 2D hybrid perovskites with a large organic cation were extensively studied in the 90s for their unique quantum-well structure that enhances exciton confinement beyond predictions for 2D systems.[14-15] This additional confinement has been attributed to the large difference between the dielectric constants of the large organic "barrier" and the inorganic "well".[9, 14, 16-18] Generation of bound and long-lived (Wannier-Mott) excitons with exciton binding energies of several hundreds of meV, renders these materials good candidates for photo-luminescent applications such as lasers and light emitting diodes (LDs and LEDs),[19-20] nonlinear optical[21] and polaritonic devices.[22-26] However, in many cases they exhibit inefficient luminescence at room temperature possibly due to thermal quenching of the excitons or strong exciton-phonon interactions. [12, 27-32]

An interesting feature of 2D hybrid perovskites is the high tunability of their chemical and physical properties. This can be achieved by exchanging the halogen[6] or by introducing both large and small organic cations and controlling the thickness of $[(MA)_{n-1}Pb_nI3_{n+1}]^{2-}$ slabs through the value of n.[7-8, 33-36] Thin films of 2D perovskites are solution-processable and exhibit a higher stability than 3D perovskites under ambient conditions.[21, 7, 36] Highly efficient solar cells (PCE of 12.5%)[11] and LEDs[12] (EQE of 8.8%) have been reported recently. These devices were based on 2D perovskites with butylammonium (BA) and phenylethylammonium (PEA) as the bulky organic cations, respectively. A key property of opto-electronic materials that characterize their performance in both solar cells and LEDs is the exciton binding energy that determines the probability of dissociation of excitons and the recombination of charges. For 3D hybrid perovskites, there has been a considerable debate on the nature of photo-excited excitons as well as the exciton binding energy values.[17, 37-44]

In this work we have studied the dynamics of charges and excited states in a series of 2D Ruddlesden-Popper lead iodide perovskites: $(BA)_2(MA)_{n-1}PbnI3_{n+1}$ (n = 1, 2, 3, 4, 5). The 2D structure consists of single (n = 1) or multiple layers of $[PbI_6]^{4-}$ octahedral containing the small MA cation $[(MA)_{n-1}Pb_nI3_{n+1}]^{2-}$ separated by the longer BA cations (Figure 1).[7] By combining distinct time-resolved microwave conductivity (TRMC) techniques we performed a detailed temperature study of the mobility (irradiation with high-energy electrons) and exciton dissociation (laser excitation) in these materials. These measurements reveal, that at low temperature the mobility of charges increases but the generation of 'free charges' that are not Coulombically bound (i.e. non-excitonic) is less efficient. Since with less thermal energy the formation of Coulombically bound (Wannier-Mott) excitons is favored. This is accompanied by an increase in the fluorescence quantum yield that follows the opposite trend as observed for the fraction of free charges, i.e. higher quantum yields at low temperature. In this work we show, for the first time, direct experimental evidence of the interconversion of excitons into free charges on going from low to high temperatures. This interconversion process is governed by an exciton binding energy that strongly depends on the thickness of the number of inorganic layers (n), ranging from ~370 meV for n = 1 to ~80 meV for n = 4. The combination of these TRMC techniques also demonstrates the strong dependence of the mobility, exciton dissociation and lifetime of charges on the thickness of the slabs (n). The mobility of charges clearly increases with the slab-thickness. This is consistent with previously shown band broadening with n thickness[45] and our own DFT calculations that predict a decrease in the effective mass of holes. In addition, the exciton dissociation becomes more efficient and the lifetime longer with increased layer thickness. Which is a direct result of the reduced Coulombic interactions between electrons and holes (exciton binding energy). This chapter gives a unique insight in the dissociation properties of excitons in perovskites materials by using a complementary combination of microwave conductivity techniques.

6.2. Results and Discussion

6.2.1. Mobility of charges as a function of temperature of $(BA)_2(MA)_{n-1}Pb_nI_{3n+1}$ (n = 1-5)

The crystal structures of the 2D perovskites studied here are shown in Figure 6.1. The materials were synthesized using our previously reported recipe, reacting stoichiometric amounts of $C_4H_9NH_2$, CH_3NH_3I and PbI_2 in excess HI/H_3PO_2 acid solution, filtering by suction filtration and drying in a vacuum oven.[7] The purity of all materials was confirmed by X-ray diffraction (Appendix Figure A6.1), uv-vis spectroscopy and photoluminescence measurements.[7, 10]

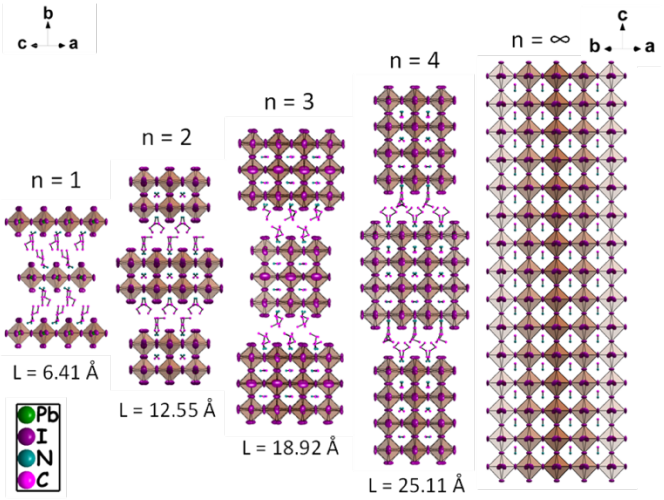

Figure 6.1. Crystal structures of 2D and 3D hybrid lead iodide perovskites, $(BA)_2(MA)_{n-1}Pb_nI_{3n+1}$, extending from n=1 to n= ∞. The thickness of the layers is defined by n.

The mobility was studied by Pulse-Radiolysis Time-Resolved Microwave Conductivity (PR-TRMC). As described in **Chapter 2**, in these measurements charge carriers are generated through irradiation by a short pulse of very high-energy electrons (3 MeV). The change in conductivity due to the generation of mobile charge carriers is monitored by measuring the absorption of high frequency microwaves (28-38 GHz).[46-48] A unique aspect of the use of high-energy electrons is the generation of a uniform concentration of free charge carriers with an average energy transfer of ~20 eV per ionization event. This high energy leads to free electrons and holes that are generated with a spatial separation larger than the thickness of the $[(MA)_{n-1}Pb_nI_{3n+1}]^{2-}$ slab, regardless of the exciton binding energy.[46-48] We emphasize that this way of generating charges is very different from the laser photo-conductivity excitation used in photoconductivity TRMC and terahertz spectroscopy. With laser excitation, charge carriers are generated very close to each other with a non-uniform concentration profile.[52] In the highly confined 2D materials, excitation by a laser will generate excitons where the electron and hole reside in the same $[(MA)_{n-1}Pb_nI_{3n+1}]^{2-}$ slab. As a consequence, the latter measurements are sensitive to the magnitude of exciton binding energies.

Radiation-induced conductivity transients obtained by PR-TRMC measurements for $(BA)_2PbI_4$ (n = 1) and $(BA)_2(MA)_3Pb_4I_{13}$ (n = 4) at different temperatures are shown in Figure 6.2. The conductivity normalized by the charge in the pulse ($\Delta\sigma/Q$) rises during the irradiation pulse as mobile charge carriers are generated. Subsequently, the conductivity decreases after the pulse as the charges recombine or become trapped. In Figure 6.2a it is seen that for $(BA)_2PbI_4$ (n = 1), the lifetime is very long at room temperature but decreases at lower temperatures. The long lifetime at room temperature implies that the electron and the corresponding hole are indeed generated in separate $[(MA)_{n-1}Pb_nI_{3n+1}]^{2-}$ slabs, resulting in a very slow bimolecular

recombination across the organic layer between the slabs. The change in the decay kinetics occurs when the temperature decreases below 0°C. Interestingly, this coincides with a structural phase transition (around 0 °C to -17 °C).[54] This structural change, leading to more disorder of BA, causes a blue shift in the bandgap[54] and higher exciton peak energy.[9] Figure 6.2b represents the radiation-induced conductivity of the $(BA)_2(MA)_3Pb_4I_{13}$ (n = 4) compound. The behavior of the remaining 2D materials is similar to the n = 4 compound and are shown in Appendix Figure A6.2. Unlike the single-layered n = 1 material, the conductivity and charge carrier lifetime gradually increase as the temperature decreases. This has recently also been reported for 3D $MAPbX_3$ perovskites shown in **Chapter 3**.[55] This shows that the presence of the MA significantly affects the charge dynamics in these materials.

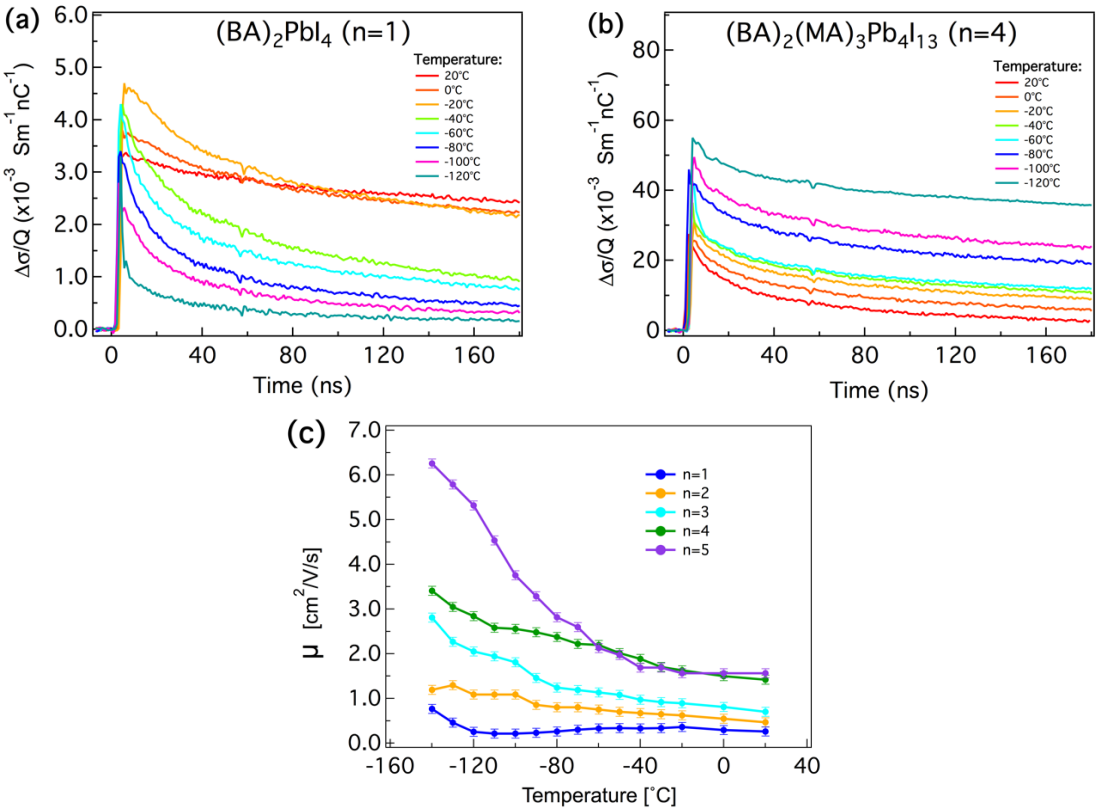

Figure 6.2. PR-TRMC experiments on $(BA)_2(MA)_{n-1}Pb_nI_{3n+1}$. a, b) Conductivity transients for (a) $(BA)_2PbI_4$ (n = 1) and (b) $(BA)_2(MA)_3Pb_4I_{13}$ (n = 4) bulk materials at different temperatures (Pulse length=0.2 ns). **c)** Mobility of charge carriers as a function of temperature in 2D perovskites: $(BA)_2PbI_4$ (n=1), $(BA)_2(MA)Pb_2I_7$ (n=2), $(BA)_2(MA)_2Pb_3I_{10}$ (n=3), $(BA)_2(MA)_3Pb_4I_{13}$ (n=4) and $(BA)_2(MA)_4Pb_5I_{16}$ (n=5).

The mobility of the charges can be determined from the change in the conductivity (Δσ) if the charge carrier concentration at the end of the electron pulse is known (from section 2.2). The mobility values for the 2D series $(BA)_2(MA)_{n-1}Pb_nI_{3n+1}$, n = 1-5, are plotted as a function of temperature in Figure 6.2c. We observe a clear increase in the mobility as the thickness increases from n = 1 to 4. Interestingly, for n = 5 the mobility is higher than that of n = 4 only at temperatures below -50 °C. We have performed DFT band structure calculations,

summarized in Appendix Figure A6.3, that relate this increase in mobility to changes in the band structure. As the thickness increases, the effective mass of the holes steadily decreases, explaining the observed increase in mobility. This agrees with DFT calculations that demonstrated band broadening with the increase of the layer thickness.[45] Furthermore, the mobility increases as the temperature decreases. The temperature-dependent mobility follows an electron-phonon scattering transport mechanism in the n = 1 to 4 compounds (Appendix Figure A6.4). However, this trend deviates in n = 5 at temperature below -80 °C. We have shown in **Chapter 3** that in $MAPbX_3$ (X = I, Br), the trend in mobility as a function of temperature deviates from electron-phonon scattering transport below the β/γ phase transition.[55] This deviation (abrupt increase in mobility and lifetime) was attributed to the restriction of the rotational freedom of the MA cations on going through a structural phase transition. In n = 5 the mobility and lifetime (Appendix Figure A6.4) considerably increase at temperatures below -100 °C. These results suggest that as the thickness increases the charge dynamics approach the behavior of their 3D analogue. Possibly, as the $[(MA)_{n-1}Pb_nI3_{n+1}]^{2-}$ slab becomes thicker there is more freedom for the MA cations to rotate. This dynamic disorder affects the structure (see DSC measurements in Appendix Figures A6.5 and A6.6) and the charge dynamics (as seen in PR-TRMC measurements) in a similar way as in 3D perovskites.

6.2.2. Photogeneration of mobile charge carriers

From the above measurements we have obtained information on the temperature dependence of the charge carrier mobility. In order to gain insight into the dissociation of photo-generated excitons into free charges, we proceeded with microwave photoconductivity measurements on thin films of the same materials. In these measurements, charge carriers are generated using laser photo-excitation instead of an electron pulse. As discussed above, in such an experiment electron-hole pairs are generated in a single slab. Due to the strong confinement for n = 1 (Eb = ~370 meV),[14-15, 18] it is likely that a large fraction of the photo-generated species exist as bound excitons at room temperature and these do not contribute to the conductivity signal. Therefore the result of such measurements is not a direct measure of the charge mobility but the product of charge mobility ($\sum\mu = \mu_e + \mu_h$) and quantum yield of charge formation (x). However, from the PR-TRMC measurements, we already know how the mobility varies with temperature and thickness of the slabs. Therefore, combining this information with photoconductivity TRMC we can obtain information on the yield of exciton dissociation, which is intrinsically related to the exciton binding energy.

The normalized photoconductivity and the photoconductivity half-lifetime are plotted as a function of the thickness (n) in Figure 6.3. It is clear that the photo-conductivity and half-lifetime depend strongly on the thickness. As the slab thickness increases, the photo-

conductivity and half-lifetime also increase. The increase in photo-conductivity is a result of increases in both the charge mobility (∑μ) and the quantum yield of charge formation (x). However, the change in charge mobility with slab thickness is much smaller than the observed variation in photoconductivity. This indicates that the exciton dissociation also varies strongly with the slab thickness. As shown in Figure 6.3b, the lifetime is very short for n = 1 as electrons and holes are generated in the same slab and can recombine easily. The exciton binding energy decreases as the slab thickness increases, resulting in an increase in the yield of free charges and also in the lifetime. The lifetimes measured with the different TRMC techniques differ by one order of magnitude due to the influence of the exciton binding energy. In the photoconductivity TRMC the free charges generated by laser excitation are closer to each other. As a consequence, they recombine faster due to the strong Coulombic interactions between electrons and holes. In addition, the lifetimes measured by TRMC are longer than fluorescence (0.03-0.5 ns)[56-57] and terahertz (<1ps)[58] lifetimes reported in literature. The conductivity lifetimes do not correspond to fluorescence measurements as the species that are detected in both measurements are different. The fluorescence lifetime is determined by band to band recombination of electrons and holes (radiative recombination) that can either exist as free charges or as bound electron-hole pairs. In the case of TRMC measurements, we selectively detect mobile free carriers that either recombine with each other (radiatively) or via trap states. At room temperature, the pure 2D $(BA)_2PbI_4$ exhibits mostly bound excitons after excitation, not free charges, that recombine very fast due to the high exciton binding energy. This is why the PL lifetime is orders of magnitude shorter that in the TRMC experiments. In the case of the very short (<1ps) free carrier lifetime determined by terahertz measurements, this lifetime is so short as in terahertz measurements the excitation density is very high (>10^{17} cm^{-3}).[58] In our TRMC experiments the excitation density is orders of magnitude lower (~10^{14} cm^{-3} - 10^{16} cm^{-3}).

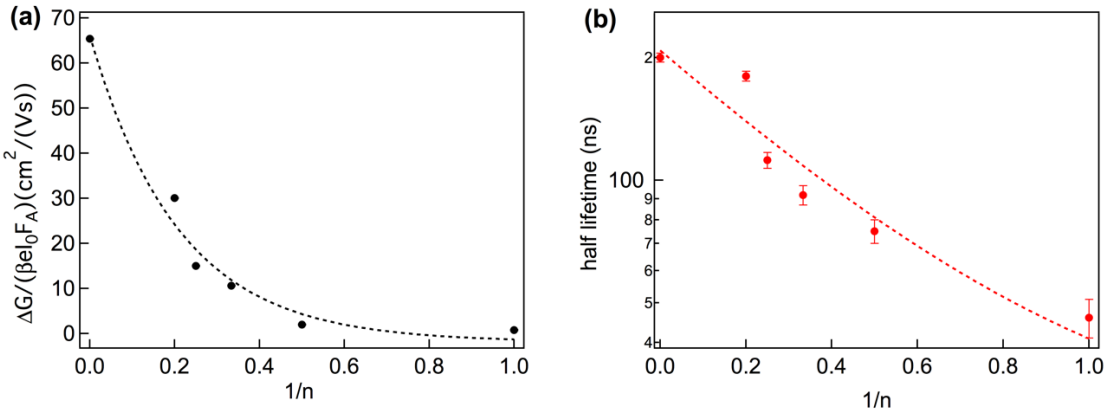

Figure 6.3. Photo-conductivity TRMC of $(BA)_2(MA)_{n-1}Pb_nI_{3n+1}$ thin-films. a) Maximum photoconductance and **b)** half-lifetime as a function of the thickness of the $[(MA)_{n-1}Pb_nI3_{n+1}]^{2-}$ slabs. Measurements performed at room temperature. Excited at the emission wavelength. The dotted lines are a guide to the eye.

To examine how the formation of free charges depends on temperature we have performed temperature-dependent photo-conductivity measurements. The maximum photoconductivity is shown as a function of temperature for n = 1 and n = 4 in Figure 6.4a (See Appendix Figure A6.7 for n = 2 and 3). Interestingly, the photo-conductivity decreases as the temperature decreases. However, as discussed above, the charge carrier mobility was shown to increase with decreasing temperature. Therefore, these measurements directly indicate that at low temperature fewer free charges are formed upon photo-excitation, i.e. the yield of exciton dissociation is lower.

A clearer picture of the relative yield of free charges as a function of temperature (x (T)) is obtained when the photoinduced conductivity, $[x \sum\mu]_{PC}$, is normalized by the mobility from the pulse radiolysis experiments, $[\sum\mu]_{PR}$. It is important to note that this normalization gives the trend of x with temperature and not the absolute values. The large difference in the nature of the samples examined in the two techniques, polycrystalline powders in pulse radiolysis and thin spin-coated films in photoconductivity experiments, can result in different mobility values.[55] This makes necessary to define the yield of dissociation at room temperature. We define each yield separately using theoretical values previously reported for a similar 2D perovskite (~4% for n = 1, ~50% for n = 2, ~85% for n = 3 and ~95% for n = 4).[44] These values are reasonable as for n = 1 the exciton binding energy is known to be very high (~370 meV[14-15, 18, 44]). This is consistent with the very low photo-conductivity signals observed here. For n=4, the yield is expected to be very close to 100% at room temperature[11-12] which is consistent with the almost constant photoconductivity at higher temperatures.

Theoretically, the yield of free charges can be estimated using the Saha equation. This equation relates the yield of free charges to the excitation density, effective mass of the exciton, temperature, and exciton binding energy (Eq. 2.12). In Figure 6.4b, we compare the experimental yield of dissociation with a fit using the Saha equation with the effective mass obtained from DFT calculations and excitation densities around $5x10^{14}$ cm^{-3} to $1x10^{15}$ cm^{-3} (details in Appendix Table A6.1 and Table A6.2). At high temperatures the yield of dissociation is constant and steeply decreases as the temperature falls. Using this analysis, we estimate that the exciton binding energy is approximately 370 meV for n = 1, 170 meV for n = 2, 120 meV for n = 3 and 80 meV for n = 4. These values are smaller than those calculated by Koutselas et al. but are close to the experimental values determined from optical absorption spectra.[16, 44, 59]

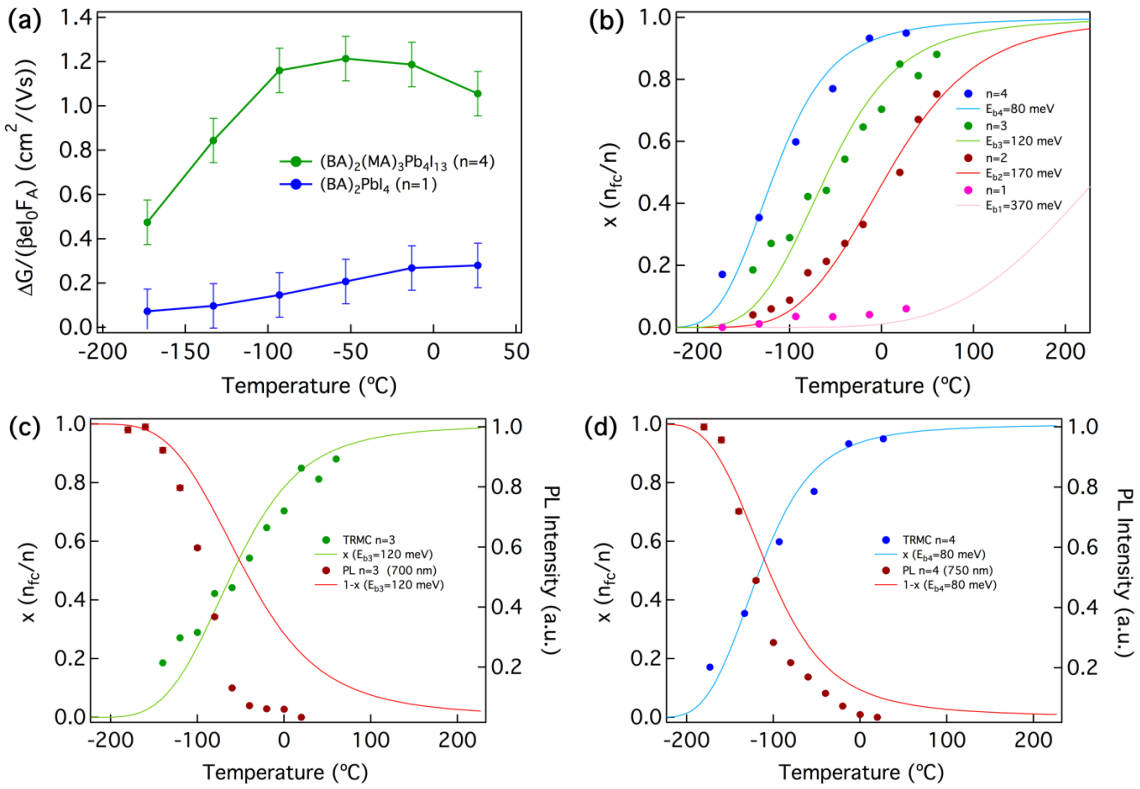

Figure 6.4. Photo-conductivity TRMC of $(BA)_2(MA)_{n-1}Pb_nI_{3n+1}$ thin-films as a function of temperature. a) BA_2PbI_4 (n = 1) and $(BA)_2(MA)_3Pb_4I_{13}$ (n = 4); samples were excited at 473 nm with a photon intensity of $2x10^{11}$ cm^{-2}. **b) Fraction of free charges as a function of temperature.** The full lines are modeled using the Saha equation with an excitation density of $5x10^{14}$ cm^{-3}. The symbols indicate the experimental estimates. **c, d) Fraction of free charges estimated from TRMC measurements (green and blue symbols) and the fraction of bound excitons obtained from PL (red symbols) as a function of temperature. c)** $(BA)_2(MA)_2Pb_3I_{10}$ (n = 3). **d)** $(BA)_2(MA)_3Pb_4I_{13}$ (n = 4)**.** Excited at 405 nm, 1 MHz, with a photon intensity of ~$1x10^{12}$ cm^{-2}. The full lines are modeled using the Saha equation with excitation densities of $8x10^{14}$ cm^{-3} (PL) and $5x10^{14}$ cm^{-3} (TRMC).

The photoconductivity experiments clearly show a decrease in the yield of free charges. This should be accompanied by an increase in the yield of bound excitons and hence an increase in the fluorescence quantum yield at low temperatures. To confirm this, we have performed temperature dependent photoluminescence measurements (Appendix Figure A6.8). The normalized photoluminescence intensities for the n = 3 and n = 4 materials are plotted as a function of temperature in Figure 6.4c and 6.4d, respectively. In addition, the experimental yield of dissociation obtained from our photoconductivity measurements and the fraction of free charges (x) and bound excitons (1-x) obtained from the Saha equation are also included. In Figure 6.4c and 6.4d, we observed that for n = 3 and n = 4 both the photoluminescence intensity (related to the yield of bound excitons) and the dissociation yield closely follow the trend predicted by the Saha equation. In fact, the normalized photoluminescence intensity is almost exactly opposite to the decrease in the yield of free charges. In the case of n = 1 and n = 2 the normalized photoluminescence trend with temperature does not follow this trend so clearly (Appendix Figure A6.9). Nevertheless, the relative fluorescence intensity increases as the temperature decreases, pointing to a larger fraction of bound excitons. This deviation

from the simple behavior observed for n = 3 and n = 4 is likely to be the result of structural changes that can lead to changes in the non-radiative decay of the excitons.[12, 27-28] This is consistent with photoluminescence quantum yield measurements in which for n = 1 the quantum yield is very low and have a maximum value for n = 3 to n = 5.[12] Moreover, the n = 1 and n = 2 compounds exhibit multiple bands in the emission spectrum that change in opposite ways with temperature (Appendix Figure A6.8). The latter is currently not fully understood (see **Chapter 7**). Overall, the combination of the experiments presented here clearly shown the interconversion between excitons and free charges when the temperature is varied. This temperature behavior closely follows the trend predicted by the Saha equation. It should be noted that the we do not obtain information on the specific nature of the excitons, we merely observe the interconversion between mobile unbound charge carriers and Coulomb-bound excitons, which can either be freely moving in the material or bound to a defect. It was shown recently that edge states play an important role in the photogeneration of charges in exfoliated 2D perovskites.[60] Such edge state are expected to play a smaller role here due to the parallel orientation of the perovskite layers with respect to the substrate, it cannot be excluded that the exciton binding energy that we obtain is influenced by this.

6.3. Conclusions

In this chapter we have studied 2D $(BA)_2(MA)_{n-1}Pb_nI_{3n+1}$ Ruddlesden-Popper hybrid perovskites using two distinct microwave conductivity techniques with different pulsed excitation sources: high-energy electron pulse and laser photo-excitation. Our combined experimental results show a clear increase of the mobility of charge, the probability of exciton dissociation, and the lifetime of charges with the thickness of the $[(MA)_{n-1}Pb_nI_{3n+1}]^{2-}$ slabs. The increase in mobility is consistent with DFT calculations that show a decrease of the effective mass of holes. The larger exciton dissociation yield and longer lifetime of charges are explained by an increased dielectric shielding of the electron-hole interactions and hence a lower exciton binding energy. From temperature dependent microwave conductivity experiments the trend in the yield of exciton dissociation was obtained and analyzed in the framework of the Saha equation. This comparison shows that the exciton binding energies range between ~80 meV and ~370 meV depending on the thickness of the $[(MA)_{n-1}Pb_nI_{3n+1}]^{2-}$ slabs. Temperature dependent photoluminescence experiments show that the free charges combine into excitons as the temperature is lowered. This results in an increased photoluminescence intensity with a temperature trend that almost exactly opposite to that in the yield of free charges.

Depending on the opto-electronic application, either excitons can be required (light-emitting diodes, nano-lasers) or free charge carriers (solar cells, photo-catalysis). The approach

presented in this chapter shows that by varying the dimensionality of 2D perovskites by combining large and small organic cation gives a handle on these properties. In the following chapters, we will further explore possibilities to tune the properties 2D perovskites by including organic cations with specific functionality.

6.4. Materials and Methods

Starting materials. All chemicals were purchased from Sigma-Aldrich and used as received. Methylammonium iodide (MAI) was synthesized by neutralizing equimolar amounts of a 57% w/w aqueous hydriodic acid (HI) and 40% w/w aqueous methylamine (CH3NH2) (pH ~ 7). The white precipitate was collected by evaporation of the solvent using rotary evaporation at 60 °C under reduced pressure.

2D Hybrid Perovskites Synthesis. $(BA)_2(MA)_3Pb_4I_{13}$ (n = 4). PbO powder (2232 mg, 10 mmol) was dissolved in a mixture of 57% w/w aqueous HI solution (10.0 mL, 76 mmol) and 50% aqueous H_3PO_2 (1.7 mL, 15.5 mmol), by heating to boiling under constant magnetic stirring for about 5 minutes, forming a bright yellow solution. Subsequent addition of solid CH_3NH_3I (1192 mg, 7.5 mmol) to the hot yellow solution initially caused the precipitation of a black powder which rapidly re-dissolved under stirring to afford a clear bright yellow solution. In a separate beaker, n-$CH_3(CH_2)_3NH_2$ (BA) (248 µL, 2.5mmol) was neutralized with HI 57% w/w (5mL, 38 mmol) in an ice bath resulting in a clear pale yellow solution. Addition of the n-$CH_3(CH_2)_3NH_3I$ solution to the $MAPbI_3$ solution initially produced a black precipitate which subsequently dissolved under heating the combined solution to boiling. The stirring was then discontinued and the solution was left to cool to room temperature during which time black rectangular-shaped plates started to crystallize. The precipitation was deemed to be complete after ~ 2 h. The crystals were isolated by suction filtration and thoroughly dried under reduced pressure. For a detailed description of the synthesis of the remaining compounds in the series, refer to Stoumpos et al.[10]

Preparation of PR-TRMC sample holders. A small amount of material (~45 mg) is placed in a Polyether ether ketone (PEEK) holder and filled by pouring droplets of poly methyl methacrylate (PMMA) dissolved in chlorobenzene at a concentration of 10 mg/ml every 10 min until the perovskite material is fully covered by PMMA. Then, the sample holder is left overnight to ensure the complete evaporation of the solvent. The PMMA filling is done in order to protect the samples from moisture and air and diminish the background conductivity of the material (which affects the PR-TRMC measurements).

Preparation of Thin-films. Quartz substrates were cleaned with oxygen plasma-treated immediately prior to film fabrication. Fabrication of the 2D hybrid perovskites thin-films was

carried out in a nitrogen-filled glovebox. The precursor solutions were prepared by mixing 100 mg of bulk material in 1.5 mL of anhydrous dimethylformamide (DMF). The solutions were filtered using a 0.45 µm pore size filter before spin coating. For the spin coating step, 100 µL of the perovskite solution was spin coated on the substrate for 30 sec at 8000 rpm. Directly after spin-coating the films were annealed at 100 °C for 2 min.

Photo-conductivity measurements. Thin films on quartz substrates were placed in a sealed resonance cavity inside a nitrogen-filled glovebox. The TRMC technique was used to measure the change in microwave (8−9 GHz) power after pulsed excitation (repetition rate 10 Hz) of the OMHPs at 520 nm, 620 nm, 760 nm, 780 nm and 775 nm for n=1, 2, 3, 4 and ∞, respectively. Before and during the photo-conductance measurements, the samples were not exposed to moisture and air to prevent degradation.[52-53]

Optical characterization. Absorption spectra were recorded with a Perkin-Elmer Lambda 1050 spectrophotometer equipped with an integrated sphere. The thin films were placed under an angle of 10° inside the sphere to detect the total fraction of reflected and transmitted photons (F_{R+T}).

Photo-luminescent measurements. Thin films on quartz substrates were placed in a sealed cryostat under nitrogen flow. The PL emission spectra were recorded using an Edinburgh LifeSpec spectrometer equipped with a single photon counter. The 2D films were excited at 405 nm with a picosecond pulsed diode laser (Hamamatsu, M8903-01, I_0 ~ $1x10^{12}$ photons/cm^2, repetition rate 1 MHz).

DFT calculations. All DFT calculations were performed with the BAND program included in the Amsterdam Density Functional suite. During the calculation the experimental geometry was used. The electronic structure calculations were performed using a triple-zeta basis set (TZP) and without using frozen cores. The PBEsol functional was used to account for exchange and correlation. Relativistic effects were included via a scalar correction of the ZORA. The effective masses were calculated using the internal capabilities of BAND.

6.5. References

1. Snaith, H. J. Perovskites: The Emergence of a New Era for Low-Cost, High-Efficiency Solar Cells. J. Phys. Chem. Lett. 2013, 4, 3623-3630.
2. Brenner, T. M.; Egger, D. A.; Kronik, L.; Hodes, G.; Cahen, D. Hybrid Organic—Inorganic Perovskites: Low-Cost Semiconductors with Intriguing Charge-Transport Properties. Nat. Rev. Mater. 2016, 1, 15007.
3. Mitzi, D. B. Synthesis, Structure, and Properties of Organic-Inorganic Perovskites and Related Materials. Prog. Inorg. Chem. 1999, 48, 1-121.
4. Jeon, N. J.; Noh, J. H.; Yang, W. S.; Kim, Y. C.; Ryu, S.; Seo, J.; Seok, S. I. Compositional Engineering of Perovskite Materials for High-Performance Solar Cells. Nature 2015, 517, 476-480.

5. (NREL), N.R.E.L. Best Research-Cell Efficiencies. https://www.nrel.gov/pv/assets/images/efficiency-chart.png (accessed 03/08/2019).
6. Lanty, G.; Jemli, K.; Wei, Y.; Leymarie, J.; Even, J.; Lauret, J. S.; Deleporte, E. Room-Temperature Optical Tunability and Inhomogeneous Broadening in 2d-Layered Organic-Inorganic Perovskite Pseudobinary Alloys. J. Phys. Chem. Lett. 2014, 5, 3958-3963.
7. Cao, D. H.; Stoumpos, C. C.; Farha, O. K.; Hupp, J. T.; Kanatzidis, M. G. 2d Homologous Perovskites as Light-Absorbing Materials for Solar Cell Applications. J. Am. Chem. Soc. 2015, 137, 7843-7850.
8. Wu, X. X.; Trinh, M. T.; Zhu, X. Y. Excitonic Many-Body Interactions in Two-Dimensional Lead Iodide Perovskite Quantum Wells. J. Phys. Chem. C 2015, 119, 14714-14721.
9. Yaffe, O.; Chernikov, A.; Norman, Z. M.; Zhong, Y.; Velauthapillai, A.; van der Zande, A.; Owen, J. S.; Heinz, T. F. Excitons in Ultrathin Organic-Inorganic Perovskite Crystals. Phys. Rev. B 2015, 92, 045414.
10. Stoumpos, C. C.; Cao, D. H.; Clark, D. J.; Young, J.; Rondinelli, J. M.; Jang, J. I.; Hupp, J. T.; Kanatzidis, M. G. Ruddlesden–Popper Hybrid Lead Iodide Perovskite 2d Homologous Semiconductors. Chem. Mater. 2016, 28, 2852-2867.
11. Tsai, H.; Nie, W.; Blancon, J. C.; Stoumpos, C. C.; Asadpour, R.; Harutyunyan, B.; Neukirch, A. J.; Verduzco, R.; Crochet, J. J.; Tretiak, S., et al. High-Efficiency Two-Dimensional Ruddlesden-Popper Perovskite Solar Cells. Nature 2016, 536, 312-316.
12. Yuan, M.; Quan, L. N.; Comin, R.; Walters, G.; Sabatini, R.; Voznyy, O.; Hoogland, S.; Zhao, Y.; Beauregard, E. M.; Kanjanaboos, P., et al. Perovskite Energy Funnels for Efficient Light-Emitting Diodes. Nat. Nanotechnol. 2016, 11, 872-877.
13. Milot, R. L.; Sutton, R. J.; Eperon, G. E.; Haghighirad, A. A.; Martinez Hardigree, J.; Miranda, L.; Snaith, H. J.; Johnston, M. B.; Herz, L. M. Charge-Carrier Dynamics in 2d Hybrid Metal–Halide Perovskites. Nano Lett. 2016, 16, 7001-7007.
14. Tanaka, K.; Takahashi, T.; Kondo, T.; Umebayashi, T.; Asai, K.; Ema, K. Image Charge Effect on Two-Dimensional Excitons in an Inorganic-Organic Quantum-Well Crystal. Phys. Rev. B 2005, 71, 045312.
15. Ishihara, T.; Takahashi, J.; Goto, T. Exciton-State in Two-Dimensional Perovskite Semiconductor (C10h21nh3)2pbi4. Solid State Commun. 1989, 69, 933-936.
16. Ishihara, T. Optical-Properties of Pbi-Based Perovskite Structures. J. Lumin. 1994, 60-1, 269-274.
17. Muljarov, E. A.; Tikhodeev, S. G.; Gippius, N. A.; Ishihara, T. Excitons in Self-Organized Semiconductor-Insulator Superlattices - Pbi-Based Perovskite Compounds. Phys. Rev. B 1995, 51, 14370-14378.
18. Ishihara, T.; Takahashi, J.; Goto, T. Optical-Properties Due to Electronic-Transitions in 2-Dimensional Semiconductors (Cnh2n + 1nh3)2pbi4. Phys. Rev. B 1990, 42, 11099-11107.
19. Hattori, T.; Taira, T.; Era, M.; Tsutsui, T.; Saito, S. Highly Efficient Electroluminescence from a Heterostructure Device Combined with Emissive Layered-Perovskite and an Electron-Transporting Organic Compound. Chem. Phys. Lett. 1996, 254, 103-108.
20. Gebauer, T.; Schmid, G. Inorganic-Organic Hybrid Structured Led's. Z. Anorg. Allg. Chem. 1999, 625, 1124-1128.
21. Kondo, T.; Iwamoto, S.; Hayase, S.; Tanaka, K.; Ishi, J.; Mizuno, M.; Ema, K.; Ito, R. Resonant Third-Order Optical Nonlinearity in the Layered Perovskite-Type Material (C6h13nh3)(2)Pbi4. Solid State Commun. 1998, 105, 503-506.
22. Fujita, T.; Sato, Y.; Kuitani, T.; Ishihara, T. Tunable Polariton Absorption of Distributed Feedback Microcavities at Room Temperature (Vol, 57, Pg 12428, 1998). Phys. Rev. B 1998, 58, 7456-7456.
23. Yablonskii, A. L.; Muljarov, E. A.; Gippius, N. A.; Tikhodeev, S. G.; Fujita, T.; Ishihara, T. Polariton Effect in Distributed Feedback Microcavities. J. Phys. Soc. Jpn. 2001, 70, 1137-1144.
24. Brehier, A.; Parashkov, R.; Lauret, J. S.; Deleporte, E. Strong Exciton-Photon Coupling in a Microcavity Containing Layered Perovskite Semiconductors. Appl. Phys. Lett. 2006, 89, 171110.
25. Wenus, J.; Parashkov, R.; Ceccarelli, S.; Brehier, A.; Lauret, J. S.; Skolnick, M. S.; Deleporte, E.; Lidzey, D. G. Hybrid Organic-Inorganic Exciton-Polaritons in a Strongly Coupled Microcavity. Phys. Rev. B 2006, 74, 235212.
26. Lanty, G.; Lauret, J. S.; Deleporte, E.; Bouchoule, S.; Lafosse, X. Uv Polaritonic Emission from a Perovskite-Based Microcavity. Appl. Phys. Lett. 2008, 93, 081101.
27. Chondroudis, K.; Mitzi, D. B. Electroluminescence from an Organic-Inorganic Perovskite Incorporating a Quaterthiophene Dye within Lead Halide Perovskite Layers. Chem. Mater. 1999, 11, 3028-3030.
28. Dou, L. T.; Wong, A. B.; Yu, Y.; Lai, M. L.; Kornienko, N.; Eaton, S. W.; Fu, A.; Bischak, C. G.; Ma, J.; Ding, T. N., et al. Atomically Thin Two-Dimensional Organic-Inorganic Hybrid Perovskites. Science 2015, 349, 1518-1521.

29. Zhang, S.; Yi, C.; Wang, N.; Sun, Y.; Zou, W.; Wei, Y.; Cao, Y.; Miao, Y.; Li, R.; Yin, Y., et al. Efficient Red Perovskite Light-Emitting Diodes Based on Solution-Processed Multiple Quantum Wells. Adv. Mater. 2017, 29, 1606600.
30. Li, R. Z.; Yi, C.; Ge, R.; Zou, W.; Cheng, L.; Wang, N. N.; Wang, J. P.; Huang, W. Room-Temperature Electroluminescence from Two-Dimensional Lead Halide Perovskites. Appl. Phys. Lett. 2016, 109, 151101.
31. Gauthron, K.; Lauret, J. S.; Doyennette, L.; Lanty, G.; Al Choueiry, A.; Zhang, S. J.; Brehier, A.; Largeau, L.; Mauguin, O.; Bloch, J., et al. Optical Spectroscopy of Two-Dimensional Layered (C6h5c2h4-Nh3)2-Pbi4 Perovskite. Opt. Express 2010, 18, 5912-5919.
32. Hong, X.; Ishihara, T.; Nurmikko, A. V. Dielectric Confinement Effect on Excitons in Pbi4-Based Layered Semiconductors. Phys. Rev. B 1992, 45, 6961-6964.
33. Mitzi, D. B.; Wang, S.; Feild, C. A.; Chess, C. A.; Guloy, A. M. Conducting Layered Organic-Inorganic Halides Containing (110)-Oriented Perovskite Sheets. Science 1995, 267, 1473-1476.
34. Smith, I. C.; Hoke, E. T.; Solis-Ibarra, D.; McGehee, M. D.; Karunadasa, H. I. A Layered Hybrid Perovskite Solar-Cell Absorber with Enhanced Moisture Stability. Angew. Chem. Int. Edit. 2014, 53, 11232-11235.
35. Wu, X. X.; Trinh, M. T.; Niesner, D.; Zhu, H. M.; Norman, Z.; Owen, J. S.; Yaffe, O.; Kudisch, B. J.; Zhu, X. Y. Trap States in Lead Iodide Perovskites. J. Am. Chem. Soc. 2015, 137, 2089-2096.
36. Kenichiro, T.; Takashi, K. Bandgap and Exciton Binding Energies in Lead-Iodide-Based Natural Quantum-Well Crystals. Sci. Technol. Adv. Mater. 2003, 4, 599-604.
37. Wang, H.; Whittaker-Brooks, L.; Fleming, G. R. Exciton and Free Charge Dynamics of Methylammonium Lead Iodide Perovskites Are Different in the Tetragonal and Orthorhombic Phases. J. Phys. Chem. C 2015, 119, 19590-19595.
38. Miyata, A.; Mitioglu, A.; Plochocka, P.; Portugall, O.; Wang, J. T. W.; Stranks, S. D.; Snaith, H. J.; Nicholas, R. J. Direct Measurement of the Exciton Binding Energy and Effective Masses for Charge Carriers in Organic-Inorganic Tri-Halide Perovskites. Nat. Phys. 2015, 11, 582-587.
39. Even, J.; Pedesseau, L.; Jancu, J. M.; Katan, C. Importance of Spin-Orbit Coupling in Hybrid Organic/Inorganic Perovskites for Photovoltaic Applications. J. Phys. Chem. Lett. 2013, 4, 2999-3005.
40. D'Innocenzo, V.; Grancini, G.; Alcocer, M. J. P.; Kandada, A. R. S.; Stranks, S. D.; Lee, M. M.; Lanzani, G.; Snaith, H. J.; Petrozza, A. Excitons Versus Free Charges in Organo-Lead Tri-Halide Perovskites. Nat. Commun. 2014, 5, 3586.
41. Tanaka, K.; Takahashi, T.; Ban, T.; Kondo, T.; Uchida, K.; Miura, N. Comparative Study on the Excitons in Lead-Halide-Based Perovskite-Type Crystals Ch3nh3pbbr3ch3nh3pbi3. Solid State Commun. 2003, 127, 619-623.
42. Hirasawa, M.; Ishihara, T.; Goto, T.; Uchida, K.; Miura, N. Magnetoabsorption of the Lowest Exciton in Perovskite-Type Compound (Ch3nh3)Pbi3. Physica B 1994, 201, 427-430.
43. Galkowski, K.; Mitioglu, A.; Miyata, A.; Plochocka, P.; Portugall, O.; Eperon, G. E.; Wang, J. T. W.; Stergiopoulos, T.; Stranks, S. D.; Snaith, H. J., et al. Determination of the Exciton Binding Energy and Effective Masses for Methylammonium and Formamidinium Lead Tri-Halide Perovskite Semiconductors. Energ. Environ. Sci. 2016, 9, 962-970.
44. Koutselas, I. B.; Ducasse, L.; Papavassiliou, G. C. Electronic Properties of Three- and Low-Dimensional Semiconducting Materials with Pb Halide and Sn Halide Units (Vol 8, Pg 1217, 1996). J. Phys-Condens. Mat. 1996, 8, 5953-5953.
45. Umebayashi, T.; Asai, K.; Kondo, T.; Nakao, A. Electronic Structures of Lead Iodide Based Low-Dimensional Crystals. Phys. Rev. B 2003, 67, 155405.
46. Warman, J. M.; Gelinck, G. H.; de Haas, M. P. The Mobility and Relaxation Kinetics of Charge Carriers in Molecular Materials Studied by Means of Pulse-Radiolysis Time-Resolved Microwave Conductivity: Dialkoxy-Substituted Phenylene-Vinylene Polymers. J. Phys-Condens. Mat. 2002, 14, 9935-9954.
47. Warman, J. M.; de Haas, M. P.; Dicker, G.; Grozema, F. C.; Piris, J.; Debije, M. G. Charge Mobilities in Organic Semiconducting Materials Determined by Pulse-Radiolysis Time-Resolved Microwave Conductivity: Pi-Bond-Conjugated Polymers Versus Pi-Pi-Stacked Discotics. Chem. Mater. 2004, 16, 4600-4609.
48. Grozema, F. C. Opto-Electronic Properties of Conjugated Molecular Wires. . Doctoral Thesis, Delft University of Technology, Delft, The Netherlands, 2003.
49. Klein, C. A. Bandgap Dependence and Related Features of Radiation Ionization Energies in Semiconductors. J. Appl. Phys. 1968, 39, 2029-2038.
50. Alig, R. C.; Bloom, S. Electron-Hole-Pair Creation Energies in Semiconductors. Phys. Rev. Lett. 1975, 35, 1522-1525.

51. Klein-Kedem, N.; Cahen, D.; Hodes, G. Effects of Light and Electron Beam Irradiation on Halide Perovskites and Their Solar Cells. Accounts Chem Res 2016, 49, 347-354.
52. Savenije, T. J.; Ferguson, A. J.; Kopidakis, N.; Rumbles, G. Revealing the Dynamics of Charge Carriers in Polymer:Fullerene Blends Using Photoinduced Time-Resolved Microwave Conductivity. J. Phys. Chem. C 2013, 117, 24085-24103.
53. Hutter, E. M.; Eperon, G. E.; Stranks, S. D.; Savenije, T. J. Charge Carriers in Planar and Meso-Structured Organic-Inorganic Perovskites: Mobilities, Lifetimes, and Concentrations of Trap States. J. Phys. Chem. Lett. 2015, 6, 3082-3090.
54. Billing, D. G.; Lemmerer, A. Synthesis, Characterization and Phase Transitions in the Inorganic-Organic Layered Perovskite-Type Hybrids [(Cnh2n+1nh3)(2)Pbi4], N=4, 5 and 6. Acta Cryst. B 2007, 63, 735-747.
55. Gélvez-Rueda, M. C.; Cao, D. H.; Patwardhan, S.; Renaud, N.; Stoumpos, C. C.; Schatz, G. C.; Hupp, J. T.; Farha, O. K.; Savenije, T. J.; Kanatzidis, M. G., et al. Effect of Cation Rotation on Charge Dynamics in Hybrid Lead Halide Perovskites. J. Phys. Chem. C 2016, 120, 16577-16585.
56. Straus, D. B.; Parra, S. H.; Iotov, N.; Gebhardt, J.; Rappe, A. M.; Subotnik, J. E.; Kikkawa, J. M.; Kagan, C. R. Direct Observation of Electron-Phonon Coupling and Slow Vibrational Relaxation in Organic-Inorganic Hybrid Perovskites. J. Am. Chem. Soc. 2016, 138, 13798-13801.
57. Kitazawa, N.; Aono, M.; Watanabe, Y. Temperature-Dependent Time-Resolved Photoluminescence of (C6h5c2h4nh3)(2)Pbx4 (X = Br and I). Mater. Chem. Phys. 2012, 134, 875-880.
58. Hu, T.; Smith, M. D.; Dohner, E. R.; Sher, M. J.; Wu, X. X.; Trinh, M. T.; Fisher, A.; Corbett, J.; Zhu, X. Y.; Karunadasa, H. I., et al. Mechanism for Broadband White-Light Emission from Two-Dimensional (110) Hybrid Perovskites. J. Phys. Chem. Lett. 2016, 7, 2258-2263.
59. Papavassiliou, G. C.; Koutselas, I. B. Structural, Optical and Related Properties of Some Natural Three- and Lower-Dimensional Semiconductor Systems. Synth. Met. 1995, 71, 1713-1714.
60. Blancon, J. C.; Tsai, H.; Nie, W.; Stoumpos, C. C.; Pedesseau, L.; Katan, C.; Kepenekian, M.; Soe, C. M. M.; Appavoo, K.; Sfeir, M. Y., et al. Extremely Efficient Internal Exciton Dissociation through Edge States in Layered 2d Perovskites. Science 2017, 355, 1288-1291.

Chapter 7

Exciton and Excited State Dynamics of 2D Perovskites (n=1)

In this chapter we discuss the relation between the nature of the organic cation in 2D perovskites and the the exciton and excited state dynamics. Changes in the nature of the organic cations (butylammonium, benzylammonium, phenylethylammonium, histammonium) alter the distortion of the inorganic $[PbI_6]^{2-}$ octahedral layers, thereby influencing the optoelectronic properties. We have performed an in-depth temperature-dependent study of changes in absorption and photoluminescence emission. We have found that despite the confinement of the excitons in 2D perovskites to the inorganic octahedral layers, there is a large influence of the organic compound on the sample reproducibility and excited state dynamics. This seems to be related to the interactions between the organic molecules and/or between the organic molecules and the inorganic octahedral layer, affecting the octahedral distortion and dynamic disorder of the 2D lattice. Although is not completely clear how these effects relate to the exciton dynamics in 2D perovskites, this chapter highlights the importance of the organic cation and the study of the optoelectronic properties as a function of temperature with a variety of spectroscopy techniques.

This chapter is based on:

María C. Gélvez-Rueda, Lingling Mao, Constantinos Stoumpos , Mercouri Kanatzidis and Ferdinand C. Grozema. Exciton and Excited State Dynamics in 2D Perovskites. *In preparation.*

7.1. Introduction

2D perovskite materials have improved moisture stability, promising device efficiency, and intriguing optoelectronic properties.[1–9] These intriguing optoelectronic can be easily modified by varying the compounds in the 2D structure. As described in **Chapter 6**, 2D perovskites are layered materials that are formed by partially or fully replacing the small methylammonium (MA) cation with a larger cation, reducing the 3D perovskite framework to 2D layered structures.[10] In **Chapter 6** we determined the effect of partially replacing MA in order to tune the number of inorganic layers in between the large organic cation (butylammonium), leading to substantial variations in the exciton binding energy. While , pure 2D perovskites (n=1) with butylammonium have been widely studied, there is almost no information on the relation between excited state dynamics and the structure of the organic cation.[11] 2D hybrid perovskites have a unique quantum-well structure that enhances exciton confinement beyond predictions for 2D systems to values between 260 meV to 400 meV.[12,13] These large exciton binding energies should result in the formation of stable long-lived excitons at room temperature, making 2D perovskites ideal candidates for photoluminescent applications such as light emitting diodes (LEDs),[14,15] nonlinear optical[16] and polaritonic devices.[17–21] However, in many cases, 2D perovskites exhibit inefficient photoluminescence at room temperature, possibly due to thermal quenching of the excitons or strong exciton-phonon interactions caused by lattice fluctuations and dynamic disorder.[4,13,22–27] Simultaneously, stable bi-excitons have been determined at room temperature with a large binding energy (~44 meV), similar to the bi-exciton binding energy of strong excitonic 2D transition-metal dichalcogenides.[13,28,29] An in-depth study of the exciton dynamics in 2D perovskites considering the effect of the organic cation on the lattice fluctuations is currently lacking. The organic cation is known to affect the exciton binding energy of 2D perovskites by dielectric confinement.[6,12,30,31] However, the nature of the organic cation and interaction between the organic molecules should also have an influence on the distortions of the inorganic layer, the dynamic disorder and ultimately the exciton dynamics in 2D perovskites.

In this chapter we studied the exciton dynamics in 2D perovskites varying the organic component from the common butylammonium (BA) alkyl-chain to molecules containing aromatic moieties with possible π-π interactions such as benzylammonium (BZA), phenylethylammonium (PEA), and a double valence molecule histammonium (HA), see molecules in Figure 7.1. It is known that the band gap of 2D perovskites is modulated by the organic compound and its interaction with the inorganic $[PbI_6]^{2-}$ octahedral layers.[32] In general, a larger distortion of the inorganic octahedral layer leads to a larger band gap while maintaining the corner shared connectivity of the inorganic octahedral layers as shown in Figure 7.1.[32] Changes in the connectivity of the inorganic octahedral to edge-sharing or face-

sharing octahedral layers can lead to additional confinement effects that are not discussed in this chapter.[33,34] Our methodology in this chapter was to study the opto-electronic properties as a function of temperature with a variety of spectroscopy techniques: steady-state absorption, steady-state photoluminescence and fs-transient absorption (TA). For this we prepared thin films of the different 2D compounds: BA_2PbI_4, BZA_2PbI_4, PEA_2PbI_4, $HAPbI_4$. However, we found that depending on the organic cation the optoelectronic properties can strongly depend on the preparation conditions. This is particularly evident at low temperature in BA_2PbI_4 due a phase transition (at ~253K) which increases the band gap of the material from ~2.4 eV to 2.56 eV.[35] The homogeneity of the phase transition varies for different thin films of the same material, resulting in inconsistent absorption or photoluminescence emission intensities from each phase at temperatures below 253K. This inhomogeneity may be due to the relative 'softness' of 2D structures with alkyl chains which leads to larger dynamic disorder of the 2D structure. In the case of the compounds with aromatic rings, BZA_2PbI_4, PEA_2PbI_4, the optoelectronic properties are more reproducible for different films and exhibit a single strong excitonic transition at all temperatures studied. The reproducibility in the properties with these aromatic molecules may arise from stronger intermolecular interactions that result in a more rigid 2D structure than with alkyl-chains. Finally, the introduction of the divalent organic molecule to form $HAPbI_4$ results in a broader excitonic transition that is actually composed by two transitions. By fs-TA it is observed that there may be energy transfer from the high-energy band to the low-energy band. This chapter indicates that there is a clear influence of the organic compound on the exciton dynamics via distortion and dynamic disorder of the inorganic lattice, although a more detailed explanation is currently lacking.

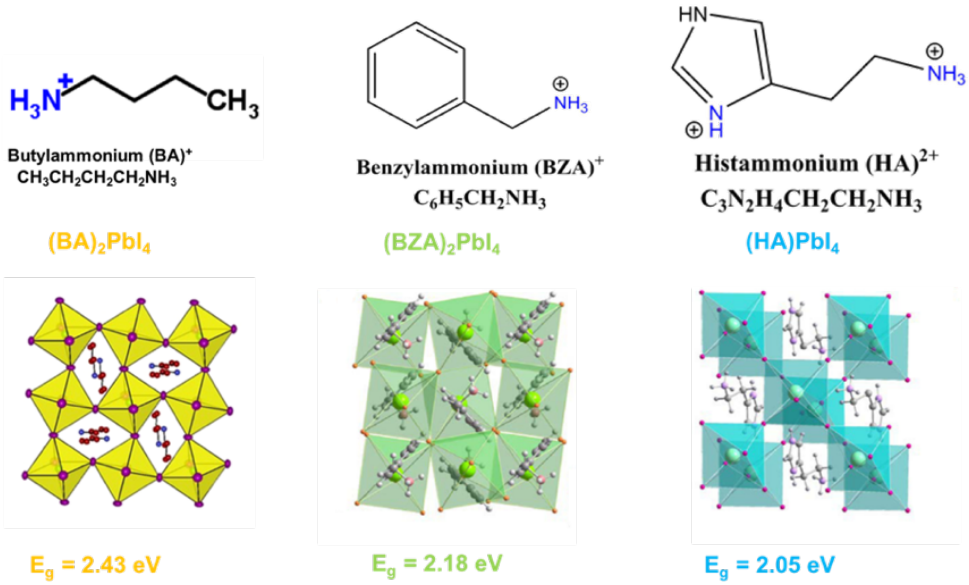

Figure 7.1. Organic molecules and 2D perovskite inorganic octahedral distortion of BA_2PbI_4, BZA_2PbI_4, and $HAPbI_4$. PEA_2PbI_4 octahedral distortion and band gap is very similar to BZA_2PbI_4 as benzylammonium (BZA) and phenylethylammonium (PEA) vary by a carbon in the alkyl linker.

7.2. Results and Discussions

The organic compounds butylammonium (BA), benzylammonium (BZA), phenylethylammonium (PEA), histammonium (HA) were dissolved in stoichiometric amounts with PbI_2 in HI at 70°C and precipitated by cooling to room temperature to form the 2D perovskites: BA_2PbI_4, BZA_2PbI_4, PEA_2PbI_4, $HAPbI_4$ (Figure 7.1). To prepare thin films, the crystals were re-dissolved in dimethylformamide (DMF) and spin-coated on a substrate either by hot-casting[9] (spin-coating of the solution on pre-heated (~433K) quartz substrates) or by post-annealing (spin-coating on quartz and subsequent annealing at ~383K)[32] (section 7.4). Depending on the organic cation, the synthesis and spin-coating conditions turn out to be critical for the optoelectronic properties of the 2D perovskites formed. In section 7.2.1 the optoelectronic properties of BA_2PbI_4 are discussed as a function of temperature and synthesis conditions. Subsequently, the optoelectronic properties of BZA_2PbI_4, PEA_2PbI_4, $HAPbI_4$ are discussed in section 7.2.2.

7.2.1. Optoelectronic properties of BA_2PbI_4

2D BA_2PbI_4 was synthesized by the common precipitation method in HI acid (section 7.4).[2] Depending on the cooling ramp and precipitation time it is possible to prepare nanometer to millimeter size single crystals or powders with micrometer size domains.[2] Subsequently, thin films were prepared by dissolving the BA_2PbI_4 crystals or powders in DMF and spin-coat the solution on hot quartz at 433K (hot-casting method section 7.4). In Figure 7.2 the x-ray diffraction patterns of the crystals, powders and thin-films (TF) prepared from single crystals (TF-C) or from powders (TF-P) are shown. The single crystals and powders synthesized exhibit the main peaks from the simulated BA_2PbI_4 structure oriented in the (00 *l*) direction. Similarly, the thin films made from either crystals (TF-C) or powders (TF-P) also exhibit the (0 0 *l)* reflections characteristic of a preferential growth along the (1 1 0) direction parallel to the substrate.[1] From the XRD perspective, BA_2PbI_4 thin-films have been prepared and there is no difference between starting with millimeter size crystals or powders. Nevertheless, non-optimized spin-coating conditions (for example, use of old starting solutions, higher temperatures or longer annealing time) can result in thin-films with an additional XRD peak at ~5.2 2θ (Appendix Figure A7.1). The origin of this peak is not clear, but it can be linked to thin-films with different absorption spectrum and larger emission intensity from defect states (Appendix Figure A7.2).

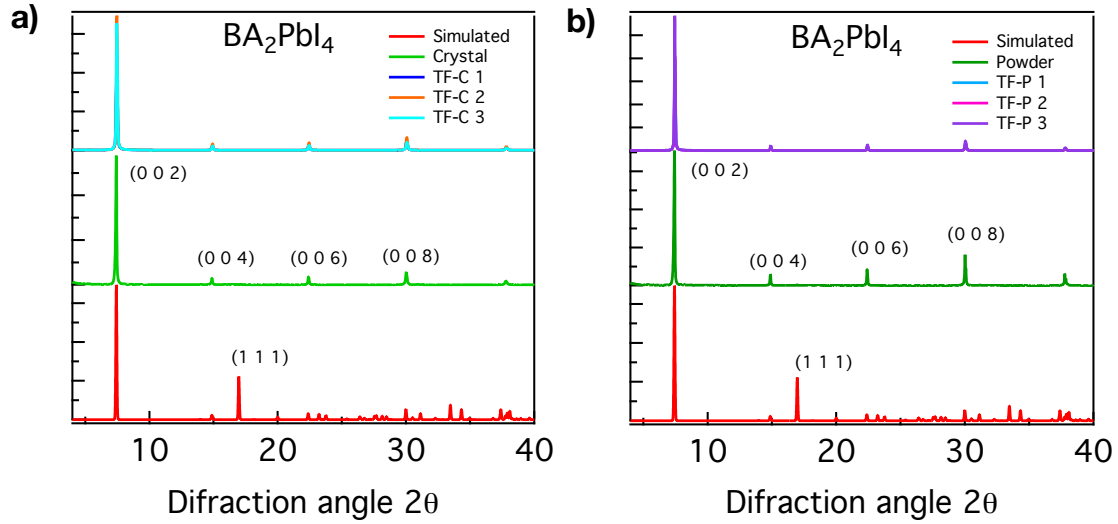

Figure 7.2. X-ray diffraction of BA_2PbI_4. a) BA_2PbI_4 crystal and films prepared from crystals. **b)** BA_2PbI_4 powder and thin-films prepared from powders.

The steady-state absorption of the thin films measured in a UV/Vis spectrometer with an integrating sphere to correct for reflection is shown in Figure 7.3. The absorption spectra exhibit the typical features of 2D perovskites: an excitonic peak at ~510 nm with a continuum band absorption at shorter wavelengths.[1,2,32] Apart from the strong primary absorption edge there is an additional peak that has been associated to the formation of stable excitons at room temperature.[1,2] In addition, the absorption spectra of BA_2PbI_4 thin-films made from powders tend to be slightly blue-shifted compared to those made from single crystals.[1,2]

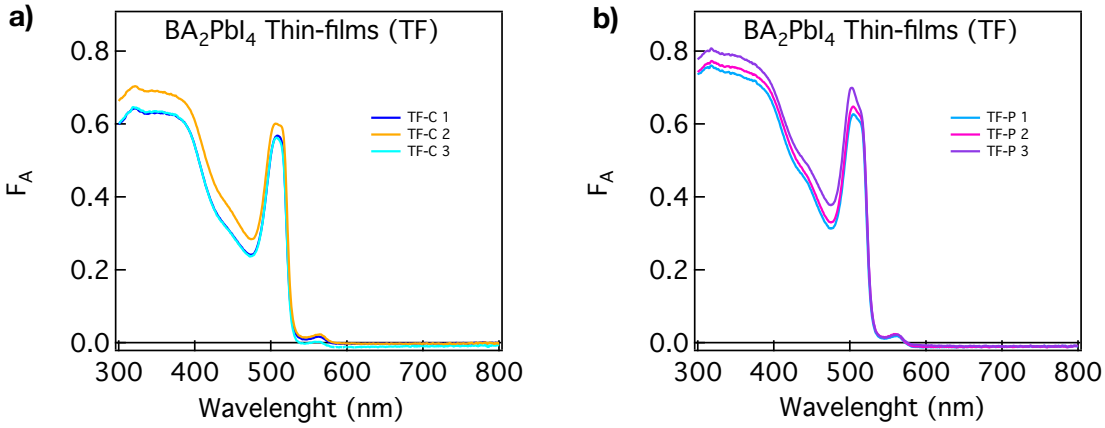

Figure 7. 3. Steady-state absorption measured inside an integrating sphere. a) Films from BA_2PbI_4 crystalline precursors. **b)** Films from BA_2PbI_4 powder precursors.

In Figure 7.4 the steady-state transmission and photoluminescence of thin films of BA_2PbI_4 measured as a function of temperature in a helium cryostat are shown. Inside the cryostat it is only possible to measure the change in transmission of the materials, which is not corrected for reflection. For all BA_2PbI_4 films, the main absorption peak shifts from ~510 nm at 294K to ~484 nm below 253K (Figure 7.4a,c). This shift is associated with a phase transition (occurring between 280K and 260K) caused by reorientation of the BA in between the inorganic

octahedral layers.[35] This reorientation increases the distortion of the inorganic octahedral layers (increases corrugation) resulting in an increase of the band gap.[32,35] At temperatures below the phase transition (253K) the absorption spectrum of BA_2PbI_4 still exhibits a shoulder at the position of the room temperature peak (~510 nm). This indicates that the phase transition to the low temperature phase (phase II) is not complete and there is partial presence of the room temperature phase (phase I). The absorption intensity of the different phases in the film, (phase II at ~484 nm and phase I at ~510 nm), vary from sample to sample. From Figures 7.4a,c it can be observed that below 253K, the room temperature peak at 510 nm is more pronounced in the thin-film prepared from crystals than in the sample prepared from amorphous powders.

The photoluminescence emission spectra of BA_2PbI_4 films are shown for different temperature in Figure 7.4b,d. In general, the photoluminescence intensity increases at low temperature due to larger exciton radiative recombination (less thermal energy to dissociate).[36] At room temperature, the emission spectrum of BA_2PbI_4 films exhibits a single emission peak (~516 nm) corresponding to the exciton absorption peak (~510 nm). When lowering the temperature an additional peak at lower energy (489 nm) appears, while the peak near 510nm remains. In addition, below 200 K, weak emission features appear between 560 and 600 nm below 200K. These low wavelength emission peaks (~560 nm and 600 nm) have a longer lifetime than the exciton emission (see Appendix Figure A7.3) and are attributed in literature to emissions related to defect states.[37] The intensity of the defect emission (and hence the concentration of defects) is higher for the films prepared from amorphous powders than for the ones prepared from more crystalline precursors (see Figure 7.4b,d and Appendix Figures A7.2 and A7.3). The emission peaks at 489 nm and 516 nm correspond to the absorption peaks of the room (phase I) and low (phase II) temperature phases that are both present at low temperatures, as discussed above. The ratio between the intensities from these two excitonic peaks varies between samples as can be seen from comparing Figure 7.4b and d. In the films prepared from crystalline precursors the lowest-energy exciton emission is the most intense, even at low temperatures where the composition of the material is dominated by the phase with a higher energy emission. As the samples are excited at 405 nm (~4.05 mW, ~1.6×10^{17} photon/(s cm^2)) relaxation and energy transfer takes place before emission. As the emission from the TF-C films is dominated by the 516 nm exciton emission the energy is funneled to the remaining high temperature phases and also to the defect states that are more emissive at low temperature.[37] In the films prepared from amorphous powders, both the higher-energy exciton peak and the low-energy defect emission (550-600 nm) are more pronounced than in the TF-C film, compared to the 516 exciton emission. This indicates that the concentration of defect states present in these films is higher, but also that the energy transfer to the lower energy exciton state is less efficient. This illustrates that the

quality of the precursor material has pronounced effects on the quality of the deposited films, even if the differences in the X-ray and UV/Vis characterization are negligible.

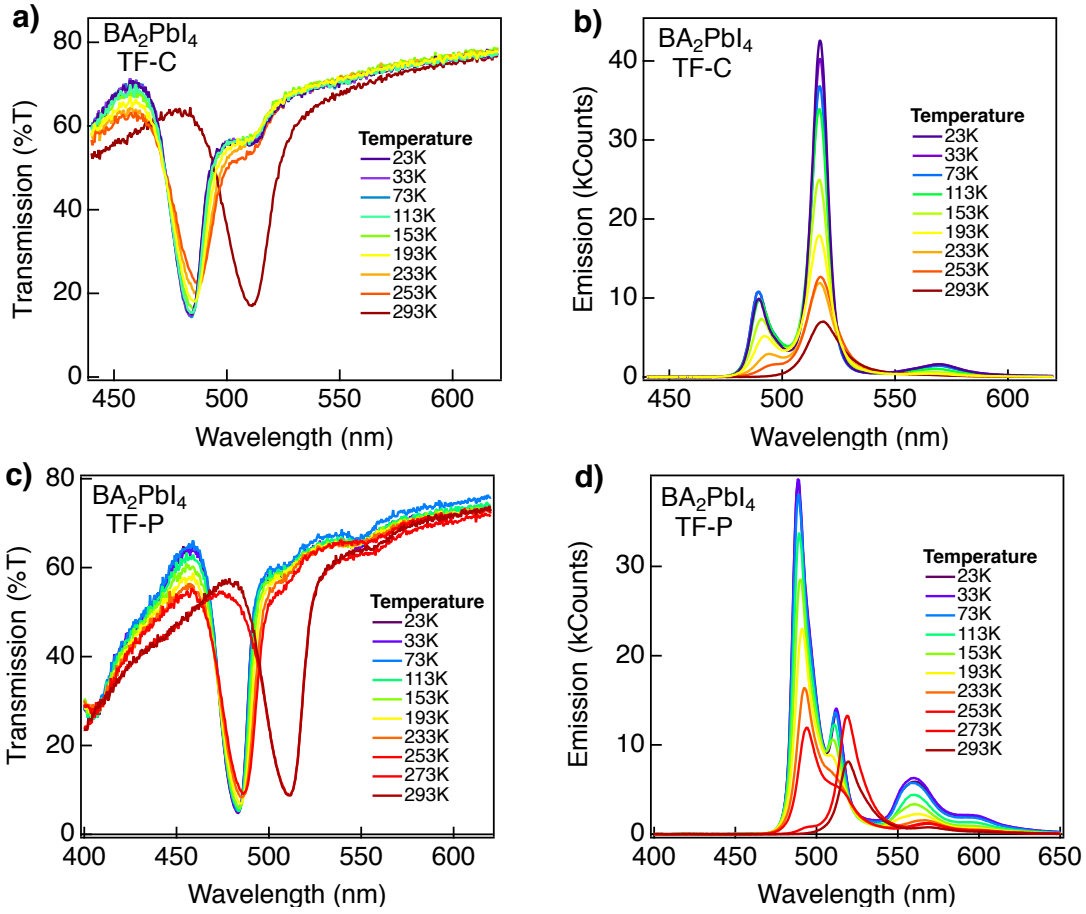

Figure 7.4. Temperature dependent steady-state absorption and photoluminescence emission measured inside a Helium cryostat. a,b) Films from BA_2PbI_4 crystalline precursors. **c,d)** Films from BA_2PbI_4 powder precursors. Photoluminescence excitation at 405 nm with a photon intensity ~ $1.7x10^{17}$ photon/(s cm^2).

In order to clarify the temperature dependence of the different energy states at low temperature in more detail we performed temperature dependent transient absorption (TA) measurements. In these measurements the films were excited at 405 nm with absorbed photon intensities around ~$1.6x10^{12}$ ph/(cm^2 pulse). The changes in absorption due to photoexcitation were detected using short broadband pulses obtained from continuum generation in a calcium fluoride (CaF_2) crystal in the range of 450 nm to 800 nm. We measured BA_2PbI_4 thin films made from crystals as they exhibit less emission from trap states. The TA spectra at room temperature (294K) for different samples (TF-C 1, TF-C 2) are shown in Appendix Figure A7.4. At room temperature the TA spectra exhibits the typical features of 2D perovskites or 2D quantum wells determined in literature: a bleach of the exciton (XB) at ~512 nm, corresponding to band-edge filling by photogenerated excitons. There is additional photoinduced absorption (PA) around the main XB which has been attributed to band gap renormalization (BGR) due to exciton-exciton interactions.[38] In Figure 7.5a,b the TA spectra

of BA_2PbI_4 thin-films made from crystals at 77K are shown. The TA spectra are more complex than the room temperature spectra and exhibit two bleach features, originating from the exciton transition of the low temperature phase (~484 nm) and the room temperature phase (~512 nm) in addition to photoinduced absorption (PA) around the XB peaks. The relative TA intensities from the different phases (484 nm and ~512 nm) vary with sample even under the exact processing conditions and precursor materials (see also Appendix Figure A7.5), as evident from comparing the TA spectra in Figure 7.5.a and b. For the film TF-C1 in Figure 7.5a the exciton features are more pronounced, while this is reversed for TF-C2 in Figure 7.5b. These differences are likely a result of variations in the efficiency of energy migration through the film, which is tightly linked to the crystallinity and morphology. These observations are consistent with the fluorescence measurements discussed above.

In Figure 7.5c the temporal dynamics obtained from the TA measurements at the different wavelengths are show; the exciton bleach (XB at ~485 and ~512 nm) and photoinduced absorption (PA at ~475 nm, 496 nm and 524 nm). These temporal decay from each transition also vary per sample (TF-C1 and TF-C 2). While this complicates the analysis of the data some clear observation can be made. For both samples the contribution from the high-energy exciton peak (characterized by the decay of the XB at 485/489 nm in Figure 7.5c) decays relatively slowly than that of the low energy exciton peak (~512 nm). For high-energy exciton peak (~485 nm) the initial decay is much faster, followed by a slow component. This shows that the photo-physics of these different excitonic states are quite distinct. It also sheds some light on the possible energy transfer from the high-energy to the low-energy exciton states. While there is some funneling from the high- to the low-energy excitons, on the time scales shown in Figure 7.5c there does not seems to be a clear transfer, which would result in a faster decay of the high-energy excitons and a slower decay of the low-energy ones.

The variation related to TA features from the different phases in thin films made from single crystal precursors should be related to the film crystallization on the substrate. On the other hand, films that are obtained from amorphous powder precursors invariably contain more trap states (bound excitons) that lead to substantial (longer-lived) emission around 560 nm and 600 nm (Appendix Figure A7.3) or even changes in absorption in the TA spectra (Appendix Figure A7.6). These measurements show that BA based 2D perovskites are very sensitive to deposition conditions and most of the effects are seen by studying the optoelectronic properties as a function of temperature. This is important to take into account in previous studies in literature where the interpretation of the exciton bands can be severely affected by the film crystallization and presence of trap states.[13,26,31,37,39]

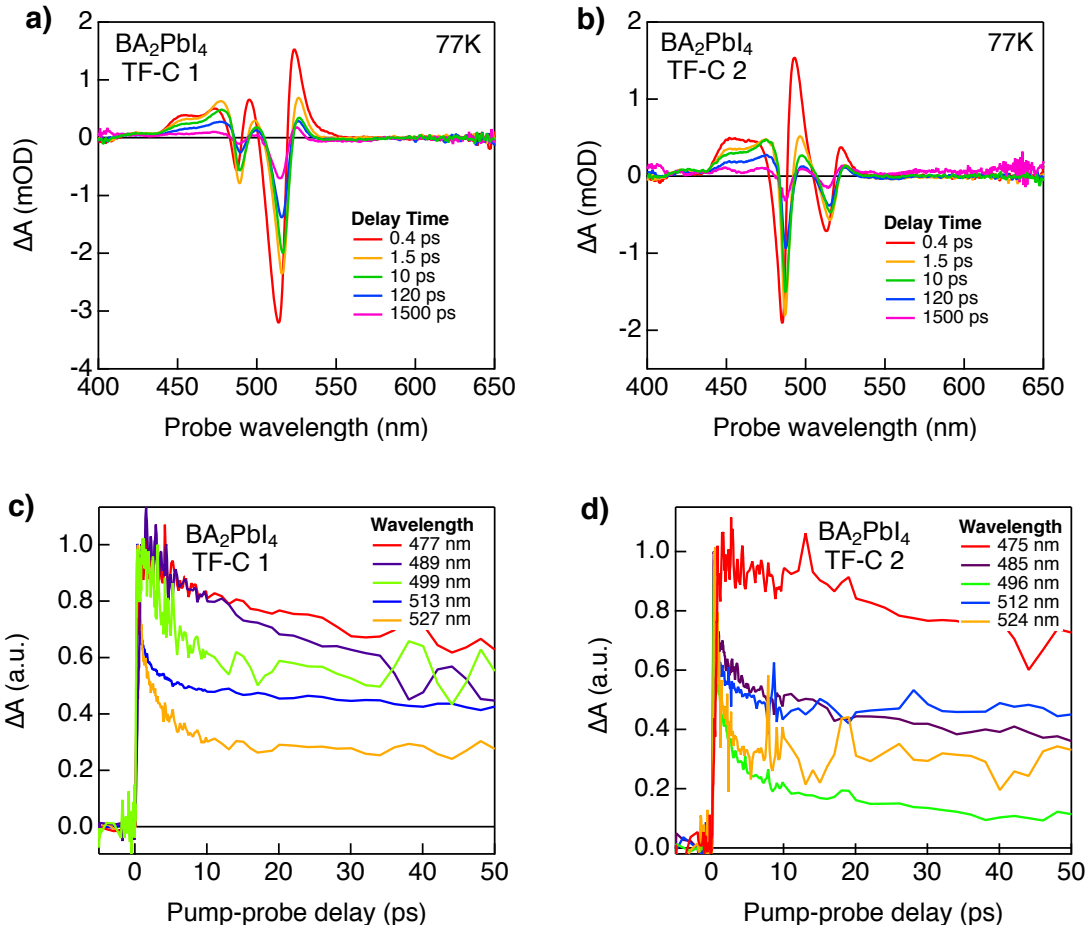

Figure 7.5. Femtosecond transient absorption (TA) experiments on BA_2PbI_4 films made from crystalline precursors at 77K. a, b) TA spectra as a function of delay times. **c, d)** Temporal dynamics of different transitions, exciton bleach (XB at ~485 and ~512 nm) and photoinduced absorption (PA at ~475 nm, 496 nm and 524 nm). Absorbed photon intensities around ~1.6×10^{12} ph/(cm^2 pulse).

7.2.2. Optoelectronic properties of BZA_2PbI_4, PEA_2PbI_4 and HA_2PbI_4

Among 2D perovskites BA_2PbI_4, is the most studied materials, especially in terms of photo-physical properties. However, there is a wealth of ammonium compounds other than BA that can be included in the 2D perovskite structure. Modifications of the organic ammonium compound can have pronounced effects on the packing and possible distortions in the inorganic layers. In order to gain more insight in such effects we have studied the optoelectronic properties of three more 2D perovskites where BA is replaced by benzylammonium (BZA), phenylethylammonium (PEA) or histammonium (HA). In Figure 7.6 the XRD spectra are shown of thin films made by spin-coating and post-annealing at 383K of BZA_2PbI_4, PEA_2PbI_4, $HAPbI_4$ powder solutions (section 7.4). Thin films of BZA_2PbI_4 and PEA_2PbI_4 exhibit the (0 0 *l*) reflections characteristic of a preferential growth along the (1 1 0) direction parallel to the substrate, while $HAPbI_4$ exhibits a different orientation along the (*l* 0 *l*) reflections with a preferential growth along (0 1 0) plane perpendicular to the substrate.

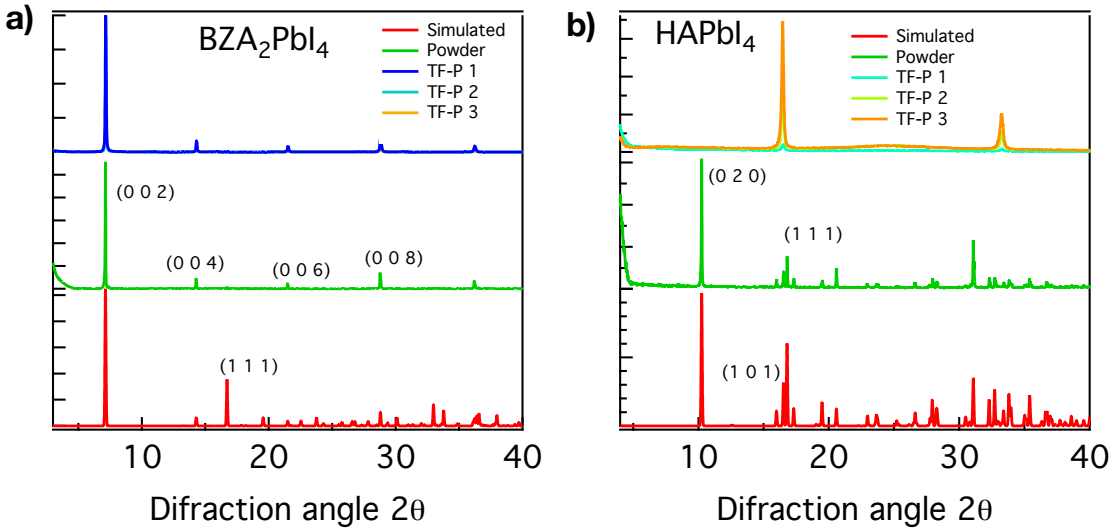

Figure 7.6. X-ray diffraction. a) BZA_2PbI_4 powder and films. **b)** $HAPbI_4$ powder and films.

The steady-state absorption spectra for BZA_2PbI_4, PEA_2PbI_4 and PEA_2PbI_4 measured inside an integrating sphere in a UV/Vis spectrometer is shown in Figure 7.7. For all compounds the absorption spectra exhibits a pronounced excitonic peak at ~520 nm for BZA_2PbI_4, PEA_2PbI_4 and slightly blue-shifted at ~500 nm for $HAPbI_4$ with a continuous absorption at shorter wavelengths. For $HAPbI_4$ the absorption onset is at longer wavelengths (lower energy) as expected from the less distorted structure shown in Figure 7.1. In addition, the exciton peak in the absorption spectrum of $HAPbI_4$ is broader than for BA_2PbI_4, BZA_2PbI_4, PEA_2PbI_4 and exhibits a less sharp excitonic transition.

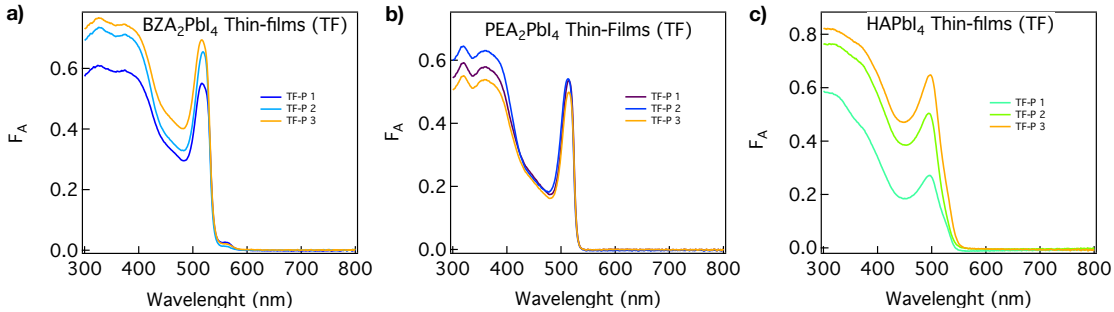

Figure 7.7. Steady-state absorption measured inside an integrating sphere. a) BZA_2PbI_4 films. **b)** PEA_2PbI_4 films. **c)** $HAPbI_4$ films.

As demonstrated above, the UV/Vis transmission spectrum of 2D perovskites can give a good indication of structural rearrangements when the temperature is varied, which was very clear for BA_2PbI_4. In Figure 7.8 the UV/Vis and photoluminescence spectra for thin films of BZA_2PbI_4, PEA_2PbI_4 and $HAPbI_4$ are shown for several temperatures. For BZA_2PbI_4 and PEA_2PbI_4, the absorption and photoluminescence spectra are closely related. The absorption spectrum exhibits a single transition, at ~523 nm for BZA_2PbI_4 and 515 nm for PEA_2PbI_4, that slightly shifts to lower energy at low temperatures due to a decrease of the thermal vibrations and less distortion of the inorganic octahedra. Similarly, the photoluminescence is characterized

by a single transition, at ~530 nm for BZA_2PbI_4 and 522 nm for PEA_2PbI_4, that increases in intensity and becomes narrower at low temperature due to an increasing radiative recombination of excitons (less thermal energy to dissociate) and reduced lattice vibrations. The observation of a single absorption and emission transition in PEA_2PbI_4 is in disagreement with previous reports where a biexciton transition has been mentioned at low temperature.[13,28] However, in our work we very reproducibly observe only a single peak the film of BZA_2PbI_4 and PEA_2PbI_4 made from the powder precursors and the emission from defects at lower energy are minor.

For $HAPbI_4$, the optical absorption spectrum is broad and exhibits two features at room temperature, at ~500 nm and ~520 nm, which both shift to shorter wavelengths as the temperature is decreased. Surprisingly, in the photoluminescence experiments, it was only possible to measure emission from this material at 17K with a three orders of magnitude lower intensity than for the other 2D perovskites. Despite the reduced distortion of the inorganic octahedral layer, the photoluminescence is completely quenched. A possible explanation maybe lie in the separation between the inorganic layers for the different compounds. For the bifunctional HA, the coupling on both sides to the adjacent inorganic layers results in a much shorter distance (~3 Å) compared to BA_2PbI_4 (~7.8 Å), BZA_2PbI_4 (~8 Å) and PEA_2PbI_4 (~8.6 Å). This can lead to some small electronic coupling between neighboring layers, but also should increase the dielectric screening. Both of these effects would result in a lower exciton binding energy and hence to more efficient dissociation of excitons.[5,32]

As for BZA_2PbI_4 and PEA_2PbI_4 films, the deposition of $HAPbI_4$ in thin films is very reproducible from a photophysical point of view. These results show that 2D perovskites made from BZA, PEA, HA have more stable optoelectronic properties than when BA is used. This may be related to interactions between the aromatic rings in BZA, PEA, resulting in a more stable structure.[40] In the 2D perovskite structure, no specific π-π stacking interactions are obvious due to large distances and displacement between the organic cations.[32] Nevertheless, there is a weak intralayer stabilization force between the C-H vector and the aromatic ring centroid.[32] These forces may result in more stable and rigid 2D perovskites. In the case of alkyl-chains (such as BA) the specific intermolecular interactions in the organic interlayer are much smaller making the 2D structure 'soft'. This softness increases the structural fluctuations and disorder, resulting in phase transitions and pronounced non-radiative recombination of excitons despite the large exciton binding energies.[4]

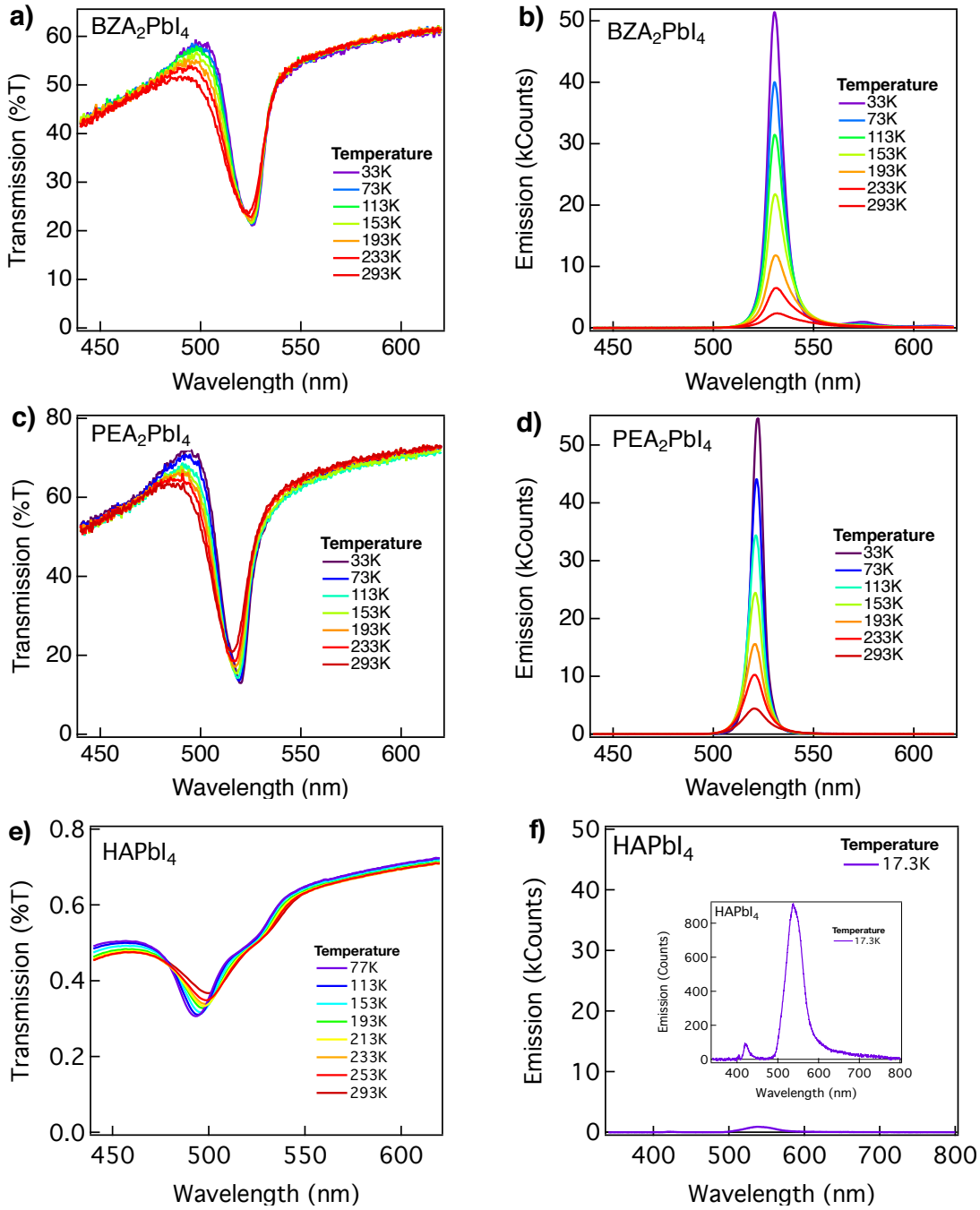

Figure 7.8. Temperature dependent steady-state absorption and photoluminescence emission measured inside a Helium cryostat. a,b) BZA_2PbI_4 films. **c,d)** PEA_2PbI_4 films. **e,f)** $HAPbI_4$ films. Photoluminescence excitation at 405 nm with a photon intensity ~ $1.7x10^{17}$ photon/(s cm^2).

As shown above for BZA_2PbI_4, temperature dependent TA measurements can give valuable insight in their structural and photophysical properties. Therefore we have performed such measurements on BZA_2PbI_4, PEA_2PbI_4 and $HAPbI_4$ thin films, photo exciting at 405 nm with absorbed photon intensities ~$1.9x10^{12}$ ph/(cm^2 pulse), ~$1.3x10^{12}$ ph/(cm^2 pulse) and ~$1.8x10^{12}$ ph/(cm^2 pulse), respectively. The TA spectra of BZA_2PbI_4, PEA_2PbI_4 and $HAPbI_4$ at room temperature (294K) are shown in Appendix Figure A7.7. Similar as for BA_2PbI_4, the TA spectra of BZA_2PbI_4 and PEA_2PbI_4 at 294K exhibit the typical features of 2D quantum well

semiconductors: a bleach of the exciton (XB), at ~523 nm for BZA_2PbI_4 and ~520 nm for PEA_2PbI_4, and photoinduced absorption (PA) around the main XB attributed to band gap renormalization (BGR) due to exciton-exciton interactions.[38] The TA spectra of $HAPbI_4$ exhibit different features that will be discussed below.

The TA spectra of BZA_2PbI_4 and PEA_2PbI_4 at 77K are shown in Figure 7.9a and b. The shape of these spectra is similar to the 294K spectra and no additional bleach or photoinduced absorption features are observed. This is consistent with the single absorption and photoluminescence emission peak observed in these materials in Figure 7.8. From comparing to the results for BA above, it is clear that in 2D perovskites the excitonic dynamics are affected by the organic cation despite the fact that the excitons are confined in the inorganic octahedral layers. As mentioned above, this could be caused by the interaction between the organic molecules and the stiffness of the whole 2D structure.

In the case of $HAPbI_4$, the TA spectra exhibits two exciton bleach (XB) features at ~500 nm and ~520 nm, in addition to photoinduced absorption (PA) around them due to either band gap renormalization (BGR) or exciton-exciton interactions (Appendix Figure A7.7 at 294K and Figure 7.9c at 77K). The two exciton bleach features can be related to the ground state absorption spectra in Figures 7.7 and 7.8 where the main absorption maximum is at ~500 nm but with a shoulder near 520 nm. In the TA spectra of $HAPbI_4$ shown in Appendix Figure A7.7 and Figure 7.9c it is clear that the exciton bleach at ~500 nm disappears after ~1.5 ps, while the exciton bleach at 520 nm increases over the same time scale. Subsequently, the exciton bleach at 520 nm decays in time. The decay dynamics are shown in Figure 7.9d at 294K and 77K. The XB feature at ~503 nm decays very fast while the bleach at 520 nm lives up to 1 ns at 294 K and even longer at 77K. As the exciton bleach features do not decay similarly from two states, we attribute the TA features to energy transfer from the high energy exciton species at ~500 nm to a lower energy species at ~520 nm. This process occurs in a 1.5 ps time scale.

The bleach signal that we observe can be due to excitons, but charge carriers created by dissociation of excitons would result in a very similar bleach. Therefore, we cannot rule out that the observed bleach is, at least in part, due to charge carriers. This would be consistent with the very weak fluorescence for this material discussed above, and can be attributed to a larger effective dielectric constant caused by the closer proximity of the neighboring inorganic layers. At room temperature the lifetime of the bleach signal is relatively short as shown in Figure 7.9d, suggesting a fast decay of the separated charges. At 77 K, a much longer bleach signal is observed, suggesting that the decay of charges is thermally activated.

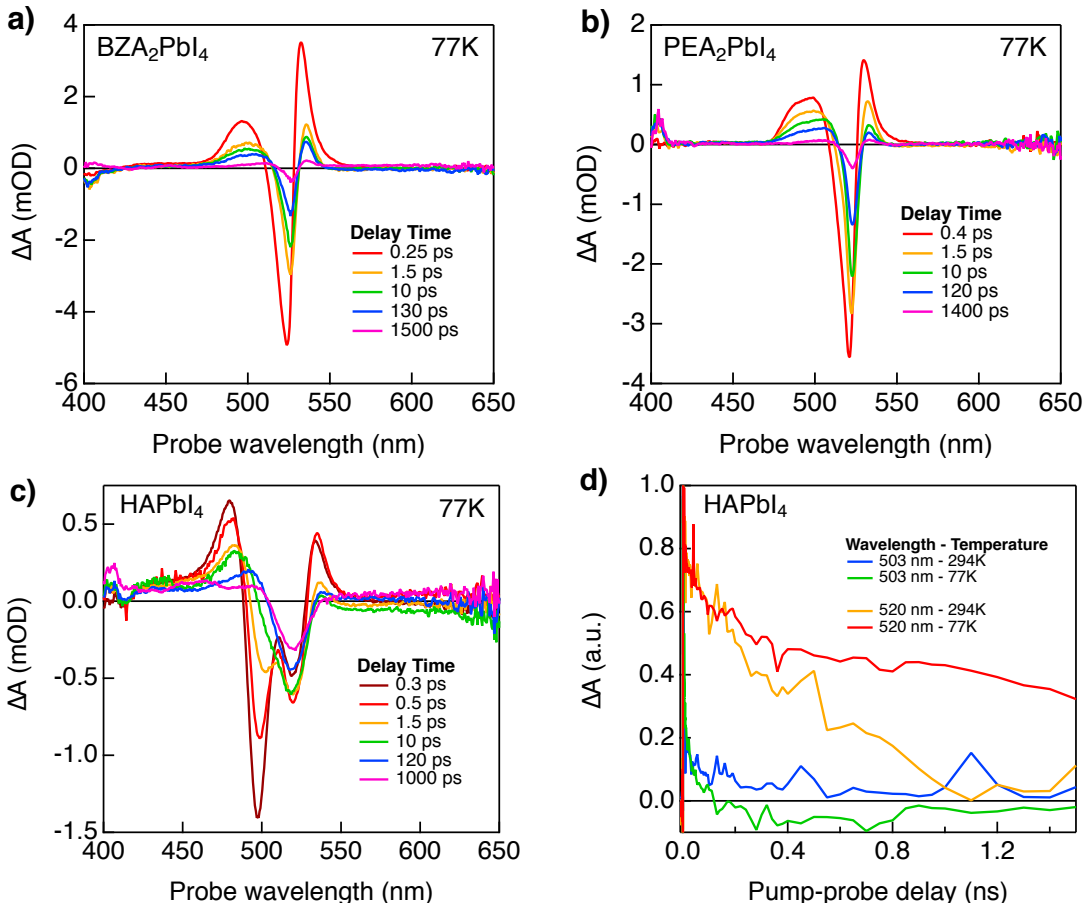

Figure 7.9. Femtosecond transient absorption (TA) experiments at 77K. TA spectra as a function of delay time. a) BZA_2PbI_4 films. **b)** PEA_2PbI_4 films. **c)** $HAPbI_4$ films. **d)** Temporal dynamics of $HAPbI_4$ films at 294K and 77K of the different exciton bleach (XB at ~503 and ~542 nm). Absorbed photon intensities ~$1.9x10^{12}$ ph/(cm^2 pulse), ~$1.3x10^{12}$ ph/(cm^2 pulse) and ~$5.1x10^{12}$ ph/(cm^2 pulse), respectively.

7.3. Conclusions

In this chapter a detailed study of the ground state absorption, emission and excited state dynamics is presented for a series of 2D perovskites where the nature of the organic cation is varied. It is shown that the optoelectronic properties and exciton dynamics in 2D perovskites are significantly influenced by the nature organic cation through their effect on the distortions in the inorganic octahedral layers. In addition, the nature of the organic cation also influences the effective dielectric properties by modulating the distance between the inorganic layers. 2D perovskites with alkyl-chains (BA) have a relative soft structure due to weak interaction between the alkyl chains, leading to increased octahedral (dynamic) disorder. This also introduces structural phase transitions and high sensitivity to precursors and the processing conditions. Introduction of aromatic rings (BZA, PEA) in the sidechain of the ammonium cations leads to a decreased disorder in the organic layer due to stronger intermolecular interactions. This results in decreased structural disorder in the inorganic layers and makes the optoelectronic properties reproduceable for different samples. Introduction of a

bifunctional histamonium (HA) group as the organic component leads to markedly different photophysical properties compared the other three materials. The structure of the 2D perovskite containing HA is more ordered and has a strongly reduced separation between the inorganic layers. For this material on a very weak emission is observed which we attribute to an increased formation of free charges, due to the increased effective dielectric constant (which reduces the exciton binding energy). The decay of the exciton bleach at room temperature is very fast, indicating that these charges are not long-lived.

Overall, we have shown that the nature of the organic ammonium cation used in 2D perovskites has a pronounced effect on the photo-physics. Firstly, it affects the structure and rigidity of the inorganic layers, and in that way indirectly affects the behavior of excitons that are confined to these layers. Secondly, the organic layer also modulates the distance between the neighboring inorganic layers, which has an effect on the dielectric environment of the excitons in the inorganic layer. As a results, the exciton binding energy can be indirectly influenced by the decreased interlayer distance.

7.4. Methods

Starting materials. All chemicals were purchased from Sigma-Aldrich and used as received.

Synthesis of BA_2PbI_4, BZA_2PbI_4, PEA_2PbI_4, $HAPbI_4$. PbO powder (1 mmol) was dissolved in a mixture of 57% w/w aqueous HI solution (7.6 mmol) and 50% aqueous H_3PO_2 (1.5 mmol) by heating to 393K under constant magnetic stirring. In a separate beaker, the organic compound, n-BA, BZA, PEA (2 mmol)or HA (1 mmol) was neutralized with HI 57% w/w (3.8 mmol) in an ice bath (BA) or under heating (BZA, PEA, HA). Then, the organic solution was slowly added to the PbI_2 solution while heating to 393K. Subsequently, the stirring was stopped and the solution was left to cool to room temperature precipitating the 2D powders (~2h). The powders were isolated by suction filtration and thoroughly dried under reduced pressure. For BA_2PbI_4 crystals, the starting solutions have ~10 mmol of precursors and are cooled slowly for ~ 2 to 6 h.

Deposition of films. Quartz substrates were cleaned by submerging in a vial with a mixture of distilled water and soap, which is then put in a sonic bath at 323K for 15 minutes. Afterwards the quartz substrates are rinsed with distilled water, acetone and propyl ethanol and put in an oven at 373K for 20 min. Fabrication of the 2D hybrid perovskites layers was carried out in a nitrogen-filled glovebox. Prior to film fabrication, the quartz substrates were treated with oxygen plasma for 3 min. The starting solutions were prepared by dissolving BA_2PbI_4, BZA_2PbI_4, PEA_2PbI_4, $HAPbI_4$ (0.25 M or 0.1125M) in dimethylformamide (DMF) at 343K for 2 h. Then, the precursor solution was filtered with a 0.45 µm pore size. Films were prepared by

spin-coating 100 µL of starting solution (ramp 1000 rpm/s, 4000 rpm for 40 s) on the plasma-treated quartz substrate either by hot-casting[9] (spin-coating of the solution on pre-heated (~433K) quartz substrates) or by post-annealing (spin-coating on quartz and subsequent annealing at ~383K). The hot casting method was used for BA_2PbI_4, while BZA_2PbI_4, PEA_2PbI_4, $HAPbI_4$ were prepared by post-annealing.

Optical characterization. Absorption spectra were recorded with a uv-vis Perkin-Elmer Lambda 1050 spectrophotometer equipped with an integrated sphere. The films were placed under an angle of 10° inside the sphere to detect the total fraction of reflected and transmitted photons (F_{R+T}).

Temperature dependent absorption (% Transmission) and Photoluminescent measurements. Thin films on quartz substrates were placed in a sealed cryostat under helium flow (temperatures down to 18K). The absorption was measured with an Oceanoptics Maya 2000 pro spectrometer (196 nm to 1120 nm, 100 µm slit) coupled with a uv-vis light source DH-2000 (halogen lamp). The photoluminescent emission spectra were recorded using a Oceanoptics flame-s miniature spectrometer FLM500719 (350 nm to 1000 nm, grating #03 600/500) coupled with a Thorlabs collimated laser diode with a 405 nm excitation wavelength (CPS405, Power ~ 4.05 mW, A= 0.0482 cm^2, photon intensity (I_0) ~$1.7x10^{17}$ photons/(s cm^2)).

Femtosecond Transient Absorption (TA) Spectroscopy. Pump-probe transient absorption measurements were performed using a tunable laser system comprising a Yb:KGW laser source (1028 nm) operating at 5 KHz (2.5 KHz repetition rate) with a pulse duration of 180 fs (PHAROS-SP-06-200, Light Conversion) and an optical parametric amplifier (ORPHEUS-PO15F5HNP1, light conversion). Probe light was generated by continuum generation, focusing a small fraction of the fundamental laser light in a CaF_2 crystal (350 nm to 800 nm). The two-dimensional data was acquired with a transient absorption spectrometer (HELIOS, Ultrafast Systems). The samples were placed inside a sealed holder and excited at 405 nm with a photon intensity of ~$3.2x10^{12}$ ph/(cm^2 pulse), and 200 µm probe spot size in quasi parallel pump-probe geometry.

7.5. References

1. Cao, D. H., Stoumpos, C. C., Farha, O. K., Hupp, J. T. & Kanatzidis, M. G. 2D Homologous Perovskites as Light-Absorbing Materials for Solar Cell Applications. *J. Am. Chem. Soc.* **137**, 7843–7850 (2015).
2. Stoumpos, C. C. *et al.* Ruddlesden-Popper Hybrid Lead Iodide Perovskite 2D Homologous Semiconductors. *Chem. Mater.* **28**, 2852–2867 (2016).
3. Tsai, H. *et al.* High-efficiency two-dimensional ruddlesden-popper perovskite solar cells. *Nature* **536**, 312–317 (2016).
4. Yuan, M. *et al.* Perovskite energy funnels for efficient light-emitting diodes. *Nat. Nanotechnol.* **11**, 872–877 (2016).
5. Milot, R. L. *et al.* Charge-Carrier Dynamics in 2D Hybrid Metal − Halide Perovskites. (2016).

doi:10.1021/acs.nanolett.6b03114
6. Yaffe, O. *et al.* Excitons in ultrathin organic-inorganic perovskite crystals. **045414**, 1–7 (2015).
7. Lanty, G. *et al.* Room-Temperature optical tunability and inhomogeneous broadening in 2D-layered organic-inorganic perovskite pseudobinary alloys. *J. Phys. Chem. Lett.* **5**, 3958–3963 (2014).
8. Blancon, J. C. *et al.* Scaling law for excitons in 2D perovskite quantum wells. *Nat. Commun.* **9**, 1–10 (2018).
9. Blancon, J. C. *et al.* Extremely efficient internal exciton dissociation through edge states in layered 2D perovskites. *Science (80-.).* **355**, 1288–1292 (2017).
10. Mitzi, D. B. Synthesis, Structure, and Properties of Organic-Inorganic Perovskites and Related Materials. *Progress in Inorganic Chemistry* 1–121 (1999). doi:doi:10.1002/9780470166499.ch1
11. Brenner, T. M., Egger, D. A., Kronik, L., Hodes, G. & Cahen, D. Hybrid organic - Inorganic perovskites: Low-cost semiconductors with intriguing charge-transport properties. *Nat. Rev. Mater.* **1**, 1–16 (2016).
12. Tanaka, K., Takahashi, T., Kondo, T. & Ema, K. Image charge effect on two-dimensional excitons in an inorganic-organic quantum-well crystal. 1–6 (2005). doi:10.1103/PhysRevB.71.045312
13. Ishihara, T., Hong, X. & Ding, J. Dielectric confinement effect for exciton and biexciton states in Pbla-based two-dimensional semiconductor structures. 1–4 (1992).
14. Hattori, T., Taira, T., Era, M., Tsutsui, T. & Saito, S. Highly efficient electroluminescence from a heterostructure device combined with emissive layered-perovskite and an electron-transporting organic compound. *Chem. Phys. Lett.* **254**, 103–108 (1996).
15. Gebauer, T. & Schmid, G. Inorganic-organic Hybrid Structured LED ' s Anorganisch-organische Hybrid-LEDs. **5**, 4–8 (1999).
16. Kondo, T. *et al.* Resonant third-order optical nonlinearity in the layered perovskite-type material (C6H13NH3)2PbI4. **105**, 503–506 (1998).
17. Fujita, T., Sato, Y., Kuitani, T. & Ishihara, T. Tunable polariton absorption of distributed feedback microcavities at room temperature. **57**, 428–434 (1998).
18. Yablonskii, A. L., Muljarov, E. A., Gippius, N. A. & Tikhodeev, S. G. Polariton Effect in Distributed Feedback Microcavities. **70**, 1137–1144 (2001).
19. Brehier, A. *et al.* Strong exciton-photon coupling in a microcavity containing layered perovskite semiconductors Strong exciton-photon coupling in a microcavity containing layered perovskite semiconductors. **171110**, 2004–2007 (2016).
20. Wenus, J. *et al.* Hybrid organic-inorganic exciton-polaritons in a strongly coupled microcavity. 1–6 (2006). doi:10.1103/PhysRevB.74.235212
21. Lanty, G. *et al.* UV polaritonic emission from a perovskite-based microcavity UV polaritonic emission from a perovskite-based microcavity. **081101**, 2006–2009 (2016).
22. Chondroudis, K. & Mitzi, D. B. Electroluminescence from an Organic - Inorganic Perovskite Incorporating a Quaterthiophene Dye within Lead Halide Perovskite Layers. 3028–3030 (1999).
23. Dou, L. *et al.* Atomically thin two-dimensional organic-inorganic hybrid perovskites. **349**, (2015).
24. Zhang, S. *et al.* Efficient Red Perovskite Light-Emitting Diodes Based on Solution-Processed Multiple Quantum Wells. **1606600**, 1–6 (2017).
25. Li, R. *et al.* Room-temperature electroluminescence from two-dimensional lead halide perovskites Room-temperature electroluminescence from two-dimensional lead halide perovskites. **151101**, (2016).
26. Gauthron, K. *et al.* Optical spectroscopy of two-dimensional layered (C 6 H 5 C 2 H 4 -NH 3) 2 -PbI 4 perovskite. **18**, 5912–5919 (2010).
27. Hirasawa, M., Ishihara, T., Goto, T., Uchida, K. & Miura, N. compound (CH3NH3)PbI3. **201**, 427–430 (1994).
28. Thouin, F. *et al.* Stable biexcitons in two-dimensional metal-halide perovskites with strong dynamic lattice disorder (a) (c) (b). **034001**, 1–10 (2018).
29. Thouin, F. *et al.* Phonon coherences reveal the polaronic character of excitons in two-dimensional lead halide. *Nat. Mater.* **18**, 349–356 (2019).
30. Muljarov, E. A., Tikhodeev, S. G., Gippius, N. A. & Ishihara, T. Excitons in self-organized semiconductor/insulator superlattices: PbI-based perovskite compounds. *Phys. Rev. B* **51**, 14370–14378 (1995).
31. Ishihara, T. & Takahashi, J. Optical properties due to electronic transitions in two-dimensional semiconductors (CnH2n+1NH3)2PbI4. *Phys. Rev. B* **42**, 99–107 (1990).
32. Mao, L. *et al.* Role of Organic Counterion in Lead- and Tin-Based Two-Dimensional Semiconducting Iodide Perovskites and Application in Planar Solar Cells. *Chem. Mater.* **28**, 7781–7792 (2016).
33. Kamminga, M. E. *et al.* Confinement Effects in Low-Dimensional Lead Iodide Perovskite Hybrids. *Chem.*

Mater. **28**, 4554–4562 (2016).
34. Kamminga, M. E., De Wijs, G. A., Havenith, R. W. A., Blake, G. R. & Palstra, T. T. M. The Role of Connectivity on Electronic Properties of Lead Iodide Perovskite-Derived Compounds. *Inorg. Chem.* **56**, 8408–8414 (2017).
35. Billing, D. G. & Lemmerer, A. Synthesis, characterization and phase transitions in the inorganic–organic layered perovskite-type hybrids [(CnH2n + 1NH3)2PbI4], n = 4, 5 and 6. *Acta Crystallogr. Sect. B* **63**, 735–747 (2007).
36. Gélvez-Rueda, M. C. *et al.* Interconversion between Free Charges and Bound Excitons in 2D Hybrid Lead Halide Perovskites. *J. Phys. Chem. C* **121**, 26566–26574 (2017).
37. Papavassiliou, G. C., Mousdis, G. A., Raptopoulou, C. P. & Terzis, A. Preparation and Characterization of [C6H5CH2 NH3]2PbI4, [C6H5CH2CH2SC(NH2)2]3 PbI5 and [C10H7CH2NH3]PbI3 Organic-Inorganic Hybrid Compounds. *Zeitschrift für Naturforschung B* **54**, 1405 (1999).
38. Li, Q. & Lian, T. Ultrafast Charge Separation in Two-Dimensional CsPbBr 3 Perovskite Nanoplatelets. *J. Phys. Chem. Lett.* **10**, 566–573 (2019).
39. Kitazawa, N., Aono, M. & Watanabe, Y. Temperature-dependent time-resolved photoluminescence of (C 6 H 5 C 2 H 4 NH 3) 2 PbX 4 (X ¼ Br and I) Absorbance. *Mater. Chem. Phys.* **134**, 875–880 (2012).
40. Janiak, C. A critical account on π–π stacking in metal complexes with aromatic nitrogen-containing ligands. *J. Chem. Soc. Dalt. Trans.* 3885–3896 (2000). doi:10.1039/B003010O

Chapter 8

Overcoming the Large Exciton Binding Energy in Two-Dimensional Perovskite Nanoplatelets by Attachment of Strong Organic Electron Acceptors

In this chapter we demonstrate a new approach to achieve efficient charge separation in dimensionally and dielectrically confined two-dimensional (2D) perovskite materials. 2D perovskites generally exhibit large exciton binding energies that limit their application in solar cells, photo-detectors and in photo-catalysis. By incorporating a strongly electron accepting moiety, perylene diimide (PDI) on the surface of the 2D layers, we show the efficient formation of mobile free charge carriers in 2D $CsPbBr_3$ perovskite nanoplatelets. These free charge carriers are generated with ten times higher yield and lifetimes of tens of microseconds, which is two orders of magnitude longer than without the PDI acceptor. This opens a new synergistic approach, where the inorganic perovskite layers are combined with functional organic chromophores to tune the material properties for specific device applications.

This chapter is based on:

María C. Gélvez-Rueda, Magnus B. Fridriksson, Rajeev K. Dubey, Wolter F. Jager, Ward van der Stam and Ferdinand C. Grozema. Overcoming the Large Exciton Binding Energy in Two-Dimensional Perovskite Nanoplatelets by Attachment of Strong Organic Electron Acceptors. *Submitted for publication*.

8.1. Introduction

Two-dimensional (2D) hybrid organic-inorganic perovskites are an emerging class of materials with potential application in a broad range of opto-electronic devices such as solar cells, light-emitting diodes, photo-detectors, spintronics, waveguides, nano-lasers and photo-catalysis.[1–3] 2D hybrid perovskites differ from three-dimensional perovskites, which are currently among the most promising materials for solar cell applications, due to the presence of large organic cations that lead to the formation of 2D layers of inorganic metal-halide octahedra separated by the organic cations. The large organic cations improve the stability under ambient conditions compared to the 3D analogues, and offer new possibilities to tune the opto-electronic properties.[1] Until now, the properties of 2D hybrid perovskites have been tuned by changing the nature of the large organic cations (distorting the inorganic metal-halide octahedrals)[4–10] or by combining them with small organic cations to adjust the number of stacked inorganic octahedral layers (changing the dielectric environment).[9,11–13] In the majority of previous studies, the large organic cation is an alkylammonium (mostly butyl) or phenyl-alkylammonium,[14] which lack specific functionality and do not directly contribute to the opto-electronic properties other than by affecting the structure of the inorganic layers.

There are, however, endless possibilities to engineer the electronic structure of 2D hybrid perovskites by introduction of functional organic molecules, for instance strong electron donors or acceptors. As we have shown in a recent theoretical study,[15] such donor or acceptor molecules can directly contribute to the electronic bands. This could result in enhanced charge separation, compared to current 2D perovskites where the organic cation merely acts as a non-functional dielectric spacer-layer, leading to a high exciton binding energy (ranging from ~190-400 meV for pure 2D, down to ~ 80 meV for quasi-2D system with four inorganic layers between the organic cations[16–19]), and hence inefficient optical generation of charges.

In some recent studies functional organic cations such as conjugated molecules[20,21] and charge-transfer complexes[22,23] have been introduced in 2D hybrid perovskites. However, only limited effects on the opto-electronic properties have been reported.[20,22] Some promising behavior has been observed, such as an increased out-of-plane conductivity by tunneling through the organic cations[21] and photoluminescence quenching (without clarifying whether it is caused by energy or charge transfer).[20] It should be noted that it is hard to predict a priori whether a stable 2D materials will be formed, and other dimensionalities are sometimes obtained because of the interactions between the organic chromophores. [24,25]

An attractive approach to explore the effect of organic molecules on the photophysics of 2D perovskites is the use of colloidal perovskite platelets.[26–28] This reduces the packing requirements of the organic molecules as only a small fraction of the ligands can be replaced

with the conjugated molecules. Introduction of conjugated molecules that are strong electron donors or acceptors can be an approach to the formation of long-lived mobile charge carriers. While charge separation may be achieved by adding donor and acceptor molecules in solution,[29] the eventual application in the solid state requires that they contain binding groups with affinity for the nanoplatelets.[30] For example, perylene diimides (PDI) are well-known electron acceptors used in organic electronics and photovoltaics.[31–33] Their high electron affinity and efficient charge and excited state transport, combined with their exceptional thermal and photochemical stability, makes them ideal candidates to achieve charge separation in 2D hybrid perovskites and potentially develop solution-based and solid-state optoelectronic devices.

In this chapter, we replace the non-functional organic ligands at the surface of colloidal nanoplatelets by a strong electron acceptor moiety: perylene diimide (PDI).[34] The nanoplatelets are colloidal quasi-2D cesium lead bromide nanoplatelets consisting of four layers of lead-bromide octahedra ($CsPbBr_3$ NPLs, n=4).[26–28] In contrast to previous studies,[29] the acceptors used in this work are not merely added in solution but have been modified to contain an ammonium group so that it can coordinatively attach to the surface of the platelets.[30] Using a combination of ultra-fast spectroscopy and time-resolved conductivity techniques, we unequivocally show that the introduction of electron accepting PDIs leads to strongly enhanced charge separation and the formation of long-lived charge carriers useful for optoelectronic devices. This opens up a new synergistic route to materials that are tuned for specific device applications by combining the inorganic perovskite layers with functional organic chromophores.

8.2. Results and Discussion

8.2.1. Synthesis and Characterization of CsPbBr3 nanoplatelet-PDI hybrids

The perovskite nanoplatelets and PDI molecules were synthesized with the aim to selectively photo-excite both components at different wavelengths and study the possibility of electron transfer from the NPLs to the PDI molecules, as well as hole transfer from the PDI molecules to the NPLs (Figures. 8.1a and 8.1c). Two-dimensional colloidal $CsPbBr_3$ nanoplatelets (NPLs 5x10 nm, thickness ~1.5 nm, 4 atomic monolayers (4ML)) were synthesized through a recrystallization method in which Cs-oleate and $PbBr_2$ crystallize when acetone is added as anti-solvent.[26] Their optical absorption and photoluminescence are shown in Figure 8.1b. By careful synthetic control, atomically smooth nanoplatelets surfaces are obtained (see TEM in Figure 8.1b inset) with a pronounced thickness-dependence of the excitonic absorption and fluorescence (Appendix Figure A8.1). 4ML $CsPbBr_3$ NPLs were chosen here as their main exciton peak (450 nm, Appendix Figure A8.2) does not overlap with the absorption of PDI

(520nm, Figure 8.1d).[31] The colloidal nanoplatelets are dispersed in hexane due to their oleate organic capping layer. Subsequently, these ligands were partially replaced by a strongly electron accepting perylene diimide (PDI) derivative (Figure 8.1d) to achieve efficient charge separation (see optical absorption of NPLs+PDI solution in Appendix Figure A8.2). The PDI with the alkylammonium linker at the imide position and four chlorine atoms in the "bay-area" was synthesized in two steps from a perylene monoimide monoanhydride derivative as described in section 8.4 (for synthesis steps and NMR see Appendix Figures A8.3, A8.4, A8.5).[34] The alkylammonium group is introduced so that it can coordinatively attach to the surface of the nanoplatelets,[30] while the chlorine atoms ensure sufficient solubility in common organic solvents such as dichloromethane (DCM). Full details on the synthesis procedures of the 2D NPLs and PDI can be found in section 8.4.

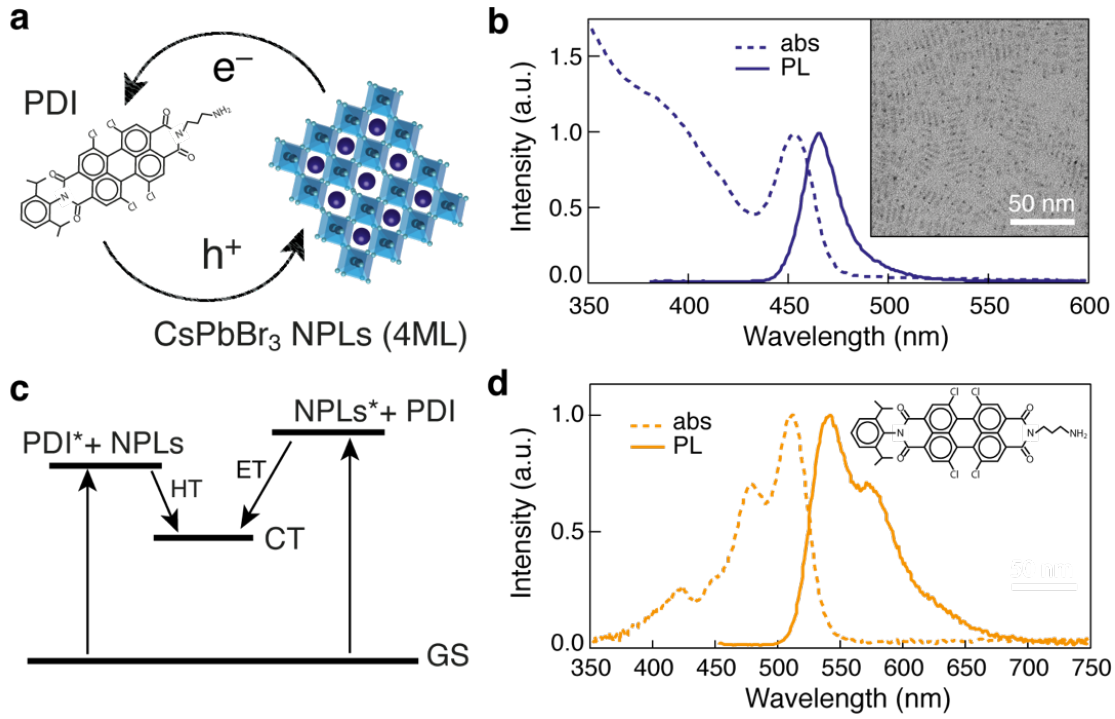

Figure 8.1. CsPbBr3 nanoplatelet-PDI hybrids. a) Schematic representation of CsPbBr3 NPLs and PDI molecules charge transfer. **b)** Optical absorption (dashed line) and photoluminescence emission (full line) spectra of CsPbBr3 NPLs (4ML), Transmission Electron Microscopy image of the NPLs (inset panel 1b). **c)** Schematic representation of the charge transfer processes indicating the formation of the charge transfer state (CT) by hole transfer (HT) from the PDI excited state (PDI*) to NPLs and electron transfer (ET) from the NPL excited state (NPLs*) to PDI. **d)** Optical absorption (dashed line) and photoluminescence emission (full line) spectra of PDI molecules.

8.2.2. Picosecond photoluminescence (PL) measurements

To study the effect of the attachment of PDI to the $CsPbBr_3$ NPLs on the lifetime of excitons we have performed picosecond photoluminescence (PL) measurements using a streak camera. The solutions are photoexcited at a wavelength of 400 nm, reaching a high absorption in the $CsPbBr_3$ NPLs while minimizing the direct absorption in the PDI. In Figure

8.2a, the photoluminescence spectrum for the NPLs without attached PDI is shown as a function of time. This decay, shown in Figure 8.2c, gives a half-life time of 600 ps, comparable to values in literature.[29] Addition of the PDI molecules leads to striking changes. The shape of the fluorescence spectrum remains the same but the lifetime is strongly reduced to ~16 ps (Figures 8.2b and 8.2c, Appendix Figure A8.6). This suggests that the excitons in the NPLs decay rapidly by electron transfer to the electron accepting PDIs. In addition, we observe a weak emission from PDI (540 nm) with a lifetime that is the same as for PDIs in solution (Appendix Figures A8.7 and A8.8). Since there is no in-growth of this feature on the time scale of the decay of the fluorescence from the platelets we attribute this to fluorescence from free PDI molecules in the solution, rather than energy transfer from the NPLs. This is confirmed by transient absorption measurements as described below in section 8.2.4.

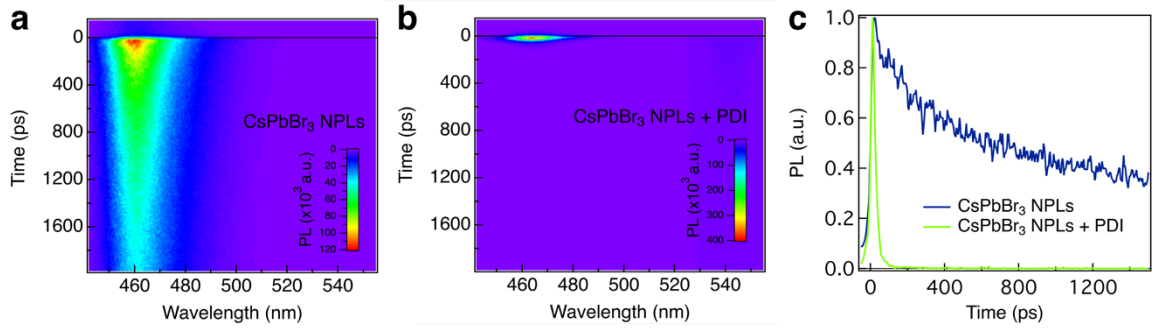

Figure 8.2. Picosecond photoluminescence (PL) measurements. a) PL of $CsPbBr_3$ NPLs (4ML) as a function of time and wavelength. **b)** PL of $CsPbBr_3$ NPLs + PDI hybrid as a function of time and wavelength. **c)** Comparison of the temporal decay of the fluorescence of $CsPbBr_3$ NPLs (4ML) and $CsPbBr_3$ NPLs + PDI hybrid at 460 nm, as a result of fluorescence quenching by electron transfer to PDI.

8.2.3. Electron transfer: Femtosecond transient absorption (TA) on photoexcitation at 400 nm

To determine whether the deactivation of the excitons in the NPLs is indeed due to electron transfer from the $CsPbBr_3$ nanoplatelets to PDI, we have studied the exciton dynamics by femto-second transient absorption (TA) measurements. The solutions were photoexcited at a wavelength of 400 nm with a ~180 fs laser pulse, similar to the fluorescence measurements described above. Subsequently, the changes in the optical absorption spectrum due to photoexcitation were monitored using short, broadband pulses that are obtained from continuum generation in a CaF_2 crystal (340 to 900 nm). All TA measurements were performed at room temperature with low absorbed pump fluences (~3.5×10^{12} photons/(cm^2 pulse)) in order to avoid second order effects due to generation of multiple excitons in a single platelet. The TA spectra of $CsPbBr_3$ NPLs and $CsPbBr_3$ NPLs + PDI are shown in Figure 8.3 at different times after the excitation pulse.

As shown in Figure 8.3a, the TA spectrum of $CsPbBr_3$ NPLs exhibit the typical features found in literature for these materials:[29] a negative exciton bleach (XB) at ~448 nm accounting for band-edge filling by photogenerated excitons superimposed on a broad photoinduced absorption (PA) between 380 to 480 nm. The shape of the TA spectrum does not change with the delay time, confirming the presence of only long-lived single-exciton states (Appendix Figure A8.9).[29] The kinetics of the ground state bleach at 448 nm are shown in Figure 8.3c. We analyzed the TA spectrum with global and target analysis using the open source software Glotaran.[35] In this procedure, the TA spectra are parametrized in time as a linear combination of absorption spectra from the different transient species that interconvert into each other according to a pre-defined kinetic scheme.[36] The target analysis was applied to the 400 nm excitation data with the kinetic scheme shown in Appendix Figure A8.12. The signal grows within time resolution of the TA setup and decays bi-exponentially with decay time constants of 3 ps and 1470 ps. The fast decay component corresponds to fast trapping due to surface defects on perovskite NPLs.[30] The second time component is comparable to the exciton lifetime obtained from the photoluminescence measurements discussed above.

Introduction of the PDI molecules in the ligand shell of the NPLs again leads to striking changes in the TA spectrum (Figure 8.3b). The XB feature at 453 nm has the same shape as observed for the $CsPbBr_3$ NPLs (Figure 8.3a), however, it decays much faster. This is also shown in Figure 8.3c where the kinetics at the maximum of the exciton bleach of the NPLs with and without PDI are compared. In addition, extra features appear in the TA spectrum that are not present in the pure $CsPbBr_3$ NPLs (see Figures 8.3a and 8.3b insets). The first is a reduced absorption (bleach) in the region from 470 nm to 540 nm, corresponding to the ground state absorption of the PDI molecule (Figure 8.1d). This indicates a decrease of the population of PDI molecules in their ground state, due to electron transfer (ET) from the $CsPbBr_3$ NPLs to the PDI, resulting in a charge transfer (CT) state. The second feature is a photoinduced absorption (PA) with a maximum at 760 nm. The shape and position of this second feature are close to the known absorption spectrum of the PDI anion (PDI^-),[37] although it is shifted to longer wavelengths because of the twisting of the PDI-core caused by the introduction of chlorines in the bay area. Note, that the photoinduced absorption of the PDI^- in Figure 8.3b inset is different from the induced absorption due to the excited state of free PDI molecules in solution (PDI*) centered at ~800 nm (Appendix Figure A8.9).[37] In Figure 8.3c, the kinetics from the PA of the PDI^- at 760 nm are also shown.

The TA data of $CsPbBr_3$ NPLs + PDI was analyzed by global target analysis based on the kinetic scheme in Figure 8.3d. This analysis yields the rates of the different processes that occur after photoexcitation, summarized in Figure 8.3d. The fits are compared to the experimental data

in Figure 8.3c (for details see Appendix 8). From this analysis we determined that electron transfer (ET) from the NPLs to the PDIs proceeds with a time constant, τ_{ET} = 12.6 ps, while decay of this CT state back to the ground state (GS) by charge recombination (CR) occurs with a time constant of τ_{CR} = 1800 ps. The value of τ_{ET} is in good agreement with the exciton lifetime obtained from the fluorescence measurements (16 ps). All these features unequivocally show that the excitons in the $CsPbBr_3$ NPLs decay by ET to the PDI molecules.

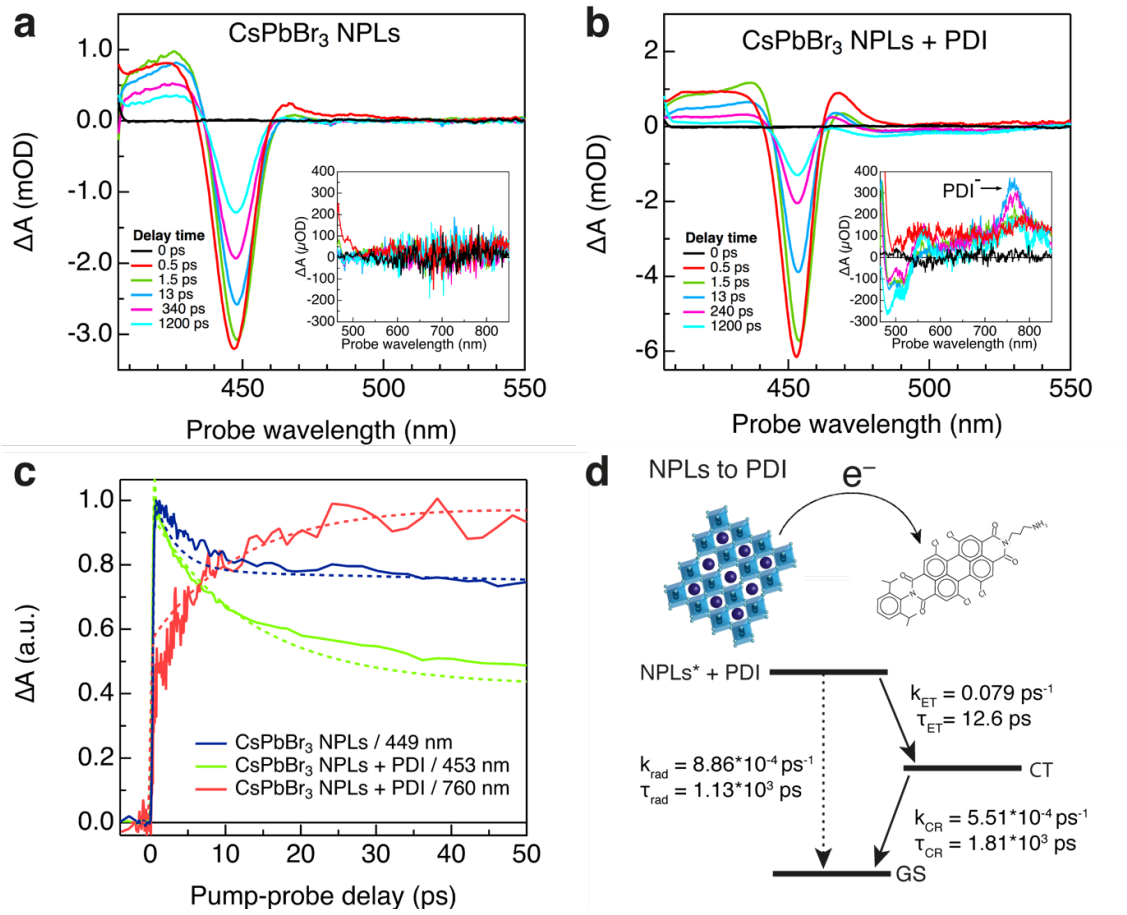

Figure 8.3. Electron Transfer (ET) from $CsPbBr_3$ NPLs* to PDI determined by Transient absorption (TA) upon exciting at 400 nm. a) TA spectrum of $CsPbBr_3$ NPLs (4ML). The inset shows the 465 to 850 nm spectral range. **b)** TA spectrum of $CsPbBr_3$ NPLs + PDI hybrid. The inset shows the 465 to 850 nm spectral range, showing the spectral features of the PDI anion (PDI^-). **c)** Comparison of temporal dynamics of main exciton bleach of $CsPbBr_3$ NPLs (~449 nm)), the main exciton bleach of $CsPbBr_3$ NPLs + PDI hybrid exciton bleach (453 nm) and the PDI anion (PDI^-) photoinduced absorption growth (~760 nm). Solid lines represent the experimental data while dotted lines are the result of the target global analysis. **d)** Kinetic model used for the target global analysis for electron transfer (ET) from NPLs to the PDI molecules in $CsPbBr_3$ NPLs + PDI hybrid.

8.2.4. Hole transfer: Femtosecond transient absorption (TA) on photoexcitation at 510 nm

In order to determine whether the inverse process, hole-transfer (HT) from the PDI molecules to the $CsPbBr_3$ NPLs also takes place, we have studied the exciton dynamics by TA

measurements photoexciting at 510 nm. This wavelength corresponds to the maximum in absorption of the PDI, while there is no absorption by the NPLs. As before, absorbed pump fluences were kept sufficiently low (~$2.7x10^{12}$ photons/(cm^2 pulse)) to avoid multiexciton generation. In addition, for reference, we measured the TA spectra of free $CsPbBr_3$ NPLs and free PDI molecules (Appendix Figure A8.10). For free $CsPbBr_3$ NPLs, no changes in the absorption are observed as expected since the NPLs do not absorb at 510 nm. For isolated PDI molecules, the TA spectrum exhibits the typical features of the PDI excited state (PDI*): a bleach of the ground state absorption at wavelengths between 470 nm and 540 nm, stimulated emission at ~580 nm and a broad photoinduced absorption (PA) from 690 nm to 900 nm with a narrow maximum at 800 nm.[31,37,38] PDI* decays with a time constant of 4ns, which is close to the fluorescence lifetime determined for this compound of (τ_{rad}=3.8 ns, Appendix Figure A8.11).

In Figures 8.4a and 8.4b, the TA spectrum of $CsPbBr_3$ NPLs + PDI upon excitation at 510 nm is shown. The TA spectra clearly illustrate the hole transfer (HT) from the PDI molecules to the $CsPbBr_3$ NPLs. In Figure 8.4b, we first observe the instantaneous formation of PDI* by the presence of the PA feature at 800 nm. Subsequently, this initial PDI* evolves (t>1 ps) into the spectrum of the PDI anion (PDI^-), characterized by photoinduced absorption at ~760 nm. Simultaneously, Figure 8.4a shows how the XB from the NPLs at 453 nm grows in time over ~30 ps as holes are transferred from the PDI* to the NPLs. The increase of the XB of the NPLs correlates with the growth of the PDI^- as shown in the experimental temporal dynamics, solid lines, as shown in Figure 8.3c. In addition, the long lifetime of the XB signal, extending into the nanosecond regime indicates the formation of long-lived charges in the NPLs.

A global and target analysis of the photophysical processes upon excitation at 510 nm was performed using the kinetic scheme shown in Figure 8.4d. This scheme accounts for both the PDIs attached to the NPLs (and subsequent hole transfer to the NPLs and formation of the PDI anion) and the unattached PDI molecules in solution. In the analysis, we fixed the decay of free PDIs in solution (τ_{rad}~4 ns, see above) and the decay of the CT state back to the ground state obtained from 400 nm excitation experiments (τ_{CR} = 1810 ps). These assumptions lead to a reasonable fit of the kinetics shown by dotted lines in Figure 8.4c. The resulting time rate of hole transfer from the PDIs to the NPLs is extremely fast (τ_{HT} = 1.5 ps), i.e. one order of magnitude faster than electron transfer (τ_{ET} = 12.5 ps) from the NPLs to the PDI molecules as discussed above. The latter is remarkable since the driving force for hole transfer (ΔG_{CT}) is smaller than for electron transfer as the energy of the initial state (PDI*) is lower, while the final charge separated (CT) state is exactly the same. This suggests that electron transfer takes place in the Marcus inverted region[39] where a smaller charge transfer rate is obtained with a larger ΔG_{CT} (see Figure 8.1c).

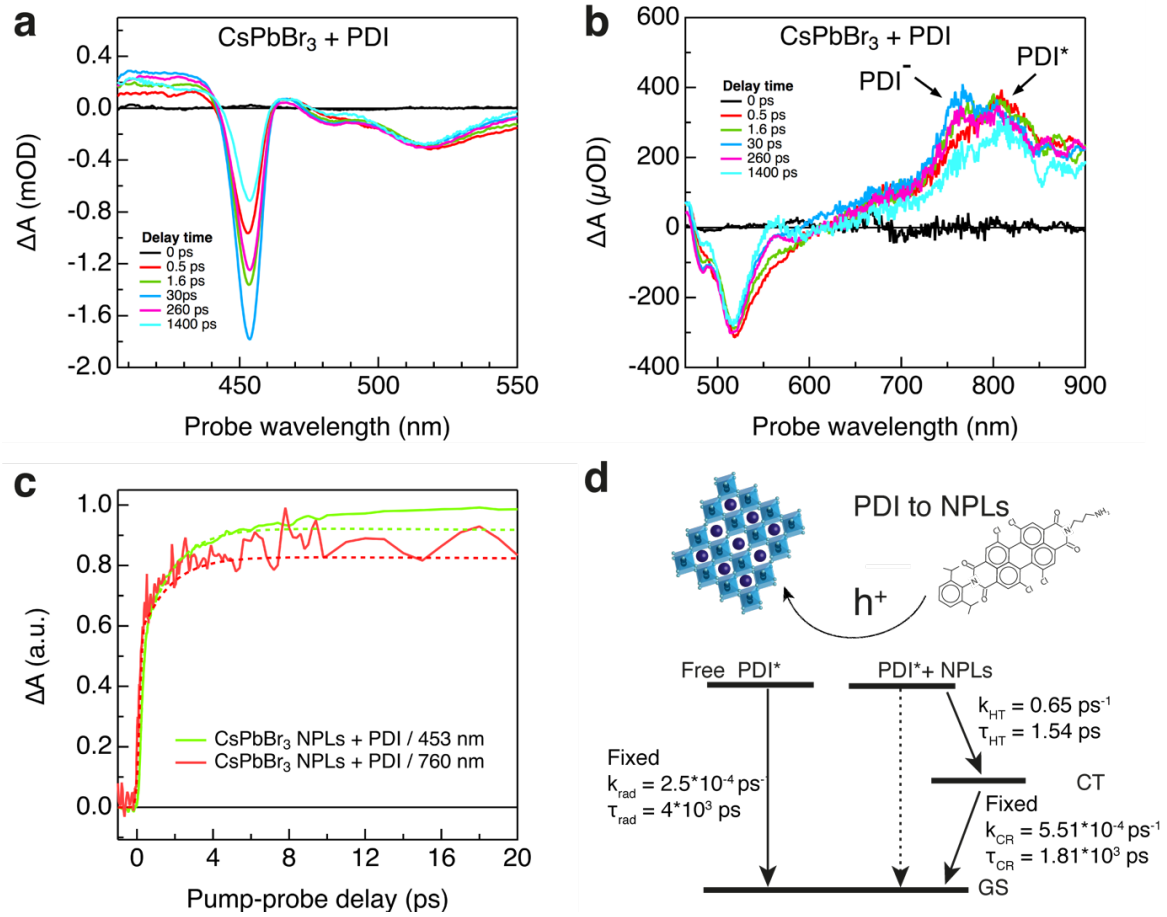

Figure 8.4. Hole Transfer (HT) from PDI* to $CsPbBr_3$ NPLs determined by Transient absorption (TA) upon exciting at 510 nm. a) TA spectrum of $CsPbBr_3$ NPLs + PDI hybrid between 400 nm and 550 nm, showing the growth (up to 30 ps) and subsequent decay of the exciton bleach of the NPLs. **b)** TA spectrum of $CsPbBr_3$ NPLs + PDI hybrid between 465 nm and 900 nm, showing the spectral features of PDI excited state (PDI*) and PDI anion (PDI^-). **c)** Comparison of the temporal dynamics of the exciton bleach of $CsPbBr_3$ NPLs + PDI hybrid exciton bleach (453 nm) and the PDI^- photoinduced absorption growth (~762 nm). Solid lines represent the experimental data while dotted lines are the result of the target global analysis. **d)** Kinetic model used for the target global analysis for hole transfer (HT) from PDI molecules to NPLs in $CsPbBr_3$ NPLs + PDI hybrid. The ratio of attached PDI vs. PDI in solution was fitted to be 4:6 (see Appendix 8 for details).

8.2.5. Photoconductivity: Time-resolved microwave conductivity measurements (TRMC)

The TA measurements presented above clearly show that charge carriers with lifetimes extending into the nanosecond regime are formed, either on exciting the NPLs or the attached PDI molecules. To establish whether the positive charges in the NPLs are actually mobile we have performed photoconductivity measurements using the time-resolved microwave conductivity (TRMC) technique on drop-casted films of the $CsPbBr_3$ NPLs and the $CsPbBr_3$ NPLs + PDI. In these measurements (described in section 2.3),[40] microwaves with a frequency close to 10 GHz are used to probe the change in conductivity upon photoexcitation with a ~2.5 ns laser pulse. TRMC measurements are only sensitive to the presence of free mobile

charge carriers, trapped charges or neutral Coulomb-bound electron-hole pairs (excitons) will not be detected. Importantly, the photoconductivity is a product of the mobility and dissociation yield of excitons. This yield is determined by the exciton binding energy of the material. Due to the large exciton binding energy of 2D $CsPbBr_3$ NPLs (~260 meV)[29] a low and short-lived photoconductivity signals is expected for these materials.[19] The photo-induced conductivity is shown as a function of time in Figures 8.5a and 8.5b upon photoexcitation at 410 nm (exciting the NPLs) and 510 nm (exciting the PDIs), respectively. For $CsPbBr_3$ NPLs + PDI high and long-lived photoconductivity signals are observed, both for excitation of the NPLs (410 nm) and PDI (510 nm). This directly shows that the charge separation process shown by the TA measurements above leads to mobile charge carriers in the NPLs. As evident from the similar amplitude and decays kinetics in Figures 8.5a and 8.5b, the yield and mobility of the charges formed by either hole or electron transfer is similar. For comparison, the TRMC transients for the isolated NPLs and PDIs are also shown in Figures 8.5a and 8.5b, respectively. Photoexcitation of the NPLs without PDI leads to a much lower, short-lived conductivity signal, as expected. Photoexcitation of the pure PDI films yields no measurable conductivity.

As shown in **Chapter 6**,[19] we determined that the photoconductivity of 2D hybrid perovskites decreases at low temperature due to the decrease of the yield of dissociation of excitons by thermal energy. If the charge carriers are efficiently separated by electron transfer to the PDI molecules (exciting at 410 nm), the photoconductivity should increase at low temperature following the increase in mobility due to reduced lattice scattering.[19,41] As shown in Figure 8.5c, the photoconductivity at 93K for $CsPbBr_3$ NPLs + PDI excited at 410 nm is one order of magnitude larger than of the NPLs alone and the lifetime also increases (Appendix Figure A8.13). In addition, in Figure 8.5d it is shown that the maximum photoconductivity gradually increases upon lowering the temperature with the presence of the PDI molecules, while for the NPLs alone the photoconductivity is constant and up to an order of magnitude lower. These measurements unequivocally prove that the charge separation is efficient and mobile free charge carriers (free holes) are formed when the PDI molecules are attached to the NPLs. Compared to other hybrid perovskites,[19,42] the maximum photoconductivity obtained ~0.07 cm^2/Vs at 295K and 0.2 cm^2/Vs at 93K (Appendix Figure A8.14) are 1-2 orders of magnitude lower. Possible reasons for this lower photoconductivity include confinement effects because of the lateral size of the platelets or differences in morphology compared to the crystalline thin films. Nevertheless, the extremely long lifetime up to tens of microseconds (Appendix Figure A8.15), indicates the viability of this concept for application in optoelectronic devices. Long carrier lifetimes result in long diffusion lengths which are essential for efficient charge collection by electrodes in solar cells. The latter requires that also the electrons trapped in the organic part of the materials can be transported over long ranges.

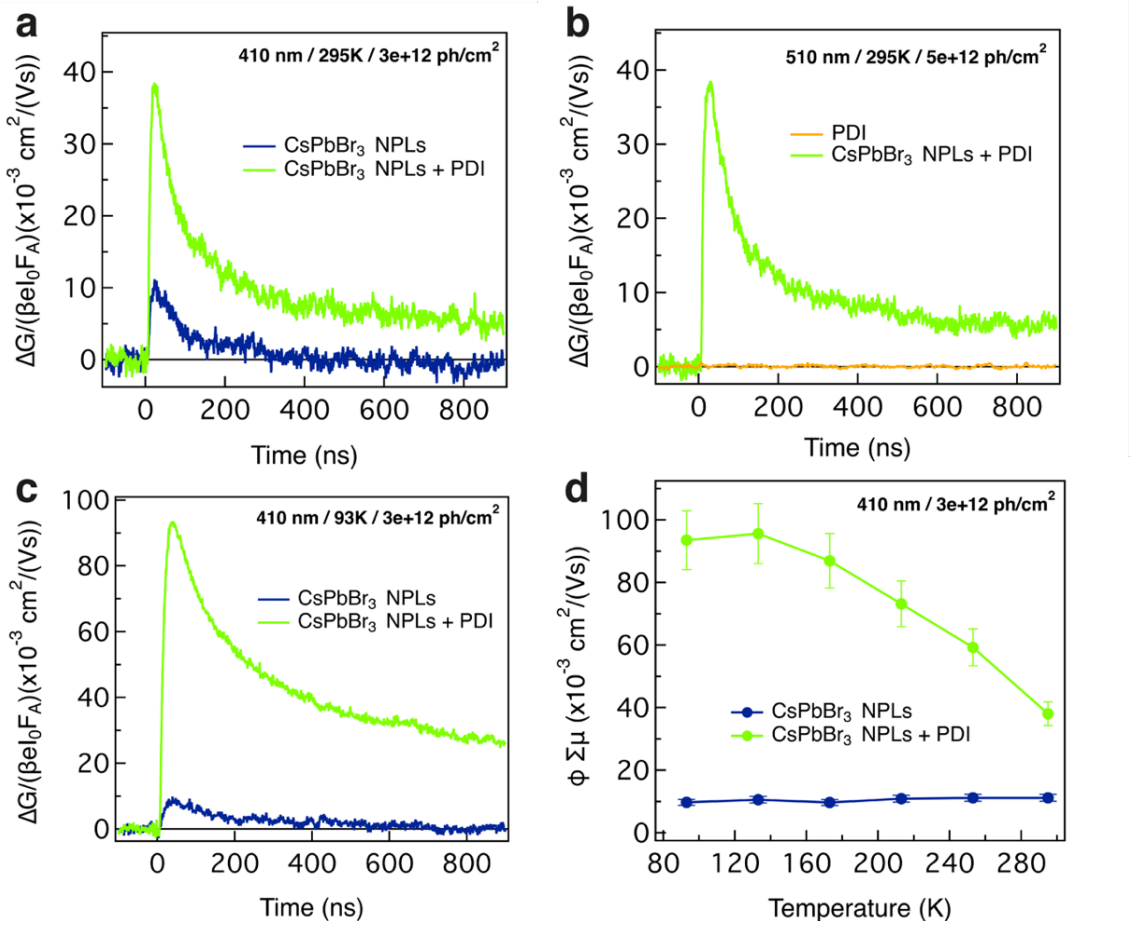

Figure 8.5. Photo-induced conductivity measurements. a) Photo-induced conductivity as a function of time at 295K of $CsPbBr_3$ NPLs and $CsPbBr_3$ NPLs + PDI hybrid on photoexcitation at 410 nm. **b)** Photo-induced conductivity as a function of time at 295K of PDI and $CsPbBr_3$ NPLs + PDI hybrid on photoexcitation at 510 nm. **c)** Photo-induced conductivity as a function of time at 93 K of $CsPbBr_3$ NPLs and $CsPbBr_3$ NPLs + PDI hybrid on photoexcitation at 410 nm. **d)** Maximum photoconductivity as a function of temperature of $CsPbBr_3$ NPLs and $CsPbBr_3$ NPLs + PDI hybrid on photoexcitation at 410 nm (relative SE 10%). The solutions were drop-casted on quartz substrates. The photon fluence is ~3-5 x 10^{12} photons/cm^2.

8.3. Conclusions

In this chapter we have demonstrated that efficient charge carrier separation and long-range free carrier conduction can be achieved in 2D perovskite nanoplatelets by smart synthetic design attaching strong electron acceptors: amine-functionalized perylene diimide (PDI) molecules. By the unique combination of several ultrafast spectroscopy techniques, such as transient absorption, picosecond photoluminescence spectroscopy and microwave conductivity measurements, we have shown that photoexcitation of either the nanoplatelets or the PDIs leads to charge separation, and we have extracted the charge transfer rates for electrons and holes (k_{ET}=0.079 ps^{-1} and k_{HT}=0.65 ps^{-1}). Using microwave photoconductivity measurements, we show that the positive charges that are located in the perovskite nanoplatelets can move around freely and have a long lifetime (tens of microseconds) that is sufficient for applications where charge extraction is required. This opens up a new synergistic

route to materials that are tuned for specific device applications by combining the inorganic perovskite layers with functional organic chromophores. The next step would therefore be the incorporation of conjugated molecules in solid state 2D perovskites where such closely packed organic acceptors support electron transport. This possibility is explored in the following **Chapter 9**.

8.4. Experimental Methods

Synthesis of $CsPbBr_3$ nanoplatelets (NPLs). The colloidal $CsPbBr_3$ nanoplatelets with varying thickness were synthesized according to a previously reported protocol by Bohn et al.[26] The ratio of the Cs-oleate and $PbBr_2$ precursor, and the amount of antisolvent used, determines the thickness of the nanoplatelets. To synthesize $CsPbBr_3$ nanoplatelets with 4 monolayers: 150 μL Cs-oleate precursor (prepared by dissolving 0.1 mmol Cs_2CO_3 in 10 mL oleic acid at 100 °C) was added to 1.2 mL $PbBr_2$ precursor (prepared by dissolving 0.1 mmol $PbBr_2$ in 10 mL toluene in the presence of 100 μL oleic acid and oleylamine at 100 °C) under continuous stirring. After ~5 s, 2 mL acetone was added, which initiated the crystallization of the nanoplatelets. After 1 min, the solution was taken from the stirring plate, and the nanoplatelets were centrifuged at 3500 rpm for 5 min in order to separate the crystalline nanoplatelets from unreacted precursor, and the precipitate was re dispersed in 2 mL hexane. All syntheses were conducted under ambient conditions.

Synthesis of *N*-(2,6-diisopropylphenyl)-*N'*-(Boc-3-aminopropyl)-1,6,7,12-tetrachloroperylene bisimide (2).[34] A mixture of *N*-(2,6-diisopropylphenyl)-1,6,7,12-tetrachloroperylene monoimide monoanhydride **1** (0.50 g, 0.73 mmol, 1 eq.) and *N*-Boc-1,3-propanediamine (0.25 g, 1.45 mmol, 2 eq.) was taken in a round-bottom flask (50 ml) equipped with a water condenser. To this mixture, toluene (14 ml) was added. The combined mixture was refluxed for 18h under argon atmosphere and then cooled to room temperature. Toluene was evaporated under vacuum and the solid residue was washed with water and methanol. Subsequently, the solid residue was dried and chromatographed on silica, with CH_2Cl_2 to afford the desired product (0.52 g, 85%). ^{1}H NMR (400 MHz, $CDCl_3$): δ = 8.74 (s, 2H), 8.71 (s, 2H), 7.51 (t, *J* = 8.1 Hz, 1H), 7.35 (d, *J* = 8.1 Hz, 2H), 5.10 (s, 1H), 4.31 (t, *J* = 6.4 Hz, 2H), 3.19 (m, 2H), 2.77–2.68 (m, 2H), 2.00–1.92 (m, 2H), 1.44 (s, 9H), 1.17 (t, *J* = 6.0 Hz, 12H). ^{13}C NMR (100 MHz, $CDCl_3$): δ = 162.485, 162.294, 155.926, 145.551, 135.584, 135.468, 133.378, 133.116, 131.616, 131.494, 129.988, 129.846, 128.849, 128.738, 124.232, 123.864, 123.339, 123.159, 123.058, 38.212, 37.568, 29.268, 28.514, 28.486, 28.423, 23.994.

Synthesis of *N*-(2,6-diisopropylphenyl)-*N'*-(3-aminopropyl)-1,6,7,12-tetrachloroperylene bisimide (3).[34] Compound **2** (0.50 g, 0.59 mmol) was dissolved in DCM (10 mL). Trifluoroacetic acid (3 mL) was added to this solution. The combined reaction mixture was stirred for 1 h at

room temperature. The progress of the reaction was thoroughly followed by TLC analysis of removed aliquots (10:1 DCM-EtOH). After complete consumption of the starting material, more DCM (100 mL) was added. The resultant solution was washed first with aqueous K_2CO_3 and then with water. The organic phase was collected and concentrated. The crude product was then chromatographed on silica with 10:1 DCM-EtOH mixture to yield the pure product (0.41 g, 93%). ^{1}H NMR (400 MHz, $CDCl_3$): δ = 8.74 (s, 2H), 8.71 (s, 2H), 7.52 (t, *J* = 8.1 Hz, 1H), 7.36 (d, *J* = 8.1 Hz, 2H), 4.34 (t, *J* = 6.8 Hz, 2H), 2.84 (s, 2H), 2.78–2.68 (m, 2H), 1.98–1.91 (m, 2H), 1.18 (t, *J* = 5.6 Hz, 12H). ^{13}C NMR (100 MHz, $CDCl_3$): δ =162.378, 162.298, 145.551, 135.538, 135.468, 135.417, 133.374, 133.056, 131.618, 131.497, 129.986, 129.846, 128.877, 128.663, 124.230, 123.866, 123.329, 123.160, 123.130, 39.224, 38.329, 31.561, 29.266, 23.997. Appendix Figures A8.3, A8.4 and A8.5.

Synthesis of $CsPbBr_3$ nanoplatelets-PDI hybrids. The PDI molecules were attached to the $CsPbBr_3$ nanoplatelets by mixing the $CsPbBr_3$ NPLs with PDI in DCM stock solution under vigorous stirring and mild heating (50°C).

Transmission electron Microscopy (TEM). TEM images were acquired using a JEOL JEM-1400 plus TEM microscope operating at 120 kV. Samples for TEM imaging were prepared by drop-casting a dilute solution of NPLs onto a carbon-coated copper (400-mesh) TEM grid.

Optical Spectroscopy. Samples for optical measurements in solution were prepared by diluting the stock solution of washed NPLs with hexane. Absorption spectra were measured on a double-beam PerkinElmer Lambda 1050 UV/vis spectrometer. For fast-spectroscopy measurements, solution with an optical density 0.1 at 400 nm and ~0.14 at 510 nm (NPLs + PDI hybrid) were prepared (Appendix Figure A8.2). Photoluminescence spectra were recorded on an Edinburgh Instruments FLS980 Spectro-fluorimeter equipped with a 450 W xenon lamp as excitation source and double grating monochromators.

Picosecond Photoluminescence spectroscopy. Time resolved fluorescence measurements are performed using Hamamatsu C5680 streak camera setup. A Chameleon Ultra II (Ti:Saph) oscillator (80 MHz) producing 140 fs pulses combined with a harmonic generator were used to excite the samples. Excitation wavelengths of 400 nm and 480 nm were used when exciting the NPLs and PDI respectively. The overall time resolution of the setup is <10 ps.

Femtosecond Transient Absorption (TA) Spectroscopy. Pump-probe transient absorption measurements were performed using a tunable laser system comprising a Yb:KGW laser source (1028 nm) operating at 5 KHz (2.5 KHz repetition rate) with a pulse duration of 180 fs (PHAROS-SP-06-200, Light Conversion) and an optical parametric amplifier (ORPHEUS-PO15F5HNP1, light conversion). Probe light was generated by continuum generation, focusing a small fraction of the fundamental laser light in a CaF_2 crystal. The two-dimensional

data was acquired with a transient absorption spectrometer (HELIOS, Ultrafast Systems). The samples were placed in a 1 mm path length quartz cuvette and excited at 400 nm and 510 nm with pump fluences of ~3.5x10^{13} ph/(cm^2 pulse) and (~1.9x10^{13} ph/(cm^2 pulse), respectively, and 200 μm probe spot size in quasi parallel pump-probe geometry.

Time-resolved microwave photo-conductivity (TRMC) measurements. Samples for TRMC were prepared by drop-casting on quartz and placed in a sealed resonant cavity inside a helium-filled glovebox. Laser pulsed excitation (repetition rate 10 Hz) at 400 nm and 510 nm in a temperature range of 295K to 93K. The time resolution is limited by the width of the laser pulse (3.5 ns fwhm) and the response time of the system (18 ns). The slow repetition rate of the laser ensures full relaxation of all photo-induced charges to the ground state before the next laser pulse hits the sample.

8.5. References

1. Straus, D. B. & Kagan, C. R. Electrons, Excitons, and Phonons in Two-Dimensional Hybrid Perovskites: Connecting Structural, Optical, and Electronic Properties. *J. Phys. Chem. Lett.* **9**, 1434–1447 (2018).
2. Mao, L., Stoumpos, C. C. & Kanatzidis, M. G. Two-Dimensional Hybrid Halide Perovskites: Principles and Promises. *J. Am. Chem. Soc.* **141**, 1171–1190 (2019).
3. Chen, Y. *et al.* 2D Ruddlesden–Popper Perovskites for Optoelectronics. *Adv. Mater.* **30**, 1–15 (2018).
4. Mao, L. *et al.* Role of Organic Counterion in Lead- and Tin-Based Two-Dimensional Semiconducting Iodide Perovskites and Application in Planar Solar Cells. *Chem. Mater.* **28**, 7781–7792 (2016).
5. Mao, L., Wu, Y., Stoumpos, C. C., Wasielewski, M. R. & Kanatzidis, M. G. White-Light Emission and Structural Distortion in New Corrugated Two-Dimensional Lead Bromide Perovskites. *J. Am. Chem. Soc.* **139**, 5210–5215 (2017).
6. Mao, L. *et al.* Hybrid Dion-Jacobson 2D Lead Iodide Perovskites. *J. Am. Chem. Soc.* **140**, 3775–3783 (2018).
7. Kamminga, M. E. *et al.* Confinement Effects in Low-Dimensional Lead Iodide Perovskite Hybrids. *Chem. Mater.* **28**, 4554–4562 (2016).
8. Soe, C. M. M. *et al.* New Type of 2D Perovskites with Alternating Cations in the Interlayer Space, (C(NH2)3)(CH3NH3)nPbnI3n+1: Structure, Properties, and Photovoltaic Performance. *J. Am. Chem. Soc.* **139**, 16297–16309 (2017).
9. Li, Y. *et al.* Bifunctional Organic Spacers for Formamidinium-Based Hybrid Dion-Jacobson Two-Dimensional Perovskite Solar Cells. *Nano Lett.* **19**, 150–157 (2019).
10. Billing, D. G. & Lemmerer, A. Synthesis, characterization and phase transitions of the inorganic-organic layered perovskite-type hybrids [(CnH2n+1NH 3)2PbI4] (n = 12, 14, 16 and 18). *New J. Chem.* **32**, 1736–1746 (2008).
11. Mitzi, D. B., Wang, S., Feild, C. A., Chess, C. A. & Guloy, A. M. Conducting Layered Organic-inorganic Halides Containing -Oriented Perovskite Sheets. *Science* **267**, 1473–6 (1995).
12. Ishihara, T. Optical properties of PbI-based perovskite structures. *J. Lumin.* **60–61**, 269–274 (1994).
13. Stoumpos, C. C. *et al.* Ruddlesden-Popper Hybrid Lead Iodide Perovskite 2D Homologous Semiconductors. *Chem. Mater.* **28**, 2852–2867 (2016).
14. Mauck, C. M. & Tisdale, W. A. Excitons in 2D Organic–Inorganic Halide Perovskites. *Trends Chem.* **1**, 380–393 (2019).
15. Maheshwari, S., Savenije, T. J., Renaud, N. & Grozema, F. C. Computational Design of Two-Dimensional Perovskites with Functional Organic Cations. *J. Phys. Chem. C* **122**, 17118–17122 (2018).
16. Muljarov, E. A., Tikhodeev, S. G., Gippius, N. A. & Ishihara, T. Excitons in self-organized semiconductor/insulator superlattices: PbI-based perovskite compounds. *Phys. Rev. B* **51**, 14370–14378 (1995).
17. Tanaka, K. & Kondo, T. Bandgap and exciton binding energies in lead-iodide-based natural quantum-well

crystals. *Sci. Technol. Adv. Mater.* **4**, 599–604 (2003).
18. Blancon, J. C. *et al.* Scaling law for excitons in 2D perovskite quantum wells. *Nat. Commun.* **9**, 1–10 (2018).
19. Gélvez-Rueda, M. C. *et al.* Interconversion between Free Charges and Bound Excitons in 2D Hybrid Lead Halide Perovskites. *J. Phys. Chem. C* **121**, 26566–26574 (2017).
20. Mitzi, D. B., Chondroudis, K. & Kagan, C. R. Design, Structure, and Optical Properties of Organic−Inorganic Perovskites Containing an Oligothiophene Chromophore. *Inorg. Chem.* **38**, 6246–6256 (1999).
21. Passarelli, J. V. *et al.* Enhanced Out-of-Plane Conductivity and Photovoltaic Performance in n = 1 Layered Perovskites through Organic Cation Design. *J. Am. Chem. Soc.* **140**, 7313–7323 (2018).
22. Van Gompel, W. T. M. *et al.* Towards 2D layered hybrid perovskites with enhanced functionality: Introducing charge-transfer complexes: Via self-assembly. *Chem. Commun.* **55**, 2481–2484 (2019).
23. Mitzi, D. B., Medeiros, D. R. & Malenfant, P. R. L. Intercalated organic-inorganic perovskites stabilized by fluoroaryl-aryl interactions. *Inorg. Chem.* **41**, 2134–2145 (2002).
24. Evans, H. A. *et al.* Mono- and Mixed-Valence Tetrathiafulvalene Semiconductors (TTF)BiI4 and (TTF)4BiI6 with 1D and 0D Bismuth-Iodide Networks. *Inorg. Chem.* **56**, 395–401 (2017).
25. Kamminga, M. E. *et al.* Electronic mobility and crystal structures of 2,5-dimethylanilinium triiodide and tin-based organic-inorganic hybrid compounds. *J. Solid State Chem.* **270**, 593–600 (2019).
26. Bohn, B. J. *et al.* Boosting Tunable Blue Luminescence of Halide Perovskite Nanoplatelets through Postsynthetic Surface Trap Repair. *Nano Lett.* **18**, 5231–5238 (2018).
27. Weidman, M. C., Seitz, M., Stranks, S. D. & Tisdale, W. A. Highly Tunable Colloidal Perovskite Nanoplatelets through Variable Cation, Metal, and Halide Composition. *ACS Nano* **10**, 7830–7839 (2016).
28. Bekenstein, Y., Koscher, B. A., Eaton, S. W., Yang, P. & Alivisatos, A. P. Highly Luminescent Colloidal Nanoplates of Perovskite Cesium Lead Halide and Their Oriented Assemblies. *J. Am. Chem. Soc.* **137**, 16008–16011 (2015).
29. Li, Q. & Lian, T. Ultrafast Charge Separation in Two-Dimensional CsPbBr 3 Perovskite Nanoplatelets. *J. Phys. Chem. Lett.* **10**, 566–573 (2019).
30. Bodnarchuk, M. I. *et al.* Rationalizing and Controlling the Surface Structure and Electronic Passivation of Cesium Lead Halide Nanocrystals. *ACS Energy Lett.* **4**, 63–74 (2019).
31. Huang, C., Barlow, S. & Marder, S. R. Perylene-3,4,9,10-tetracarboxylic acid diimides: Synthesis, physical properties, and use in organic electronics. *J. Org. Chem.* **76**, 2386–2407 (2011).
32. Würthner, F. & Stolte, M. Naphthalene and perylene diimides for organic transistors. *Chem. Commun.* **47**, 5109–5115 (2011).
33. Liu, Z., Wu, Y., Zhang, Q. & Gao, X. Non-fullerene small molecule acceptors based on perylene diimides. *J. Mater. Chem. A* **4**, 17604–17622 (2016).
34. Dubey, R. K., Westerveld, N., Sudhölter, E. J. R., Grozema, F. C. & Jager, W. F. Novel derivatives of 1,6,7,12-tetrachloroperylene-3,4,9,10-tetracarboxylic acid: Synthesis, electrochemical and optical properties. *Org. Chem. Front.* **3**, 1481–1492 (2016).
35. Snellenburg, J. J., Laptenok, S. P., Seger, R., Mullen, K. M. & van Stokkum, I. H. M. Glotaran : A Java-based graphical user interface for the R package TIMP. *J. Stat. Softw.* **49**, 1–2 (2012).
36. Van Stokkum, I. H. M., Larsen, D. S. & Van Grondelle, R. Global and target analysis of time-resolved spectra. *Biochim. Biophys. Acta - Bioenerg.* **1657**, 82–104 (2004).
37. Gorczak, N. *et al.* Different mechanisms for hole and electron transfer along identical molecular bridges: The importance of the initial state delocalization. *J. Phys. Chem. A* **118**, 3891–3898 (2014).
38. Aulin, Y. V. *et al.* Morphology-Independent Efficient Singlet Exciton Fission in Perylene Diimide Thin Films. *Chempluschem* **83**, 230–238 (2018).
39. Grampp, G. The Marcus Inverted Region from Theory to Experiment. *Angew. Chemie Int. Ed. English* **32**, 691–693 (1993).
40. Savenije, T. J., Ferguson, A. J., Kopidakis, N. & Rumbles, G. Revealing the dynamics of charge carriers in polymer:fullerene blends using photoinduced time-resolved microwave conductivity. *J. Phys. Chem. C* **117**, 24085–24103 (2013).
41. Gélvez-Rueda, M. C. *et al.* Effect of cation rotation on charge dynamics in hybrid lead halide perovskites. *J. Phys. Chem. C* **120**, 16577–16585 (2016).
42. Guo, D., Caselli, V. M., Hutter, E. M. & Savenije, T. J. Comparing the calculated fermi level splitting with the open-circuit voltage in various perovskite cells. *ACS Energy Lett.* **4**, 855–860 (2019).

Chapter 9

Incorporating Organic Charge-Transfer Complexes in Solid State 2D perovskites

This chapter describes efforts to achieve charge separation in solid state 2D perovskites. We have replaced non-functional organic cations with functional donor molecules modified by attachment of a ammonium alkyl chain (carbazole-C_n, pyrene-C_n). While it is possible to successfully prepare thin films that incorporate the conjugated molecules in 2D perovskite structures, the optoelectronic properties, in particular the charge carrier transport, was still exclusively limited to the inorganic octahedral layers. An additional possibility that is considered is the introduction of different combinations of functional organic charge-transfer complexes. It is shown, that in (Pyrene-C_4:TCNQ)PbI_4 additional optical features appear that match with absorption of the organic charge-transfer complex states. Using TRMC and fs-TA it is shown that excitation of these charge-transfer transitions (at ~575 nm) leads to long-lived conductivity of free holes in the inorganic $[PbI_6]^-$ layers. This conductivity signal is one order of magnitude lower than the conductivity of direct photogenerated carriers in the inorganic octahedral layers, indicating a relatively low efficiency. Despite this low efficiency, these experiments illustrate that it is possible to achieve enhanced charge separation in solid state 2D perovskites by engineering the properties of the organic layer. A further step would be to improve the coupling between the functional organic cation and the inorganic octahedral layer in order to increase the efficiency of charge separation.

This chapter is based on:

Roald Herckens, Wouter T.M. van Gompel, Wenya Song, María C. Gélvez-Rueda, Arthur Maufort, Bart Ruttens, Jan D'Haen, Ferdinand C. Grozema, Tom Aernouts, Laurence Lutsen and Dirk Vanderzande. Multi-layered hybrid perovskites templated with carbazole derivatives: optical properties, enhanced moisture stability and solar cell characteristics. *J. Mater. Chem. A., 2018, 6, 22899-22908.*

María C. Gélvez-Rueda, Wouter T.M. van Gompel, Roald Herckens, Laurence Lutsen, Dirk Vanderzande and Ferdinand C. Grozema. Incorporating CT complexes in 2D perovskites. *Submitted for publication.*

9.1. Introduction

Two-dimensional hybrid organic-inorganic perovskites are tunable semiconductor materials formed by layers of inorganic metal-halide octahedrals $[MX_6]^{2-}$ separated by large organic cations $[A]^+$.[1,2] So far, the role of the organic cation in these materials has been defined by the use of non-functional organic molecules such as *n*-alkylammonium, phenylethylammonium, benzylammonium and guanidinium.[2] As a result, the organic cations act as a non-conductive barrier layer while the charge carrier transport occurs exclusively in the inorganic metal-halide octahedral layers.[3–5] In the inorganic layers, the charge carriers experience a strong dimensional and dielectric confinement (exciton binding energies of ~200 to 400 meV)[4,6,7] that results in formation of stable excitons at room temperature. This is desirable for light-light-emitting diodes (LEDs) and nano-lasers but limits the application of 2D hybrid perovskites in opto-electronic devices where free charge carriers are required (such as solar cells, photo-detectors and photo-catalysts). An alternative to generate free charge carriers is to introduce functional organic compounds that can either accept or donate electrons to dissociate the excitons.[8] It has been theoretically shown that introducing strong functional organic molecules in 2D hybrid perovskites results in localization of the electronic orbitals/bands in both the inorganic octahedral layer and the organic molecules. In principle, this could result in charge separation and subsequent transport of free charge carriers.[8] Experimentally, few 2D hybrid perovskites have been synthesized using functional organic cations such as conjugated organic molecules,[9,10] chromophores[11,12] and charge-transfer complexes.[13] However, in none of these previous studies the charge or energy transfer characteristics in these materials were considered. The use of bulky functional organic compounds can also result in formation of perovskite structures of even lower dimensionality (1D, 0D) with low connectivity of the inorganic octahedral layers.[14,15] The properties and processes that leads either 2D or lower-dimensional 1D, 0D structures in the solid state is not clear and is a current challenge for the synthesis of functional 2D hybrid perovskites.[14–17] The optoelectronic properties of 1D "perovskitoids" materials synthesized when attempting to introduce bulky functional cations are discussed in **Chapter 10**.

In this chapter we discuss the photophysical properties of a series thin films in which ammonium-functionalized conjugated molecules are introduced. We have studied two electron donating moieties containing carbazole-alkylammonium (carbazole-C_n) and pyrene-alkylammonium (pyrene-C_n) groups. In addition, we consider the optoelectronic properties when a full charge-transfer (CT) complexes of these donor molecules combined with the strong electron acceptors tetracyanoquinodimethane (TCNQ) and tetracyanobenzene (TCNB). Steady state optical absorption measurements show that for the donor-only compounds the lowest energy transition in the spectrum consists of the excitonic peak at

~530 nm, similar to the spectra for the 2D materials with nonfunctionalized organic cations presented in **Chapter 7**. Only the 2D perovskite (Pyrene-C_4:TCNQ)$_2$$PbI_4$ exhibits absorption features from the organic charge-transfer (CT) complex: two broad charge-transfer bands, one between 550 nm and 750 nm and another one at ~800 nm.[18] Using laser-induced time-resolved microwave conductivity measurements (TRMC) we show that, indeed, in most of the 2D perovskites considered here the charge carriers are still confined to the inorganic layers (low photoconductivity signal and fast decay kinetics). The only exception is (Pyrene-C_4:TCNQ)$_2$$PbI_4$. The photoconductivity observed for (Pyrene-C_4:TCNQ)$_2$$PbI_4$ on photoexciting at the excitonic peak maximum (525 nm) exhibits two distinct decay times. First, a fast initial decay corresponding to the recombination of charge carriers in the inorganic layers, followed by a long-lived signal (~1-4 µs). Direct photoexcitation of the high-energy CT state at 575 nm leads to distinct charge carrier dynamics where the fast initial decay is missing only the long-living component remains. This long-lived photoconductivity signal is attributed to conduction of free holes in the inorganic $[PbI_6]^-$ octahedral layers generated by transfer of holes on photoexcitation of the (Pyrene-C_4:TCNQ) CT complex. In order to confirm this hole-transfer process, we performed fs-TA spectroscopy measurements showing that excitation of the 2D inorganic framework at the excitonic peak (~520 nm) results in distinct absorption features due to the (Pyrene-C_4:TCNQ) CT complex characterized by a bleach between 550 nm and 750 nm. In addition, excitation of the CT complex at 575 nm leads to characteristic photoinduced absorption from the (Pyrene-C_4:TCNQ) CT complex, apart from a bleach of the exciton transition at 530 nm. This bleach is caused by hole transfer into the inorganic layer, while the electrons stay localized on the TCNQ molecules. The kinetics of the exciton bleach signal at ~530 nm has a long lifetime, all the way up to the maximum time-range of our TA setup (2.7 ns). This matches with the long-lived photoconductivity signal observed in TRMC experiments. This shows, for the first time, that inclusion of charge transfer complexes in between the inorganic layers in 2D perovskites can result in charge transfer and long-lived free carrier conduction in solid state 2D hybrid perovskites. The timescale of free charge carrier conduction (1 to 4 µs) is in the relevant range for application in opto-electronic devices.

9.2. Results and Discussion

9.2.1. Synthesis and characterization of 2D perovskites thin-films

Thin-films of 2D perovskites were prepared by spin-coating and subsequent annealing of the films as described in section 9.4.[17] The functionalized donor molecules introduced in between the $[PbI_6]^{2-}$ octahedrals are: carbazole-alkylammonium (Carbazol-C_n), pyrene-alkylammonium (pyrene-C_n) and charge-transfer (CT) complexes of these donor molecules with strong

electron acceptors tetracyanoquinodimethane (TCNQ) and tetracyanobenzene (TCNB). These donor molecules or charge-transfer complexes have been extensively studied in the organic electronics field due to their photoconductive properties, ferroelectricity and low temperature superconductivity.[18–24]

The 2D perovskites considered in this chapter are: (Carbazole-C_4)$_2$$PbI_4$, (Carbazole-$C_5$)$_2$$PbI_4$, (Pyrene-$C_4$)$_2$$PbI_4$ and the CT-complex-based: (Carbazole-C_5:TCNQ)$_2$$PbI_4$, (Carbazole-$C_5$:TCNB)$_2$$PbI_4$, (Pyrene-$C_4$:TCNQ)$_2$$PbI_4$ and (Pyrene-C_4:TCNB)$_2$$PbI_4$. The formation of 2D perovskite structures was confirmed for all these materials by x-ray diffraction characterized by the (0 0 *l)* reflections characteristic of a preferential growth along the (1 1 0) direction parallel to the substrate (Appendix Figure A9.1). As it has only been possible to obtain these 2D perovskites in solution-deposited thin films, no full crystal structure has been resolved. A schematic representation of the structure of (Pyrene-C_4:TCNQ)$_2$$PbI_4$ is shown in Figure 9.1a.

To determine the ground state optical properties we have performed steady-state optical absorption measurements which show that all materials exhibit the typical absorption features of 2D perovskites: an excitonic transition at ~490-520 nm and a continuous band absorption at higher energies (see Figure 9.1b and Appendix Figure A9.2).[25–27] Interestingly, apart from the excitonic features typical of 2D perovskites, the compound (Pyrene-C_4:TCNQ)$_2$$PbI_4$ exhibits absorption features deriving from the (Pyrene-C_4:TCNQ) CT complex:[18] two broad charge transfer bands, one between ~550 nm and 700 nm and another one at ~850 nm (see Figure 9.1b). These additional features are clearly seen in Figure 9.1b in which the steady-state absorption of the control compounds (pyrene-C_4)$_2$$PbI_4$, and the non-perovskite (pyrene-C_4:TCNQ) CT-complex are also plotted for comparison. Apart from the additional absorption features, the main excitonic transition in (Pyrene-C_4:TCNQ)$_2$$PbI_4$ (~520 nm) is red-shifted compared to (Pyrene-C_4)$_2$$PbI_4$ (490 nm). This shift is likely to be caused by structural rearrangements in the inorganic octahedral layers to accommodate the bulky TCNQ molecules. Red-shifts in 2D perovskites have been associated with a decrease of the geometric distortion of the inorganic $[PbI_4]^{2-}$ octahedrals.[26]

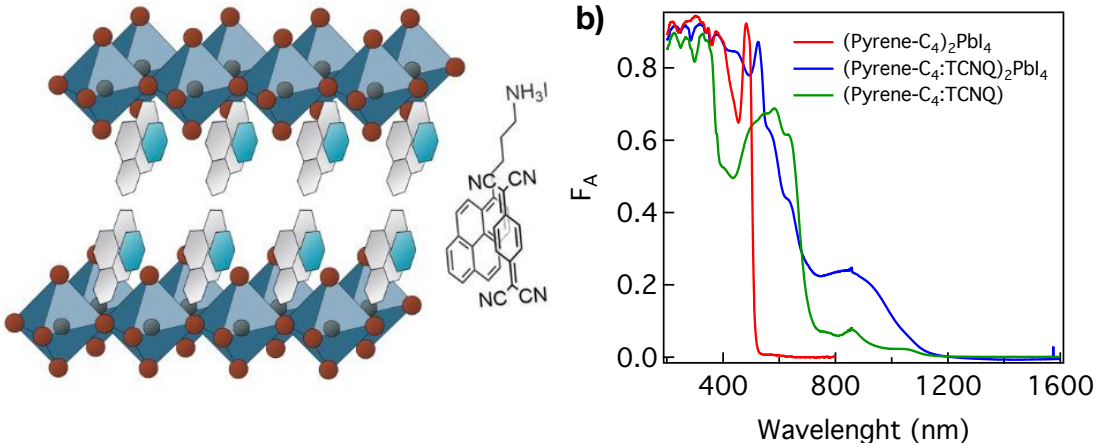

Figure 9.1. Crystal structure and steady-state absorption. a) schematic representation of the charge-transfer complex (Pyrene-C_4:TCNQ) in between the inorganic octahedral layers in (Pyrene-C_4:TCNQ)PbI_4 (taken with permission from Van Gompel *et al.*[17]). **b)** Steady state absorption of (Pyrene- C_4)$_2PbI_4$, (TCNQ:Pyrene-C_4)$_2PbI_4$ and (TCNQ:Pyrene-C_4) CT organic salt.

9.2.2. Photoconductivity time-resolved microwave-conductivity measurements

The photoinduced conductivity obtained from TRMC measurements for all the 2D perovskites with 'functional' organic chromophores discussed above on excitation at maximum of the excitonic transition (~490 nm to 530 nm) are shown in Figure 9.2 and Appendix Figure A9.3. For most compounds the photoinduced conductivity exhibits the typical features observed for 2D perovskites with non-functional organic cations that were discussed in **Chapter 6**: a photoinduced conductivity maximum, in terms of the product of mobility and yield of dissociation ($\mu\,\phi = \Delta G/\beta e I_0 F_A$), of the order of 0.01 cm^2/Vs characterized by a very fast decay caused by the high exciton binding energy that the charge carriers experience in the inorganic octahedral layer (see Figure 9.2a for (Pyrene-C_4)$_2PbI_4$ and Appendix Figure A9.3). In contrast, the photoconductivity of (Pyrene-C_4:TCNQ)$_2PbI_4$ shown in Figure 9.2b is of similar magnitude directly after the excitation pulse but exhibits two distinct decay times. First, a fast initial decay is seen that matches with the decay of electron-hole pairs in the inorganic octahedral layers similar to the decay in 2D perovskites with non-functional chromophores. Second, this decay is followed by a long-lived tail ~1 to 4 µs (see Appendix Figure A9.4) that is still present at high photon intensities, indicating that it is not significantly reduced by second order recombination effects as observed for (Pyrene-C_4)$_2PbI_4$ in Figure 9.2a.

In order to clarify the origin of the long-lived signal we performed additional experiments photoexciting (Pyrene-C_4:TCNQ)$_2PbI_4$ at a series of wavelengths: 335 nm to excite the pyrene molecules; 525 nm to excite the excitonic peak, and 575 nm, 600 nm, 630 nm to directly excite the CT states in the organic CT complex. In Figure 9.2c it is shown that excitation at energies above the CT state (335 nm and 525nm) results in a combination of two very different decay

times as described above. In contrast, direct excitation of the CT state (575 nm, 600 nm, 630 nm) leads to a photoconductivity signal that is an order of magnitude smaller but with only a slow decay that matches the slow decay-component observed after excitation at higher energies (335 nm and 525 nm). As a control measurement, the photoinduced conductivity of the (Pyrene-C_4:TCNQ) CT complex (without the perovskite component) is shown in Figure 9.2d. As can be seen, both the maximum photoconductivity and the carrier lifetime are much smaller than in (Pyrene-C_4:TCNQ)$_2$$PbI_4$. This is in agreement with typical photoconductivity measurements on organic materials where low short-lived transient are common.[28] From these measurements we conclude that the long-lived photoconductivity component in (Pyrene-C_4:TCNQ)$_2$$PbI_4$ is not from transport in the organic charge-transfer complex but due to enhanced charge separation leading to long-lived positive charges in the inorganic $[PbI_6]^-$ octahedral layers. This suggests that by excitation of the Pyrene-C_4:TCNQ) CT complex is possible to transfer holes to the inorganic octahedral layer while the electrons stay localized in the TCNQ molecules. It should be noted that the overall yield of these charge pairs separated across the built-in organic-inorganic interface is rather low and can only be observed because of the high sensitivity of the TRMC cavity.

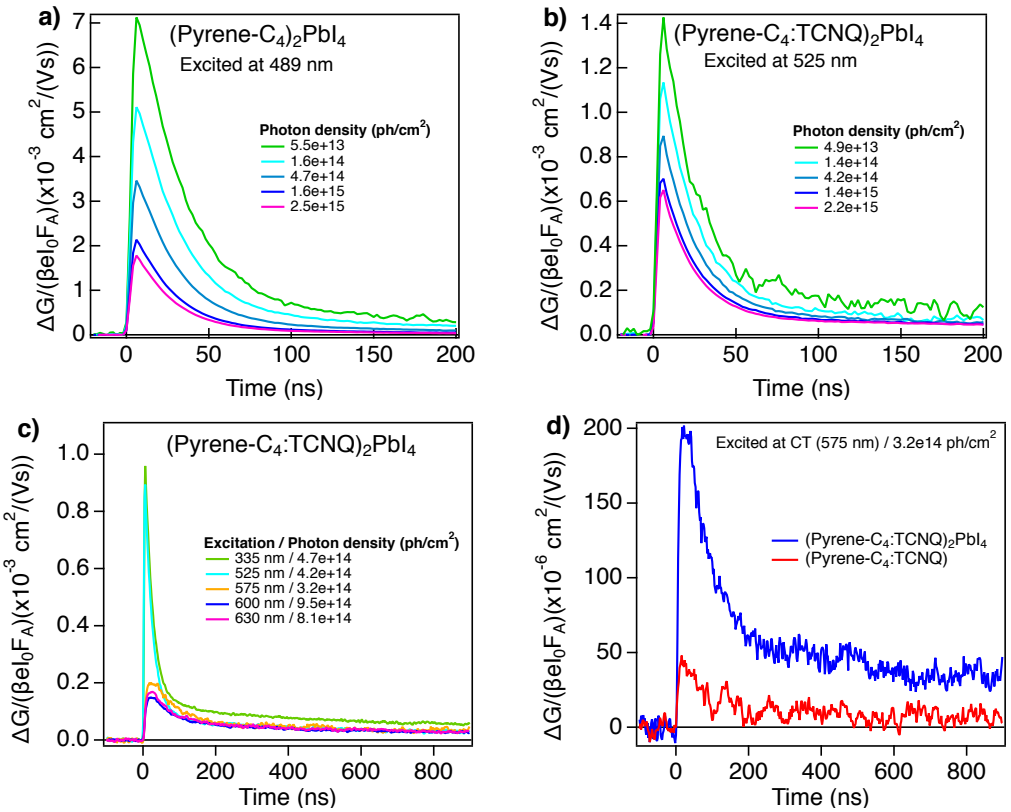

Figure 9. 2. Photoconductivity TRMC experiments. a, b) Photoconductivity as a function of the photon intensity for (a) (Pyrene- C_4)$_2$$PbI_4$ and (b) (TCNQ:Pyrene- C_4)$_2$$PbI_4$. **c)** Photoconductivity of (TCNQ:Pyrene-C_4)$_2$$PbI_4$ at different excitation wavelengths, photon intensity ~4x10^{14} ph/cm^2. **d)** Comparison between the photoconductivity of (TCNQ:Pyrene- C_4)$_2$$PbI_4$ and (TCNQ:Pyrene-C_4) CT organic salt exciting the CT state at 575 nm, photon intensity ~4x10^{14} ph/cm^2.

As demonstrated in **Chapter 6**, the fraction of absorbed photons that leads to the generation of 'free' charges in the 2D perovskites with non-functional organic components strongly depends on temperature, as it is related to the exciton binding energy. In order to characterize the formation of long-lived charges in (Pyrene-C_4:TCNQ)$_2$$PbI_4$ in more detail we have performed photoconductivity TRMC experiments as a function of temperature. The results of these measurements are shown in Figure 9.3. In Figure 9.3a the maximum conductivity of (Pyrene-C_4:TCNQ)$_2$$PbI_4$ (at the end of the excitation pulse) is plotted as a function of temperature. For excitation in both the excitonic peak and the CT state, the maximum photoconductivity decreases by roughly a factor of two on decreasing the temperature from 350 K to 90 K. As shown in Figure 9.3b and 9.3c, the carrier lifetime increases slightly over this same temperature range, especially the slow decay component. This indicates that the long-lived charges formed by charge separation between the inorganic layer and the CT complex layer recombine slower at low temperature. In **Chapter 8** it was shown that if free charge carriers were generated efficiently by charge separation between the functional organic cation and the inorganic perovskites, an increase of photoconductivity at low temperature is observed. This is a result of a higher charge mobility at low temperatures. This is not the case for (Pyrene-C_4:TCNQ)$_2$$PbI_4$ where the photoconductivity increases somewhat at higher temperature. We attribute this to more efficient dissociation of charges by charge transfer from the (Pyrene-C_4:TCNQ) CT complex. As it is known that the charge transfer process in (Pyrene-C_4:TCNQ) is extremely fast[18] we investigated the changes in excited state absorption by femtosecond transient absorption (fs-TA) measurements.

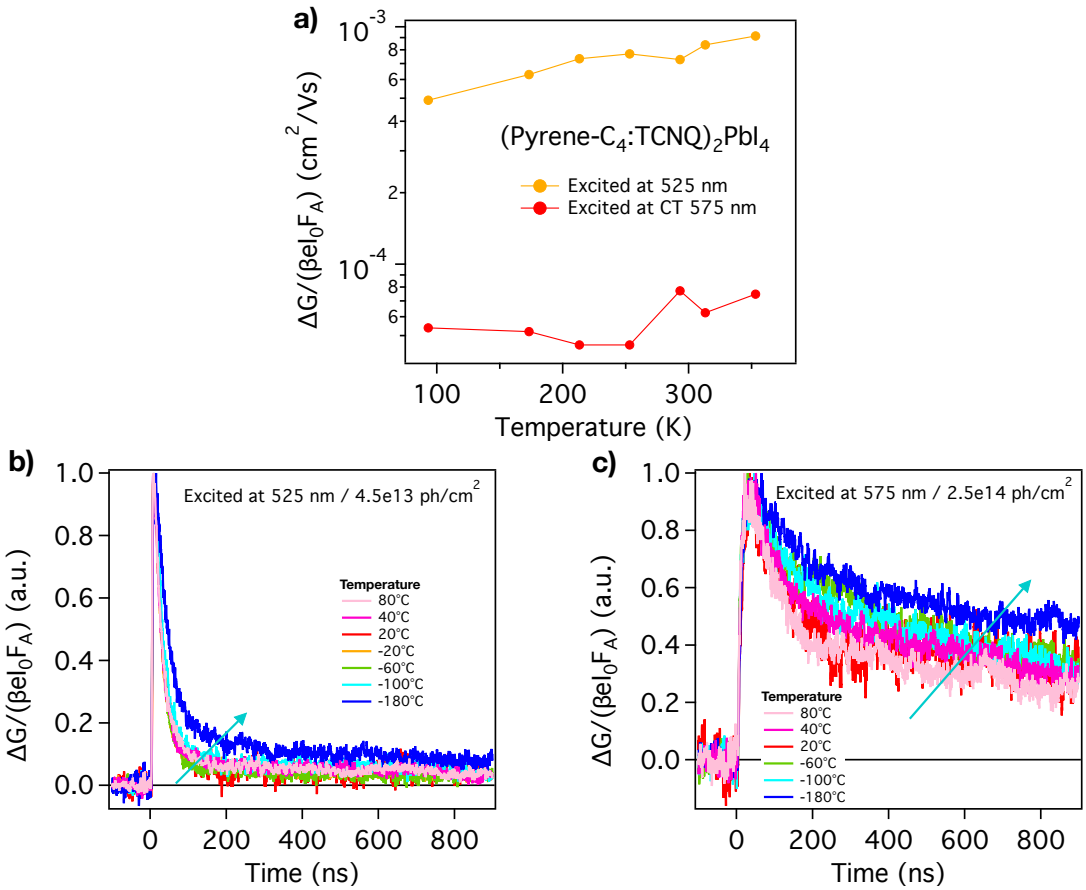

Figure 9.3. Photoconductivity TRMC experiments as a function of temperature. a) Photoconductivity of (Pyrene-C_4:TCNQ)$_2$PbI$_4$ excited at 525 nm and 575 nm. **b, c)** Normalized photoconductivity transients exciting at the excitonic peak (525 nm) and CT state (575 nm). Photon intensities 4x10^{14} ph/cm^2.

9.2.3. Femtosecond transient absorption (fs-TA)

In order to establish the processes that occur on photoexcitation of the 2D perovskites with functional organic components femto-second transient absorption (fs-TA) measurements have been performed to study the changes in absorption due to photoexcitation with a fast time resolution (~180 fs). Using this technique it should be possible to detect the fast formation of positive charges in the inorganic octahedral layers and the possible formation of TCNQ anions due to the electron localization in these molecules. These measurements were performed at various excitation wavelengths correspondent to the excitonic peak (~490 nm and 520 nm) and charge-transfer state (~575 nm) of (Pyrene-C_4:TCNQ)$_2$PbI$_4$. The absorbed photon intensities used were ~1.3x10^{13} ph/(cm^2 pulse), ~8.0x10^{12} ph/(cm^2 pulse) and ~1.7x10^{13} ph/(cm^2 pulse), respectively. The transient changes in the optical absorption spectrum due to photoexcitation were detected using short broadband pulses obtained from continuum generation in a thick sapphire crystal (490 nm to 800 nm). It is important to highlight that, as these measurements were performed in thin films, the TA absorption signals were corrected by reflection, which has a marked effect on the TA-spectra (section 9.4).

The TA spectra of (Pyrene-C_4)$_2$$PbI_4$ photoexcited at 490 nm and (Pyrene-C_4:TCNQ)$_2$$PbI_4$ photoexcited at 520 nm are shown in Figure 9.4a (full TA-spectra are given in Appendix Figure A9.5). For both compounds, the TA spectra exhibit the typical features observed non-functional 2D perovskites as described in literature: a bleach of the exciton band (XB) at ~495 nm for (Pyrene-C_4)$_2$$PbI_4$ and ~530 nm for (Pyrene-C_4:TCNQ)$_2$$PbI_4$, corresponding to band-edge filling by photogenerated excitons. An additional photoinduced absorption (PA) is observed around the main XB feature which has been attributed to band gap renormalization (BGR) due to exciton-exciton interactions.[29] Interestingly, the TA spectra of (Pyrene-C_4:TCNQ)$_2$$PbI_4$ exhibits an additional bleach between 550 nm and 750 nm shown in the inset in Figure 9.4a. This bleach peaks at ~ 575 nm and ~650 nm and is in agreement with the ground-state absorption spectra of this material shown in Figure 9.1b. As discussed above, these features correspond to the absorption of the (Pyrene-C_4:TCNQ) CT complex. This clearly indicates that photoexcitation of the inorganic layers in the materials also leads to a bleach signal due the organic part, resulting from either charge or energy transfer.

To distinguish between charge and energy transfer we have also performed fs-TA experiments photoexciting the materials at 575 nm, where the absorption of the (Pyrene-C_4:TCNQ) CT complex is centered. In Figure 9.4b the TA spectra for (Pyrene-C_4:TCNQ)$_2$$PbI_4$ on photoexcitation at 520 nm and 575 nm and for the (Pyrene-C_4:TCNQ) CT complex photoexciting at 575 nm are shown. Full TA spectra are shown in Appendix Figure A9.6. From Figure 9.4b it is clear that for both excitation wavelengths the TA spectrum for (Pyrene-C_4:TCNQ) CT complex closely matches with the ground state absorption spectrum for this material shown in Figure 9.1b. The TA spectra for (Pyrene-C_4:TCNQ)$_2$$PbI_4$ also show the bleach between 550 and 750 nm, both for excitation as 520 nm and 575 nm, even though the relative intensities of the different peaks differs slightly from the shape observed for (Pyrene-C_4:TCNQ). This difference may arise from structural reorganization of the (Pyrene-C_4:TCNQ) complexes in between the inorganic octahedral. Nevertheless, it is clear that a bleach feature is observed between 550 nm to 750 nm in Figure 9.4 for both excitation wavelengths, which is related to the high-energy charge-transfer bands of the (Pyrene-C_4:TCNQ) CT complex.[18] Notably, in Figure 9.4b it is also seen that when (Pyrene-C_4:TCNQ)$_2$$PbI_4$ is excited at 575 nm (CT states from complex) there is fast appearing feature in the TA spectrum that correspond with the features seen for the exciton in the inorganic layers, centered around 530 nm. This clearly indicates that the initially created excited state does not remain localized on the organic CT complex. Since excited state energy transfer is energetically not possible, the likely explanation is that hole transfer to the inorganic PbI_4 framework occurs, while the electron stays localized on TCNQ. Consistent with the photoconductivity TRMC measurements, the magnitude of this feature is one to two order of magnitudes lower than when the main XB is

directly excited. This supports the conclusion that this charge transfer process is rather inefficient compared to the direct generation of excitons in the inorganic layer.

In order to gain insight in the populations of the different species as a function of time, the kinetics of the XB of (Pyrene-C_4)$_2$$PbI_4$ photoexciting at 490 nm and of (Pyrene-C_4:TCNQ)$_2$$PbI_4$ photoexciting at both 520 nm and 575 nm are shown in Figure 9.4c. The decay observed for (Pyrene-C_4)$_2$$PbI_4$ corresponds to the intrinsic decay of excitons localized in the inorganic octahedral layer. In (Pyrene-C_4:TCNQ)$_2$$PbI_4$ the initial decay of the XB feature on photoexciting at 520 nm is considerably faster than in (Pyrene-C_4)$_2$$PbI_4$. This may be related to overlapping with the decay of the excited states in the (Pyrene-C_4:TCNQ) CT complex which also absorb at 520 nm (time decay time of ~290 ps[18]). The kinetics of the XB of (Pyrene-C_4:TCNQ)$_2$$PbI_4$ excited at the CT state (575 nm) exhibit a similarly fast initial decay followed by a much longer component (>2.7 ns, Appendix Figure A9.7). The latter is attributed to the presence of long-lived charge pairs, with an electron on TCNQ and a mobile hole in the inorganic layers giving rise to the long-lived photoconductivity signal in the TRMC measurements.

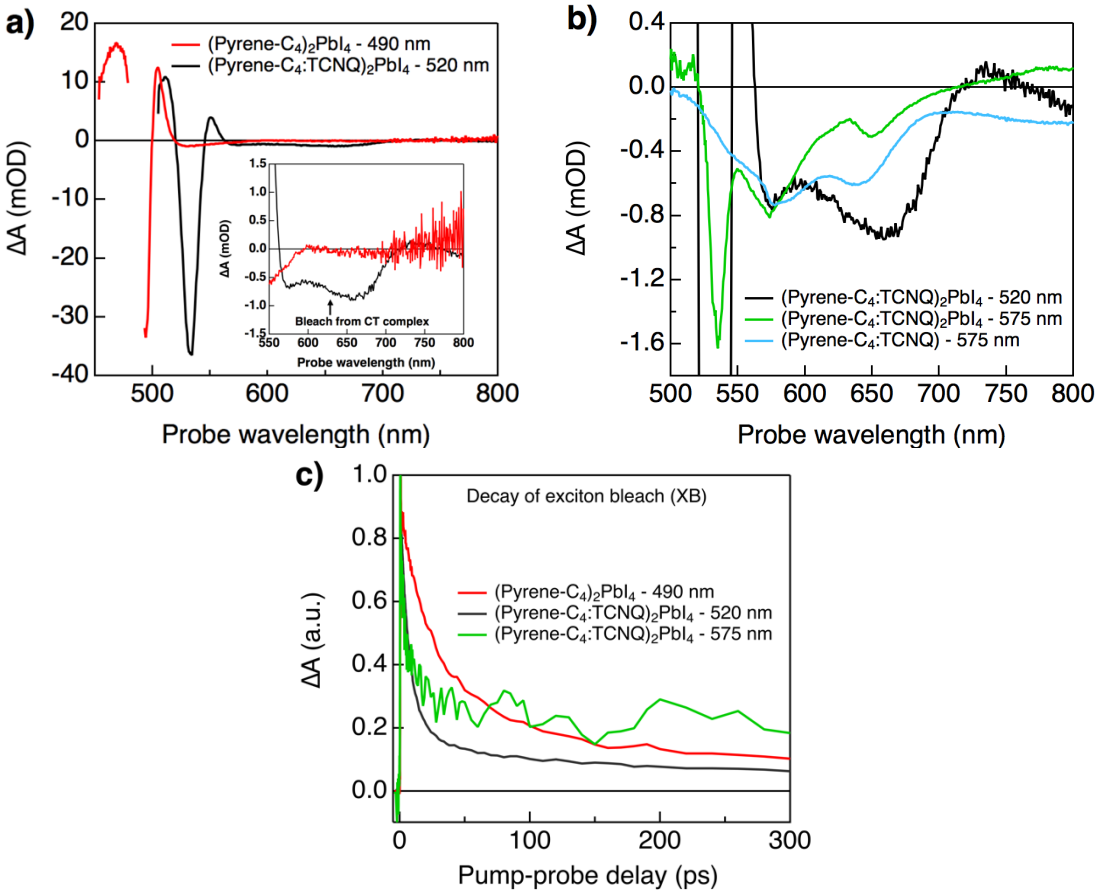

Figure 9.4. Femtosecond transient absorption experiments. a) TA spectra of (Pyrene-C_4)$_2$$PbI_4$ and (Pyrene-C_4:TCNQ)$_2$$PbI_4$ excited at the excitonic peak (490 nm and 520 nm, respectively). **b)** TA spectra of (Pyrene-C_4:TCNQ)$_2$$PbI_4$ and (Pyrene-C_4:TCNQ) CT salt excited at the CT state (575 nm). **c)** Temporal decay kinetics of the exciton bleach (XB) of (Pyrene-C_4)$_2$$PbI_4$ (~500 nm) and (Pyrene-C_4:TCNQ)$_2$$PbI_4$ (~530 nm) exciting at the excitonic peak (490 nm and 520 nm, respectively) and the CT state (575 nm). Photon fluence ~1x10^{13} photon/cm^2 pulse.

9.3. Conclusions

In this chapter we have determined the excited state dynamics of 2D perovskites in which functional organic molecules have been introduced between the inorganic octahedral layers. In most compounds studied the charge carrier dynamics exhibit a similar behavior as in 2D perovskites with non-functional organic cations. This means that the excitons are still confined to the inorganic octahedral layer, showing that the electron donation nature of the moieties used (carbozole, pyrene) is not strong enough to influence the electronic properties. An exception is found for (Pyrene-C_4:TCNQ)$_2$$PbI_4$, we determined that introducing charge-transfer complexes in between the inorganic layers leads to features in the optical absorption spectra that show the presence of the CT complexes through their characteristic CT transition. The combination of the strong CT complex between pyrene molecules and TCNQ to form (Pyrene-C_4:TCNQ)$_2$$PbI_4$ leads to a markedly different decay of charge carriers in photoconductivity TRMC experiments and in TA measurements. We confirm, by direct excitation of the CT state at 575 nm, that there is hole transfer to the inorganic octahedral layers shown by the bleach of the excitons at ~530 nm, together with long-lived hole conduction in the inorganic layers shown by a combination of TA and TRMC experiments. The yield of this charge transfer process is rather low, however, this chapter reveals that charge separation can occur in solid state 2D perovskites. In order to improve the yield of the charge separation process a redesign of the organic molecules is necessary, for instance decreasing the average distance between the organic chromophores and the inorganic layers. Nevertheless, the results presented here do illustrate the potential of including organic molecules with specific functionality in the 2D perovskites to optimize their properties for specific applications.

9.4. Methods

Thin-films deposition.[17] Stoichiometric amounts of the respective precursors Carbazole-C_n, Pyrene-C_n, TCNQ, TCNB, and PbI_2 were dissolved in dry dimethylformamide (DMF) at 50°C-70°C for 15 min under constant stirring. The resulting clear solutions were filtered through a syringe filter (0.45 mm pore size). Quartz substrates were cleaned through consecutive sonication steps in a series of solvents (detergent water, deionized water, acetone, isopropanol) for 15 min each, followed by a UV ozone treatment for 15 min. Films for optical measurements, TRMC and XRD analysis were deposited on quartz substrates using spin coating in a glovebox with nitrogen atmosphere (<0.1 ppm O2, < 0.1 ppm H2O) at 2000 rpm, 2000 rpm s^{-1} for 20 s. Subsequently the films were post-annealed at temperatures between 110°C to 150°C. X-ray diffraction measurements were performed at room temperature in ambient atmosphere on a Bruker D8 Discover diffractometer with CuKα radiation.

Time-resolved microwave photo-conductivity (TRMC) measurements. Samples for TRMC were placed in a sealed resonant cavity inside a helium-filled glovebox. Laser pulsed excitation (repetition rate 10 Hz) at 335 nm, 490 nm, 525 nm, 575 nm and 630 nm in a temperature range of 363K to 93K. The photon intensities were varied between $5x10^{13}$ ph/cm^2 to $3x10^{15}$ ph/cm^2 which corresponds to concentrations of ~$6x10^{17}$ cm^{-3} to ~$2x10^{19}$ cm^{-3}. The time resolution is limited by the width of the laser pulse (3.5 ns fwhm) and the response time of the system (18 ns).

Femtosecond Transient Absorption (TA) Spectroscopy. Pump-probe transient absorption measurements were performed using a tunable laser system comprising a Yb:KGW laser source (1028 nm) operating at 5 KHz (2.5 KHz repetition rate) with a pulse duration of 180 fs (PHAROS-SP-06-200, Light Conversion) and an optical parametric amplifier (ORPHEUS-PO15F5HNP1, light conversion). Probe light was generated by continuum generation, focusing a small fraction of the fundamental laser light in a thick sapphire crystal (~490 nm to 800 nm). The two-dimensional data was acquired with a transient absorption spectrometer (HELIOS, Ultrafast Systems). The thin-films were placed in an air-tight sample holder loaded inside a helium-filled glovebox and excited at 490 nm, 520 nm and 575 nm with pump fluences of ~$1.3x10^{13}$ ph/(cm^2 pulse), ~$8.0x10^{12}$ ph/(cm^2 pulse) and ~$1.7x10^{13}$ ph/(cm^2 pulse), respectively. The system is in quasi parallel pump-probe geometry with a 200 μm probe spot size. The measurements were performed in transmission and reflection and corrected with equation 1.

$$\Delta A = \log_{10}\left(10^{-\Delta A^*} + \frac{F_R}{1-F_A}\left(10^{-\Delta R} - 10^{-\Delta A^*}\right)\right)$$

9.5. References

1. Straus, D. B. & Kagan, C. R. Electrons, Excitons, and Phonons in Two-Dimensional Hybrid Perovskites: Connecting Structural, Optical, and Electronic Properties. *J. Phys. Chem. Lett.* **9**, 1434–1447 (2018).
2. Mao, L., Stoumpos, C. C. & Kanatzidis, M. G. Two-Dimensional Hybrid Halide Perovskites: Principles and Promises. *J. Am. Chem. Soc.* **141**, 1171–1190 (2019).
3. Ishihara, T. Optical properties of PbI-based perovskite structures. *J. Lumin.* **60–61**, 269–274 (1994).
4. Muljarov, E. A., Tikhodeev, S. G., Gippius, N. A. & Ishihara, T. Excitons in self-organized semiconductor/insulator superlattices: PbI-based perovskite compounds. *Phys. Rev. B* **51**, 14370–14378 (1995).
5. Mitzi, D. B., Wang, S., Feild, C. A., Chess, C. A. & Guloy, A. M. Conducting Layered Organic-inorganic Halides Containing -Oriented Perovskite Sheets. *Science* **267**, 1473–6 (1995).
6. Gélvez-Rueda, M. C. *et al.* Interconversion between Free Charges and Bound Excitons in 2D Hybrid Lead Halide Perovskites. *J. Phys. Chem. C* **121**, 26566–26574 (2017).
7. Blancon, J. C. *et al.* Scaling law for excitons in 2D perovskite quantum wells. *Nat. Commun.* **9**, 1–10 (2018).
8. Maheshwari, S., Savenije, T. J., Renaud, N. & Grozema, F. C. Computational Design of Two-Dimensional Perovskites with Functional Organic Cations. *J. Phys. Chem. C* **122**, 17118–17122 (2018).
9. Passarelli, J. V. *et al.* Enhanced Out-of-Plane Conductivity and Photovoltaic Performance in n = 1 Layered Perovskites through Organic Cation Design. *J. Am. Chem. Soc.* **140**, 7313–7323 (2018).

10. Mitzi, D. B., Chondroudis, K. & Kagan, C. R. Design, Structure, and Optical Properties of Organic−Inorganic Perovskites Containing an Oligothiophene Chromophore. *Inorg. Chem.* **38**, 6246–6256 (1999).
11. Evans, H. A. *et al.* Mono- and Mixed-Valence Tetrathiafulvalene Semiconductors (TTF)BiI4 and (TTF)4BiI6 with 1D and 0D Bismuth-Iodide Networks. *Inorg. Chem.* **56**, 395–401 (2017).
12. Evans, H. A. *et al.* (TTF)Pb 2 I 5 : A Radical Cation-Stabilized Hybrid Lead Iodide with Synergistic Optoelectronic Signatures . *Chem. Mater.* **28**, 3607–3611 (2016).
13. Mitzi, D. B., Medeiros, D. R. & Malenfant, P. R. L. Intercalated organic-inorganic perovskites stabilized by fluoroaryl-aryl interactions. *Inorg. Chem.* **41**, 2134–2145 (2002).
14. Saparov, B. & Mitzi, D. B. Organic-Inorganic Perovskites: Structural Versatility for Functional Materials Design. *Chem. Rev.* **116**, 4558–4596 (2016).
15. Kamminga, M. E. *et al.* Electronic mobility and crystal structures of 2,5-dimethylanilinium triiodide and tin-based organic-inorganic hybrid compounds. *J. Solid State Chem.* **270**, 593–600 (2019).
16. Herckens, R. *et al.* Multi-layered hybrid perovskites templated with carbazole derivatives: Optical properties, enhanced moisture stability and solar cell characteristics. *J. Mater. Chem. A* **6**, 22899–22908 (2018).
17. Van Gompel, W. T. M. *et al.* Towards 2D layered hybrid perovskites with enhanced functionality: Introducing charge-transfer complexes: Via self-assembly. *Chem. Commun.* **55**, 2481–2484 (2019).
18. Dillon, R. J. & Bardeen, C. J. Time-resolved studies of charge recombination in the pyrene/TCNQ charge-transfer crystal: Evidence for tunneling. *J. Phys. Chem. A* **116**, 5145–5150 (2012).
19. Grazulevicius, J. V, Strohriegl, P., Pielichowski, J. & Pielichowski, K. Carbazole-containing polymers: synthesis, properties and applications. *Prog. Polym. Sci.* **28**, 1297–1353 (2003).
20. Dillon, R. J. & Bardeen, C. J. The Effects of Photochemical and Mechanical Damage on the Excited State Dynamics of Charge-Transfer Molecular Crystals Composed of Tetracyanobenzene and Aromatic Donor Molecules. *J. Phys. Chem. A* **115**, 1627–1633 (2011).
21. Jiang, H. *et al.* Tuning of the degree of charge transfer and the electronic properties in organic binary compounds by crystal engineering: a perspective. *J. Mater. Chem. C* **6**, 1884–1902 (2018).
22. Goetz, K. P. *et al.* Charge-transfer complexes: new perspectives on an old class of compounds. *J. Mater. Chem. C* **2**, 3065–3076 (2014).
23. Zhang, J., Xu, W., Sheng, P., Zhao, G. & Zhu, D. Organic Donor–Acceptor Complexes as Novel Organic Semiconductors. *Acc. Chem. Res.* **50**, 1654–1662 (2017).
24. Sun, L. *et al.* Molecular cocrystals: design, charge-transfer and optoelectronic functionality. *Phys. Chem. Chem. Phys.* **20**, 6009–6023 (2018).
25. Cao, D. H., Stoumpos, C. C., Farha, O. K., Hupp, J. T. & Kanatzidis, M. G. 2D Homologous Perovskites as Light-Absorbing Materials for Solar Cell Applications. *J. Am. Chem. Soc.* **137**, 7843–7850 (2015).
26. Mao, L. *et al.* Role of Organic Counterion in Lead- and Tin-Based Two-Dimensional Semiconducting Iodide Perovskites and Application in Planar Solar Cells. *Chem. Mater.* **28**, 7781–7792 (2016).
27. Stoumpos, C. C. *et al.* Ruddlesden-Popper Hybrid Lead Iodide Perovskite 2D Homologous Semiconductors. *Chem. Mater.* **28**, 2852–2867 (2016).
28. Savenije, T. J., Ferguson, A. J., Kopidakis, N. & Rumbles, G. Revealing the dynamics of charge carriers in polymer:fullerene blends using photoinduced time-resolved microwave conductivity. *J. Phys. Chem. C* **117**, 24085–24103 (2013).
29. Li, Q. & Lian, T. Ultrafast Charge Separation in Two-Dimensional CsPbBr 3 Perovskite Nanoplatelets. *J. Phys. Chem. Lett.* **10**, 566–573 (2019).

Chapter 10
Bulky Organic Cations Leading to One-Dimensional (1D) Perovskites

In this chapter we describe how regular perovskite synthesis conditions with functionalized organic chromophores can lead to new perovskite-like materials with lower dimensionality. We investigated the synthesis mechanisms of these new one-dimensional (1D) hybrid halide perovskites, their crystal structure, and their opto-electronic properties. Although the mechanism that leads to 1D structures remains unclear, we found that is strongly dependent on synthesis conditions such as temperature, precursors, inert environment, and reaction time. In addition, we determined by combined DFT calculations and TRMC experiments that the charge transport properties are strongly influenced by the crystal structure and the interaction between the organic chromophores and the inorganic layer. The charge mobility in 1D perovskites is consistently lower (by one to two orders of magnitude) than for 2D or 3D perovskite due to the strong confinement. The transport can be dominated by either the organic chromophore or the inorganic lattice in different 1D perovskite materials. In addition, the possible coupling of the inorganic and organic component, for example by enhanced generation of free charge carriers and lifetime compared to the pure organic compounds, is a promising feature that warrants investigation.

This chapter is based on:

Machteld E. Kamminga, María C. Gélvez-Rueda, Sudeep Maheshwari, Irene S. van Droffelaar, Jacob Baas, Graeme R. Blake, Ferdinand C. Grozema and Thomas T.M. Palstra. Electronic Mobility and Crystal Structures of 2,5-dimethylanilinium Triiodide and Tin-based Organic-Inorganic Hybrid Compounds. *J. Solid State Chem., 2019, 270, 593-600.*

Nadège Marchal, Wouter van Gompel, María C. Gélvez-Rueda, Koen Vandewal, Kristof van Hecke, Hans-Gerd Boyen, Bert Conings, Roald Herckens, Sudeep Maheshwari, Laurence Lutsen, Claudio Quarti, Ferdinand C. Grozema, Dirk Vanderzande and David Beljonne. Lead-Halide Perovskites Meet Donor-Acceptor Charge-Transfer Complexes. *Chem. Mater., 2019, 31, 17, 6880-6888.*

10.1. Introduction

Low-dimensional halide hybrid perovskites are of high interest due to their improved stability and chemical flexibility compared to their three-dimensional (3D) perovskite counterparts.[1] Introducing organic cations of varying sizes, together with modified synthesis methods, has resulted in the possibility of engineering hybrid perovskites with a full range of dimensionalities: 3D to 2D, 1D, 0D.[2] As described in previous chapters, a current challenge is to design 2D perovskites with functionalized organic chromophores for specific device applications. Nevertheless, when bulky organic chromophores are introduced it is hard to predict *a priori* whether a stable 2D structure will be formed.[3] Crystallization in a 2D geometry depends very subtly on the interactions between the organic chromophores, but also on the processing conditions.[3,4] It is known that crystalline materials with a lower dimensionality (1D or 0D) can be obtained.[5,6] These materials feature different optical and electronic properties that suggest an inefficient "back-transfer charge separation" due to the poor connectivity of the inorganic octahedral layers.[5,6] However, it is not clear how the synthesis conditions results in these structures or the effect on the charge transport properties in order to apply these materials in opto-electronic devices.

In this chapter we describe the synthesis conditions and a time-resolved microwave conductivity (TRMC) study of the charge carrier transport properties of two different hybrid perovskites in which the use of bulky organic chromophores results in 1D structures. In the first case, 2,5-dimethylaniline (2,5-DMA) was introduced with the idea that this aromatic molecule can have a beneficial effect on the crystal growth and an enhance the charge carrier mobility due to possible π-π stacking. Depending on the synthesis protocol, either a 2,5-DMASnI_3 with a rhombohedral structure consisting of 1D chains of SnI_6^- octahedra or a triiodide monoclinic salt 2,5-DMAI_3 was obtained. In both compounds the charge transport is limited to the 1D SnI_6^- ribbons or I_3^- units resulting in very low mobilities (one to two orders of magnitude lower than for 3D and 2D perovskites). In the second case, a known organic charge transfer complex (CTC), pyrene-TCNQ,[7] was intercalated in between the inorganic $[PbI_6]^{4-}$ framework with the aim of achieving improved charge separation. This approach resulted in either a 2D structure on thin films[4] as described in **chapter 9**, or single crystals of a novel 1D hybrid composed of wires of face-sharing $[PbI_6]^{4-}$ octahedra separated by bilayers containing the pyrene-TCNQ complex anchored via an ammonium alkyl chain located exclusively on the pyrene molecule, $(PyrC_4NH_3)PbI_3 \cdot (TCNQ)$. A combined theoretical and experimental study reveals that (i) the inorganic lattice mostly acts as a template for the local organization of the organic conjugated molecules, and (ii) the close energy resonance between the occupied levels on the inorganic and organic parts improves photoinduced charge generation. This was shown by combining pulse radiolysis(PR) TRMC and

photoconductivity TRMC experiments. In the PR-TRMC experiments the charge mobility in the 1D hybrid and purely organic CTC pyrene-TCNQ complex were found to be similarly low (one to two order of magnitude lower than for 3D, 2D perovskites). In contrast the photoconductivity of the 1D hybrid is 5 times larger. This is attributed to a higher yield of photogenerated free charge carriers in the 1D hybrid which can be understood in terms of the localization of holes in the inorganic lattice. These two studies demonstrate the subtle interactions that affect the crystallization of hybrid perovskites and their effect on charge transport properties.

10.2. Results and Discussion

10.2.1. Synthesis, characterization and electronic properties of 2,5-DMASnI$_3$

2,5-DMASnI$_3$ single crystals were obtained by adding equimolar amounts of 2,5-DMAI and SnI$_2$ at 120°C in a solution of HI and H_3PO_2.[8] It is worth highlighting that modifying the synthesis conditions mixing SnI$_2$ in HI with methanol and 2,5-DMA at ambient conditions resulted in the synthesis of 2,5-DMAI$_3$ single crystals without tin in the structure.[9] The formation of this new salt illustrates how sensitive the crystallization process is. We found, by a rigorous analysis of the experimental synthesis conditions, that the formation of 2,5-DMASnI$_3$ strongly depends on the presence of high temperature, inert environment and H_3PO_2. In this section we will focus on the crystals structure of 2,5-DMASnI$_3$ and its electronic properties. In Figure 10.1 the crystal structure of 2,5-DMASnI$_3$ is shown. The structural refinement using polar space group *R3c*, rhombohedral setting is listed in Appendix Table A10.1. While 2,5-DMASnI$_3$ has the same structural formula as the cubic ABX$_3$ hybrid perovskite structure, the structural pattern is very different. As shown in Figure 10.1(a), the structure of 2,5-DMASnI$_3$ consists of SnI_6^- octahedra that form 1D chains along the [111] direction. This 1D nature is also apparent from the needle shape of the crystals (longest direction is [111]). As shown in Figure 10.1(b), the SnI_6^- octahedra are strongly distorted. The three I-Sn-I angles deviate from a perfect 180°, with values of 171.019(1)°, 166.243(1)° and 154.760(1)°, respectively. We believe that this distortion is caused by the interaction of the NH_3^+ group with the iodide pairs and indirectly affect the distortion of the SnI_6^- units via the Sn_2^+ lone pair. In Figure 10.1(c) a single inorganic ribbon is shown. Each ribbon consists of three strips of edge sharing SnI_6^- octahedra that are connected to each other by corner sharing. This bonding pattern is rather unusual and it has not been described for any tin-based hybrid structure reported in the literature. The organic molecules form a herringbone-type structure. Therefore, no π-π stacking is observed. The ammonium groups are oriented towards the inorganic ribbons, to create hydrogen bonding. If charge transfer would occur through both the organic and inorganic components, we believe that the polar nature of the

structure (space group *R3c*) might aid this process. However, we also argue that the band gap is quite large as the crystals are yellow in color. Moreover, the dimensionality and connectivity of the metal halide octahedra plays a significant role in determining the band gap of the compound.[10] The 1D nature and presence of edge-sharing SnI_6^- octahedra in 2,5-DMASnI_3 then contribute to the large band gap. As shown below, from DFT calculations we estimate the band gap to be 2.37 eV. For 2,5-DMAI_3 the structure is also 1D with I_3^- units (see Appendix Figure A10.1 and Table A10.1). The black color of 2,5-DMAI_3 suggest a lower band gap. However, the band gap cannot be extracted from the absorption spectra of the single crystals due to an extended tale (see Appendix Figure A10.2). In addition, no emission was detected.

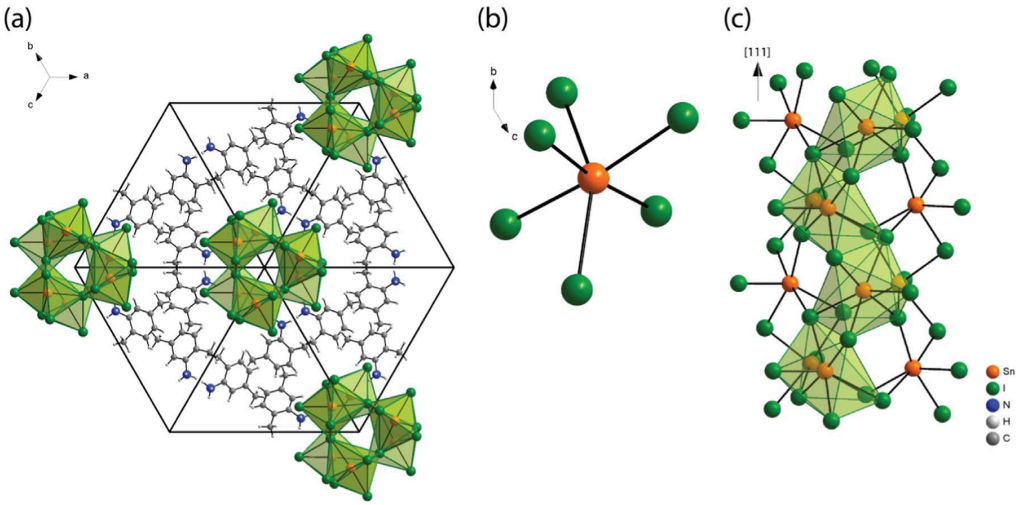

Figure 10.1. Crystal structure of 2,5-DMASnI3. a) Polyhedral model of the full crystal structure, projected along the [111] direction. **b)** A single SnI_6^- octahedron, showing severe distortion. **c)** A single inorganic ribbon. Shading represents the strip of SnI_6^- octahedra that share edges. The total inorganic ribbon consists of three such edge-sharing strips that are connected through corner-sharing.

In order to clarify the electronic properties of these materials, we performed DFT band structure calculations. The results are shown in Figure10.2 and Table 10.1. In summary, we found that 2,5-DMASnI_3 has an indirect band gap, while 2,5-DMAI_3 has a direct band gap at the D point. Moreover, the effective mass of the charge carriers in these materials is one to two orders of magnitude larger than for 3D and 2D perovskites.[11–13] This is in agreement with our experimental TRMC results shown below in Figure 10.3. We attribute these lower charge carrier mobilities to the distortions in the structure that reduce the dimensionality of charge transport to the 1D fragments (1D corner- and edge-sharing of SnI_6^- octahedra in 2,5-DMASnI_3 and I_3^- units in 2,5-DMAI_3). This is supported by the charge densities at the top of the valence band and the bottom of the conduction band for both compounds shown in Figure 10.2. It is clear that for both 2,5-DMASnI_3 and 2,5-DMAI_3, these bands are restricted to a one-dimensional region of the crystal: for 2,5-DMASnI_3 located at the Sn and I atoms (SnI_6^- ribbons) and for 2,5-DMAI3, in the I_3^- ions units. In addition, the effective mass of the hole is lower for 2,5-DMASnI_3 as the valence band orbitals are more coupled than in 2,5-DMAI_3, in which the

valence band is formed by decoupled orbitals of iodide. The effective mass of the electron for both compounds are in the same order of magnitude due to the high coupling of the conduction band seen in Figure 10.2.(a,d). The low dimensionality is also reflected by the band curvature in different directions. For directions perpendicular to the 1D pathway, the effective mass is much larger than along these pathways.

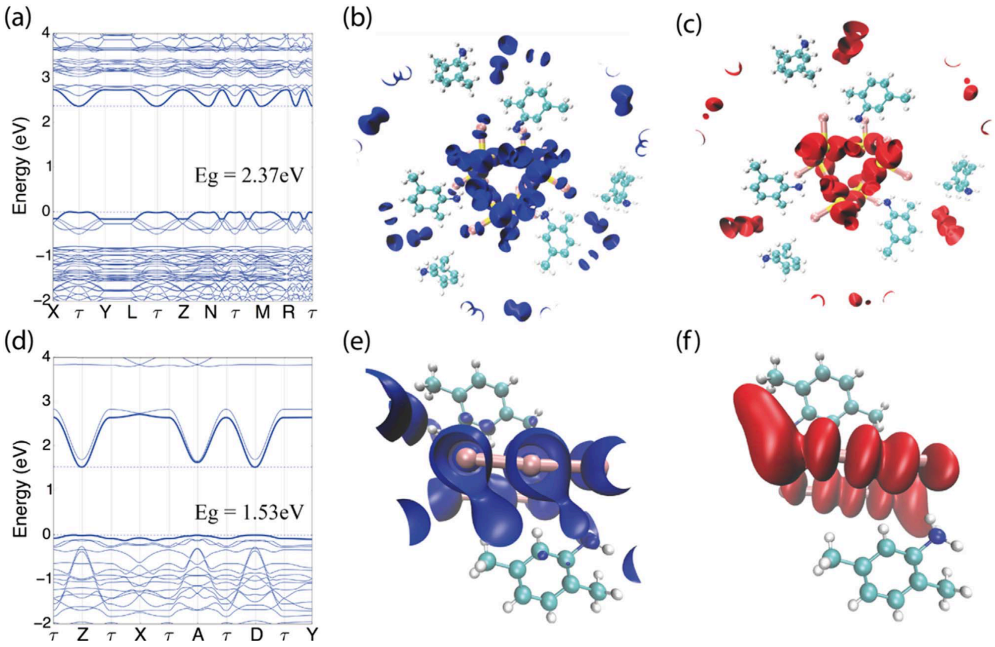

Figure 10.2. DFT band structure calculations and charge densities at the bottom of the conduction band and the top of the valence band. a, b, c) 2,5-DMASnI$_3$. **d, e, f)** 2,5-DMAI$_3$.

Table 10.1. Band gap, band width and effective mass of charge carriers for 2,5-DMASnI$_3$ and 2,5-DMAI$_3$. The effective masses for 2,5-DMASnI$_3$ are calculated at the Gamma point (0, 0, 0) between X and Y. The effective masses for 2,5-DMAI$_3$ are calculated at the D point (0.5, 0, 0.5).

	2,5-DMASnI$_3$	**2,5-DMAI$_3$**
Band gap (eV)	2.37	1.53
HOMO (eV)	0.16	0.12
LUMO (eV)	0.37	1.19
Hole effective mass (m*)	0.12	60.88
Electron effective mass (m*)	1.06	0.59

To study the mobility and recombination mechanisms of charge carriers in both 2,5-DMASnI$_3$ and 2,5-DMAI$_3$, we performed pulse-radiolysis microwave conductivity measurements (PR-TRMC)[14] shown in Figure 10.3. In Figure 10.3a it is shown that the mobilities for both compounds are very similar at room temperature, 0.006 cm^2 V^{-1}s^{-1} and 0.004 cm^2 V^{-1}s^{-1}, respectively, and are the same within the margin of error. Moreover, the values do not change significantly on increasing or decreasing the temperature. Notably, these values are three orders of magnitude lower than the values measured with the same technique for three-dimensional hybrid perovskites shown in **Chapter 3** and **Chapter 4**, such as MAPbI$_3$ (~1.5 cm^2 V^{-1}s^{-}),[12,13] and two orders of magnitude lower than for two-dimensional hybrids, such as

BA_2PbI_4 shown in **Chapter 6** (~0.3 $cm^2 V^{-1}s^{-1}$).[11] These results are in agreement with our DFT calculations. We believe that these lower mobilities are caused by the large distortions in the structure of the materials that introduce 1D structural fragments.

The radiation-induced conductivity is shown as a function of time in Figure 10.3b. The lifetime of the charge carriers is very long for both compounds: approximately 400 µs for 2,5-$DMASnI_3$ and 1 ms for 2,5-$DMAI_3$. These long lifetimes are caused by the nature of the experiment and the structure of the materials. In PR-TRMC measurements, irradiation with an electron pulse leads ionization events with an average of 20 eV.[14] Consequently, the electrons and holes are generated at a relatively large distance from each other. Considering the structure of both compounds, the electrons and holes are most likely generated in different 1D ribbons of SnI_6^- octahedra in 2,5-$DMASnI_3$ and in different I_3^- units in 2,5-$DMAI_3$. The 1D confinement and large effective masses in the perpendicular direction results in slow recombination and very long carrier lifetimes. The longer lifetime of 2,5-$DMAI_3$, compared to 2,5-$DMASnI_3$, is possibly related to the high ionic character of the I_3^- units, which aids charge separation. To study the lifetime when the charge carriers are generated close to each other, we performed photoconductivity TRMC measurements with laser excitation.[11] However, we did not obtain any appreciable photoconductivity signal. By definition, the quantity obtained from these measurements is a product of the mobility and the yield of charge dissociation.[11] From the PR-TRMC measurements, it is clear that the charge carriers are mobile. Thus, the absence of a photoconductivity signal means that the charge carriers do not dissociate or recombine very quickly due to a high exciton binding energy. We conclude that the exciton binding energy is probably very large in these materials, as a result of strong 1D confinement. This is consistent with 2D perovskite structures where much lower photoconductivity was measured, combined with very short carrier lifetimes, see for instance in **chapter 6**.[11]

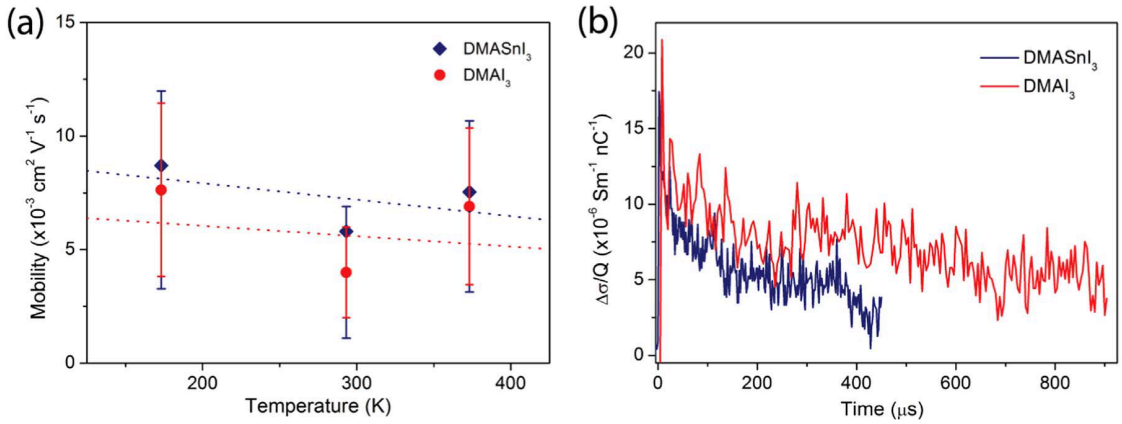

Figure 10.3. PR-TRMC experiments as a function of temperature. a) Mobility of charge carriers in 2,5-$DMASnI_3$ and 2,5-$DMAI_3$. Error bars are defined as 50% of the base value. Dotted lines are drawn to guide the eye. **b)** Change in conductivity of as 2,5-$DMASnI_3$ and 2,5-$DMAI_3$ a function of time, measured at room temperature.

10.2.2. Synthesis, characterization and electronic properties of (Pyr-C4NH$_3$)PbI$_3$ · (TCNQ)

(Pyr-C_4NH_3)PbI_3·(TCNQ) single crystals were grown using an antisolvent vapor-assisted crystallization approach[15] in which PyrC_4NH_3I, TCNQ and PbI_2 were dissolved in equimolar amounts in gamma-butyrolactone (GBL) by stirring at 50 °C for 15 min. Subsequently, dichloromethane (DCM) was slowly diffused into the GBL solution to act as antisolvent for a week. The crystal structure of (Pyr-C_4NH_3)PbI_3·(TCNQ) and organic CTC Pyrene-TCNQ are shown in Figure 10.4. The 1D hybrid present a monoclinic structure while the CTC Pyrene-TCNQ a triclinic structure previously resolved in literature (see XRD patterns in Appendix Figure A10.3).[16] The single crystals of the 1D hybrid are most likely obtained due to slow crystallization.[4] As described in **Chapter 9**, 2D (Pyr-C_4NH_3:TCNQ)$_2PbI_4$ can be obtained in thin-films with a faster spin-coated crystallization procedure than for 1D thin films (XRD in Appendix Figure A10.4).[4]

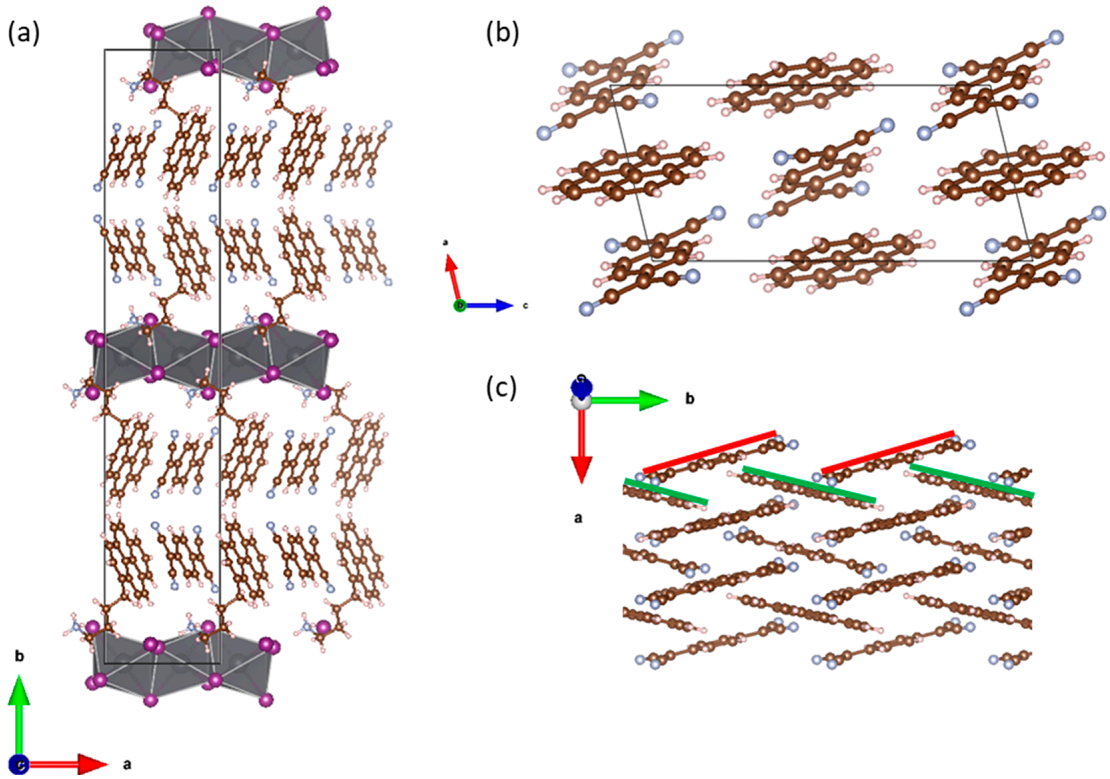

Figure 10.4. Simulated crystal structures. a) 1D hybrid (PyrC_4NH_3)PbI_3·(TCNQ); the box shows the unit cell. **b)** Unit cell and **c)** side view of the molecular arrangement of the organic CTC pyrene-TCNQ crystal, where TCNQ is highlighted by the red stick and pyrene by the green stick.[25] The atom labels represent hydrogen in white, nitrogen in blue-gray, carbon in brown, iodine in purple, and Pb in gray, inside the octahedra.

The optical absorption spectra of the 1D hybrid and organic CTC pyrene-TCNQ measured by photothermal deflection spectroscopy (PDS) is shown in Figure 10.5a where is seen that the shapes of the two spectra are similar. This points to similar nature of the involved electronic

excited states. There is a clear shift of the sharp absorption onset from ~1.3 eV for the organic CTC to ~1 eV for the hybrid. Such a spectral displacement might originate from a different molecular packing of the CTC and/or direct involvement of the lead halide inorganic layer through hybridization with the organic chromophores. The origin of the observed differences in electronic structure and optical properties can be understood by DFT electronic structure calculations. We obtain an electronic bandgap of 1.93 eV for the 1D perovskitoid system and 2.16 eV for the pure CTC crystal. Compared to the PDS data the theoretical values are expectedly blue-shifted, nevertheless the calculations correctly reproduce the observed spectral shift (~0.23 eV calculated against ~0.3 eV measured) between the two crystals. Turning to the electronic structure energy diagrams displayed in Figure 10.5b, we find from the analysis of the partial density of states (DOS) that the band-edge levels in the 1D hybrid perovskitoid are fully confined in the organic part, namely, with the conduction band-edge (CBE) dominated by TCNQ empty orbitals and the valence band-edge (VBE) governed by pyrene occupied orbitals (same as in the organic CTC salt, Appendix Figure A10.5). It is important to stress, however, that the lead-iodide inorganic layer contributes with occupied crystalline orbitals that are located in close energy proximity (within ~0.1 eV) to the VBE. In contrast, the corresponding PbI unoccupied crystalline orbitals are located at significantly higher energies than the CBE. In addition, inspection of the partial DOS reveals no or very limited hybridization between the organic molecular and inorganic crystalline orbitals. In view of the small energy difference, this absence of wave function mixing must originate from a very weak electronic coupling between the inorganic scaffold and the conjugated chromophores. Therefore, we rule out hybridization as a mechanism for the observed red shift in the absorption spectra and suggest reorganization of the donor and acceptor molecules templated by the inorganic layout.

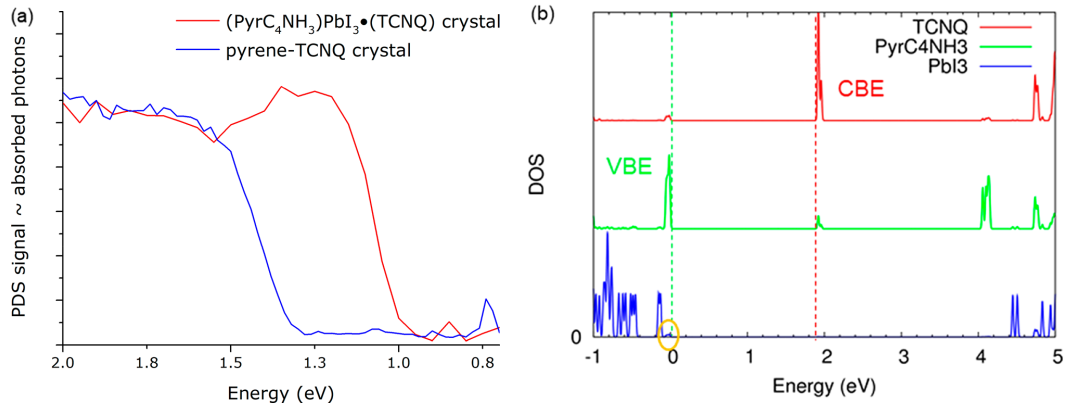

Figure 10.5. a) Optical absorption spectra of the 1D Hybrid $(PyrC_4NH_3)PbI_3$·(TCNQ) and CTC pyrene-TCNQ single crystals measured using photothermal deflection spectroscopy (using a HeNe 633 nm probe laser). **b)** Partial density of states for the different components of the 1D hybrid (PyrC4NH3)PbI3·(TCNQ). The circled region indicates weak hybridization between the inorganic lattice and the CTC. VBE = valence band edge; CBE = conduction band edge; BG =band gap.

Table 10.2. Effective Masses of Electrons and Holes for the organic CTC pyrene-TCNQ and the 1D Hybrid $(PyrC_4NH_3)PbI_3{\cdot}(TCNQ)$

	Organic CTC pyrene-TCNQ		1D CTC pyrene-TCNQ		1D hybrid $(PyrC_4NH_3)PbI_3{\cdot}(TCNQ)$	
direction	m_{e-}	m_{h+}	m_{e-}	m_{h+}	m_{e-}	m_{h+}
(100)	10.42	3.29	4.31	∞	4.63	∞
(010)	9.9	2.11	∞	∞	∞	∞
(001)	6.66	13.85	7.37	2.35	4.33	1.62

An analysis of the charge transport properties indirectly support this claim. We calculated effective masses along high-symmetry paths for (i) the hybrid 1D organic–inorganic perovskitoid, $(PyrC_4NH_3)PbI_3{\cdot}(TCNQ)$; (ii) the pure organic CTC pyrene-TCNQ; and (iii) a hypothetical system, 1D CTC pyrene-TCNQ, built by removing all lead and iodine atoms from the crystal structure of the hybrid material and (to balance the charges) substituting the nitrogen atoms of the ammonium groups with carbons (shown in Table 10.2). The hypothetical system aims at mimicking a pure template effect where the inorganic lattice only contributes indirectly to the transport by rearranging the position of the donor and acceptor molecules in comparison to the CT salt. As a matter of fact, in all relevant directions, the effective masses predicted by the DFT calculations are typical for organic molecular crystals with weak band dispersion. The differences observed between the 1D hybrid and the organic CTC primarily stem from a smaller longitudinal molecular translation, between successive donor (acceptor) molecules in the 1D hybrid structure (Figure 10.4c). While this is still far for intermolecular spatial overlap, there is improved π–π stacking interaction between the organic molecules in the perovskitoid 1D hybrid compared to the organic CTC salt, which is driven by the inorganic layout. As a result, the electron effective masses along the high-mobility direction are significantly smaller, especially for electrons, in the hybrid material with respect to the organic salt. This templated effect is confirmed by the relatively similar effective masses computed for the real hybrid and the 1D CTC pyrene-TCNQ hypothetical structure. Still, the absolute values of the effective masses remain relatively large for both holes and electrons, irrespective of the direction; hence, we expect relatively poor charge transport mobility for both organic and hybrid crystals.

This is fully confirmed by time-resolved micro-conductivity (TRMC) measurements. First, by PR-TRMC measurements we determined that the mobility of free charge carriers in the two materials is modest, 10^{-3}–10^{-2} $cm^2\ V^{-1}\ s^{-1}$, and does not vary over a broad temperature range (Figure 10.6a). In addition, similar recombination dynamics of the charge carriers for both materials are obtained (Appendix Figure A10.6). Second, by photoconductivity TRMC (which gives product of the mobility and the yield of photogenerated free electrons and holes[17]) exciting the charge-transfer band (~600 nm) we determined that the photoconductivity signal for the 1D hybrid perovskitoid is larger than for the organic salt (Figure 10.6b). Besides, the recombination lifetime of the charge carriers is longer.

As there is no appreciable difference in charge carrier mobility, we conclude that the higher photoconductivity signal in the 1D hybrid must be caused by a higher yield of mobile free charge carriers. We speculate that the larger fraction of photogenerated free charge carriers in the 1D hybrid material is related to transient localization of the holes on the inorganic lattice facilitated by the close energy spacing between the occupied inorganic crystalline and organic molecular occupied orbitals (as determined in Figure 10.5b). This idea is also consistent with the long lifetime obtained by photoconductivity TRMC.

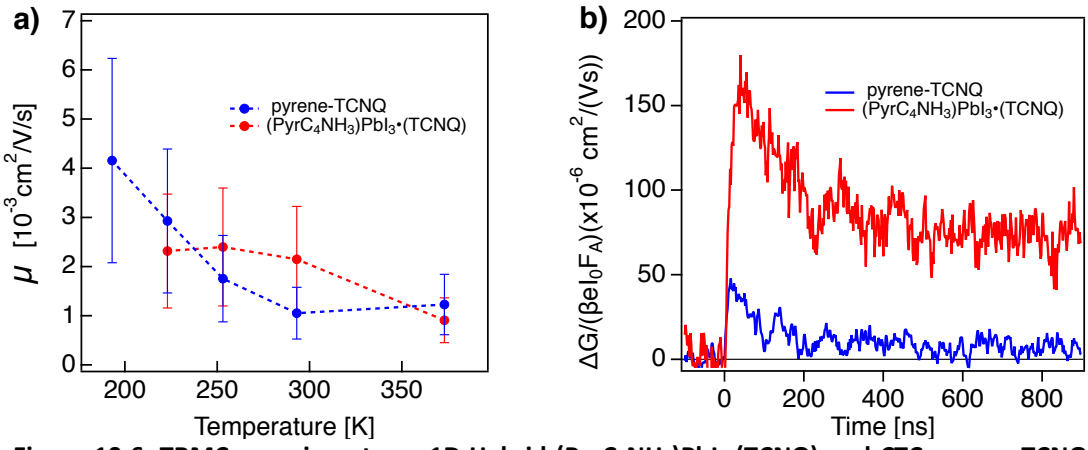

Figure 10.6. TRMC experiments on 1D Hybrid ($PyrC_4NH_3$)PbI_3·(TCNQ) and CTC pyrene-TCNQ. a) Mobility of charge carriers determined by radiation induced PR-TRMC as a function of temperature. **b)** Photoconductivity TRMC measurements excited at the CT state (~600 nm).

10.3. Conclusions

This chapter reveals that the synthesis of perovskite structures with bulky organic chromophores is strongly affected by processing conditions (temperature, inert environment, precursors, crystallization time). In addition, the electronic properties of 1D organic-inorganic perovskites are tightly connected to the interaction of the organic and inorganic layer in the structure. We determined that in the two cases studied, the charge carrier mobilities in these 1D structures are similarly low (10^{-3}–10^{-2} cm^2 V^{-1} s^{-1}). Despite these low mobilities, it is interesting that the charge transport properties can be dominated either by the inorganic layer (as in 2,5-DMASnI_3) or by the organic chromophores while the inorganic layer mostly acts as a template (as in 1D Hybrid ($PyrC_4NH_3$)PbI_3·(TCNQ)). The indication of some coupling between the inorganic and organic manifolds in the latter mixed systems, shown by the increased photoconductivity and lifetime, reveals that there is a lot of potential to optimize the opto-electronic properties of these new hybrid materials.

As can be deduced from the general formula (D-C_nH_{2n}-NH_3)PbX_3·(A), one could potentially change the core of the donor molecule (D), the alkyl chain length of the donor molecule (CnH_{2n}), the acceptor molecule (A) and the halide (X). All of these changes are suspected to

have an influence on the optical and electronic properties of these hybrid materials. Therefore, the applicability of this type of hybrids can potentially be extended by using donor:acceptor combinations with superior charge transport properties compared to pyrene-TCNQ. In addition, it would be interesting to determine how their inclusion into an inorganic scaffold influences the variety of electronic or magnetic properties that charge-transfer complexes are known to exhibit.

10.4. Experimental Methods

Crystal growth of 2,5-dimethylanilinium tin iodide. Single crystals of 2,5-dimethylanilinium tin iodide (2,5-DMASnI_3)were grown following the method previously reported by Stoumpos et al.[8] to synthesize methylammonium tin iodide and formamidinium tin iodide. First, the 2,5-dimethyliodide salt (2,5-DMAI) was synthesized from an equimolar mixture of 2,5-DMA and HI. A syringe was used to slowly add concentrated (57wt%) aqueous hydriodic acid (Sigma Aldrich; 99.95%) to 2,5-DMA (Sigma Aldrich; 99%). The mixture was heated to 70 °C to remove excess solvent. The resulting white salt was washed with diethyl ether (Avantor) and dried in air. Subsequently, a 100mL 3-necked Schlenk flask was charged with 6.8mL concentrated (57wt%) aqueous hydriodic acid (Sigma Aldrich; 99.95%) and 1.7mL concentrated (50 wt%) aqueous hypophosphorous acid, H_3PO_2 (Sigma Aldrich). This mixture was degassed with argon and kept under an argon atmosphere throughout the experiment. 373 mg (1mmol) SnI2 (Sigma Aldrich; 99%) was added to the flask and dissolved upon heating the mixture to 120 °C using an oil bath, while stirring magnetically. A yellow mixture was obtained. A stoichiometric amount of 1mmol of the 2,5-DMAI salt was added to the hot solution and dissolved immediately. Next, the solution was slowly evaporated at 120 °C to approximately half its original volume while stirred continuously. Stirring was then discontinued and the mixture was left to cool down to room temperature at a rate of approximately 20 °C/hour. Upon cooling, yellow crystals needles with a length of approximately 3mm were obtained.

Crystal growth of 2,5-dimethylanilinium triiodide. Single crystals of 2,5-dimethylanilinium triiodide (2,5-DMAI_3) were grown at room temperature, following a modified layered-solution synthesis method previously reported by Mitzi.[9] In this method, 60 mg (0.16 mmol) SnI2 (Sigma Aldrich; 99%) was added to 3.0 mL of concentrated (57 wt%) aqueous hydriodic acid (Sigma Aldrich; 99.95%). The SnI2 did not fully dissolve, and only the solution was transferred into a standard size (18 × 150 mm) glass test tube. 3.0 mL of absolute MeOH (Lab-Scan, 99.8%) was carefully placed on top of the red-brown SnI_2/HI mixture, without mixing the solutions. A sharp interface was formed between the two layers due to a large difference in densities. 2,5-DMA (Sigma Aldrich; 99%) was added in great excess by adding 15 droplets, using a glass pipette. The test tube was covered with aluminum foil and kept in a fume hood under ambient

conditions. This method turned out to be very slow. It took more than a month to grow black/red bar-shaped crystals of up to 3mm long. Moreover, as we observed that tin was not included in the final product (2,5-$DMAI_3$ was the product formed), we found that this elaborate method was not necessary. Simply adding MeOH and 2,5-DMA to the filtered SnI_2/HI mixture, briefly stirring and leaving it in the fume hood under ambient conditions gave the same result. However, using this simplified method, crystals were observed within 24 h. This led us to believe that the evaporation rate was the most important parameter for obtaining this product. Note that the addition of MeOH is not vital to the formation of 2,5-$DMASnI_3$. It does promote the solubility of the organic component, as it prevents the formation of 2,5-DMAI, necessary to form 2,5-$DMAI_3$. However, the absence of MeOH reduced the evaporation rate, obtaining larger crystals of up to ~ 8mm long.

Single-crystal X-ray diffraction of 2,5-$DMASnI_3$ and 2,5-$DMAI_3$. Single-crystal X-ray diffraction (XRD) measurements were performed using a Bruker D8 Venture diffractometer equipped with a Triumph monochromator and a Photon100 area detector, operating with Mo Kα radiation (0.71073 Å). A 0.3mm nylon loop and cryo-oil were used to mount the crystals. The crystals were cooled with a nitrogen flow from an Oxford Cryosystems Cryostream Plus. Data processing was done using the Bruker Apex III software and the SHELX97[18] software was used for structure solution and refinement. Full-matrix least squares refinement against F^2 was carried out using anisotropic displacement parameters. Multi-scan absorption corrections were performed. Hydrogen atoms were added by assuming a regular tetrahedral coordination to carbon and nitrogen, with equal bond angles and fixed distances.

Density functional theory calculations of 2,5-$DMASnI_3$ and 2,5-$DMAI_3$. The band structures of both crystals were computed at the density functional theory (DFT) level of theory using VASP 5.4.1. The calculations were performed using the projector augmented wave (PAW) pseudopotentials[19,20] with the Van-der-Waals-corrected[21] PBE exchange correlation functional.[22] The energy cutoff for the charge density calculations was 500 eV and a Gamma centered K-point grid with dimensions of 4 × 4 × 4 was chosen. A denser K-point grid of 210 K-point along the high-symmetry points in the Brillouin zone was used for the band structure calculations.

Crystal growth of (PyrC4NH3)PbI3·(TCNQ). Single crystals were grown using an antisolvent vapor-assisted crystallization approach[15] in which the components are dissolved together in a good solvent (gamma-butyrolactone; GBL) and dichloromethane (DCM) antisolvent slowly diffuses into the GBL solution. Specifically, $PyrC_4NH_3I$ (0.108 mol/L), TCNQ (0.108 mol/L), and PbI_2 (0.108 mol/L) were dissolved together in gamma-butyrolactone by stirring at 50 °C for 15 min. The precursor solution was filtered through a syringe filter (0.45 µm). The precursor solution (0.5 mL) was transferred to a small glass vial. The small vial (5 mL volume) was capped

off with aluminum foil. A small hole was made in the aluminum foil. The small vial with the aluminum foil was put in a larger glass vial (20 mL volume). A small amount of dichloromethane (2 mL) was injected in the gap between the two flasks, and the larger flask was capped off with a plastic cap and parafilm. The vials were left undisturbed at room temperature. After 1 week black crystals suitable for single-crystal X-ray diffraction were harvested. These crystals were washed three times with dry dichloromethane and were subsequently dried under reduced pressure at room temperature. The crystals of the organic CTC pyrene-TCNQ were grown by dissolving equimolar amounts of pyrene (0.025 mol/L) and TCNQ (0.025 mol/L) in tetrahydrofuran (THF) by stirring at 40 °C until full dissolution. The solution was allowed to cool down to room temperature and was filtered through a syringe filter (0.45 μm). Crystals were obtained by evaporation of the THF at room temperature.

Thin Film Deposition. Stoichiometric amounts of $PyrC_4NH_3I$ (0.3 mol/L), TCNQ (0.3 mol/L), and PbI2 (0.3 mol/L) were dissolved in dry DMF by stirring at 50 °C for 30 min. The precursor solution was filtered through a syringe filter (0.45 μm) before use. Quartz substrates were cleaned through consecutive sonication steps in a series of solvents (detergent water, deionized water, acetone, isopropanol) for 15 min each, followed by a UV-ozone treatment for 15 min. Films were obtained by drop-casting (∼30 μL on a 2.5 cm × 2.5 cm substrate) on a quartz substrate. The films were annealed at 110 °C for 15 min.

X-ray Diffraction of $(PyrC_4NH_3)PbI_3\cdot(TCNQ)$. X-ray intensity data were collected at 100 K on a Rigaku Oxford Diffraction Supernova Dual Source (Cu at zero) diffractometer equipped with an Atlas CCD detector using ω scans and CuKα (λ = 0.71073 Å) radiation. The images were interpreted and integrated with the program CrysAlisPro. Using Olex2, the structure was solved by direct methods using the ShelXS structure solution program and refined by full-matrix least-squares on F^2 using the ShelXL program package. Non-hydrogen atoms were anisotropically refined and the hydrogen atoms in the riding mode and isotropic temperature factors fixed at 1.2 times U(eq) of the parent atoms.

Density functional theory calculations of $(PyrC_4NH_3)PbI_3\cdot(TCNQ)$. Density functional theory calculations with periodic boundary conditions have been performed with the Quantum Espresso suite program[23] for the electronic properties (and Bader analysis) using a planewave/pseudopotential formalism. We adopted a norm-conserving pseudopotential, with a cutoff of 40 Ry for the expansion of the wave function and a correction for the van der Waals interactions (Grimme DFT-D2 method[21]). Different functionals (GGA and Hybrids) were applied: PBE,[22] PBE0, and HSE. In the case of the PBE functional, we also performed the same calculations with and without a spin−orbit correction. We kept the same k-points mesh for all PBE calculations, 4 × 3 × 2 for the organic crystal (pyrene-TCNQ) and 4 × 1 × 4 for the 1D perovskitoid. When using hybrid functionals, the calculations were limited at the gamma

point of the first Brillouin zone, because of computational costs. Effective mass calculations have also been performed with Quantum Espresso at the PBE level. We instead resorted to the CRYSTAL suite program (CRYSTAL14,[24] CRYSTAL17[25]) for effective mass calculations using hybrid functionals, namely, the PBE0 functional, as these are not implemented in Quantum Espresso. For consistency between the two sets of results, we paid attention to keep the same cell parameters, the same number of atoms explicitly taken into account and the same k-points mesh for the single point calculations.

Pulse-radiolysis microwave conductivity measurements. High energy electron pulse microwave conductivity measurements were performed on micrometer crystals (~45 mg) placed in a Polyether ether ketone (PEEK) holder. The PEEK block with the sample is placed inside a rectangular waveguide cell (chemically inert gold-plated copper). The cell is contained in a cryostat in which the temperature can be varied between 123K and 473K. The irradiation intensity was varied between pulse lengths of 5 ns and 50 ns (charge carrier concentrations ~ $2x10^{16}$ cm^{-3} to $2x10^{17}$ cm^{-3}) for each temperature at a frequency of 31 GHz. The frequency scan (28-38 GHz) fits were measured at a pulse length of 20 ns (~$9.9x10^{16}$ cm^{-3}).

Photo-conductivity measurements. Laser induced time-resolved microwave conductivity (TRMC) measurements were performed on thin films deposited on quartz substrates and placed in a sealed resonant cavity inside a nitrogen-filled glovebox. Photoconductivity TRMC measurements quantify the change in conductivity [microwave (8–9 GHz) power] upon pulsed excitation (repetition rate 10 Hz) due to free mobile charge carriers. The samples were kept in an inert nitrogen environment to prevent degradation by exposure to moisture.

10.5. Acknowledgements

The materials studied in this chapter were prepared by M.E.K from the University of Groningen (DMA Sn-based compounds) and by W.v.G, R.H, L.L. and D.V from Hasselt University (CT complexes). The DFT calculations were performed by S.M and F.C.G from Delft University of Technology (DMA-compounds) and N.M. and D.B. from University of Mons (CT complexes).

10.6. References

1. Mao, L., Stoumpos, C. C. & Kanatzidis, M. G. Two-Dimensional Hybrid Halide Perovskites: Principles and Promises. *J. Am. Chem. Soc.* **141**, 1171–1190 (2019).
2. González-Carrero, S., Galian, R. E. & Pérez-Prieto, J. Organometal Halide Perovskites: Bulk Low-Dimension Materials and Nanoparticles. *Part. Part. Syst. Charact.* **32**, 709–720 (2015).
3. Saparov, B. & Mitzi, D. B. Organic-Inorganic Perovskites: Structural Versatility for Functional Materials Design. *Chem. Rev.* **116**, 4558–4596 (2016).
4. Van Gompel, W. T. M. *et al.* Towards 2D layered hybrid perovskites with enhanced functionality:

Introducing charge-transfer complexes: Via self-assembly. *Chem. Commun.* **55**, 2481–2484 (2019).
5. Evans, H. A. *et al.* Mono- and Mixed-Valence Tetrathiafulvalene Semiconductors (TTF)BiI4 and (TTF)4BiI6 with 1D and 0D Bismuth-Iodide Networks. *Inorg. Chem.* **56**, 395–401 (2017).
6. Evans, H. A. *et al.* (TTF)Pb 2 I 5 : A Radical Cation-Stabilized Hybrid Lead Iodide with Synergistic Optoelectronic Signatures . *Chem. Mater.* **28**, 3607–3611 (2016).
7. Dillon, R. J. & Bardeen, C. J. Time-resolved studies of charge recombination in the pyrene/TCNQ charge-transfer crystal: Evidence for tunneling. *J. Phys. Chem. A* **116**, 5145–5150 (2012).
8. Stoumpos, C. C., Malliakas, C. D. & Kanatzidis, M. G. Semiconducting tin and lead iodide perovskites with organic cations: Phase transitions, high mobilities, and near-infrared photoluminescent properties. *Inorg. Chem.* **52**, 9019–9038 (2013).
9. Mitzi, D. B. A Layered Solution Crystal Growth Technique and the Crystal Structure of $(C_6H_5C_2H_4NH_3)_2PbCl_4$. *J. Solid State Chem.* **704**, 694–704 (1999).
10. Kamminga, M. E., De Wijs, G. A., Havenith, R. W. A., Blake, G. R. & Palstra, T. T. M. The Role of Connectivity on Electronic Properties of Lead Iodide Perovskite-Derived Compounds. *Inorg. Chem.* **56**, 8408–8414 (2017).
11. Gélvez-Rueda, M. C. *et al.* Interconversion between Free Charges and Bound Excitons in 2D Hybrid Lead Halide Perovskites. *J. Phys. Chem. C* **121**, 26566–26574 (2017).
12. Gélvez-Rueda, M. C., Renaud, N. & Grozema, F. C. Temperature Dependent Charge Carrier Dynamics in Formamidinium Lead Iodide Perovskite. *J. Phys. Chem. C* **121**, 23392–23397 (2017).
13. Gélvez-Rueda, M. C. *et al.* Effect of cation rotation on charge dynamics in hybrid lead halide perovskites. *J. Phys. Chem. C* **120**, 16577–16585 (2016).
14. Warman, J., Haas, M. De, Dicker, G. & Grozema, F. Charge Mobilities in Organic Semiconducting Materials Determined by Pulse-Radiolysis Time-Resolved Microwave Conductivity:-Bond-Conjugated Polymers. *Chem. Mater* 4600–4609 (2004).
15. Shi, D. *et al.* Low trap-state density and long carrier diffusion in organolead trihalide perovskite single crystals. *Science (80-.).* **347**, 519 LP – 522 (2015).
16. Dobrowolski, M. A., Garbarino, G., Mezouar, M., Ciesielski, A. & Cyrański, M. K. Structural diversities of charge transfer organic complexes. Focus on benzenoid hydrocarbons and 7,7,8,8-tetracyanoquinodimethane. *CrystEngComm* **16**, 415–429 (2014).
17. Savenije, T. J., Ferguson, A. J., Kopidakis, N. & Rumbles, G. Revealing the dynamics of charge carriers in polymer:fullerene blends using photoinduced time-resolved microwave conductivity. *J. Phys. Chem. C* **117**, 24085–24103 (2013).
18. Sheldrick, G. SHELX-97: Programs for Crystal Structure Analysis. *SHELX-97 Programs Cryst. Struct. Anal.* (1997). doi:citeulike-article-id:2966527
19. Blöchl, P. E. Projector augmented-wave method. *Phys. Rev. B* **50**, 17953–17979 (1994).
20. Kresse G.a Joubert, D. . From ultrasoft pseudopotentials to the projector augmented-wave method. *Phys. Rev. B - Condens. Matter Mater. Phys.* **59**, 1758–1775 (1999).
21. Grimme, S., Antony, J., Ehrlich, S. & Krieg, H. A consistent and accurate ab initio parametrization of density functional dispersion correction (DFT-D) for the 94 elements H-Pu. *J. Chem. Phys.* **132**, 154104 (2010).
22. Perdew, J. P., Burke, K. & Ernzerhof, M. Generalized gradient approximation made simple. *Phys. Rev. Lett.* **77**, 3865–3868 (1996).
23. Giannozzi, P. *et al.* QUANTUM ESPRESSO: a modular and open-source software project for quantum simulations of materials. *J. Phys. Condens. Matter* **21**, 395502 (2009).
24. Dovesi, R. *et al.* CRYSTAL14: A program for the ab initio investigation of crystalline solids. *Int. J. Quantum Chem.* **114**, 1287–1317 (2014).
25. Dovesi, R. *et al.* Quantum-mechanical condensed matter simulations with CRYSTAL. *Wiley Interdiscip. Rev. Comput. Mol. Sci.* **8**, e1360 (2018).

Summary

In this thesis we have aimed to tune and control the optoelectronic properties of organic-inorganic metal halide perovskites by systematically changing components in the structure and studying the charge carrier dynamic mechanisms. **Chapter 3** and **Chapter 4** describe our findings for 3D perovskites. Particularly, the effect of the small organic cation (methylammonium, formamidinium or inorganic cesium) on the charge carrier dynamics (mobility and lifetime). Opposite to the common belief in the field, we found that the charge dynamics are significantly influenced by the organic cation. If the dipole moment is small or non-existent (formamidinium and cesium) the charge carriers mobility follows the same phonon-scattering temperature behavior as common inorganic semiconductors, where the mobility of charges increases with decreasing temperature. In contrast, when the dipole moment is high (methylammonium) and the rotation of the organic cations is restricted (at low temperature), the organic cations freezes with certain disordered orientation of dipoles in the system. This leads to local, polarized regions that enhance the separation of the electron and hole, increasing their mobility and lifetime.

A common concern for commercial application of organic-inorganic perovskites is the high toxicity from lead. In **Chapter 5**, the charge carrier dynamics is discussed of alternative materials with lower-toxicity such as lead replacement with tin (Sn) or a combination of a monovalent and a trivalent metal such as silver (Ag^{+}) and bismuth (Bi^{3+}) forming the so-called double perovskites. These substitutions come with challenges such as the low stability of Sn-based perovskites due to oxidation of Sn^{2+} to Sn^{4+} and larger band gaps in double perovskites, making them unsuitable for single-junction solar cells. It is shown that it is possible the improve the electronic properties of Sn-based perovskites by addition of SnF_2 and Pb-mixing during synthesis. In the case of double perovskites, we reduced the band gap by doping with antimony without increasing the trap density and maintaining the phonon-scattering charge transport common in 3D perovskites.

In 3D perovskites the inorganic lattice severely restricts the size of the organic cation that can be included and only a few small organic cations fit inside the structure. In addition, possible substitutions of the divalent metal and halide components are also limited. An alternative is to use larger organic ammonium cations (such as alkyl-ammonium, phenyl-alkyl-ammonium), which make the hybrid perovskites more stable due to water repulsion by the hydrophobic organic molecules. The inclusion of such large cations reduces the dimensionality to a two-dimensional (2D) structure inorganic metal-halide octahedral layers, separated by layers of

large organic cations. In **Chapter 6** and **Chapter 7** we studied these 2D perovskites in which the charge dynamics are fundamentally different from their 3D counterparts. After excitation, the electrons and holes are dimensionally and dielectrically confined in the inorganic layer, this increases their coulombic attraction energy forming stable excitons (electron and hole move together). Although this is not desirable for opto-electronic devices that require charge separation such as solar cells, this property is suitable for light emitting diodes (LEDs) or nano-lasers which use efficiently electricity to generate light. This not only extends the application of hybrid perovskites to new devices but also increases the freedom of modifying the opto-electronic properties through organic molecular design. In **Chapter 6**, we first studied the mixing of small and large organic cations. In this case, the number of inorganic layers in between the large organic cations can be tuned. As the number of inorganic layers increases, the opto-electronic properties are more like those in 3D hybrid perovskites. We studied these structures in between 2D and 3D to understand the intrinsic transition between excitonic and free charge carrier dynamics. Ultimately, we determined how the different coulombic attraction energy varies between 2D and 3D hybrid perovskites. In **Chapter 7** effect of the structure of the large organic cation on the optoelectronic properties is considered. In all compounds studied in this chapter, there is no direct contribution of the organic cation to the electronic structure but the optoelectronic properties are affected because changes in the organic component leads to distortions in the inorganic layers.

In the 2D structures studied in chapter 6 and 7 the large organic cations act as a barrier without directly contributing to the charge transport. However, it is also possible to introduce specific functionality in the organic cations, for instance strong electron donors or acceptors to enhance the dissociation of excitons in 2D hybrid perovskites. This idea is explored in **Chapter 8**, **Chapter 9** and **Chapter 10**. The focus in these chapters is on the incorporation of functional organic cations in 2D hybrid perovskites to overcome that large exciton binding energies in these systems and achieve efficient charge separation. Several approaches using different functional organic molecules have been explored and the strategy to achieve this has been shifted several times due to incompatibilities in synthesis and solubility between these bulky organic molecules and the inorganic framework. In **Chapter 8**, a study on a solution phase model system consisting of colloidal 2D perovskite nanoplatelets is presented to prove the concept. The packing requirements for the organic molecules in between the inorganic octahedral layers that dictate the crystallization into a 2D materials in the solid state is lifted in this case since the ligands of the colloidal nanoplatelets are only partially replaced with functional peryline diimide (PDI) molecules. We show that is possible to achieve charge transfer of electrons from the 2D nanoplatelets to PDI, as well as hole transfer from the PDI molecules to the nanoplatelets. This leads to long-lived charge separation, which is essential for use in solar cells and photo detectors. In **Chapter 9**, the attention is turned to the solid

state and different organic donors, acceptors and complete charge-transfer complexes are introduced in the structure. This chapter shows that a range of relatively large conjugated chromophores can be introduced into the structure, however, in most cases the effect on the electronic properties is limited. Only in the case of materials where organic charge-transfer complexes are introduced and enhanced photoinduced formation of charges is observed. Finally, **Chapter 10** describes the properties of perovskite-like one-dimensional compounds that are obtained when bulky functional organic cations are introduced. These materials exhibit poor transport properties due to the strong 1D confinement but an interesting electronic structure where the band structure can be dominated by either the inorganic framework or the functional organic cation.

Samenvatting

In dit proefschrift wordt getracht de opto-elektronische eigenschappen van organisch-anorganische metaalhalogenide perovskieten te beïnvloeden door de verschillende componenten in de chemische structuur systematisch te veranderen en vervolgens de mobiliteit en verval kinetiek van de ladingsdragers te bestuderen. **Hoofdstuk 3** en **hoofdstuk 4** beschrijven onze bevindingen voor perovskieten met een driedimensionale (3D) structuur. Bijzondere aandacht gaat uit naar het effect van het kleine organische kation (methylammonium, formamidinium of anorganisch cesium) op de dynamica van de ladingdragers (mobiliteit en levensduur). In tegenstelling tot wat algemeen wordt aangenomen, laten we zien dat de dynamica van de ladingen aanzienlijk wordt beïnvloed door de eigenschappen van het organische kation. Als het elektrische dipoolmoment klein of gelijk aan nul is (formamidinium en cesium) gedraagt het materiaal zich als gewone anorganische halfgeleiders waar de interactie met roostervibraties leidt tot een toenemende mobiliteit bij lagere temperaturen. Wanneer het dipoolmoment hoog is (methylammonium) en de rotatie van de organische kationen wordt beperkt is (zoals bij lage temperatuur), komen de organische kationen vast te zitten met een bepaalde wanordelijke oriëntatie van de dipolen in het systeem. Dit leidt tot lokale, gepolariseerde gebieden die de scheiding van het elektron en het gat verbeteren, waardoor hun mobiliteit en levensduur toenemen.

Een centraal issue voor commerciële toepassing van organisch-anorganische perovskieten is de hoge toxiciteit van lood. In **hoofdstuk 5** bespreken we daarom de dynamica van ladingdragers in alternatieve materialen met lagere toxiciteit zoals vervanging van lood door tin (Sn) en combinatie van eenwaardige en driewaardige metalen zoals zilver (Ag^{+}) en bismut (Bi^{3+}) die de zogenaamde dubbele perovskieten vormen. Deze substituties gaan gepaard met uitdagingen zoals de lage stabiliteit van Sn-gebaseerde perovskieten als gevolg van oxidatie van Sn^{2+} tot Sn^{4+} en grotere 'bandgaps' in dubbele perovskieten, waardoor ze ongeschikt zijn voor single-junction zonnecellen. In hoofdstuk 5 wordt aangetoond dat het mogelijk is om de elektronische eigenschappen van Sn-gebaseerde perovskieten te verbeteren door toevoeging van SnF_2 tijdens de synthese. In het geval van dubbele perovskieten hebben we de 'bandgap' verkleind door kleine concentraties antimoon toe te voegen, zonder dat dit leidt tot hogere trap concentraties. Hiernaast blijft ook het band-type ladingstransport dat gebruikelijk is in 3D perovskieten behouden.

In 3D perovskieten wordt de grootte van het organische kation dat past in de structuur beperkt door het anorganische rooster, en er zijn slechts enkele kleine organische kationen die passen in de structuur. Bovendien zijn mogelijke substituties van de divalente metaal- en halogenidecomponenten ook beperkt. Een alternatief is om grotere organische ammoniumkationen (zoals alkylammonium, fenyl-alkylammonium) te gebruiken, die de hybride perovskieten stabieler maken door waterafstoting als gevolg van de hydrofobe organische moleculen. Dit vermindert echter de dimensionaliteit naar een tweedimensionale (2D) structuur waardoor lagen gevormd worden van de anorganische metaalhalogenide octaëders, gescheiden door de grotere organische moleculen. In **hoofdstuk 6** en **hoofdstuk 7** hebben we deze 2D-perovskieten bestudeerd en laten we zien dat de dynamica van ladingsdragers fundamenteel anders is dan hun 3D-tegenhangers. Na excitatie zijn de elektronen en gaten opgesloten in de 2D anorganische laag, als gevolg van 'dielectric confinement'. Hierdoor is de Coulomb aantrekking groter en worden er stabiele excitonen gevormd waarin een elektron en gat gebonden zijn en samen bewegen. Hoewel dit niet wenselijk is voor opto-elektronische componenten die ladingsscheiding vereisen, zoals bijvoorbeeld zonnecellen, is deze eigenschap wel geschikt voor licht-emitterende diodes (LED's) of nanolasers die efficiënt elektriciteit gebruiken om licht te genereren. Dit vergroot niet alleen de toepassing van hybride perovskieten in nieuwe 'devices', maar leidt ook tot meer vrijheid om de opto-elektronische eigenschappen te aan te passen door organisch moleculair ontwerp. In **hoofdstuk 6** hebben we eerst het mengen van kleine en grote organische kationen bestudeerd. In dit geval kan het aantal anorganische lagen tussen de grote organische kationen worden gevarieerd. Naarmate het aantal anorganische lagen toeneemt, gedragen de materialen zich meer zoals 3D hybride perovskieten. We hebben deze structuren tussen pure 2D en 3D materialen bestudeerd om de overgang tussen excitonische en vrije ladingdragers te begrijpen. Uiteindelijk hebben we bepaald hoe de exciton bindingsenergie varieert tussen 2D en 3D hybride perovskieten. In **hoofdstuk 7** wordt het effect van de structuur van het grote organische kation op de opto-elektronische eigenschappen beschouwd. In alle in dit hoofdstuk bestudeerde verbindingen is er geen directe bijdrage van het organische kation aan de elektronische structuur, maar de opto-elektronische eigenschappen worden wel beïnvloed doordat veranderingen in de organische component leiden tot vervormingen in de anorganische lagen.

In de 2D-structuren die in hoofdstuk 6 en 7 zijn bestudeerd, fungeren de grote organische kationen als een energetische en dielectrische barrière zonder direct bij te dragen aan het ladingstransport. Het is echter ook mogelijk om specifieke functionaliteit in de organische kationen te introduceren, bijvoorbeeld sterke elektronendonoren of acceptoren om de dissociatie van excitonen in 2D hybride perovskieten te verbeteren. Dit idee wordt

onderzocht in **hoofdstuk 8**, **hoofdstuk 9** en **hoofdstuk 10**. De nadruk in deze hoofdstukken ligt op de integratie van functionele organische kationen in 2D hybride perovskieten om de excitonbindingsenergieën die in deze systemen in het algemeen groot zijn te overwinnen en een efficiënte ladingscheiding te bereiken. Verschillende benaderingen met verschillende functionele organische moleculen zijn onderzocht en de strategie om dit te bereiken is verschillende keren aangepast vanwege incompatibiliteit in synthese en oplosbaarheid tussen deze omvangrijke organische moleculen en het anorganische framework. In **hoofdstuk 8** wordt een onderzoek gepresenteerd naar een modelsysteem dat bestaat uit colloïdale 2D perovskiet nanoplatelets in oplossing om het concept van de introductie van moleculen met een grote elektronaffiniteit te bewijzen. In dit modelsysteem worden complicaties als gevolg van de pakking van organische moleculen tussen de anorganische octaëdrische lagen voorkomen als gevolg van het feit dat de de liganden van de colloïdale nanoplatelets slechts gedeeltelijk worden vervangen door functionele peryline diimide (PDI) moleculen. We laten zien dat het mogelijk is om ladingsoverdracht van elektronen van de 2D nanoplatelets naar PDI te realiseren, evenals gatenoverdracht van de PDI-moleculen naar de nanoplatelets. Dit leidt tot langlevende ladingsscheiding, wat essentieel is voor toepassing in zonnecellen en fotodetectoren. In **hoofdstuk 9** wordt de aandacht gevestigd op de vaste stof en worden verschillende organische donoren, acceptoren en complete 'charge-transfer' complexen in de structuur geïntroduceerd. Dit hoofdstuk laat zien dat een reeks van relatief grote geconjugeerde chromoforen in de structuur kan worden geïntroduceerd, maar in de meeste gevallen is het effect op de elektronische eigenschappen beperkt. Alleen in het geval van materialen waarin organische 'charge-transfer' complexen worden geïntroduceerd wordt een verbeterde foto-geïnduceerde ladingscheiding waargenomen. Ten slotte beschrijft **hoofdstuk 10** de eigenschappen van perovskietachtige eendimensionale (1D) verbindingen die worden gevormd in de synthese wanneer grote functionele organische kationen worden geïntroduceerd. Deze materialen vertonen relatief slechte transporteigenschappen vanwege de sterke 1D-confinement maar hebben wel een interessante elektronische structuur waarbij de bandstructuur kan worden gedomineerd door of het anorganische framework of de functionele organische kationen.

Appendix

Appendix Chapter 3

Figure A3.1 $CH_3NH_3PbX_3$ (X = I, Br, Cl) powder materials. Left) Camera image. Right) SEM image of polycrystalline micrometer crystals of $MAPbI_3$.

<u>Characterization of $CH_3NH_3PbX_3$ (X= I, Br) and mixed $CH_3NH_3PbI_{3-x}Br_x$ perovskites</u>

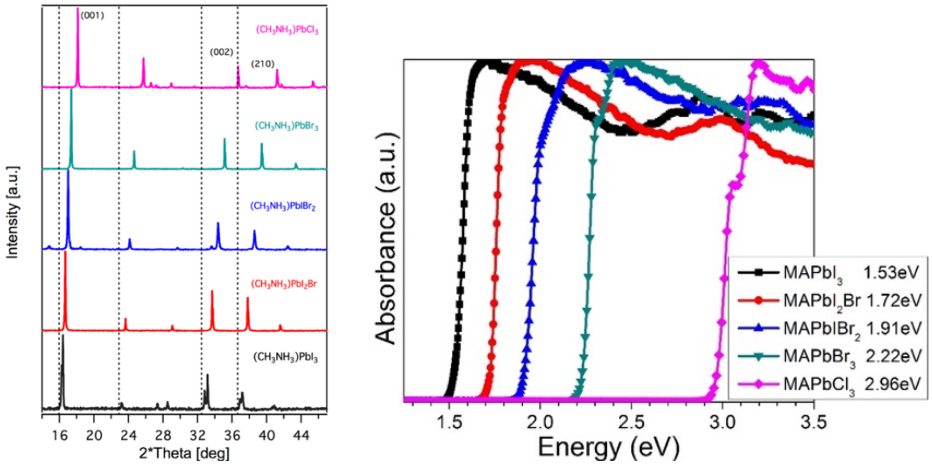

Figure A3.2. Characterization of $MAPbX_3$ and $MAPbI_{3-x}Br_x$. Left) XRD patterns. Rigth) Optical bandgaps of powder materials of $MAPbX_3$ perovskites.

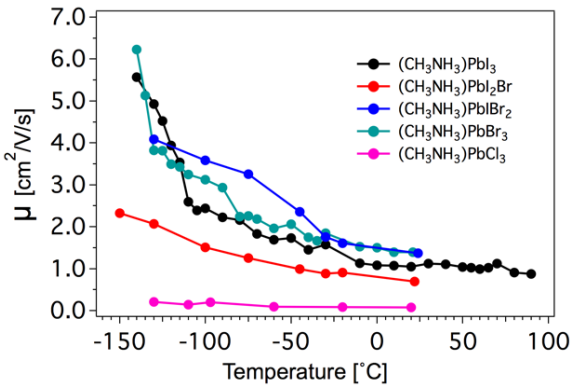

Figure A3.3. Mobility of charge carrier in $CH_3NH_3PbX_3$ (X=I, Br, Cl) and mixed $CH_3NH_3PbI_{3-x}Br_x$ perovskites as a function of temperature.

Alternative Synthesis of $CH_3NH_3PbX_3$ (X= I, Br) crystals

Perovskite precipitation (PP) in a HX/H_3PO_2 solution. To synthesize $(CH_3NH_3)PbX_3$ a 2-necked round bottom flask was charged with HX (6.8 ml, 57 wt.% in water) and H_3PO_2 (1.7 ml, 50 wt.% in water). Hypo-phosphorous acid was used in order to assure that no oxidation products would be present during precipitation. The liquid was degassed by passing a stream of nitrogen for 1 min and kept it under a nitrogen atmosphere. Then, 1 mmol of PbI_2, $PbBr_2$ or $PbCl_2$ was dissolved in the magnetic stirred HI/H_3PO_2 mixture while the flask was heated to 120°C using an oil bath. When the mixture temperature stabilized at 120°C, 1 mmol of solid $(CH_3NH_3)X$ was added to the hot solution. Subsequently, the solution was left to evaporate to half of its original volume. After this, the magnetic stirring and oil bath were discontinued leaving the solution to cool back to room temperature. During cooling, the perovskites crystals precipitate and were left to grow for 24 h. After this time, the crystals were filtered and washed with anhydrous ethanol to remove rests of precursors. Polycrystalline micrometer size $(CH_3NH_3)PbX_3$ crystals were obtained.

Synthesis of $MAPbX_3$ single crystals. A concentrated one molar solution containing PbX_2 and MAX was prepared in dimethylformamide (DMF) for iodide at 60°C or γ-butyrolactone (GBL) for bromide at room temperature. The solutions were filtered using PTFE filter with 0.2-µm pore size. Two milliliters of the filtrate were placed in a 5 ml vial and the vial was kept undisturbed in an oil bath. Then, the temperature was raised to 60°C and subsequently gradually increased 5 degrees every 30 min. Once a crystal is observed, the temperature is kept to grow the nucleation into a big crystal. The slower you raise the temperature – the larger crystals are obtained. The growth temperatures were ~80°C for $MAPbBr_3$ and ~110°C for $MAPbI_3$, respectively. The crystals (3-4 mm) used for measurements were grown for 3 h. After the crystal is taken from the growing solution, place quickly on a filter paper, wash with 4-5 drops of a pure solvent (GBL for $MAPbI_3$, DMF for $MAPbBr_3$), and dry with a filter paper, blow with dry nitrogen for 2-3 min, keep overnight in the oven at 60°C.

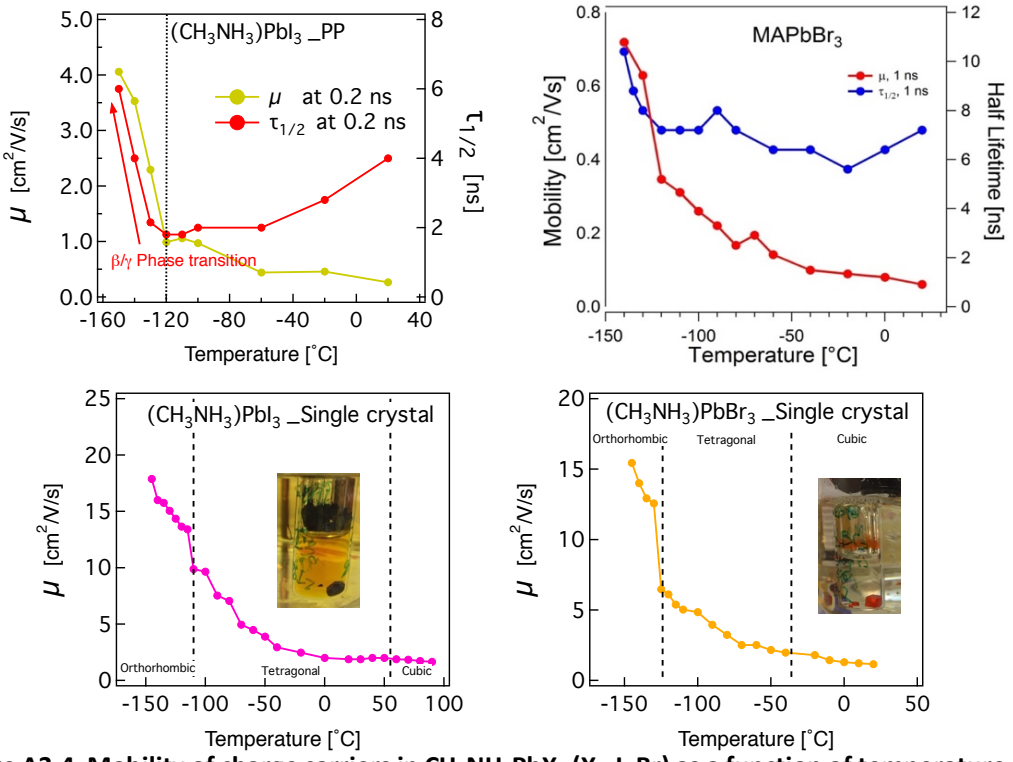

Figure A3.4. Mobility of charge carriers in $CH_3NH_3PbX_3$ (X= I, Br) as a function of temperature and synthesis method. Top) By powder precipitation in HI. **Bottom) Single crystals** by inversed crystallization in DMF and γ-butyrolactone.

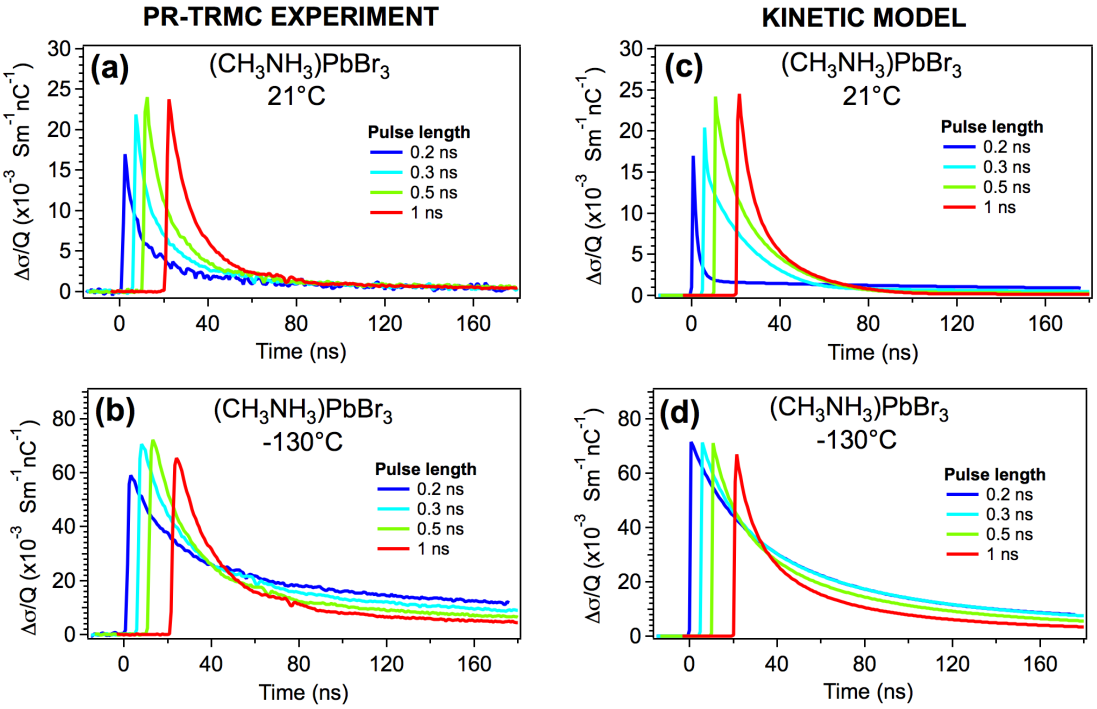

Figure A3.5. Charge Carrier decay dynamics of $MAPbBr_3$ at 21°C and -130°C as a function of initial concentration of charge carriers (pulse length). a, b) Experimental data. **c, d)** kinetic model fit.

Table A3.1. Kinetic fitting parameters for $CH_3NH_3PbBr_3$ at 20°C and -130°C.

Perovskite	$CH_3NH_3PbBr_3$	
Description/Temperature	20°C	-130°C
Mobility: e- / h+ [$cm^2/V/s$]	1.7 / 0.1	3.7 / 0.4
Generation yield (k_1) [$1/cm^3/nC$]	1.12E+15	1.12E+15
Second order recombination rate (k_2) [cm^3/s]	4.00E-08	1.90E-08
Second order trap filling rate (k_3) [cm^3/s]	2.50E-06	6.40E-08
Second order trap emptying rate (k_4)	1.50E-08	2.00E-10
Trap state concentration N_t [$1/cm^3$]	5.00E+14	4.00E+14

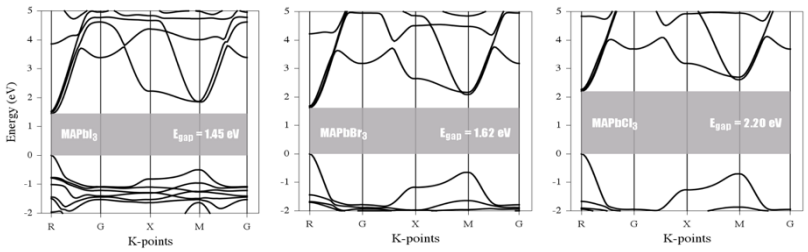

	$MAPbI_3$		$MAPbBr_3$		$MAPbCl_3$	
	hole	elec	hole	elec	hole	elec
m_1	-0.129	0.841	-0.148	1.034	-0.187	2.411
m_2	-0.172	0.767	-0.181	0.891	-0.213	1.582
m_3	-0.189	0.139	-0.190	0.112	-0.246	0.107
m^*	-0.159	0.310	-0.171	0.272	-0.213	0.289

$$m^* = 3\left(\frac{1}{m_1}+\frac{1}{m_2}+\frac{1}{m_3}\right)^{-1}$$

Figure A3.6. Band structure calculation of $(CH_3NH_3)PbX_3$ (X=I, Br, Cl) perovskites. Effective mass of charge carriers of $CH_3NH_3PbX_3$ (X=I, Br, Cl) perovskites.

Appendix Chapter 4

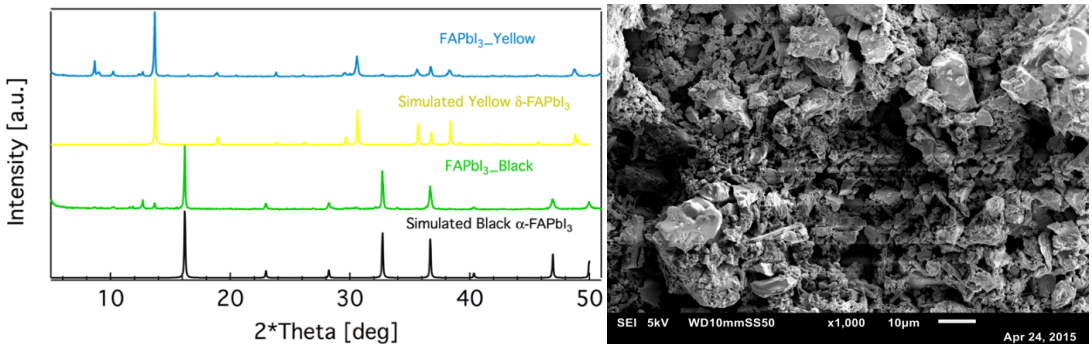

Figure A4.1. Characterization of black and yellow $FAPbI_3$. left) XRD diffraction patterns. Right) SEM Image of $FAPbI_3$ micrometer crystals

Table A4.1. Band gap and effective mass of black and yellow determined by DFT calculations

	Black α-$HC(NH_2)_2PbI_3$		**Yellow δ-$HC(NH_2)_2PbI_3$**	
Band Gap [eV]	**1.25**		**2.25**	
	Electron	Hole	Electron	Hole
m_1	-0.985	-0.086	1.192	-0.485
m_2	0.226	-0.093	0.356	-1.346
m_3	0.075	3.711	0.338	1.255
m*	**0.179**	**-0.136**	**0.454**	**-1.495**

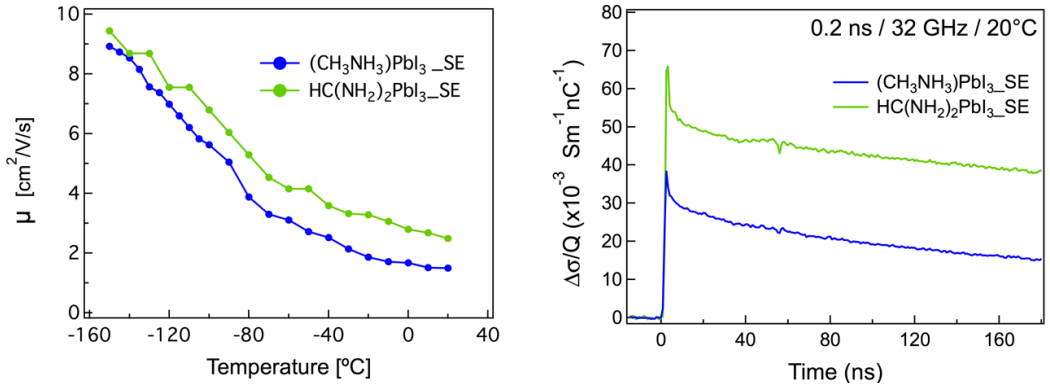

Figure A4.2. Mobility and lifetime of $MAPbI_3$ and $FAPbI_3$ synthesized by solvent evaporation.

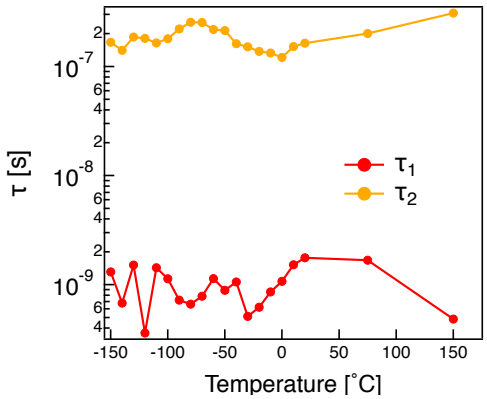

Figure A4.3. Decay time constants obtained from a double exponential fit of black $FAPbI_3$ conductivity traces as a function of temperature. Determined at 32.5 GHz.

Appendix Chapter 5

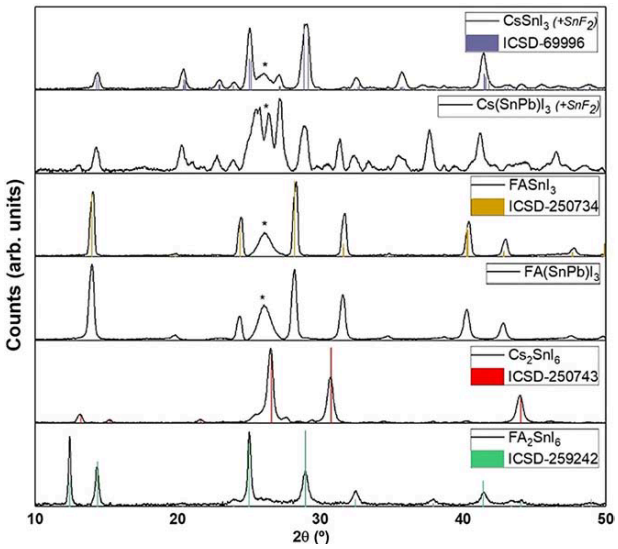

Figure A5.1. XRD diffractograms of mechanochemically synthesized tin perovskites (black lines) together with reference bulk patterns from Inorganic Crystal Structure Database (ICSD; color columns). A broad peak around 2Θ= 26° and marked with an asterisk is visible in most diffractograms due to parasitic diffraction from the adhesive tape used to fix the powder samples on the substrate. In Sn-Pb mixed compounds the main peaks' positions match the reference pure-tin counterpart with a slight shift to lower angles due to the incorporation of the larger lead cation.

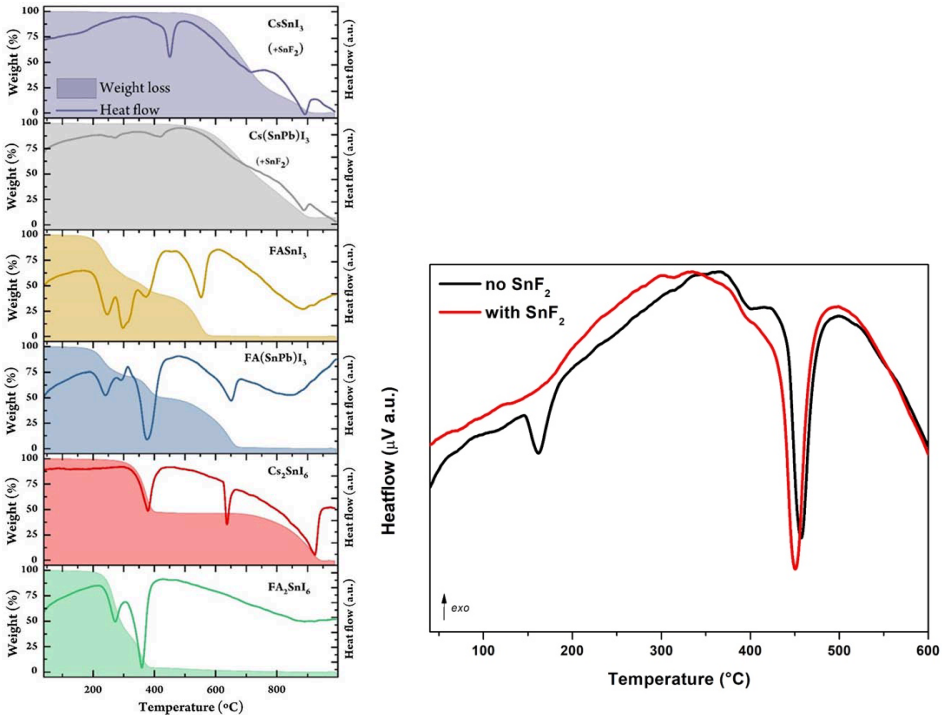

Figure A5.2. Thermal Analysis of Sn-based perovskites. Left) TG (filled area) and DTA (simple line) curves of all compounds in the 40–1000°C range. **Right)** Differential thermal analysis (DTA) of ball-milled CsI+SnI_2 with (red curve) and without SnF_2 (black curve). SnI_4 is detected (identified by the peak at ~ 160°C in the black curve) only in absence of SnF_2.

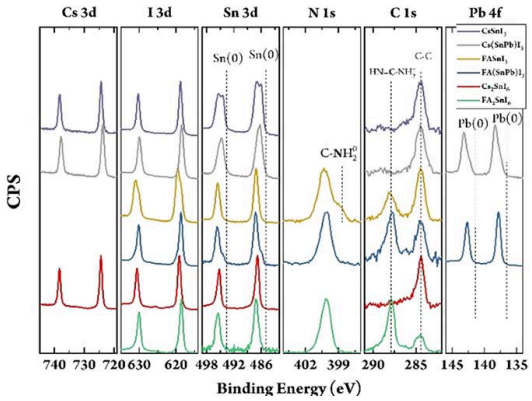

	Cs [at%]	I [at%]	Sn [at%]	N [at%]	C [at%]	Pb [at%]
$CsSnI_3$	23.8	50.6	25.5	–	–	–
$Cs(SnPb)I_3$	26.4	50.7	11.5	–	–	11.4
$FASnI_3$	–	25.9	21.2	34.6	17.7	–
$FA(SnPb)I_3$	–	34.5	9.3	31.0	17.0	8.2
Cs_2SnI_6	28.0	57.3	14.7	–	–	–
FA_2SnI_6	–	26.8	1.2	47.4	24.6	–

Figure A5.3. High-resolution XPS spectra . Left) Main elements from the different compounds: Cs 3D, I 3D, Sn 3D, N 1s, C1s, and Pb 4f regions. **Right)** Atomic percentages of relevant elements.

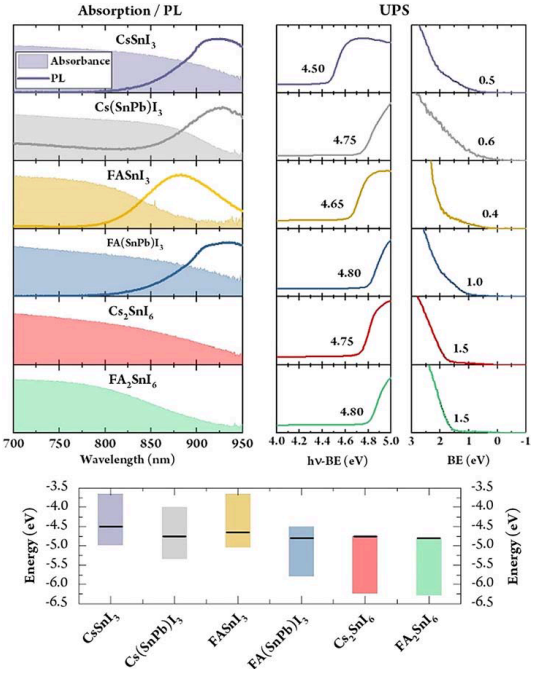

Figure A5.4. Optical characterization, UPS, and derived energy diagram of Sn-based perovskites.

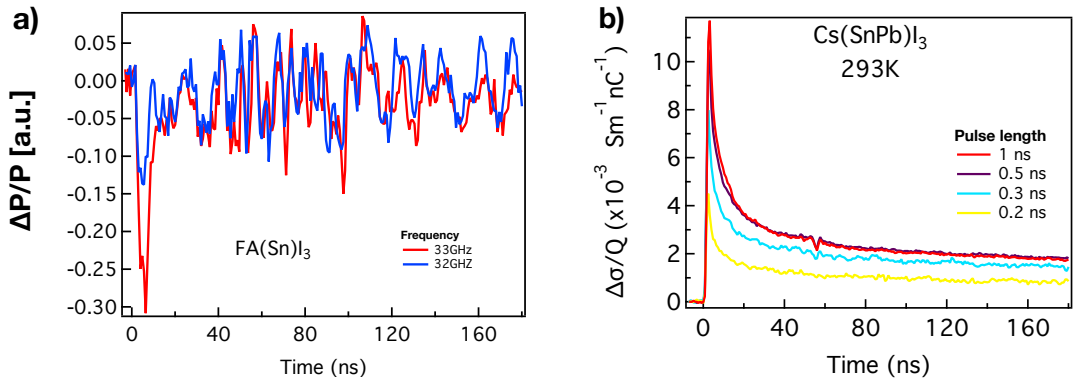

Figure A5.5. PR-TRMC experiments on Sn-perovskites. a) Change of reflected microwave power as a function of time for $FASnI_3$. Shown at different microwave frequencies (32 to 33 GHz). **b)** Charge of conductivity transients of 3D $CsSnPbI_3$ at different pulse lengths.

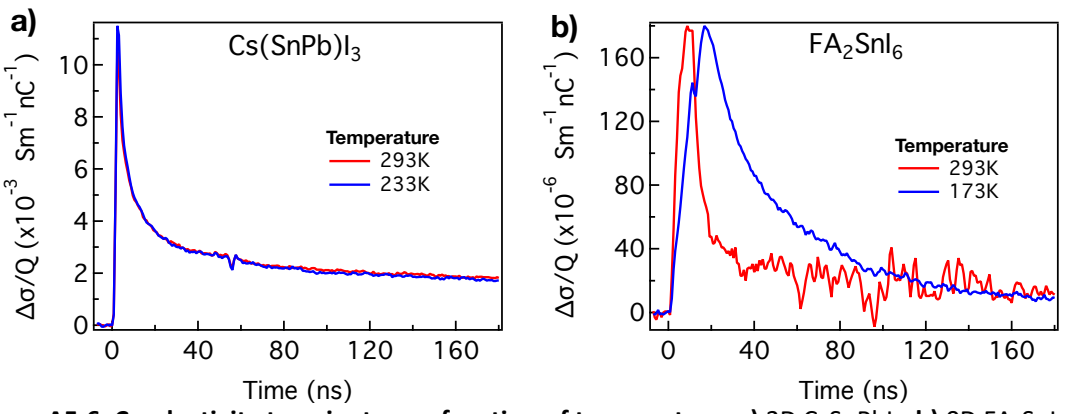

Figure A5.6. Conductivity transients as a function of temperature. a) 3D $CsSnPbI_3$. **b)** 0D FA_2SnI_6.

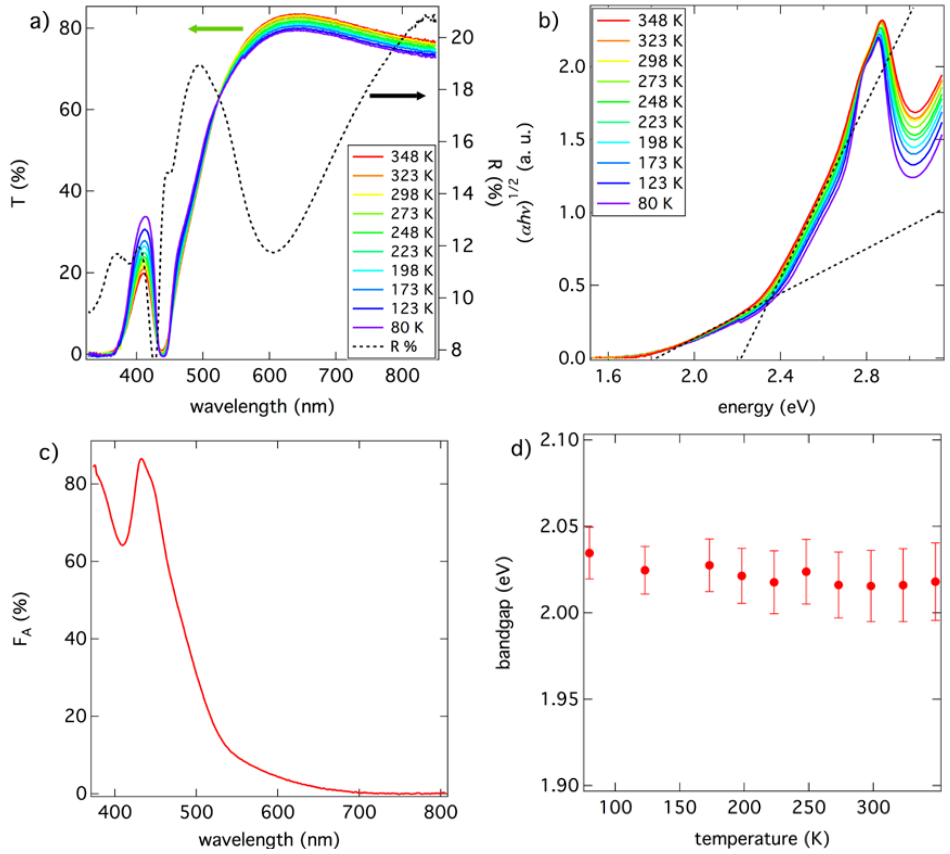

Figure A5.7. Temperature dependent optical characterization of $Cs_2AgBiBr_6$ single crystals. a) Temperature dependent transmittance (colored solid lines) and room temperature reflectance (black dashed line) of the Cs2AgBiBr6 thin film. **b)** Tauc plot calculated assuming indirect allowed transition. The linear regions at lower and higher energy correspond to photon absorption assisted by the absorption or the emission of a phonon, respectively. The fit of these regions for the room temperature data is represented by black dashed lines. The bandgap is the midpoint between the two x-intercepts of the linear regions. **c)** Fraction of absorbed photons measured at room temperature for the Cs2AgBiBr6 thin film characterized by means of TRMC measurement in this paper. **d)** Temperature dependent bandgap of $Cs_2AgBiBr_6$ obtained from the fit of the linear regions of the Tauc plot.

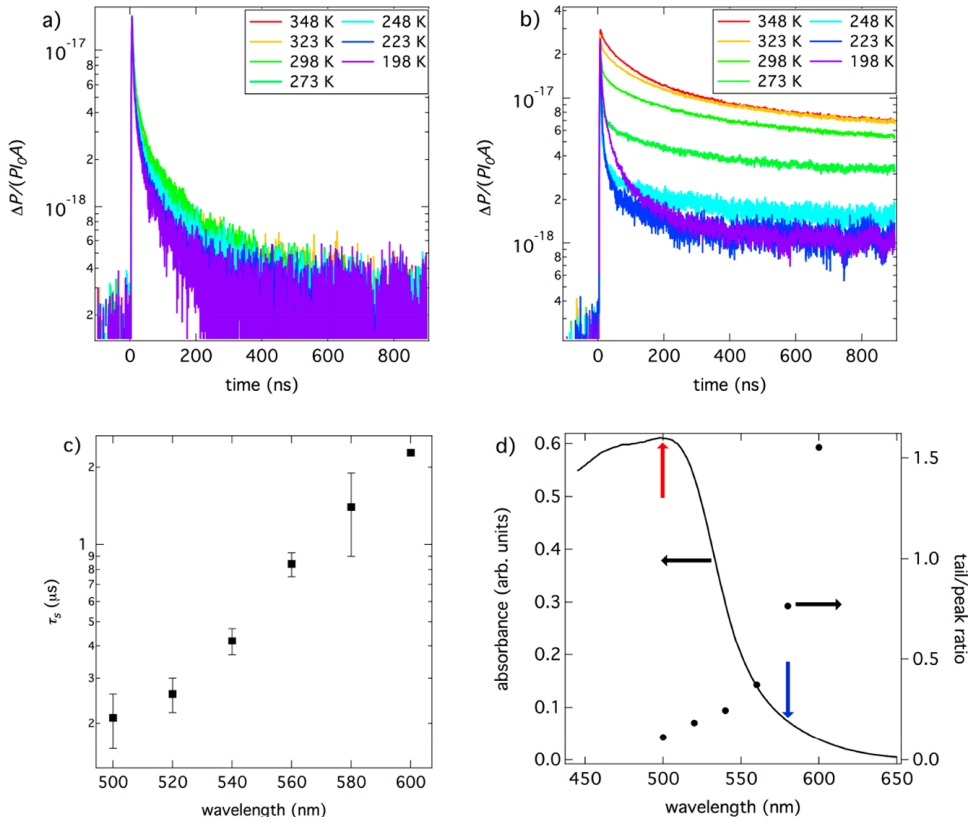

Figure A5.8. Photoconductivity TRMC experiments on $Cs_2AgBiBr_6$ crystals. a, b) TRMC traces for recorded upon pulsed laser excitation at 500 (a) and 580 nm (b) at indicated temperatures. The fraction of absorbed microwave power ΔP/P is normalized for the number of incident photons (I_0 ≈ 1.1 × 10^{15} cm^{-2}) and for the surface area of the sample (A ≈ 0.12 cm^2). **c)** Decay constant of the slow component of the room temperature TRMC traces measured upon pulsed laser excitation at different wavelengths. **d)** Absorbance spectrum of $Cs_2AgBiBr_6$ (solid line) and the tail/peak ratio of the TRMC traces measured upon pulsed laser excitation at different wavelengths, with incident photon fluence I_0 ≈ 1.1 × 10^{15} cm^{-2} (dots). The red and blue arrows indicate the absorbance at 500 and 580 nm, respectively.

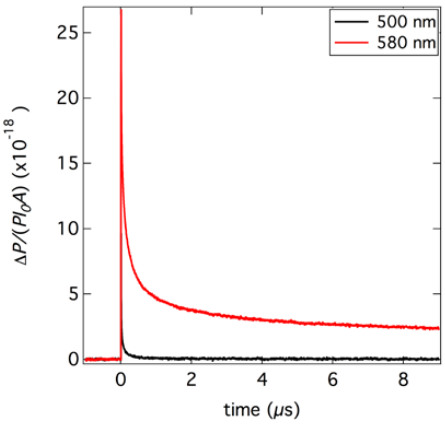

Figure A5.9. TRMC traces at room temperature for $Cs_2AgBiBr_6$ crystals recorded upon pulsed laser excitation at 500 (black) and 580 nm (red). The fraction of absorbed microwave power ΔP/P is normalized for the number of incident photons (I_0 ≈ 2.5 × 10^{15} cm^{-2}) and for the surface area of the sample (A ≈ 0.12 cm^2).

Table A5.1. XPS elemental analysis of $Cs_2AgBi_{1-x}Sb_xBr_6$ powders.

x		% Cs	% Ag	% Bi	% Sb	% Br	Sb/(Sb+Bi)
0	*spot 1*	34.26	8.67	8.79	0.09	48.20	0.010
	spot 2	26.09	6.06	8.30	0.03	59.52	0.004
	average	30.18	7.37	8.55	0.06	53.86	**0.007**
0.05	*spot 1*	24.60	9.14	7.62	0.66	57.97	0.080
	spot 2	25.28	10.21	7.10	0.42	57.00	0.056
	average	24.94	9.68	7.36	0.54	57.49	**0.068**
0.1	*spot 1*	25.57	8.91	7.06	1.66	56.80	0.190
	spot 2	26.00	8.85	6.56	1.51	57.09	0.187
	average	25.79	8.88	6.81	1.59	56.95	**0.189**
0.4	*spot 1*	24.41	9.32	5.00	3.73	57.54	0.427
	spot 2	25.09	9.11	4.85	3.80	57.15	0.439
	average	24.75	9.22	4.93	3.77	57.35	**0.433**

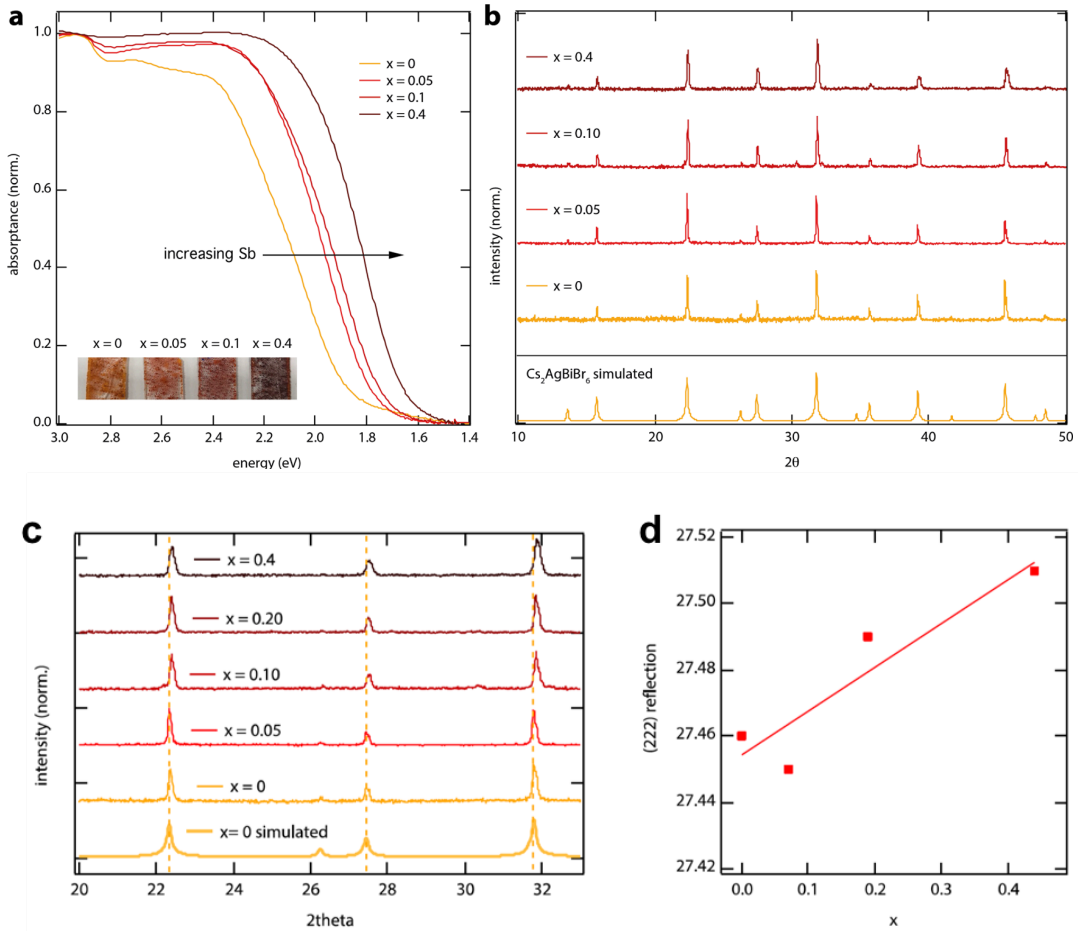

Figure A5.10. Characterization of $Cs_2AgBi_{1-x}Sb_xBr_6$ powders. a) Absorptance spectra normalized to unity to account for different surface coverages. **b)** Powder X-ray diffraction (XRD) patterns (Cu Kα radiation, λ = 1.54 Å) of mixed antimony–bismuth HDP powders with the general formula $Cs_2AgBi_{1-x}Sb_xBr_6$. Inset shows images of the powders with different Sb content. **c)** Zoom-in of the X-Ray Diffraction patterns of $Cs_2AgBi_{1-x}Sb_xBr_6$ from Figure 1b. The yellow dotted lines indicate the positions of the (022), (222) and (004) reflections, respectively, for $Cs_2AgBiBr_6$, showing that these shift to larger 2θ values for increasing x. This confirms that the lattice contracts on replacing Bi with the smaller Sb. **d)** 2θ value of (222) reflection as function of Sb-content (using the x values from Table S1).

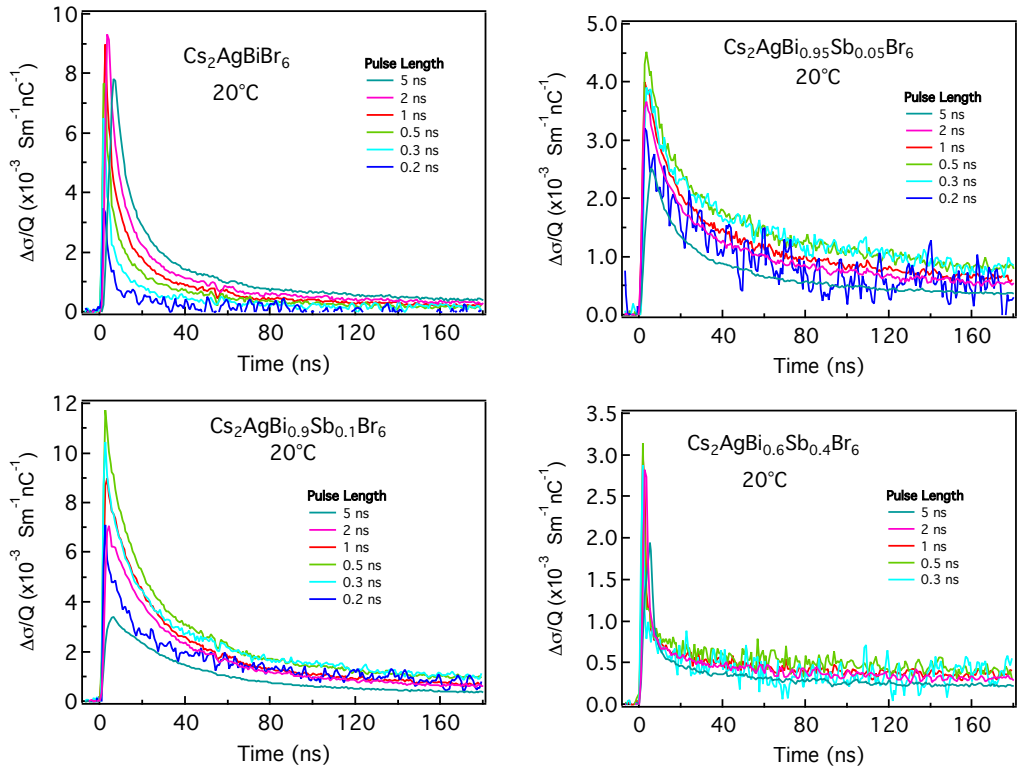

Figure A5.11. PR-TRMC lifetimes for the different $Cs_2AgBi_{1-x}Sb_xBr_6$ powders.

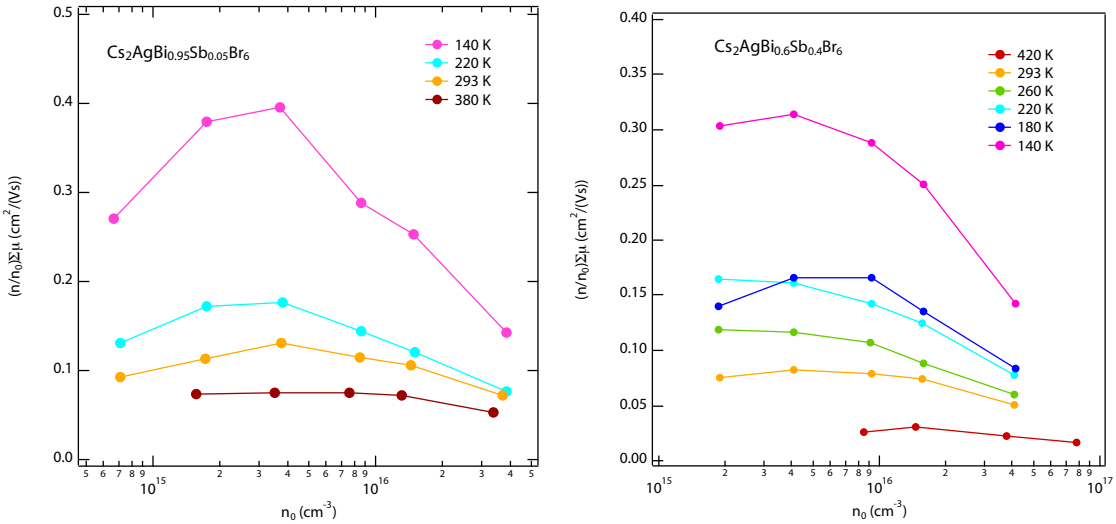

Figure A5.12. $(n/n_0)\sum\mu$ as function of n_0 and temperature for $Cs_2AgBi_{1-x}Sb_xBr_6$ with x = 0.05 (left) and x = 0.4 (right). Similar to the data shown in Figure 2b in the main text, we used the maximum $(n/n_0)\sum\mu$ at each temperature to estimate the trap saturation density, which is shown in Figure 2c. Note that for $Cs_2AgBi_{0.6}Sb_{0.4}Br_6$, at 220 K and higher the $\sum\mu$ (T) is nearly flat up to ~4 x 10^{15} cm^{-3}, suggesting that trap saturation occurs at or below the lowest densities used for the measurements.

Appendix Chapter 6

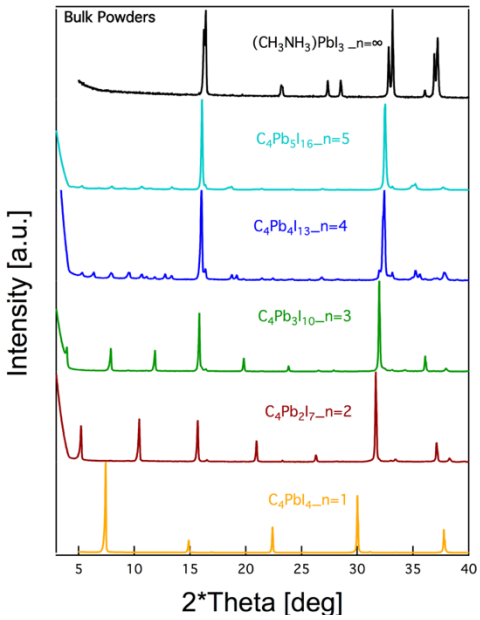

Figure A6.1. XRD of $(BA)_2(MA)_{n-1}Pb_nI_{3n+1}$ (n = 1-5) and $MAPbI_3$ powders.

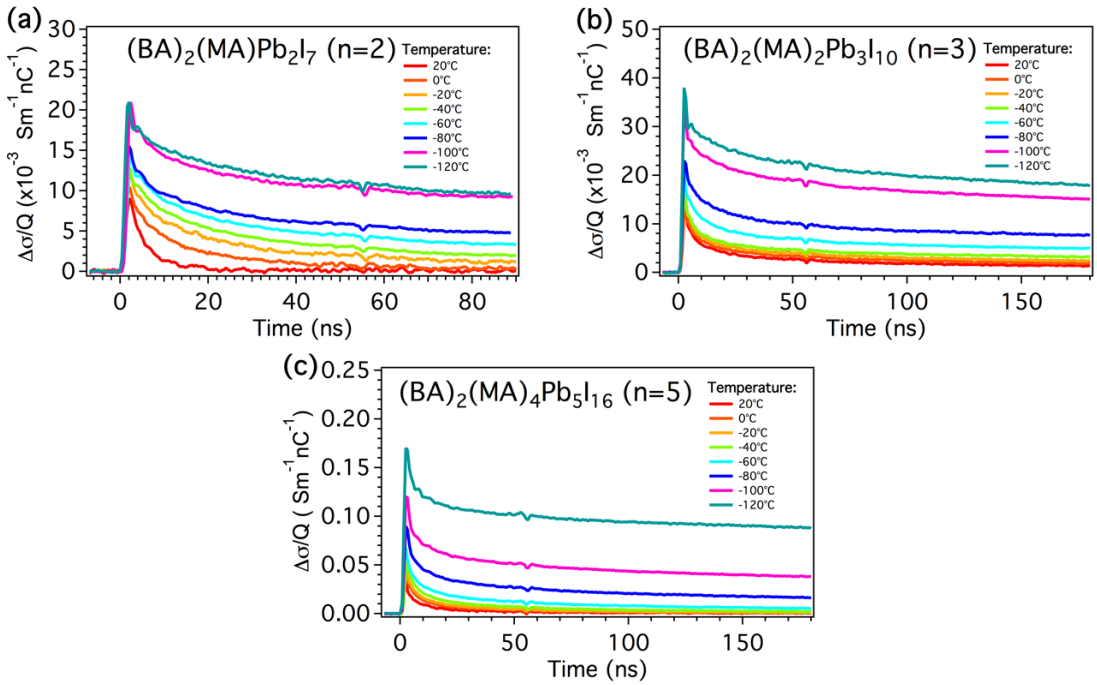

Figure A6.2. Temperature dependence of the radiation induced Conductivity (PR-TRMC) as a function of time. a) $(BA)_2(MA)Pb_2I_7$ (n=2). **b)** $(BA)_2(MA)_2Pb_3I_{10}$ (n=3). **c)** $(BA)_2(MA)_4Pb_5I_{16}$ (n=5) at different temperatures.

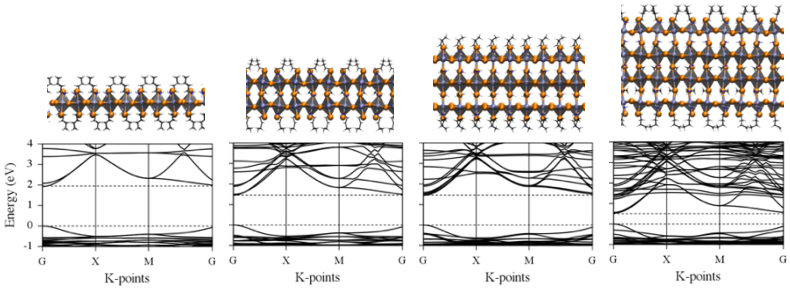

	n=1		n=2		n=3		n=4	
	hole	elec	hole	elec	hole	elec	hole	elec
m_1	-0.24	0.21	-0.18	0.16	-0.16	0.15	-0.13	0.16
m_2	-0.26	0.15	-0.20	0.13	-0.17	0.13	-0.15	0.13

Figure A6.3. DFT Band Structure Calculation of multilayered 2D Perovskites

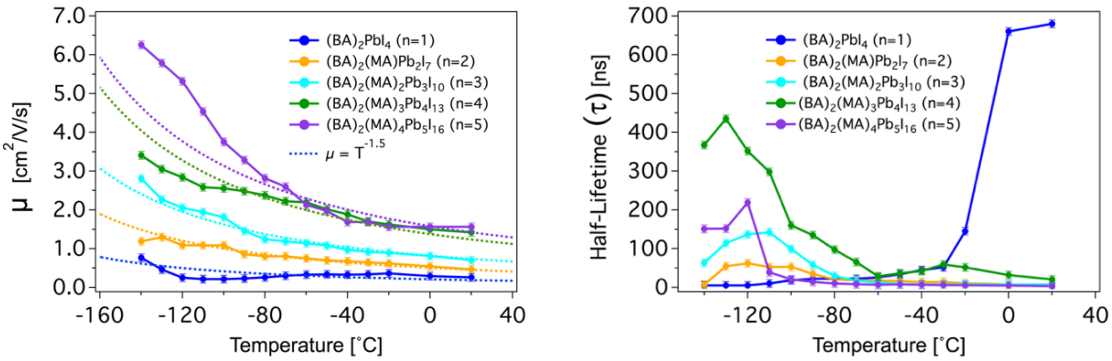

Figure A6.4. PR-TRMC experiments of 2D perovskites (n= 1-5) as a function of temperature. a) Mobility of charges fitted to $\mu=T^{-1.5}$**. b)** Half-lifetime.

Differential Scanning Calorimetry (DSC) measurements

Below -60°C, larger increments are observed in Figure A6.2. Motivated by the phase change present in $(BA)_2PbI_4$ (n=1), we have performed DSC measurements on these compounds to identify possible changes in the phase structure that affect the charge dynamics. These measurements reveal a reversible phase transition at ~0°C that is present in all 2D materials (n=1, 2, 3, 4, 5) but not in $MAPbI_3$ (Figure A6.5 and Figure A6.6a). In addition, we observe a phase transition at temperatures lower than -60°C in the multilayered n=2, 3, 4, 5 (Figure A6.5 and Figure A6.6b). The latter transition appears with the inclusion of MA, and approach closer to the tetragonal (β) to orthorhombic (γ) phase transition (-115°C) of $MAPbI_3$ as the PbI_6^{4-} with MA layers become thicker. Further research is required in order to determine the structural behavior of these compounds at different temperatures and its relation with the charge dynamics.

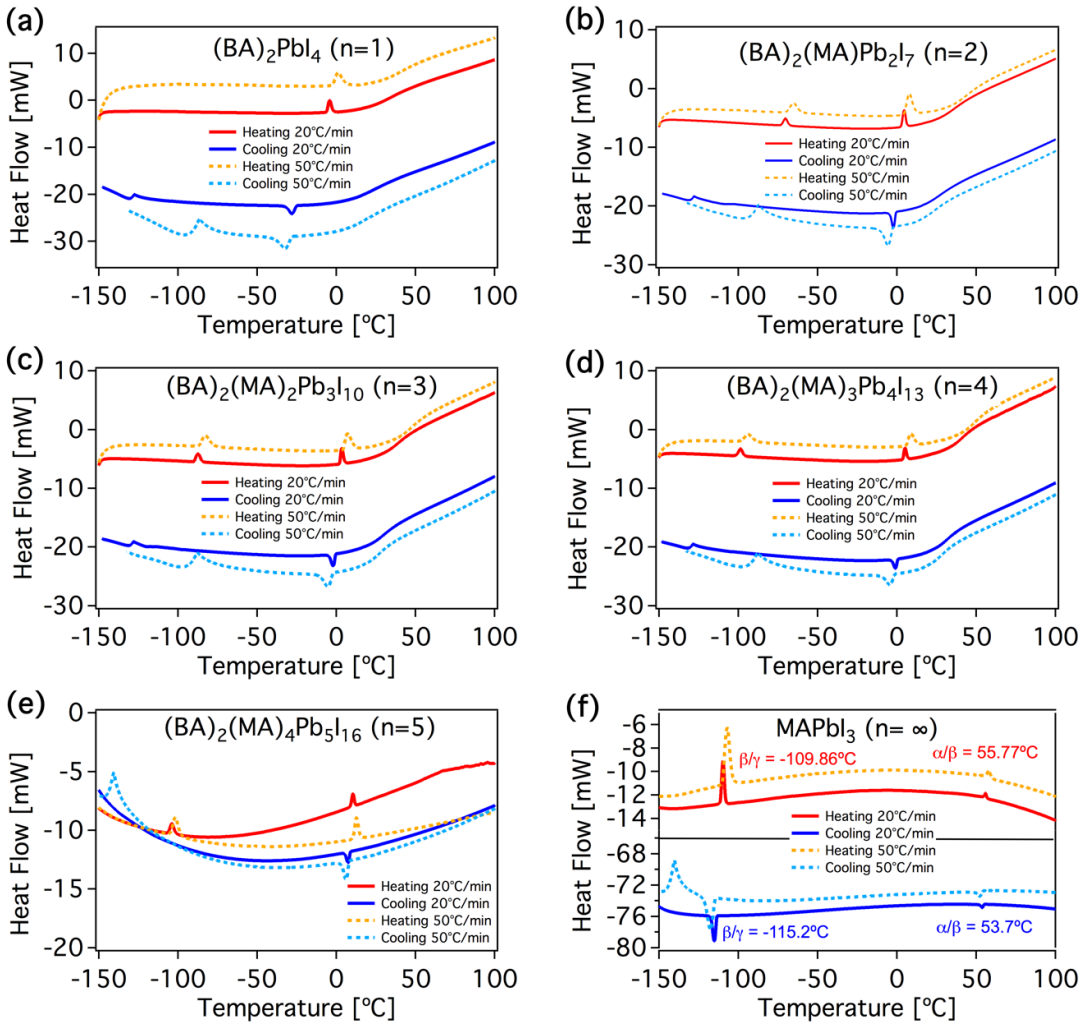

Figure A6.5. Differential scanning calorimetry (DSC) measurements. a) $(BA)_2PbI_4$ (n=1). **b)** $(BA)_2(MA)Pb_2I_7$ (n=2). **c)** $(BA)_2(MA)_2Pb_3I_{10}$ (n=3). **d)** $(BA)_2(MA)_3Pb_4I_{13}$ (n=4). **e)** $(BA)_2(MA)_4Pb_5I_{16}$ (n=5). **f)** $MAPbI_3$ (n= ∞).

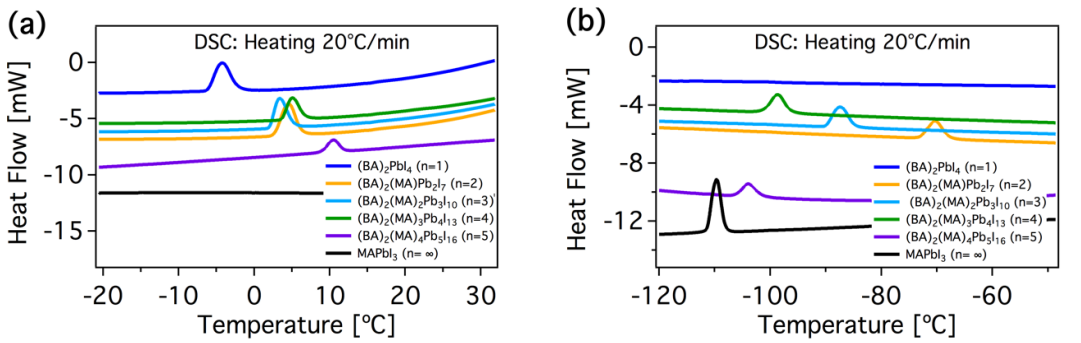

Figure A6.6. Zoom inset of DSC Measurements. a) Temperature around the 253K phase transition of BA_2PbI_4. **b)** Temperature around the 160K phase transition of $MAPbI_3$. Heating with a heat rate of 20˚C/min.

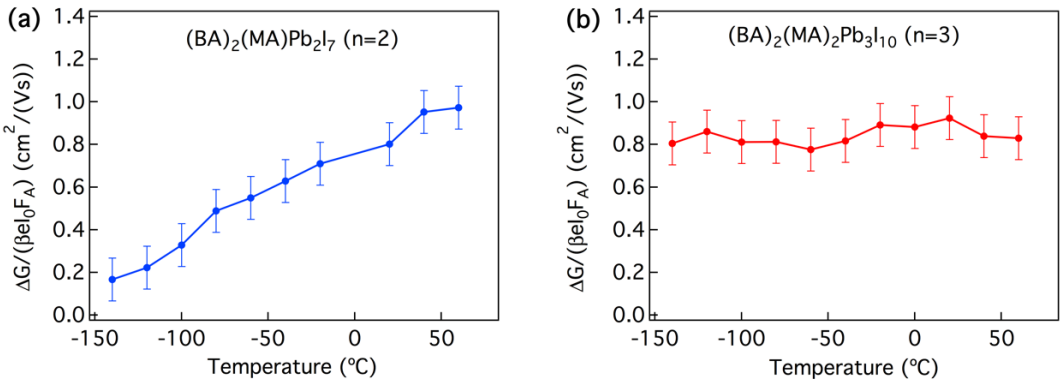

Figure A6.7. Photo-conductivity TRMC as a function of temperature. a) $(BA)_2(MA)Pb_2I_7$ (n = 2). **b)** $(BA)_2(MA)_2Pb_3I_{10}$ (n = 3). Excited at 473 nm with a photon intensity of $2x10^{11}$ cm^{-2}.

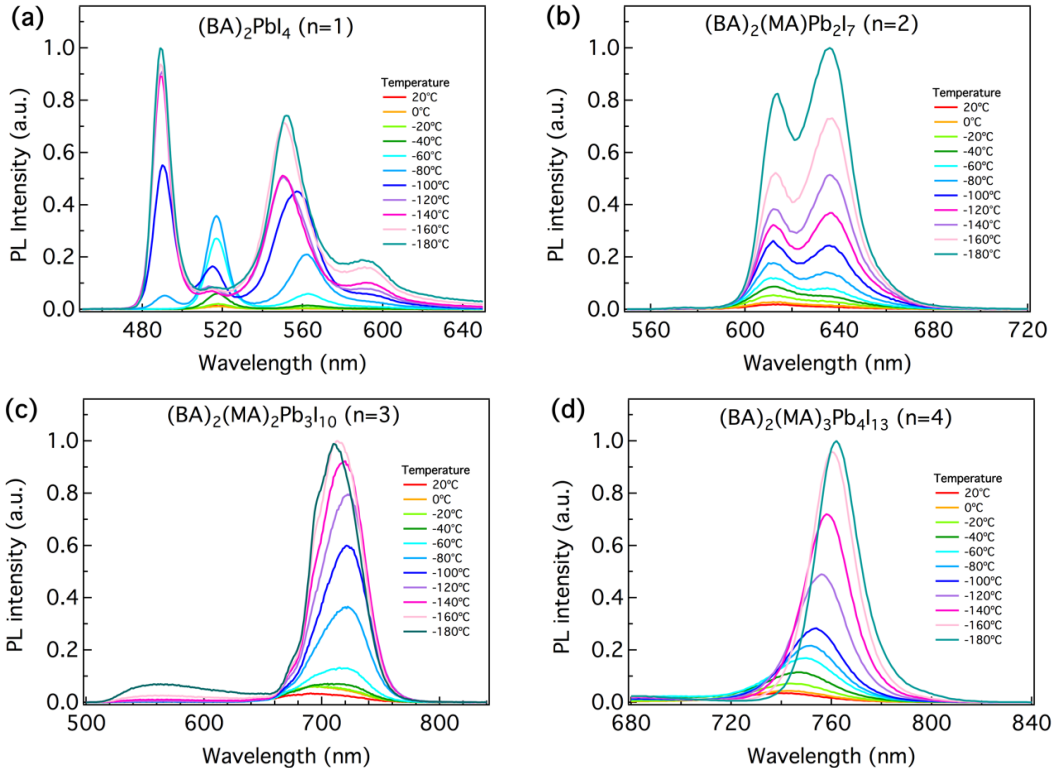

Figure A6.8. Photoluminescence emission spectra as a function of temperature. a) $(BA)_2PbI_4$ (n=1). **b)** $(BA)_2(MA)Pb_2I_7$ (n=2). **c)** $(BA)_2(MA)_2Pb_3I_{10}$ (n=3)**. d)** $(BA)_2(MA)_3Pb_4I_{13}$ (n=4).

Excitation densities on multilayered 2D hybrid perovskites films

We estimated the thickness of the films using a Bruker Dektak Profilometer 8. Knowing the approximate thickness of the films we calculated the excitation density ($n=F_AI_0/L$).

Where n is the excitation density (cm^{-3}), I_0 is the photon intensity (cm^{-2}), F_A is the fraction of absorbed light at the excitation wavelength and L is the thickness of the films. The results are summarized in Table A6.1 and Table A6.2 for the photo-conductivity TRMC and photo-luminescent measurements, respectively. The absorption measurements of the films were measured using a Perkin-Elmer Lambda 1050 spectrophotometer equipped with an

integrated sphere between 200 nm – 850 nm. The photo-luminescent were measured using an Edinburgh LifeSpec spectrometer equipped with a single photon counter between 450 nm – 850 nm. The laser wavelength in the PL set up is 405 nm, 1 MHz, with an approximate photon intensity of $1x10^{12}$ cm^{-2}. We estimated that the excitation density on the films ranges between $5x10^{14}$ cm^{-3} and $1x10^{15}$ cm^{-3} in the photo-conductivity TRMC measurements and $8x10^{14}$ cm^{-3} and $1x10^{16}$ cm^{-3} in the photo-luminescent measurements.

Table A6.1 Excitation density for photo-conductivity TRMC measurements

	n=1	n=2	n=3	n=4
Average thickness L (nm)	321.38	546.34	329.43	175.13
L standard deviation S^2 (nm)	103.95	129.22	138.10	102.79
Photon intensity I_0 (cm^{-2})	2.00E+11	1.55E+11	1.87E+11	1.63E+11
FA at 473nm	0.163	0.293	0.272	0.323
Excitation density n (cm^{-3})	1.02E+15	8.31E+14	1.55E+15	3.01E+15
Excitation density n- (cm^{-3})	1.50E+15	1.09E+15	2.66E+15	7.29E+15
Excitation density n+ (cm^{-3})	7.68E+14	6.72E+14	1.09E+15	1.90E+15

Table A6.2. Excitation density for PL measurements

	n=1	n=2	n=3	n=4
Average thickness L (nm)	321.38	546.34	329.43	175.13
L Standard deviation S^2 (nm)	103.95	129.22	138.10	102.79
Photon intensity I0 (cm^{-2})	1.00E+12	1.00E+12	1.00E+12	1.00E+12
FA at 405nm	0.238	0.325	0.314	0.294
Excitation density n (cm^{-3})	7.39E+15	5.95E+15	9.54E+15	1.68E+16
Excitation density n- (cm^{-3})	1.09E+16	7.80E+15	1.64E+16	4.06E+16
Excitation density n+ (cm^{-3})	5.58E+15	4.81E+15	6.72E+15	1.06E+16

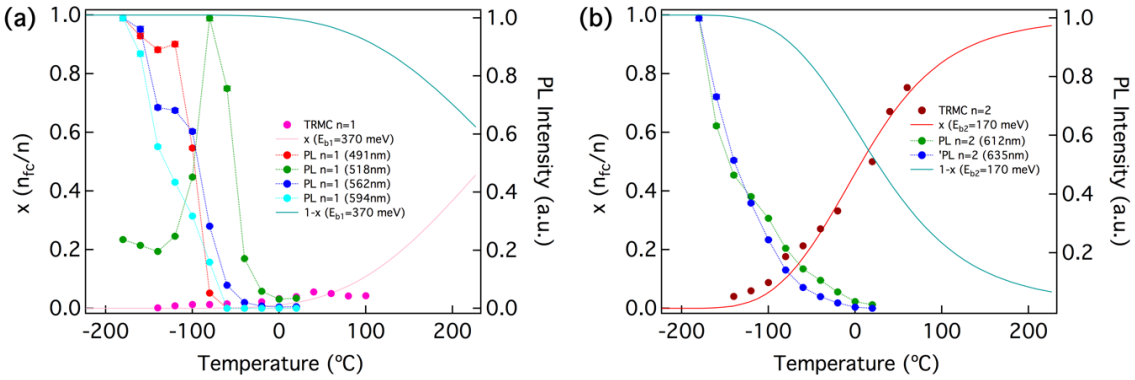

Figure A6.9. Fraction of free charges estimated from TRMC measurements (pink and red symbols) and the fraction of bound excitons obtained from PL as a function of temperature. a) $(BA)_2PbI_4$ (n=1). **b)** $(BA)_2(MA)Pb_2I_7$ (n=2). Excited at 405 nm with a photon intensity of ~$1x10^{12}$ cm^{-3}. For comparison, we plotted the fraction of free charges as a function of temperature determined by TRMC. The full lines are modeled using the Saha equation with excitation densities of $8x10^{14}$ cm^{-3} (PL) and $5x10^{14}$ cm^{-3} (TRMC).

Appendix Chapter 7

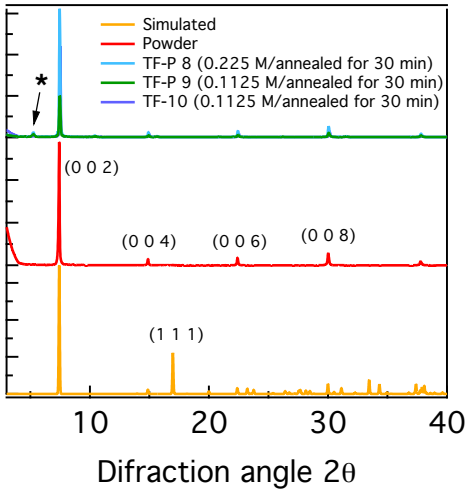

Figure A7.1. X-ray diffraction of BA_2PbI_4 thin films at unoptimized spin-coating conditions (high quartz temperature, aged precursors solutions, post-annealing at 383K).

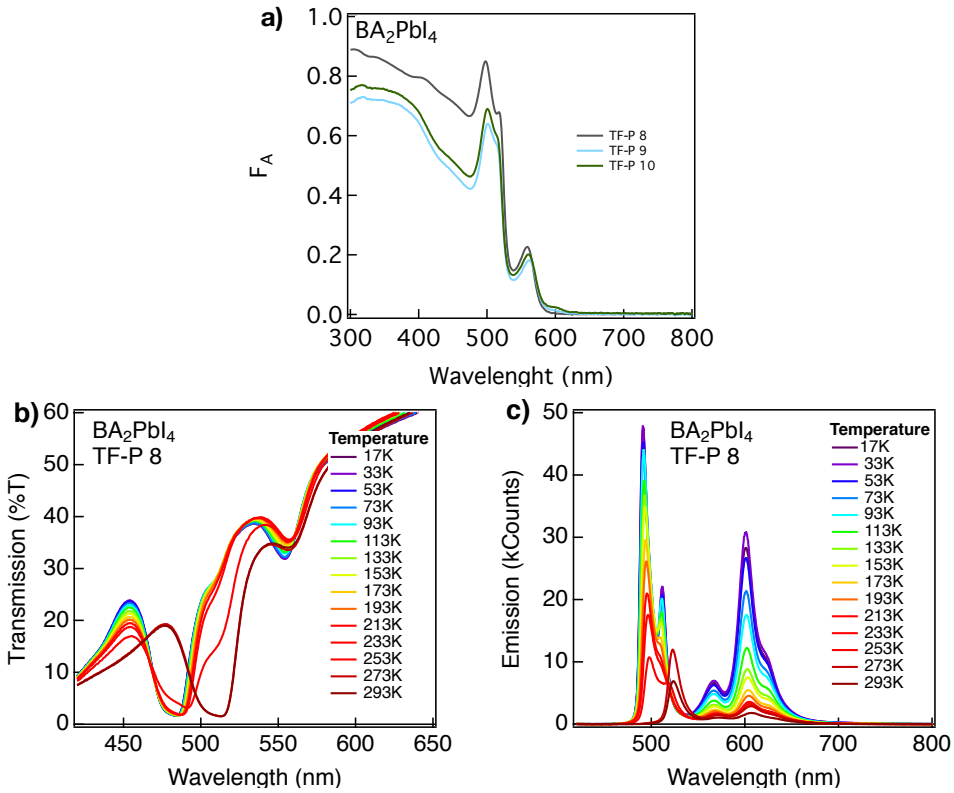

Figure A7.2. Optoelectronic properties of BA_2PbI_4 thin-films at unoptimized spin-coating conditions (high quartz temperature, aged precursors solutions, post-annealing at 383K). a) Steady-state absorption. **b)** Temperature dependent steady-state absorption and **c)** Photoluminescence emission measured inside a Helium cryostat. Photoluminescence excitation at 405 nm with a photon intensity ~ 1.7×10^{17} photon/(s cm^2).

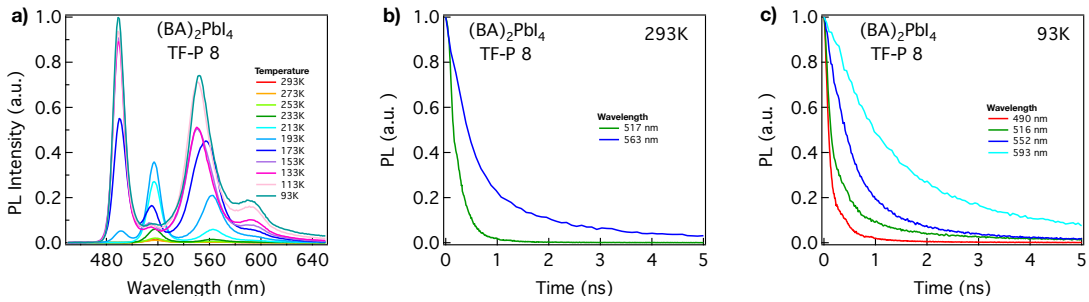

Figure A7.3. Temperature dependent photoluminescence (PL) measured in an Edinburgh LifeSpec spectrometer inside a nitrogen-cryostat. a) PL emission spectra. **Photoluminescent decay lifetime at maximum emission peaks. b)** At 294 K from 517 nm and 563 nm. **c)** At 93K from 490 nm, 516 nm, 552 nm and 593 nm. Excitation at 405 nm, 1 MHz, photon intensity ~1x10^{12} photon/(cm^2).

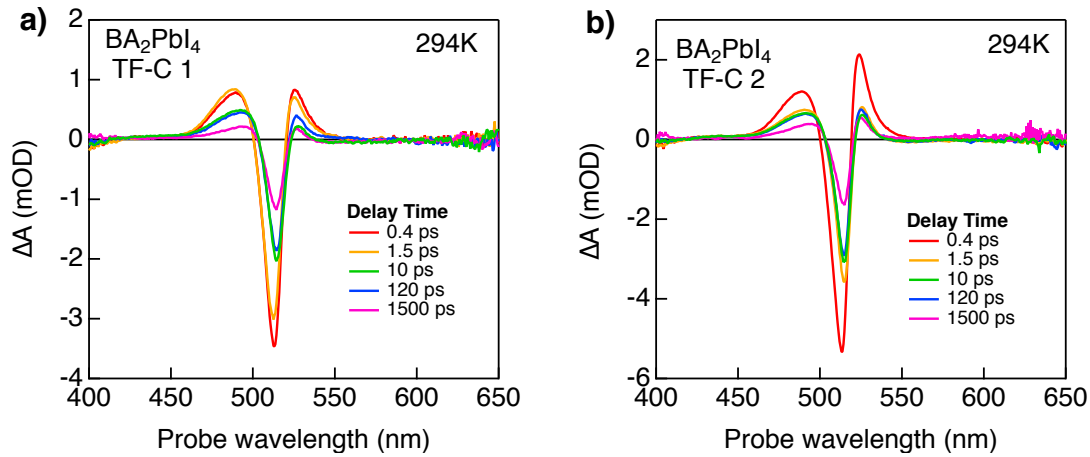

Figure A7.4. a, b) TA spectra as a function of delay times at 294K of BA_2PbI_4 thin-films made from crystals. Absorbed photon intensities ~1.5x10^{12} ph/(cm^2 pulse).

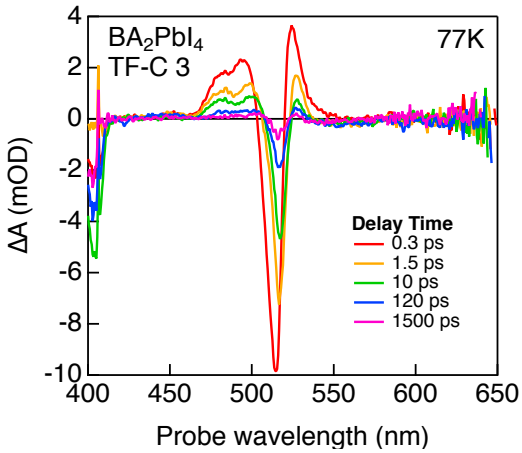

Figure A7.5. TA spectra as a function of delay times at 77K of BA_2PbI_4 thin-film made from crystals. Absorbed photon intensities ~1.5x10^{12} ph/(cm^2 pulse).

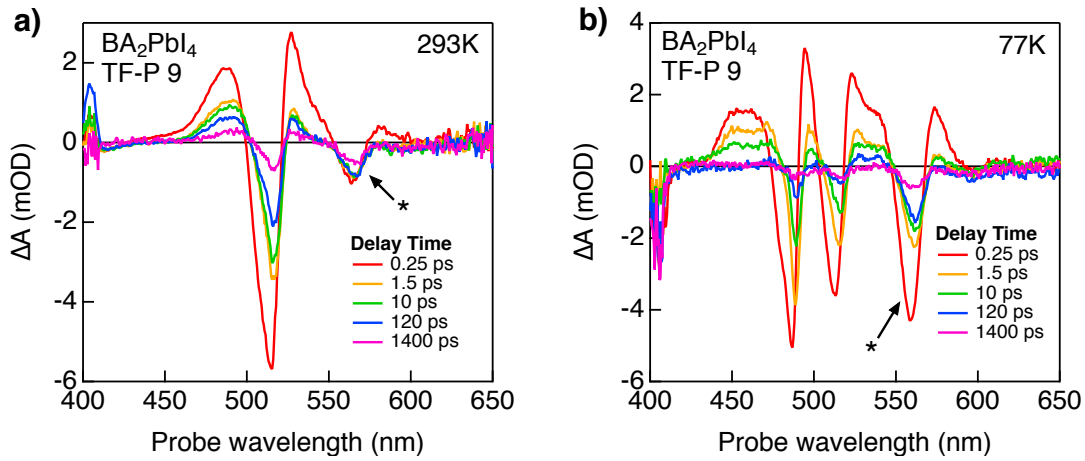

Figure A7.6. TA spectra as a function of delay times of BA_2PbI_4 thin-films from powders at unoptimized spin-coating conditions (high quartz temperature, aged precursors solutions, post-annealing at 383K). a) At 293K. **b)** At 77K. Absorbed photon intensities ~$3.2x10^{12}$ ph/(cm^2 pulse).

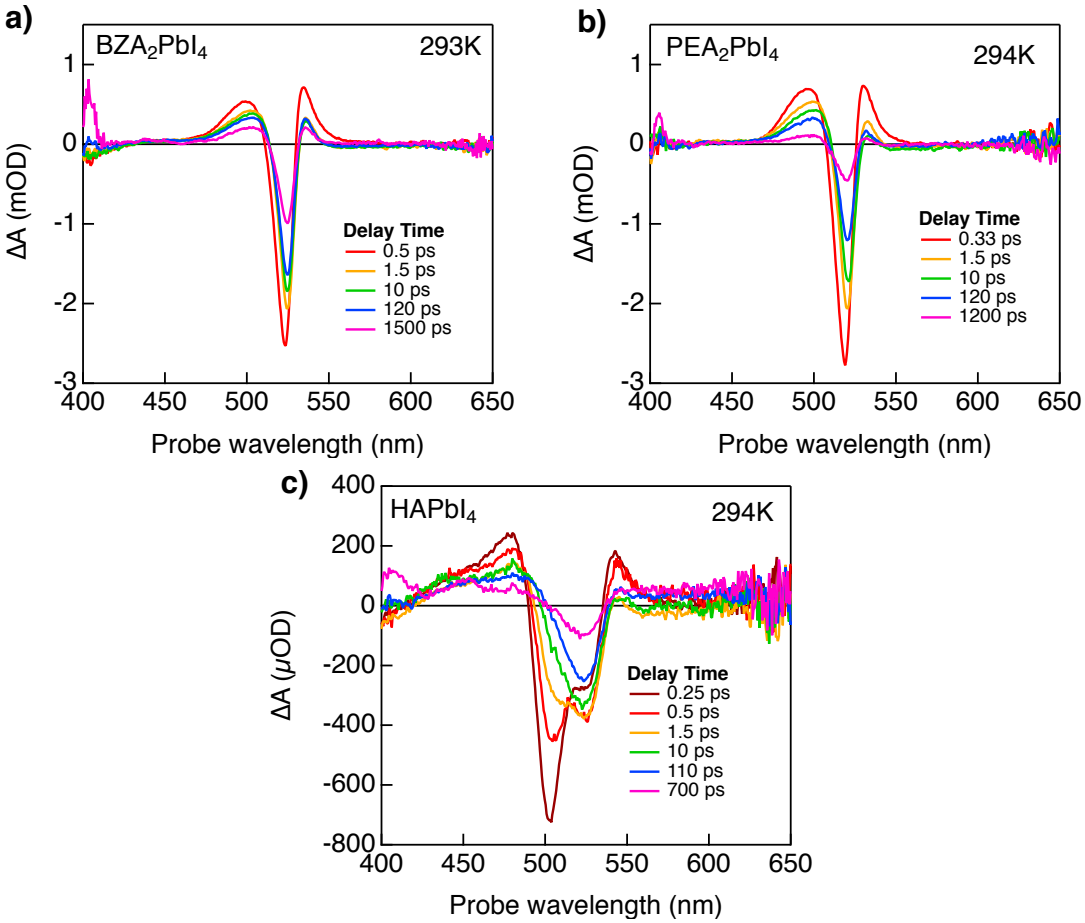

Figure A7.7. TA spectra as a function of delay times at 294K. a) BZA_2PbI_4 films. **b)** PEA_2PbI_4 films. **c)** $HAPbI_4$ films. Absorbed photon intensities ~$1.9x10^{12}$ ph/(cm^2 pulse), ~$1.3x10^{12}$ ph/(cm^2 pulse) and ~$1.8x10^{12}$ ph/(cm^2 pulse), respectively.

Appendix Chapter 8

Optical Properties of $CsPbBr_3$ Nanoplatelets (n=1 to n=6)

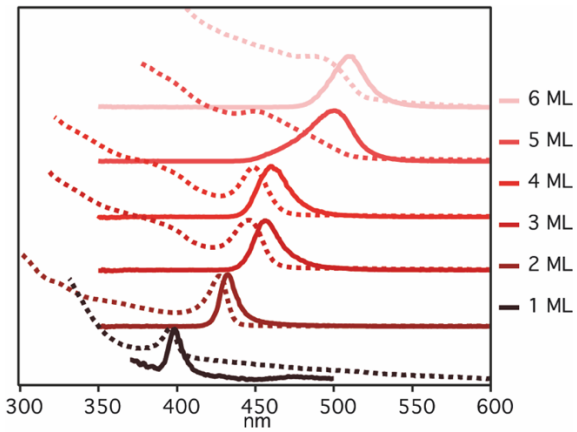

Figure A8.1. Absorption (dashed lines) and photoluminescence (full lines) spectra of CsPbBr3 nanoplatelets with varying thickness, ranging from 1 monolayer (ML) to 6 monolayers (6 ML).

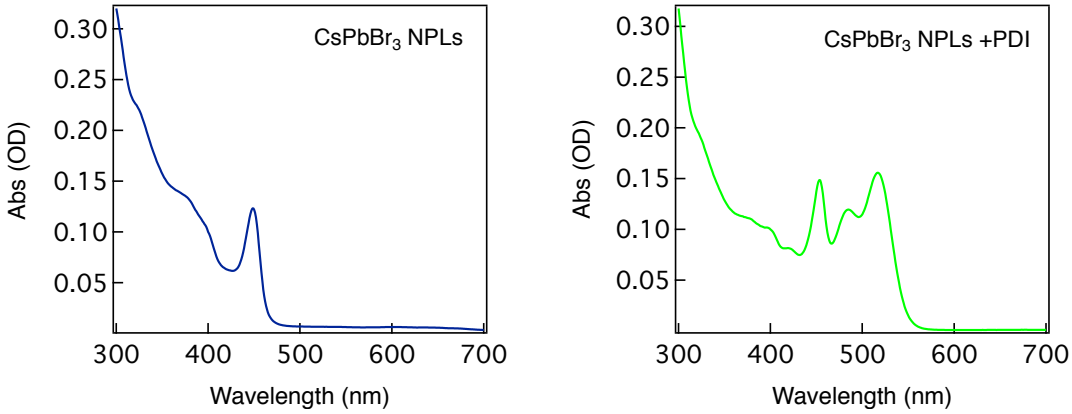

Figure A8.2. Fraction of absorbed light for $CsPbBr_3$ NPLs (left) and $CsPbBr_3$ + PDI hybrid (right)

NMR of PDI molecule

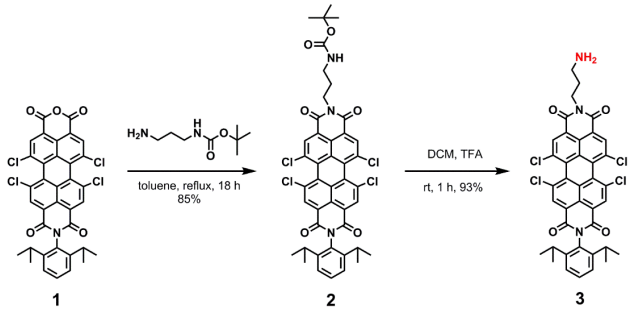

Figure A8.3. Synthesis scheme of N-(2,6-diisopropylphenyl)-N'-(3-aminopropyl)-1,6,7,12-tetrachloroperylene bisimide (3).

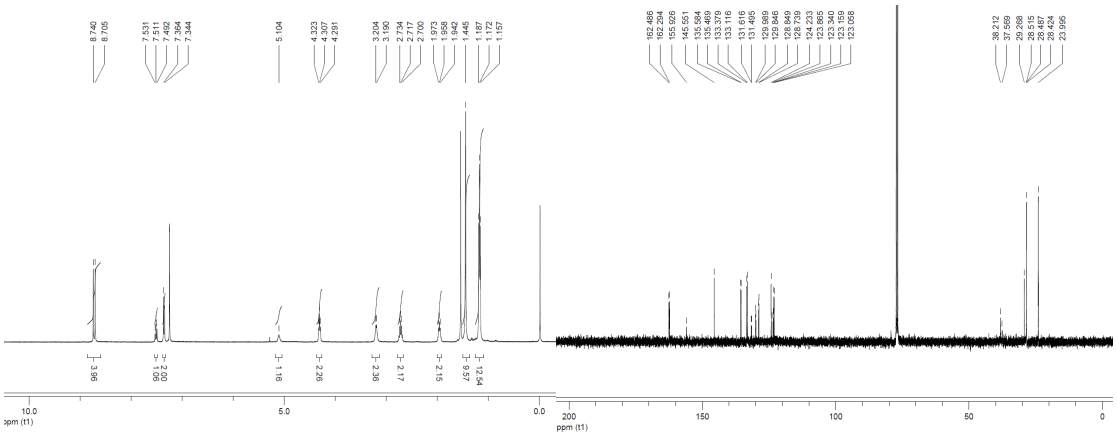

Figure A8.4. 1H and 13C NMR spectra of compound 2 in $CDCl_3$.

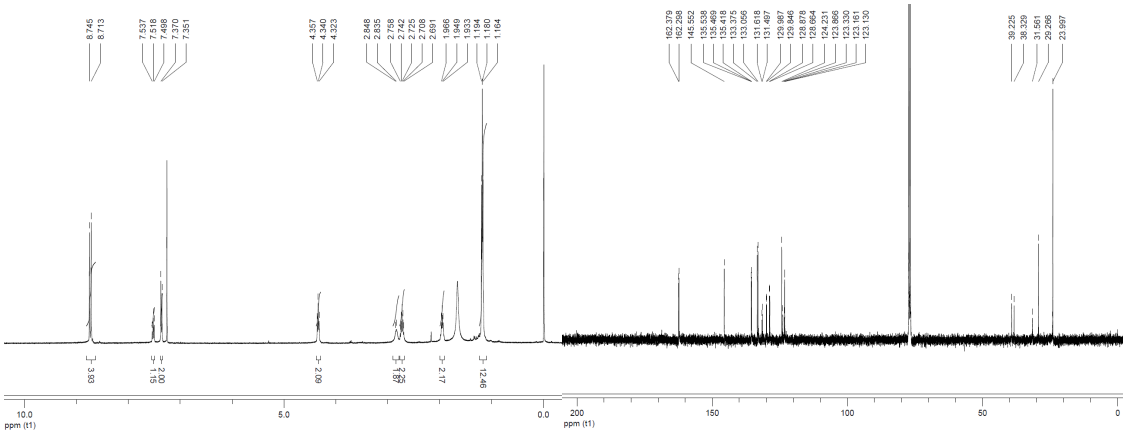

Figure A8.5. 1H and 13C NMR spectra of compound 3 in $CDCl_3$.

Picosecond Photoluminescence (PL) measurements

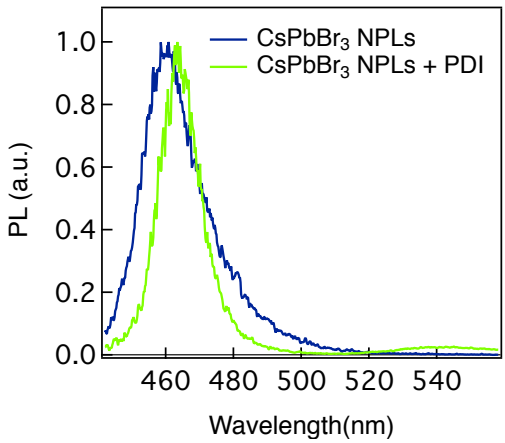

Figure A8.6. Photoluminescence emission slices of $CsPbBr_3$ and $CsPbBr_3$ + PDI hybrid excited at 400 nm at 60 ps (spectral range 450 nm to 550 nm).

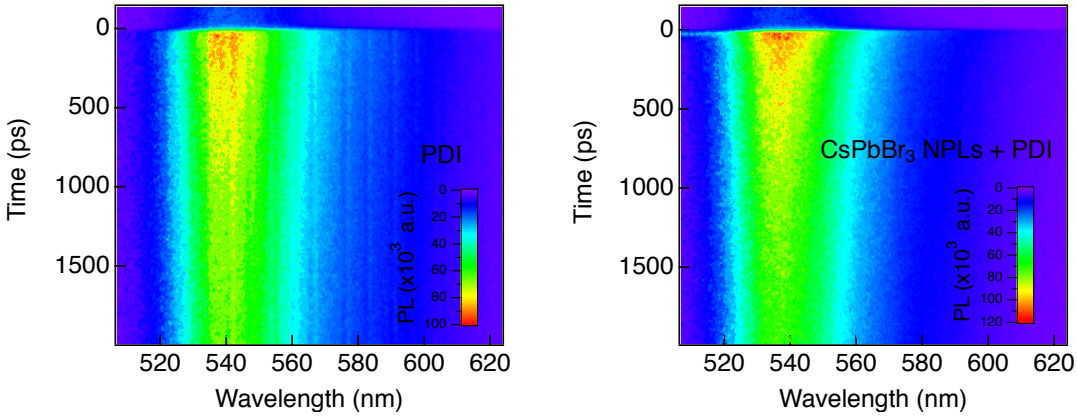

Figure A8.7. Photoluminescence emission slices of PDI (left) and $CsPbBr_3$ + PDI hybrid (left) excited at 400 nm (spectral range 500 nm to 625 nm).

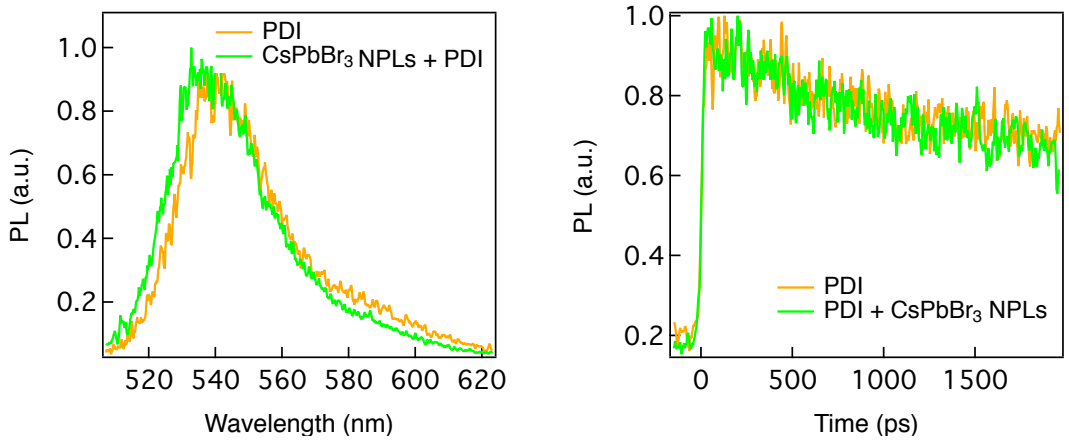

Figure A8.8 Photoluminescence emission slices of PDI and $CsPbBr_3$ + PDI hybrid excited at 400 nm at 60 ps (left) and comparison of the temporal decay of PDI and $CsPbBr_3$ + PDI hybrid at 540 nm (right).

Femtosecond Transient Absorption (TA)

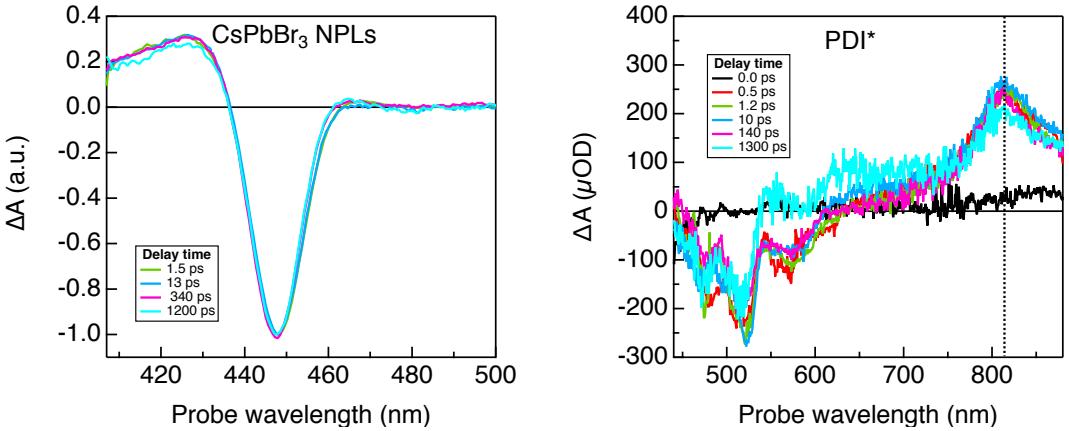

Figure A8.9. TA spectra as a function of time exciting at 400 nm. left) Normalized TA spectrum of $CsPbBr_3$ NPLs. **right)** TA spectrum of free PDI molecules in solution.

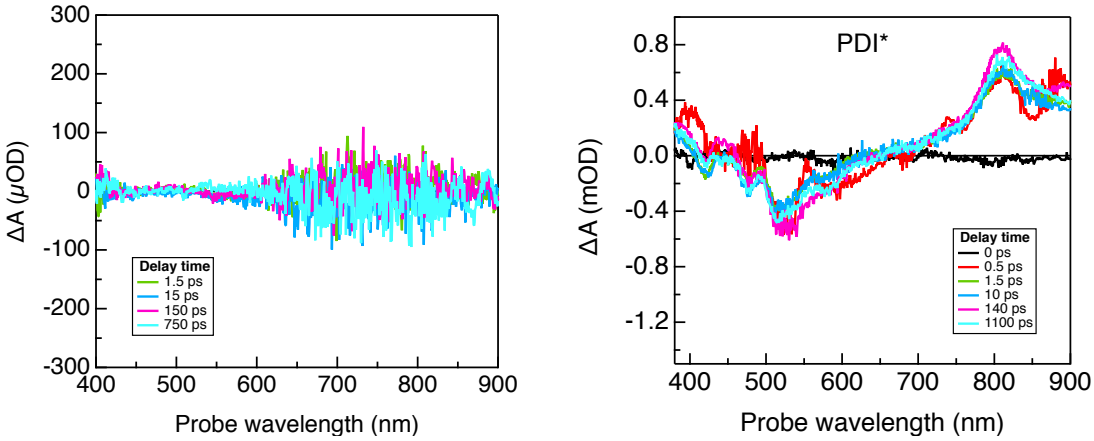

Figure A8.10. TA spectra as a function of time exciting at 510 nm. left) TA Spectrum of free CsPbBr3 NPLs. **Right)** TA Spectrum of free PDI molecules in solution.

Glotaran Global Target Analysis

The global and target analysis is performed with the Glotaran software. We have modelled the radiative recombination of both the perovskite NPLs and the PDI molecules; and also the electron and hole transfer between the two materials. Here we will describe each model along with the assumptions used and list the results. The models and the fitted rates are summarized in Supplementary Fig. 14.

PDI excited state kinetics. The radiative recombination of the PDI molecules was modelled with a simple single rate constant model. The decay of the PDI excited state (~4ns) is considerably longer than the time-window of the TA experiment, making it impossible to derive an accurate estimate of the decay time. Therefore, we measured the fluorescence lifetime of PDI molecules in solution on longer timescales by time-correlated single photon counting (TCSPC) using a Lifespec fluorescence lifetime spectrometer (Edinburgh Instruments). The resulting fluorescence lifetime (3.8 ns) was used as a fixed decay time for PDI* in the global analysis.

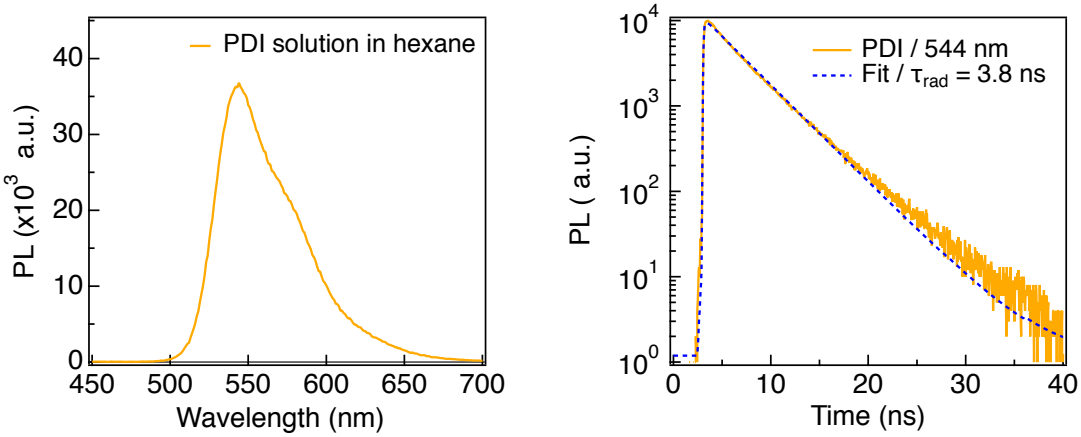

Figure A8.11. Photoluminescence lifetime from PDI molecules in hexane

$CsPbBr_3$ NPLs excited state kinetics. If a similar single rate constant model is used for the perovskite NPLs the model fails to fit the early timescales. Therefore, a sequential two rate constant model is used where the short lifetime of 3 ps is assigned to shallow trapping and the longer lifetime of 1.5 ns as the radiative recombination rate.

$CsPbBr_3$ NPLs + PDI hybrid exciting the NPLs at 400 nm. In order to keep the model for the electron transfer from the NPLs to the PDI molecules as simple as possible we again model it with a sequential two rate constant model. This first of all assumes that every NPL is connected to a PDI which is reasonable as the concentration of PDI molecules is much higher than the concentration of NPLs. The second thing to note about this model is that the fast rate constant in this model will not only be influenced by the electron transfer rate but also, to a small extent, the fast trapping in the NPLs. The second rate constant will then describe the charge recombination from the charge transfer state. We obtain an electron transfer rate of 12.6 ps and charge recombination of roughly 1.8 ns.

$CsPbBr_3$ NPLs + PDI hybrid exciting the PDI at 510 nm. When the hole transfer from the PDI to the NPLs is modelled a more complex model has to be used. Since the concentration of PDI is much higher than that of the NPLs there will be two different populations of PDI; (1) PDI connected to a NPL which will undergo hole transfer and (2) free PDI in solution that will decay radiatively as described above. The ratio between these populations is unknown and has to be modelled along with the hole transfer rate. The radiative recombination rate is assumed to be 3.8 ns as previously mentioned and the charge recombination rate is taken to be the same as it was for recombination of CT states formed by electron transfer. The ratio between the two PDI populations that we obtain is 6:4 and the hole transfer rate is 1.5 ps.

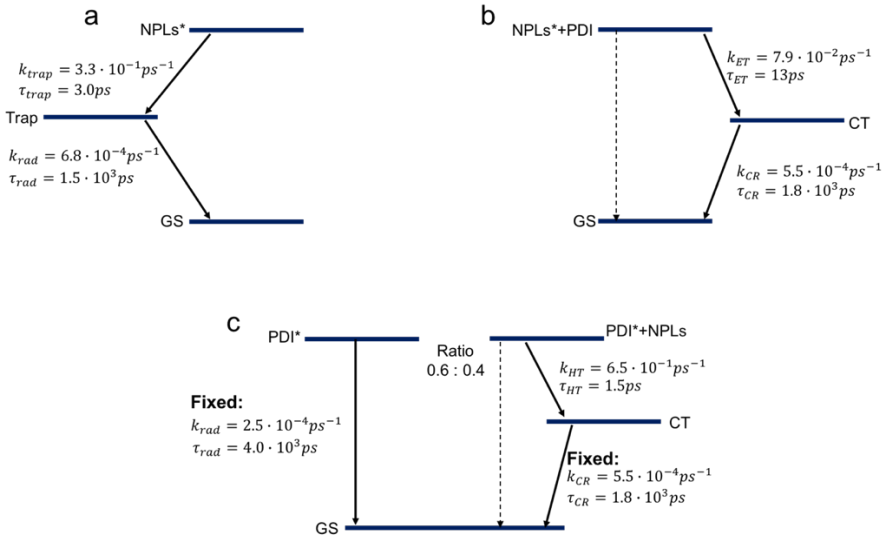

Figure A8.12. Global and target models used along with the fitted rates. a – only NPLs, b – electron transfer from NPLs* to PDI, c – hole transfer from PDI* to NPLs.

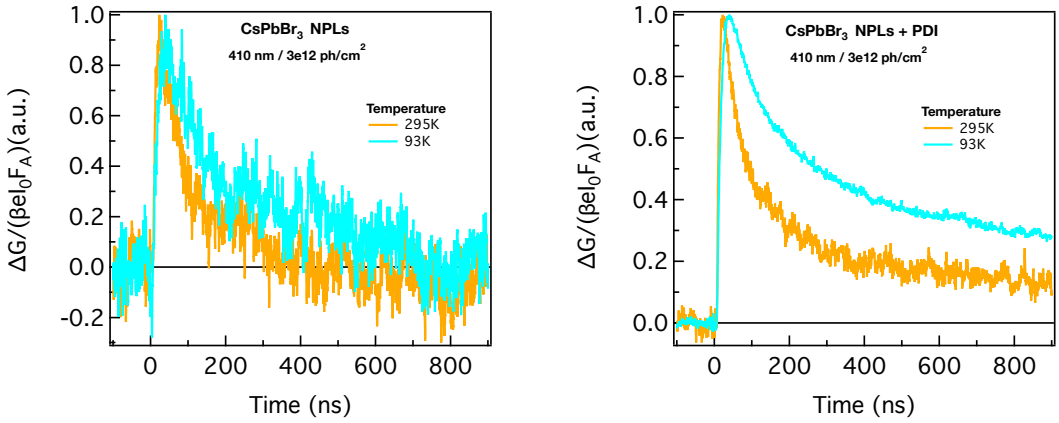

Figure A8.13. Normalized photoconductivity of CsPbBr3 NPLs and CsPbBr3 NPLs + PDI.

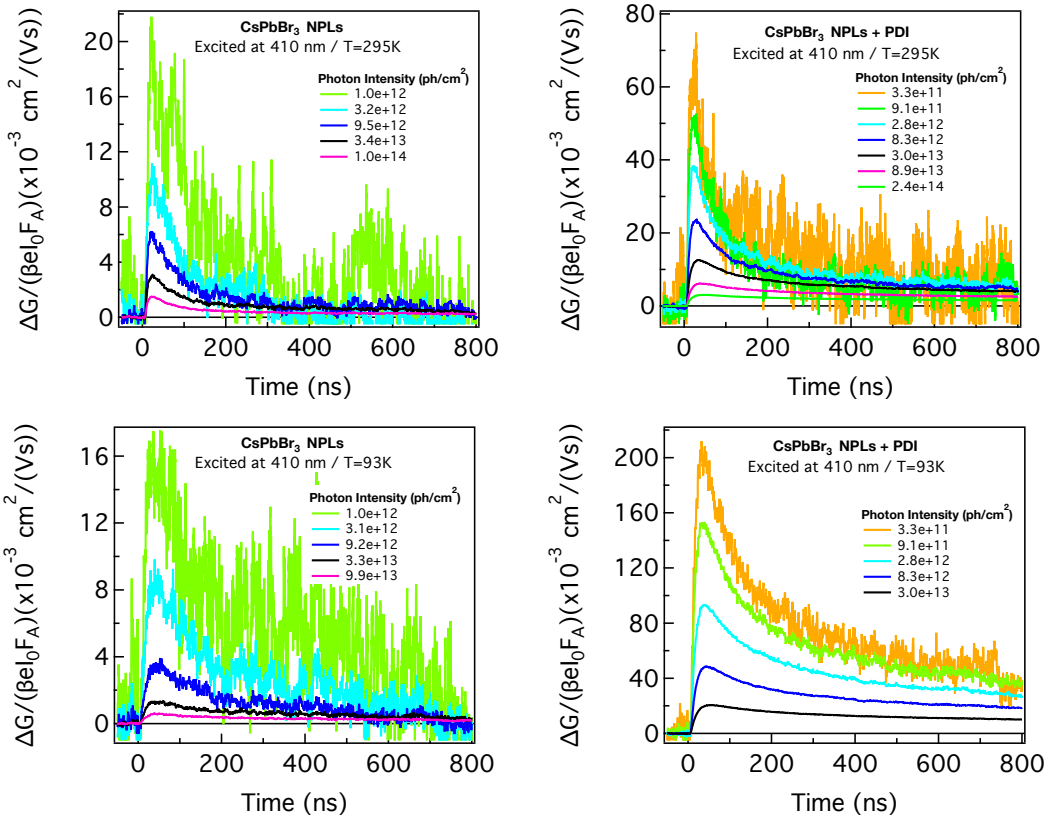

Figure A8.14. Photoconductivity transients as a function of photon intensity.

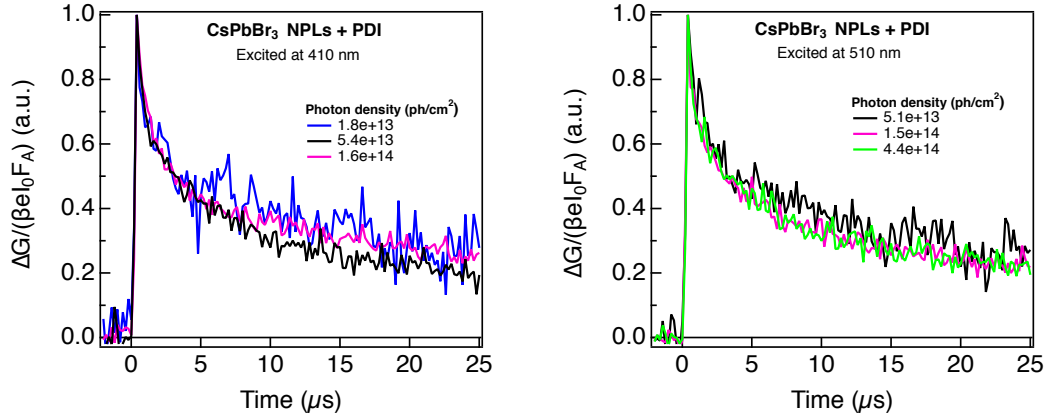

Figure A8.15. Normalized photoconductivity of $CsPbBr_3$ NPLs + PDI at 295K (μs time scale).

Appendix Chapter 9

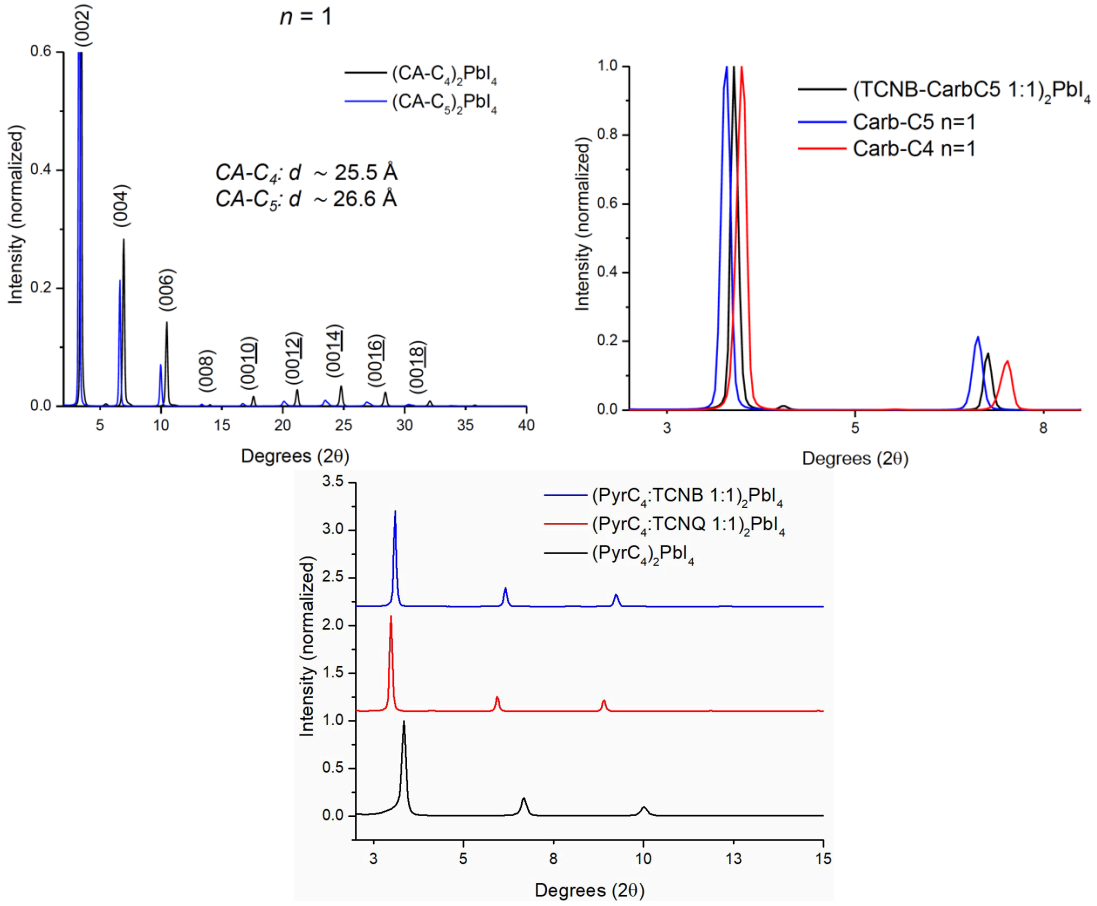

Figure A9.1. X-ray diffraction of 2D perovskite layers with functionalized organic donors and char-transfer complexes. Top, Carbazole based 2D perovskites. Bottom, Pyrene based 2D perovskites

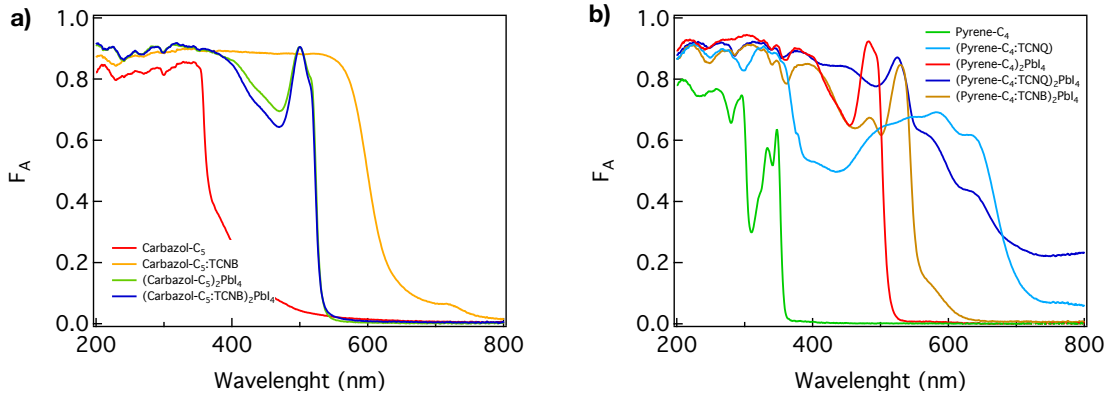

Figure A9.2. Steady state absorption of functionalized 2D perovskites. a) Carbazole based 2D perovskites. **b)** Pyrene based 2D perovskites.

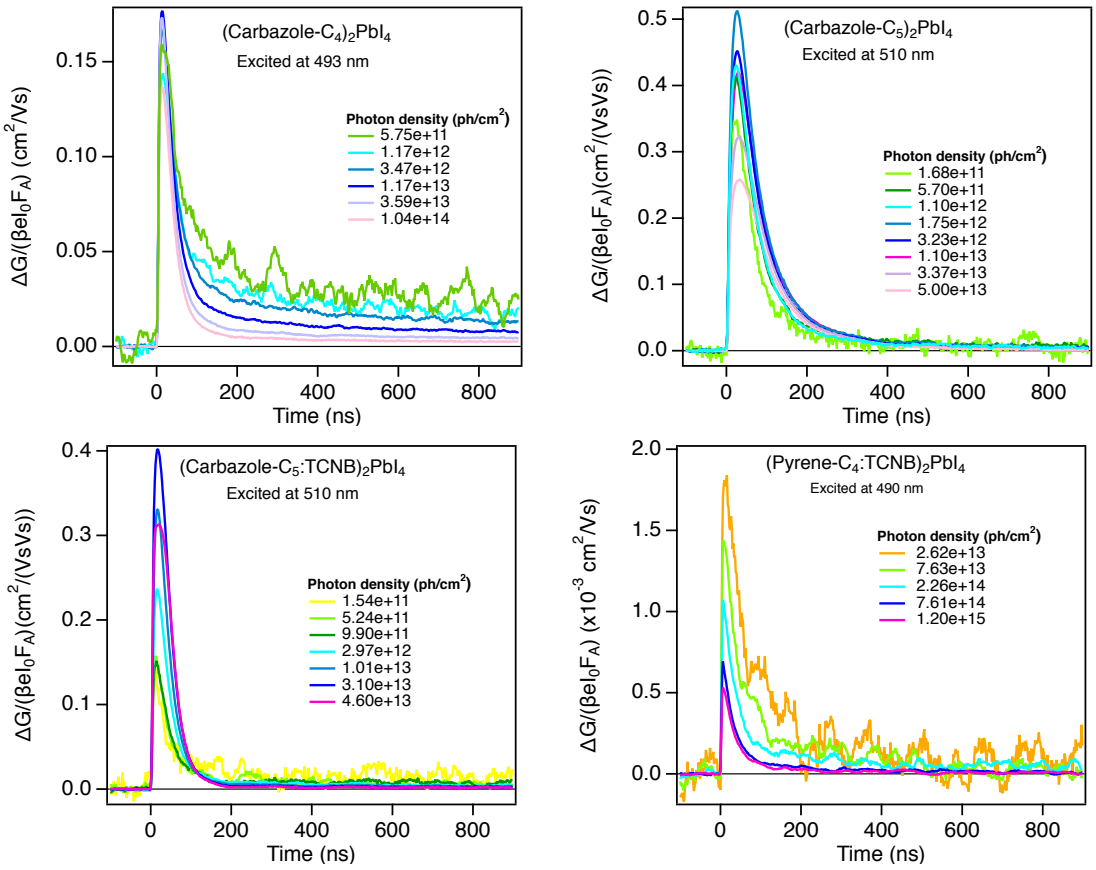

Figure A9.3. Photoconductivity TRMC of functionalized 2D perovskites.

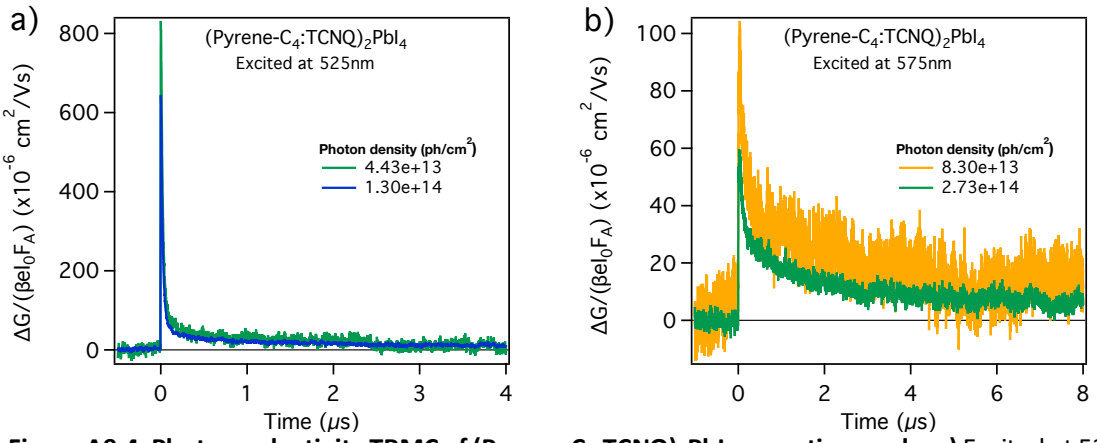

Figure A9.4. Photoconductivity TRMC of (Pyrene-C$_4$:TCNQ)$_2$PbI$_4$ on µs time scale. a) Excited at 525 nm. **b)** Excited at 575 nm.

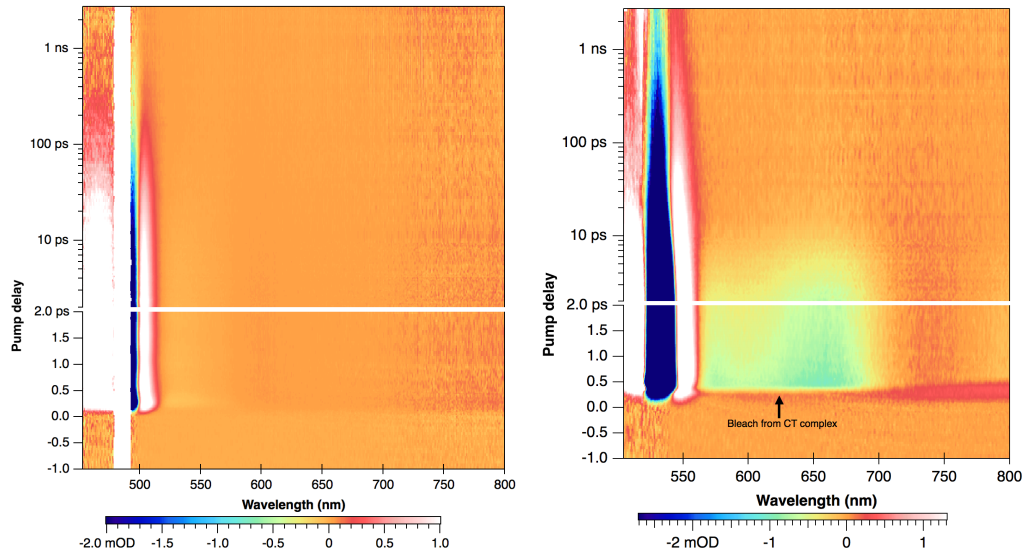

Figure A9.5. TA spectra photoexciting at excitonic peaks. Left) ($(Pyrene\text{-}C_4)_2PbI_4$ photoexcited at 490 nm. **Right)** $(Pyrene\text{-}C_4{:}TCNQ)_2PbI_4$ photoexcited at 520 nm.

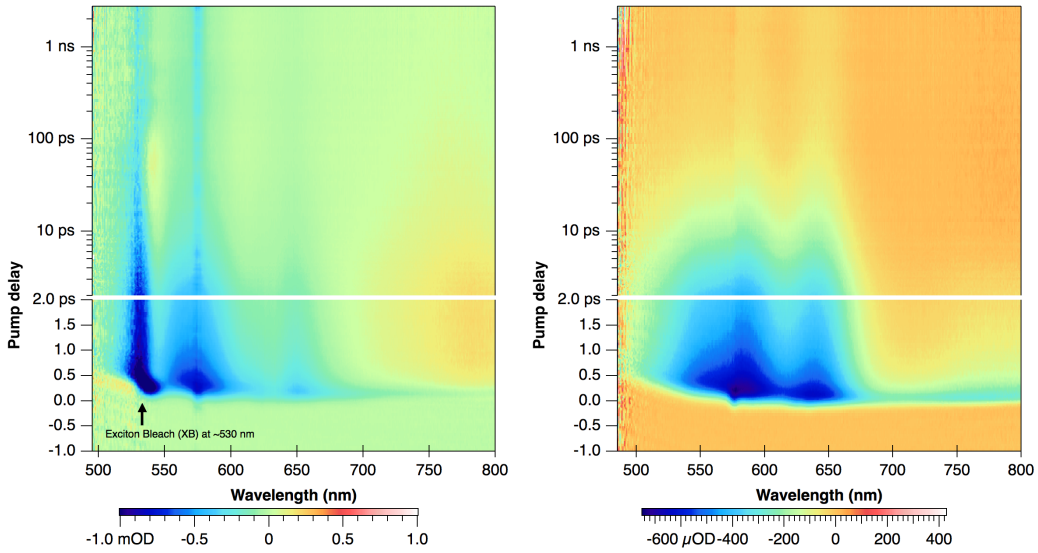

Figure A9.6. TA spectra photoexciting at CT State (575 nm). Left) $(Pyrene\text{-}C_4{:}TCNQ)_2PbI_4$. **Right)** $(Pyrene\text{-}C_4{:}TCNQ)$ CT organic complex.

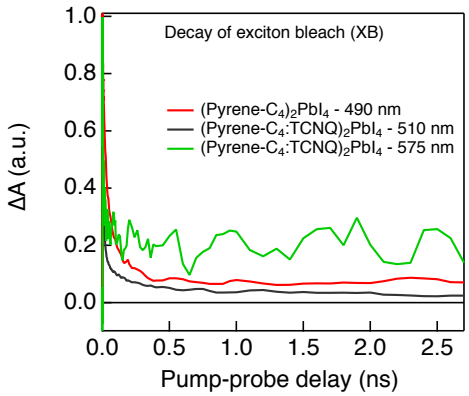

Figure A9.7. Temporal decay kinetics of the exciton bleach (XB) of (Pyrene-C4)2PbI4 (~500 nm) and (Pyrene-C4:TCNQ)2PbI4 (~530 nm) exciting at the excitonic peak (490 nm and 520 nm, respectively) and the CT state (575 nm).

Appendix Chapter 10

Table A10.1. Crystallographic and refinement parameters of 2,5-DMAI$_3$ and 2,5-DMASnI$_3$

	2,5-DMAI$_3$	**2,5-DMASnI$_3$**
Temperature (K)	100(2)	100(2)
Formula	$C_8H_{12}I_3N$	$C_8H_{12}I_3NSn$
Formula weight (g/mol)	502.89	621.58
Crystal size (mm^3)	0.08 × 0.10 × 0.16	0.02 × 0.06 × 0.22
Crystal color	Black/dark red	Yellow
Crystal system	Monoclinic	Rhombohedral
Space group	$P2_1/m$ (no. 11)	$R3c$ (no. 161)
Symmetry	Centrosymmetric	Non-centrosymmetric (polar)
Z	2	6
D (calculated) (g/cm^3)	2.686	2.900
F(000)	452	2208
a (Å)	9.3195(8)	17.2991(9)
b (Å)	6.6052(6)	17.2991(9)
c (Å)	11.0657(9)	17.2991(9)
α (°)	90.0	117.373(2)
β (°)	114.095(3)	117.373(2)
γ (°)	90.0	117.373(2)
Volume (Å^3)	621.82(9)	2143.5(4)
μ (mm^{-1})	7.497	8.980
Min/max transmission	0.380/0.585	0.196/0.810
θ range (degrees)	3.08–36.39	2.76–27.22
Index ranges	−13 < h < 13	−24 < h < 24
	−9 < k < 9	−24 < k < 24
	−15 < l < 15	−24 < l < 24
Data/restraints/parameters	2051/0/76	4367/1/110
GooF of F^2	1.195	1.200
No. total reflections	28,187	113,765
No. unique reflections	2051	4367
No. obs Fo > 4σ(Fo)	1983	3746
R_1 [Fo > 4σ(Fo)]	0.0197	0.0494
R_1 [all data]	0.0205	0.0683
wR_2 [Fo > 4σ(Fo)]	0.0512	0.1128
wR_2 [all data]	0.0518	0.1347
Largest peak and hole (e Å^3)	0.48 and −2.71	1.61 and −1.76

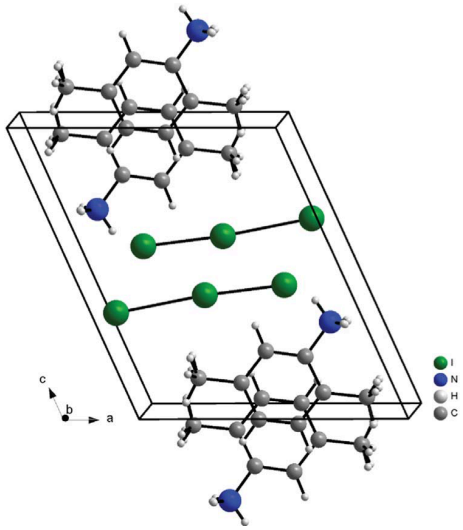

Figure A10.1. Crystal structure of 2,5-DMAI$_3$. The hydrogen atoms of the methyl groups are split over two positions by symmetry and should be considered illustrative only.

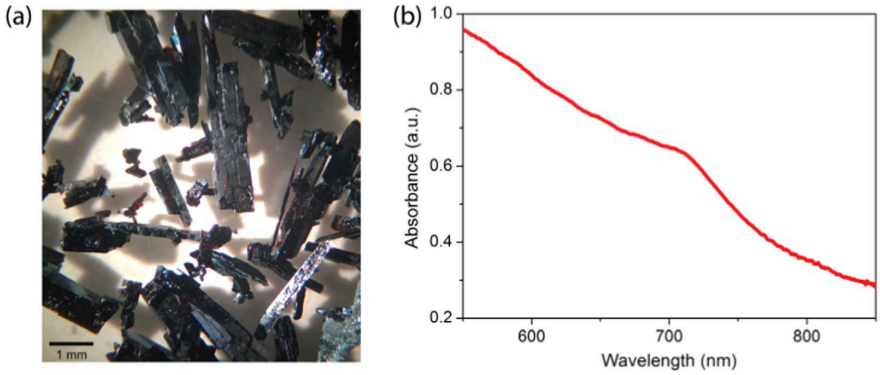

Figure A10.2. a) Photograph of 2,5-DMAI$_3$ single crystals. **b)** Absorption spectrum of 2,5-DMAI$_3$ single crystal, showing excitonic absorption at around 720 nm.

Experimental details of the single crystal XRD measurement

For the structure of (PyrC$_4$NH$_3$)PbI$_3$·(TCNQ), X-ray intensity data were collected at 100 K on a Rigaku Oxford Diffraction Supernova Dual Source (Cu at zero) diffractometer equipped with an Atlas CCD detector using ω scans and CuKα (λ = 0.71073 Å) radiation. The images were interpreted and integrated with the program CrysAlisPro. Using Olex2, the structure was solved by direct methods using the ShelXS structure solution program and refined by full-matrix least-squares on F^2 using the ShelXL program package. Non-hydrogen atoms were anisotropically refined and the hydrogen atoms in the riding mode and isotropic temperature factors fixed at 1.2 times U(eq) of the parent atoms.

Crystal data for compound (PyrC$_4$NH$_3$)PbI$_3$·(TCNQ). $C_{32}H_{24}I_3N_5Pb$, M = 1066.46, monoclinic, space group *I*a (No. 9), a = 8.0302(2) Å, b = 42.3950(9) Å, c = 9.4390(2) Å, β = 97.458(2)˚, V = 3186.23(13) Å3, Z = 4, T = 100 K, ρ_{calc} = 2.223 cm^{-3}, μ(Cu-Kα) = 8.232 mm^{-1}, F(000) = 1968, 46480 reflections measured, 8105 unique (R_{int} = 0.0523) which were used in all calculations. The final R1 was 0.0260 (I >2σ (I)) and *wR2* was 0.0556 (all data).

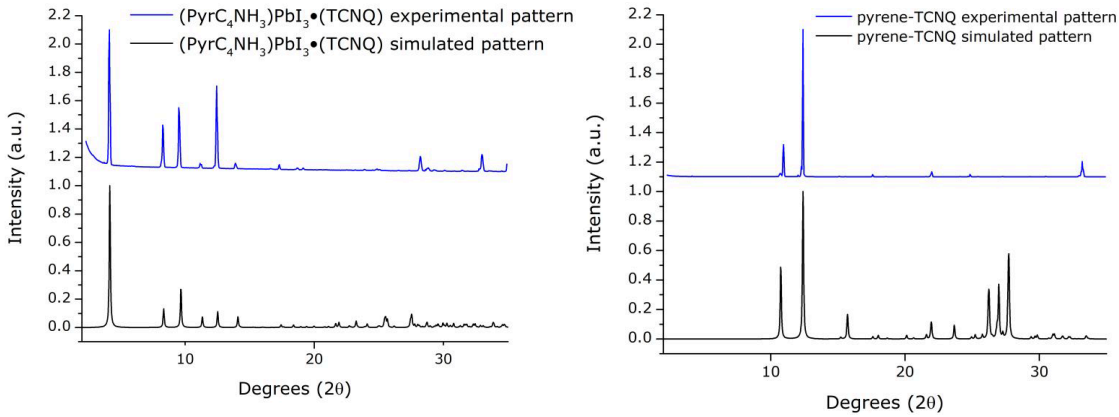

Figure A10.3. X-ray diffraction. Left) 1D hybrid (PyrC$_4$NH$_3$)PbI$_3$•(TCNQ)**. Right)** Organic pyrene-TCNQ charge-transfer complex.

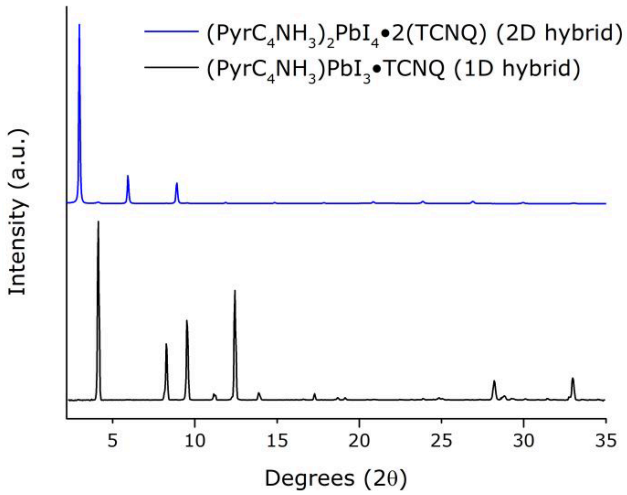

Figure A10.4. X-ray diffraction 2D vs 1D. Top, blue) thin film $(PyrC_4NH_3)_2PbI_4$•2(TCNQ). **bottom, black)** Crystals of $(PyrC_4NH_3)PbI_3$•(TCNQ).

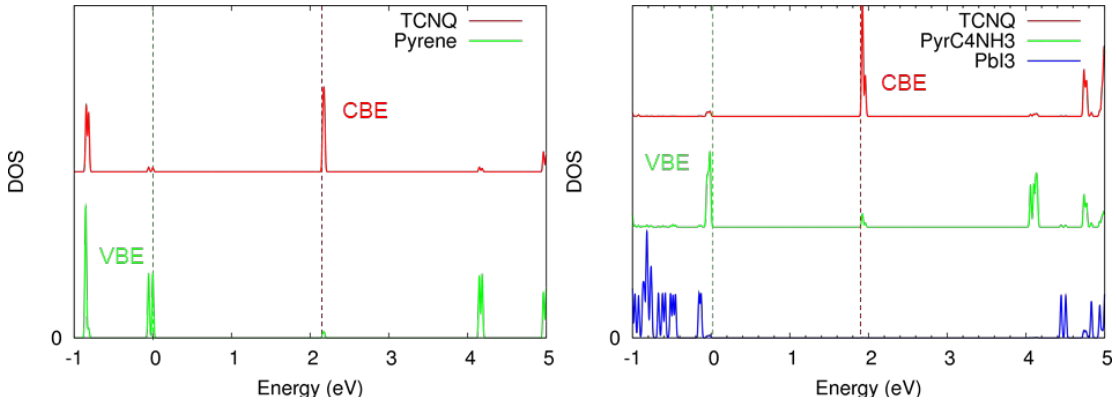

Figure A10.5. Comparison between the partial density of states (DOS). Organic charge transfer complex (on the left) and the 1D hybrid (PyrC4NH3)PbI3•(TCNQ) perovskitoids crystal (on the right). Calculation performed at the same level of theory (PBE0 hybrid functional).

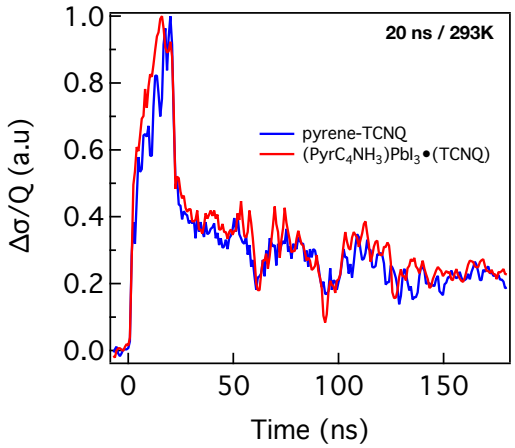

Figure A10.6. Normalized PR-TRMC Conductivity transients at 293K.

Curriculum Vitae

María Camila Gélvez Rueda was born in Bucaramanga, Colombia, on the 7th of October of 1989. She obtained her Bachelor degree in Chemical Engineering (*cum laude)* at the Industrial University of Santander (UIS) in 2012. Afterwards, María worked in Colombia as researcher for the National Research Center of Tropical Aromatic and Medicinal Plant Species (CENIVAM) and as process engineer in the petrochemical industry.

In August of 2013, María moved to the Netherlands to study a Masters in Sustainable Energy Technology at Delft University of Technology (TUDelft). She graduated with a thesis entitled "Revealing the Charge Carriers Dynamics in Perovskites for Photovoltaics" under the supervision of Dr. Ir. Tom J. Savenije and Dr. Ferdinand C. Grozema.

In September 2015, she started working in the PhD project 'In Control of Exciton and Charge Dynamics in Molecular Crystals (ICONICAL)' in the Opto-electronic Materials Section at Delft University of Technology under the supervision of Dr. Ferdinand C. Grozema. She carried out experimental research on the optoelectronic properties of hybrid organic-inorganic perovskites. In addition, she assisted laboratory first year courses and supervised two bachelor and two master students.

List of Publications

(1) Gélvez-Rueda, M. C., Cao, D. H., Patwardhan, S., Renaud, N., Stoumpos, C. C., Schatz, G. C., Hupp, J. T., Farha, O. K., Savenije, T. J., Kanatzidis, M. G., Grozema, F.C. Effect of Cation Rotation on Charge Dynamics in Hybrid Lead Halide Perovskites. *J. Phys. Chem. C.* **2016**. *120* (30), 16577–16585; https://doi.org/10.1021/acs.jpcc.6b06722.

(2) Hutter, E. M., Gélvez-Rueda, M. C., Osherov, A., Bulović, V., Grozema, F. C., Stranks, S. D., Savenije, T. J. Direct-Indirect Character of the Bandgap in Methylammonium Lead Iodide Perovskite. *Nat. Mater.* **2017**. *16* (1), 115–120; https://doi.org/10.1038/nmat4765.

(3) Gélvez-Rueda, M. C., Renaud, N., Grozema, F. C. Temperature Dependent Charge Carrier Dynamics in Formamidinium Lead Iodide Perovskite. *J. Phys. Chem. C.* **2017**. *121* (42), 23392–23397; https://doi.org/10.1021/acs.jpcc.7b09303.

(4) Gélvez-Rueda, M. C., Hutter, E. M., Cao, D. H., Renaud, N., Stoumpos, C. C., Hupp, J. T., Savenije, T. J., Kanatzidis, M. G., Grozema, F. C. Interconversion between Free Charges and Bound Excitons in 2D Hybrid Lead Halide Perovskites. *J. Phys. Chem. C.* **2017**. *121* (47), 26566–26574; https://doi.org/10.1021/acs.jpcc.7b10705.

(5) Bartesaghi, D., Slavney, A. H., Gélvez-Rueda, M. C., Connor, B. A., Grozema, F. C., Karunadasa, H. I., Savenije, T. J. Charge Carrier Dynamics in Cs2AgBiBr6 Double Perovskite. *J. Phys. Chem. C.* **2018**. *122* (9), 4809–4816; https://doi.org/10.1021/acs.jpcc.8b00572.

(6) Hutter, E. M., Gélvez-Rueda, M. C., Bartesaghi, D., Grozema, F. C., Savenije, T. J. Band-Like Charge Transport in Cs2AgBiBr6 and Mixed Antimony-Bismuth Cs2AgBi1- XSbxBr6 Halide Double Perovskites. *ACS Omega.* **2018**. *3* (9), 11655–11662; https://doi.org/10.1021/acsomega.8b01705.

(7) Herckens, R., Van Gompel, W. T. M., Song, W., Gélvez-Rueda, M. C., Maufort, A., Ruttens, B., D'Haen, J., Grozema, F. C., Aernouts, T., Lutsen, L., et al. Multi-Layered Hybrid Perovskites Templated with Carbazole Derivatives: Optical Properties, Enhanced Moisture Stability and Solar Cell Characteristics. *J. Mater. Chem. A.* **2018**. *6* (45), 22899–22908; https://doi.org/10.1039/c8ta08019d.

(8) Kamminga, M. E., Gélvez-Rueda, M. C., Maheshwari, S., van Droffelaar, I. S., Baas, J., Blake, G. R., Grozema, F. C., Palstra, T. T. M. Electronic Mobility and Crystal Structures of 2,5-Dimethylanilinium Triiodide and Tin-Based Organic-Inorganic Hybrid Compounds. *J. Solid State Chem.* **2019**. *270* (November 2018), 593–600; https://doi.org/10.1016/j.jssc.2018.12.029.

(9) Marchal, N., Van Gompel, W.T.M., Gélvez-Rueda, M. C., Vandewal, K., Van Hecke, K., Boyen, H.G., Conings, B., Herckens, R., Maheshwari, S., Lutsen, L., Quarti, C., Grozema, F.C., Vanderzande, D., Beljonne, D. Lead-halide perovskites meet donor-acceptor charge-transfer complexes: a new class of perovskitoids. *Chem. Mater.* **2019***.* 31, 17, 6880-6888; *https://doi.org/10.1021/acs.chemmater.9b01289.*

(10) Hartono, N.T.P., Sun, S., Gélvez-Rueda, M. C., Pierone, P.J., Erodici, M.P., Yoo, J., Wei, F., Bawendi, M., Grozema, F. C., Sher, M., Buonassisi,T., Correa-Baena, J.P. Structural Dimensionality Affects Carrier Mobility and Performance in Lead Halide Perovskites. *J. Mater. Chem. A.* **2019***. doi: 10.1039/C9TA05241K.*

(11) El Ajjouri, Y., Locardi, F., Gélvez-Rueda, M.C., Prato, M., Sessolo, M., Ferretti, M., Grozema, F.C., Palazon, F., Bolink, H. Mechanochemical Synthesis of Sn(II) and Sn(IV) Iodide Perovskites and Study of Their Structural, Chemical, Thermal, Optical, and Electrical Properties. *Energy Technol.* **2019***. 1900788; https://doi.org/10.1002/ente.201900788.*

(12) Gélvez-Rueda, M.C., Fridriksson, M.B., van der Stam, W., Dubey, R.K., Jager, W.F., Grozema, F.C. Overcoming the Large Exciton Binding Energy in Two-Dimensional Perovskite Nanoplatelets by Attachment of Strong Organic Electron Acceptors. *Submitted for Publication.* **2019***.*

(13) Gélvez-Rueda, M.C., Van Gompel, W.T.M., Herckens, R., Lutsen, L., Vanderzande, D., Grozema, F.C. Inducing charge separation in solid state 2D hybrid perovskites through the incorporation of organic charge-transfer complexes. *Submitted for publication.* **2019***.*

(14) Hong, L., Milić, J.V., Ahlawat, P., Mladenović, M., Kubicki, D.J., Jahanabkhshi, F., Ren, D., Gélvez-Rueda, M.C., Ruiz-Preciado, M.A., Ummadisingu, A., Liu, Y., Tian, C. Pan, L., Zakeeruddin, S.M., Hagfeldt, A., Grozema, F.C., Rothlisberger, U., Emsley, L., Han, H. and Graetzel, M. Guanine-Stabilized Formamidinium Lead Iodide Perovskites. *Just Acceptted in Angewandte Chemie.* **2019***.*

(15) Jahanbakhshi, F., Mladenović, M., Merten, L., Gelvez-Rueda, M.C., Ahlawat, P., Li, Y., Hinderhoffer, A., Dar, M.I., Tress, W., Carlson, B., Ummadisingu, A., Zakeeruddin, S.M., Schreiber, F., Hagfeldt, A., Rothlisberger, U., Grozema, F.C., Milić, J.V., and Graetzeld, M. Theoretical insights on structural and photophysical properties of adamantyl-based layered hybrid perovskites. *In Preparation.* **2020***.*

(16) Gelvez-Rueda, M.C., Ahlawat, P., Merten, L., Jahanbakhshi, F., Mladenović, M., Hinderhoffer, A., Dar, M.I., Li, Y., Dučinskas, A., Carlson, B., Tress, W., Ummadisingu, A., Zakeeruddin, S.M., Schreiber, F., Hagfeldt, A., Rothlisberger, U., Grozema, F.C., Milić, J.V., and Graetzeld, M. High Photoconductivity and Long Charge Carrier Lifetimes in Formamidinium−Based Low–Dimensional Hybrid Perovskites. *In Preparation.* **2020***.*

(17) Gélvez-Rueda, M.C., Mao, L., Stoumpos, C.C., Kanatzidis, M.G., and Grozema, F.C. Exciton and Excited State Dynamics in 2D Perovskites. In preparation. **2020***.*

List of Oral Presentations

(1) “Charge Mobility and Recombination Dynamics in CH3NH3PbI3” –Dutch Perovskite workshop – Delft, The Netherlands- June 2015.

(2) “Charge Mobility and Recombination Dynamics in CH3NH3PbI3” – The Dutch Chemistry Conference (CHAINS 2015) – Veldhoven, The Netherlands- December 2015.

(3) “Charge Mobility and Recombination dynamics in Hybrid Halide Perovskites” - Perovskite Thin Film Photovoltaics Conference 2016 (ABXPV16) – Barcelona, Spain - March 2016.

(4) “Charge and Excited State Dynamics in 2D Halide Perovskites” – Physics@Veldhoven (FOM 2017) – Veldhoven, The Netherlands- January 2017.

(5) “Interconversion between Free Charges and Bound Excitons in 2D “Ruddlesden–Popper” Perovskites” – Dutch Perovskite workshop – Groningen, The Netherlands - June 2017

(6) “Effect of the Organic Cation on Organic-Inorganic Perovskites” - Perovskite Photonics and Optoelectronic 2018 (PEROPTO18) – Rennes, France - March 2018.

(7) “Extending the Functionality of the Organic Cation in 2D Hybrid Perovskites” – Dutch Perovskite workshop – Eindhoven, The Netherlands- June 2018.

(8) “Interconversion between Free Charges and Bound Excitons in 2D “Ruddlesden–Popper” Perovskites” – European Optical Society Biennial Meeting (EOSAM2018) – Delft, The Netherlands - October 2018

(9) “Extending the Functionality of the Organic Cation in 2D Hybrid Perovskites: Introduction of Organic Charge-Transfer Complexes” – The Dutch Chemistry Conference (CHAINS 2018) – Veldhoven, The Netherlands- December 2018.

(10) “Extending the Functionality of 2D Hybrid Perovskites by Organic Charge-transfer Complexes” – International Conference on Perovskite Solar Cells, Photonics and Optoelectronics (NIPHO19) – Jerusalem, Israel - February 2019

(11) “Efficient photo-generation of mobile free charge carriers in 2D hybrid perylene diimide-perovskite nanoplatelets” - The 29th International Conference on Photochemistry (ICP2019) – Boulder, Colorado, The United States of America – July 2019